Durham E-Theses

Multi-band Wideband Channel Measurements in Indoor and Outdoor Environments above 6 GHz for 5G Networks

EL-FAITORI, SAIED,O,ALI

How to cite:

EL-FAITORI, SAIED,O,ALI (2020) *Multi-band Wideband Channel Measurements in Indoor and Outdoor Environments above 6 GHz for 5G Networks*, Durham theses, Durham University. Available at Durham E-Theses Online: http://etheses.dur.ac.uk/13669/

Use policy

Multi-band Wideband Channel Measurements in Indoor and Outdoor Environments above 6 GHz for 5G Networks

By

SAIED EL FAITORI

A thesis submitted to Durham University
for the degree of Doctor of Philosophy

Department of Engineering
Durham University, United Kingdom
Submitted March 2020

Abstract

This document presented the results of ultra-wideband of multi-bands measurements performed in three different indoor environments such as large office, factory like and small office and one outdoor street canyon scenario at the science site of Durham University, United Kingdom. The measurements conducted using a wideband chirp sounder developed at Durham University. An analytical review of the radio wave propagation mechanisms and formulas is presented in addition to the background of the channel characteristics parameters and statistics. The parameters reviewed are the received signal strength, path loss, the excess, average and RMS delay spread, in addition to the angular parameters such as the angle of arrival (AoA), angle of departure (AoD) and the RMS angular spread. A literature survey for about 80 paper of the previous work are studied and summarised for the measurements and simulation performed to estimate different parameters in both indoor and outdoor scenarios.

Two different measurements set up were performed in three indoor environments and one outdoor scenario to measure mainly, the frequency dependency in various channel characteristics parameters. In the first set the measured parameters are the received signal strength, path loss, and the excess, average and the cumulative distribution function (CDF) and the RMS delay spread in three indoor environments. While in the second set the 3D angular parameters such as AoA, AoD and RMS angular spread in both Tx and Rx sides are studied in three indoor and one outdoor environment mentioned earlier. The measurements set up and procedures are presented for each set of measurement. The measurements were performed using a wideband channel sounder up to 6 GHz for both sets. Five different frequency bands (i.e.13.4 GHz, 26.8 GHz, 54.2 GHz, 62.6 GHz and 70 GHz) were used in the first set and three bands (i.e.13.4 GHz, 26.8 GHz, 62.6 GHz) for the second set. A steerable horn antenna at both side using 3D positioner in the second set of measurements, while an omnidirectional antenna was used at the receiver side in the first set. A summary and discussion the extracted results for each set of measurements are given. Conclusions about the achieved results and the recommended future work are provided.

Declaration

No portion of this work referred to in this thesis has been submitted in support of an application for another degree or qualification of this or any other university, or institution of learning.

Statement of Copyright

"The copyright of this thesis rests with the author. No quotation from it should be published without the author's prior written consent and information derived from it should be acknowledged."

Dedication

This thesis is dedicated

To

The soul of my parents and my niece

(Nairooz)

Acknowledgment

List of Contents

List of Tables

List of Figures

List of Symbols

ABG	Alpha Beta Gamma
ADC	Analogue-to-Digital Converter
AoA	Angle of Arrival
AoD	Angle of Departure
CDF	Cumulative Distribution Function
CI	Close-In
CW	Continuous Wave
dB	Decibel
dBi	dB Gain with respect to an isotropic antenna
dBm	dB referred to one milliwatt
DDFS	Direct Digital Frequency synthesiser
FI	Floating-Intercept
FMCW	Frequency Modulated Continuous Wave
Gbps	Gaga bit per second
HPBW	Half-Power Beamwidth
IEEE	Institute of Electrical and Electronic Engineers
ITU-R	International Telecommunication Union Recommendations
LED	Light Emitting Diode
LMDS	Local Multipoint Distribution Service
LMCS	Local Multipoint Communication Systems
LNA	Low Noise Amplifier
LO	Local Oscillator
LoS	Line-of-Sight
MED	Maximum Excess Delay
MIMO	Multiple-Input Multiple-Output
MMSE	Minimum Mean Square Error
mmWave	millimetre-wave
NLoS	Non-Line-of-Sight
PDP	Power Delay Profile
PLE	Path Loss Exponential
RF	Radio Frequency
RMS	Root Mean Square

Rx	Receiver
Tx	Transmitter
US	Uncorrelated Scattering
UEs	Users equipment
VNA	Vector Network Analyser
WSS	Wide-Sense Stationary
WSSUS	Wide-Sense Stationary Uncorrelated Scattering

CHAPTER 1

INTRODUCTION

1.1 Introduction

1.1.1 Motivation

The spectrum of wireless communication below 6 GHz band has become congested through the world, as a result of the extensive use of smart devices such as phones and tablets. The usage of the Wireless network is expected to increase steeply throughout the next decade by a factor of 1000 [1]. Therefore, several researchers believe that the millimetre-wave (mmWave) spectrum can meet the enormous demand for broadband wireless communications, where the huge amount of mmWave bandwidth can accommodate the ever-escalating consumption for wireless. To provide giga-bit per second (Gbps) data rate, a new and suitable wireless infrastructure is needed between a transmitter and a receiver, which the existing Ultra High Frequency and Microwave networks cannot offer. The spectrum of mmWave can offer bandwidths between 30 and 50 GHz that can be used to provide data rates of multi-Gbps [2]. There are a number of candidate frequency bands that are considered to meet the needed high data rates for wideband communication systems such as 28 GHz and 38 GHz bands which recently have been used for Local Multipoint Distribution Service (LMDS) and Local Multipoint Communication Systems (LMCS), and for mobile cellular, the 60 GHz which currently used wireless wideband in indoor short range systems, and the E-band range between 70 and 80 GHz band is under investigation for the wideband applications such as backhaul to backhaul, backhaul to mobile and short range indoor wireless communication systems. Therefore, it is important to develop an accurate and reliable channel model at the mmWave frequency bands above 6 GHz. To investigate the channel characteristics at these frequency bands there are several measurement techniques and systems normally used. The most widely techniques are the wideband sounding systems such as pulse compression, periodic pulse sounding, convolution matched filter, swept time delay correlation and the use of vector network analyser. There are mainly two important technical limitations constrained by these techniques:

1- The maximum measured resolution of the multipath echoes in the typical impulse response.

2- To keep the synchronisation between the transmitter and receiver, some techniques need a physical connection (cable) between them all the time during the measurement.

The sounding system used in the project deal with these limitations, where firstly, there is no need to use physical connection between the receiver and transmitter during the measurement where they are synchronised on-air which allowing the receiver to move freely in the measurement environment without any range limitation except for the transmitted power. Secondly, the large measurement bandwidth, the sounding method used in this sounder is the FMCW (frequency modulation continuous wave) or chirp method which is a wideband channel sounder, where this sounding system can measure up to 6 GHz, which can measure time resolution up to 0.16 nanoseconds between the multipath echoes arriving at the receiver side. There is another way of classifying the channel sounders based on the number of transmitting and receiving antennas such as single input single out put (SISO) where single antenna used at both sides, single input multiple output (SIMO) where single transmit antenna and two antennas or more at the receiver side, multiple input single output (MISO) where two antennas or more used at the transmitter and one antenna at the receiver and finally, multiple input multiple output (MIMO) in this type two antennas or more used at both sides. The used architecture depends on the application and the required information. One of the applications of using more than one antenna either at the receiver or the transmitter is to mitigate and overcome the effects of depolarization that caused by multipath phenomena due to multiple reflection, diffraction and scattering from the natural and artificial obstructions located in the areas around the transmitter and the receiver antennas by using polarization diversity antennas. In this project the SISO architecture was used for all the performed measurements and the antennas at both sides were vertically polarised.

1.1.2 Objectives and contribution

The target of this thesis is to study and investigate the channel characteristics such as path loss, delay spread and 3D angular spread at different frequency bands above 6 GHz and establish experimental models of wireless mmWave channels in both indoor and outdoor environments.

The frequency dependence of different channel parameters is one of the main aims of this study, since the research work included up to five different frequency bands at each measured scenario, and the capability of the channel sounder used, which has been developed at Durham University, where the time resolution of this sounder is much higher than all the other sounders were used in the reviewed studies and meet the measurement requirement for the channel parameters in the 5G system design. An extensive measurements camping was performed in three typical indoor scenarios including (large office, factory like and small office) where these scenarios represented the most common indoor environments and an outdoor environment (street canyon). Different controlling C codes and computation MATLAB codes have been created to measure, process, analyse and plot the collected data to estimate the desired parameters. Some of the research results have been contributed in ITU recommendation.

1.2 Review of chapter contents

This thesis contains six chapters. Chapter Two provides a brief description of the theoretical background for the radio propagation channel characteristics such as free space propagation, propagation in different environments, propagation mechanisms, path loss models and multipath phenomena in addition to the estimated statistical parameters such as signal strength, delay spread and angular spread parameters. A literature review of the previous work conducted using wideband measurements to study different channel characteristics in various indoor and outdoor environments at different frequency bands is presented. The literature review includes different path loss models, penetration and reflection loss of different materials, delay spread, and angular spread studies. The sounding technique used and the measurements set-up and the type of used antennas for each measurement scenario were also presented.

Chapters Three and Four present a description of three indoor measurement environments (large office, small office and factory like) set-up and hardware used such as the wideband channel sounder specifications, and the related equipment and procedures used to extract the power delay profile, subsequently the received power and other estimated parameters form the collected data. Chapters Three and Four also present detailed description of the performed extensive measurement campaign in three different indoor environments including the measurements layouts, configurations and locations, for the line-of-sight (LoS) and non-line-of-sight (NLoS) situations. Finally, the data analysis and extracted path loss models and the delay spread parameters are presented. Moreover, a summary discussion of the extracted results at the end of each chapter were presented.

Chapter Five presents a description of the directional measurement set-up and hardware used including the channel sounder, 3D positioner and antenna types and mounting, to extract the angular power delay profile. Then the received power at each azimuth/elevation pointing angle and other estimated parameters from the collected data are calculated. Moreover, chapter five presents a detailed description of the conducted measurement campaigns at three different indoor environments (large office, small office and factory like) and one outdoor scenario (street canyon) with the measurement's layouts, configurations and locations, for both LoS and NLoS situations. Furthermore, the data analysis and extracted directional parameters such as angle of arrival (AoA), angle of departure (AoD) and angular spread parameters are presented in various graph forms such as polar plot, 3D plot and tables for each scenario.

Chapter Six gives the overall conclusions of the thesis and possibilities for future work and recommendations.

1.3 Published work

The publications and conference papers contributed in.

1. S. El-Faitori and S. Salous, "Wideband channel characterization measurements in outdoor environment scenarios for 5G Networks," Festival of Radio Science (FRSci- Dec 2017).

2. S. El-Faitori and S. Salous, "Wideband 3D channel measurements in indoor and outdoor environment scenarios for 5G Networks, " The 2019 UK URSI Symposium (UK-URSI-2019) poster presented.

3. X. Raimundo, S. El-Faitori, Y. Cao, and S. Salous, "Outdoor directional radio propagation measurements in the V-band," in *2018 IEEE 29th Annual International Symposium on Personal, Indoor and Mobile Radio Communications (PIMRC)*, 9-12 Sept. 2018 2018, pp. 790-794, doi: 10.1109/PIMRC.2018.8580771.

4. X. Raimundo, S. El-Faitori and S. Salous, "Multi-band outdoor measurements in a residential environment for 5G networks," 12th European Conference on Antennas and Propagation (EuCAP 2018), London, 2018, pp. 1-4.

5. J. Towers, S. El-Faitori, and S. Salous, "Wideband 3D Performance Analysis of a Modular Antenna Array in a Street Canyon Scenario for 5G Networks," IET Antennas and Propagation Conference APC 2019.

6. J. Towers, S. El-Faitori, and S. Salous, "Performance Analysis of a V-Band Modular Antenna Array in a Street Canyon Scenario," The 2019 UK URSI Symposium (UK-URSI-2019).

7. Xavier Z. Raimundo, Adnan A. Cheema, S. El-faitori, and Sana Salous, "Simultaneous outdoor channel sounding in the V and K bands," *32nd URSI GASS, Montreal, August 2017*

CHAPTER 2

CHARACTERISTICS OF THE RADIO PROPAGATION CHANNEL

Undoubtedly, the propagation channel is the essential constraint of all radio communication networks. The radio channel between the transmitter and receiver can change considerably from a simple Line-of-Site (LoS) situation to a compound non line-of-site one, which is strictly blocked in outdoor environments by buildings, mountains and foliage or by partitions, furniture and walls in indoor scenarios. Whereas in the wire-line communication systems, the features of the link (e.g. Coax, Fibre) are well-known, radio channels are specified as being enormously complicated and random in nature. There are many different propagation mechanisms that complicate radio wave propagation such as: reflection, refraction, diffraction, and scattering.

According to their propagation environments, radio channels can be categorised into two different types: large-scale and small-scale. The large-scale is described by the long-distance path loss and it is affected by the reflection, diffraction, and scattering, whereas small-scale fading is defined as the rapid changes in the level of received signal over very short travel distances as shown in figure 2-1. Thus, small scale fading is affected by the multipath propagation delays encountered in the channel [3].
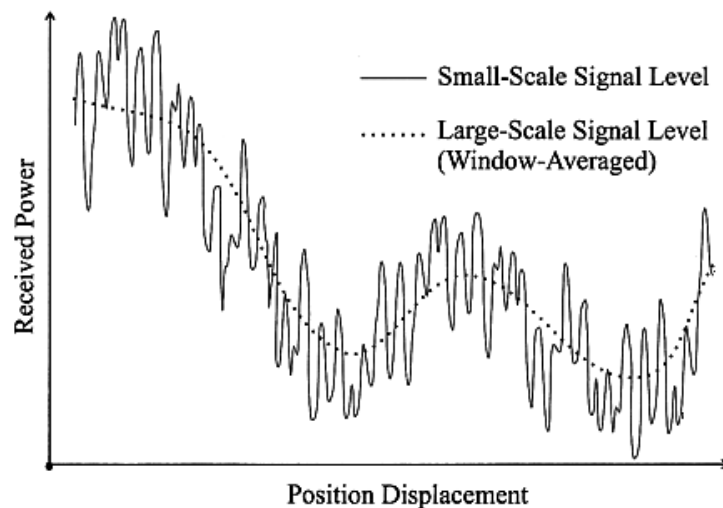
Figure 2-1 Small-scale and large-scale spatial channel fading [4]

2.1 Radio wave propagation

Radio systems are becoming an essential part of our daily life routine. To build a good radio system, radio transmission characteristics in different media such as transmission loss (path loss), and the power level required to provide good coverage over a given area, have to be known. The basic form of studying radio wave propagation is free space propagation, and the other forms of transmission loss due to absorption, scattering, reflection, refraction and diffraction in different environments [5].

2.1.1 Free space propagation

In this type of propagation, the transmit antenna should be located at a certain height above the ground surface to guarantee no obstacles between the transmit and receive antennas. Assuming a transmit antenna, gain is G_T. The power density P_d at a distance d is given by.

$$P_d = \frac{P_T G_T}{4\pi d^2}$$

2-1

At the receiving side, the antenna has an effective area A called the aperture. This gives an effective power P_R as in equation 2-2

$$P_R = \frac{P_T G_T}{4\pi d^2} A$$

2-2

where

$$A = \frac{\lambda^2 G_R}{4\pi}$$

2-3

The ratio between received and transmitted power is known as the free space equation, which is equal to

$$\frac{P_R}{P_T} = G_T G_R \left(\frac{c}{4\pi f d}\right)^2$$

2-4

where $c = f\lambda$

The free space equation can be written in logarithmic form in dB units as follows

$$FSPL = 10 \, log_{10} \left(\frac{P_T}{P_R}\right)$$

2-5

$$\text{FSPL} = -10 \, log_{10} \, G_T - 10 \, log_{10} \, G_R + 20 \, log_{10} \, f + 20 \, log_{10} \, d + K \qquad \textbf{2-6}$$

where

$$K = 20 \, log_{10} \left(\frac{4\pi}{3 \times 10^8} \right) = -147.56 \qquad \text{2-7}$$

2.1.2 Propagation in different environments

The free space model is different from the practical situation, where the environment most of the time contains obstacles between the transmitter and the receiver such as: trees, walls, buildings, persons, etc. To predict the signal strength in practical situations, researchers have studied different scenarios, such as irregular terrain, flat terrain, urban, suburban, rural and indoor areas [5].

Flat terrain: in this scenario, the direct line of sight component and the ground reflected signal are the main components of the received field strength as shown in figure 2-1. The direct signal follows the free space model and the reflected signal equals the product of the reflection index and cosine of the reflection angle with the ground.
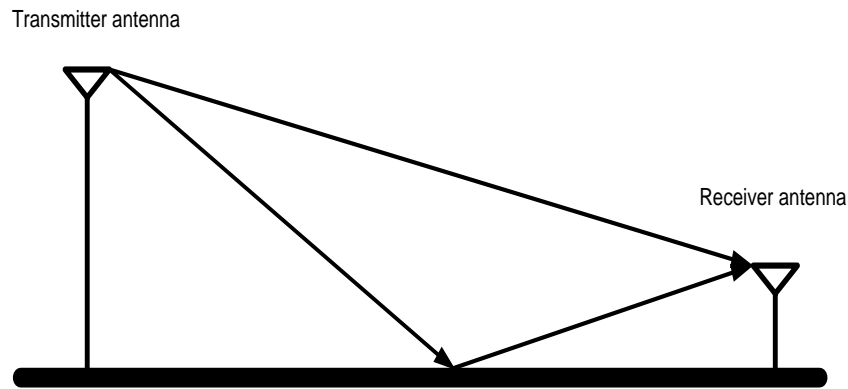
Figure 2-2 propagation over flat terrain

Rough terrain: this scenario is more practical than the flat terrain, where the assumption that when the incident signal touches the ground there is a specular reflection. In the rough terrain, there are many sides, that may cause diffuse reflection or scattering, which depends on the rough surface dimensions comparable to the incident signal wavelength and the incident angle. For some incident angles, the surface can be considered as a smooth surface. A principle known as Rayleigh criterion is normally used, as illustrated in figure 2-3.
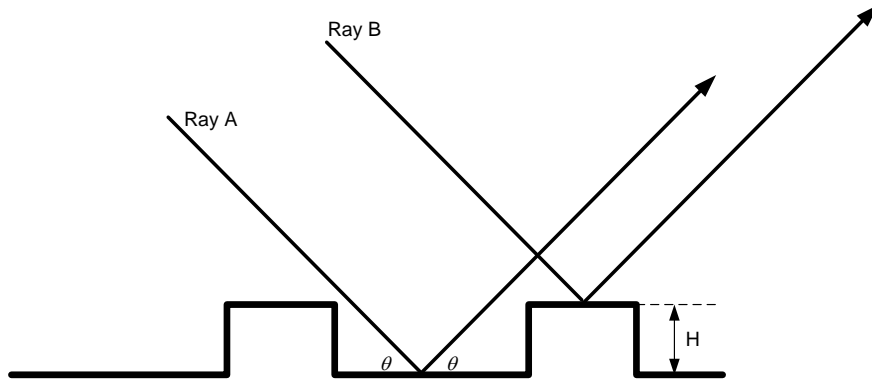
Figure 2-3 Rayleigh criterion for irregular surfaces

The path difference between the two rays A and B is given by.

$$\Delta d = 2Hsin\theta \hspace{6cm} \textbf{2-8}$$

and the phase difference

$$\Delta\theta = \frac{4\pi H}{\lambda} sin\theta \hspace{5cm} \textbf{2-9}$$

The value of θ is quite small in practical radio propagation and the height H is replaced by its standard deviation σ, so equation 2-9 can be rewritten as

$$k \cong \frac{4\pi\sigma\theta}{\lambda} \hspace{6cm} \textbf{2-10}$$

When $k < 0.1$, the surface can be considered as smooth. $If\ k > 10$, the surface is considered as a highly diffused reflector and the reflected signal is sufficiently small that it can be ignored.

2.1.3 Propagation mechanisms

In real environments electromagnetic waves, meet different media. According to the media properties there are three basic propagation mechanisms: reflection, diffraction and scattering [5].

I-Reflection**:**

Electromagnetic waves are reflected if incident on a medium which has dimensions significantly large compared to the wavelength. Depending on the media properties, it can be specular or diffuse. In specular reflection, the incident and reflected angles are equal as shown in figure 2-4.
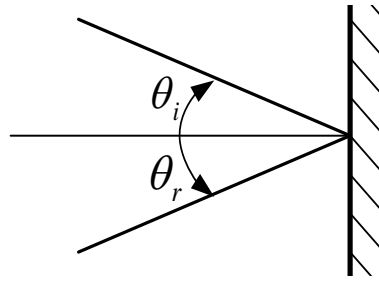
Figure 2-4 specular reflection

In perfect conductor the electric and magnetic fields are equal to zero, where the normal incident signal will be entirely reflected in the opposite direction with the same magnitude as shown in figure 2-5.
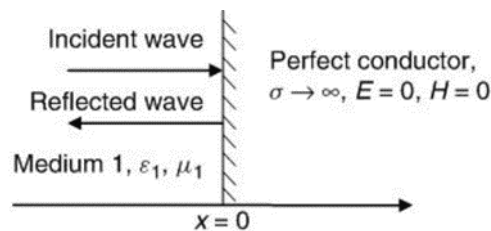
Figure 2-5 Reflection by a perfect conductor [3]

While in perfect dielectric for normal incidence, some of the wave will be transmitted and some reflected as shown in figure 2-6.
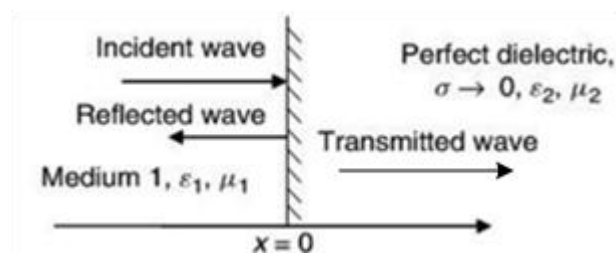
Figure 2-6 Reflection by a perfect dielectric [3]

II- Diffraction:

Normally happens when there is an obstacle between the transmitter and the receiver. According to Huygen's principle as shown in figure 2-7, waves can be formed behind the obstacle even if there is no line-of-sight (LoS) between the two sides of the antennas. Diffraction illustrates how radio wave signals can travel in different environments without a LoS path. The other name for this phenomenon is "shadowing," because the diffracted signal can reach the receiver even without a line of sight path.
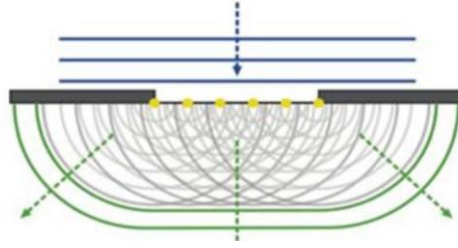
Figure 2-7 Illustration of Huygen's principle [3]

III- Scattering:

Occurs when the electromagnetic wave is incident on an object with dimensions that are equal to or less than the wavelength of the wave, where the relative intensity is proportional to $1/\lambda^4$. This means that scattering will increase as the frequency increases. The same physical principles of diffraction can be applied for scattering, where the energy from a transmitter is reradiated in many different directions.

2.1.4 Path loss models

Prediction of the signal strength is very important in any wireless communication system design. Accurate prediction models are necessary for each different environment. The two main factors that determine the classification parameters are: the terrain surface characteristics (flat, rough, forest, etc.) and the man-made objects (vehicles, buildings, etc.). For more common scenarios there are some models that have been developed.

2.1.4.1 The Egli model

An experimental model has been developed by Egli for irregular terrains in the frequency range between 90 and 900 MHz. the propagation characteristics are following the inverse of the fourth power law of the plane earth propagation [6].

$$L = G_R G_T \left(\frac{h_T h_R}{d^2}\right)^2 \left(\frac{40}{f}\right)^2 \qquad\qquad \textbf{2-11}$$

where: h_T : Transmit antenna height, h_R : Receive antenna height, d : Path length,

2.1.4.2 The JRC method

This model is based on a topographic computer database to predict the path loss between the transmitter and the receiving selected point. There are two ways of calculation based on the LoS situation. If there is a LoS, the program will calculate the path loss using the free space and

plan earth equation. If not, it will calculate the diffraction loss by using mathematical calculations [7, 8].

2.1.4.3 The Longley-Rice model

In this technique the median path loss is predicted over irregular terrain using a computer program. It is also defined as the irregular terrain model and it provides variability with location, situation and time. The frequency range covered by this method between 20 MHz and 40 GHz and for path lengths from 1 km to 2000 km. There are many input parameters required for this program including: antenna heights, horizon elevation, surface refractivity, effective earth radius, and ground constant and many other inputs [9].

2.1.4.4 The Okamura model

This model is based on experimental data collected in charts. Prediction of path loss is performed by following some certain steps. Starting with the basic chart for quasi-smooth terrain which provides the median attenuation. A correction factor chart is used for some other terrain types. There is a certain chart for antenna heights compensation. Some other correction factors can be used for each different scenario, such as for hilly terrain, street orientation, rolling terrain, etc. The Okumura model served as a base for the Hata model, but it is applicable only for a certain range of parameters over quasi-smooth terrain. It was extended in Europe for some other environments by COS231-Hata model [10].

2.1.4.5 Other methods

Some other methods used analytical tools rather than empirical ones. Such as ray tracing, uniform geometrical theory of diffraction, Bullintons method, Epstein-Peterson method, Japanese method and Deygout method. These methods mainly deal with knife-edge diffractions loss [11].

2.1.5 Multipath phenomena

Multipath is one of the most important characteristics of wireless communication systems. Defined as several radio signals reaching the receiving antenna from at least two different paths in a short period of time for the same transmitted signal as shown in figure 2-8. Since, they come from different paths, it is more likely that they arrive with different magnitudes and phases. Consequently, the resultant waveform of the collected signals at the receiving antenna, is a vectorial summation of all signals. According to the magnitude and phase of each signal, it

will add to or subtract from the final signal. Therefore, the resultant signal can be either strong or faded signal. There are two types of fading: long-term fading and short-term fading.

The long-term results from the movement of the receiver over long distances and causes variations in the signal magnitude. While the short-term essentially relates to the multipath phenomena, where several replicas of the transmitted signal caused by close scatterers arrive at the receiver antenna with different time delays, phases and magnitudes.
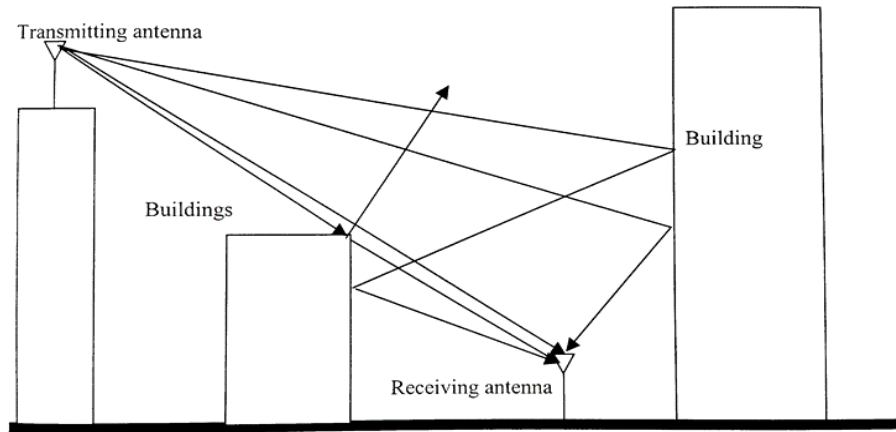
Figure 2-8 Propagation via different line-of-sight and non-line-of-sight paths

2.2 Wideband channel characterisation

The signal in a typical radio environment arrives to the receiver through multipath propagation. Several signals with different phases, time delays and magnitudes will produce the resultant signal at the receiver antenna. If the receiver moves, all these parameters are changing. In this case the transmission channel becomes very complex time varying channel. This complexity indicates a need for developing a way to characterise it. For the signal resultant from multipath propagation or scattering process, the Rayleigh distribution is a good approximation of the envelope statistics. Whereas, the Rician distribution is the best way when the resultant signal comprises of line-of-sight component or dominant specular reflection. There are many different channel models such as deterministic and random linear time-variant channel.

2.2.1 Deterministic channels

Defining the deterministic channel parameters enables practical channel characterisation. An equivalent linear filter whose characteristics are time-varying, could be the basic channel model. According to Bello [8], the input-output relationship of the filter may be described in

the frequency or/and time domains. It means that, the channel can be described by several system functions. Namely, the time domain function, the frequency domain function, the time-variant transfer function and the delay/Doppler spread function. To characterise deterministic time-variant channels, the Fourier transform, and the inverse Fourier transform can be related between a dual correspondence of the time and frequency functions.

2.2.2 Random time-variant linear channels

In real situations the radio channel is randomly time-variant, so the channel functions are governed by stochastic processes. The joint probability density functions have to be understood for an accurate channel characterisation, which is not an easy task. To get the statistical characterisation of the channel, the autocorrelation functions could be used for various system functions to facilitate the problem. Furthermore, a complete statistical description can be obtained by using the mean and the autocorrelation function, if the output is a Gaussian process [12].

Classification of channel models

The complexity of the radio propagation channel makes it very difficult to represent in an accurate way. Therefore, it is necessary to make some assumptions to simplify the channel model without losing too much accuracy. The most common simplified channel models used are the wide-sense stationary channel (WSS) and the uncorrelated scattering channel (US).

i- Wide-sense stationary channel (WSS)
The fading characteristics of the radio channel are not stationary, when the receiver is in motion. The channel can be considered as wide sense or weakly stationary for a short time interval ξ, if the fading statistics do not change during this time interval. The channel correlation functions in WSS channels are invariant under a translation in time and space. This means the autocorrelation function is dependent only on the time difference.

ii- Uncorrelated scattering channel (US)
The second common model which is called uncorrelated scattering is based on the assumption that there is no correlation between the elemental scatterers from different paths delay. These two common channel types (WSS, US) are considered as time-frequency duals. This means that if the channel is US in one domain it is WSS in the other one.

iii-Wide-sense stationary uncorrelated scattering Channel (WSSUS)

This combines the two former modes, where it is WSS in the time domain and US in the time delay variable.

2.3 Parameters and statistics

In the practical situation, there are many parameters that can be used to define the channel characteristics. Most of them are according to statistical analysis. The power delay profile, the RMS and the average delay spread are the most common parameters used to measure the channel time dispersion. In case of measuring the channel power loss, the parameters mostly used are the path loss, the received signal strength and fading. For measuring the angular parameters, the angle of arrival (AoA), angle of departure (AoD) and their RMS angular spread are mostly used. These parameters are important where they give required information that needed for the channel modelling and system design.

2.3.1 Power delay profile

The power delay profile (PDP) gives the received signal intensity over a multipath channel as a function of propagation delays. It can be empirically measured and used to obtain some channel parameters such as the delay spread, signal strength, path loss and angular parameters (i.e. Angle of arrival, Angle of departure and RMS angular spread). The average power of a multipath channel can be estimated using the power delay profile, from the first signal that arrives to the receiver to the last signal whose power level is to above a certain threshold.

2.3.2 Average, RMS delay spread, and excess delay spread

The channel time dispersion properties can be mainly defined by using these three parameters. The power delay profile analysis is the main key to define them, where the first moment of the power delay profile is equal to the average excess delay ($\bar{\tau}$).

$$\bar{\tau} = \frac{\sum_k P(\tau_k)\tau_k}{\sum_k P(\tau_k)} \qquad\qquad \textbf{2-12}$$

The maximum excess delay (MED) is an important characteristic, defined as the delay time of the relative echoes' magnitude under selected limit. The time dispersion created due to multipath effects, where the signal spreading out is known as delay spread. The square root of the second central moment of the power delay profile is equal to the RMS delay spread (σ_τ) and is given by:

$$\sigma_\tau = \sqrt{\overline{\tau^2} - (\overline{\tau})^2}$$
<div align="right">**2-13**</div>

<div align="center">where</div>

$$\overline{\tau^2} = \frac{\sum_k P(\tau_k)\tau_k^2}{\sum_k P(\tau_k)}$$
<div align="right">**2-14**</div>

The first echo of the power delay profile that arrives at the receiver is taken as a reference point at $\tau = 0$, where the delays are measured relative to this point.

<div align="center">(a)   (b)</div>
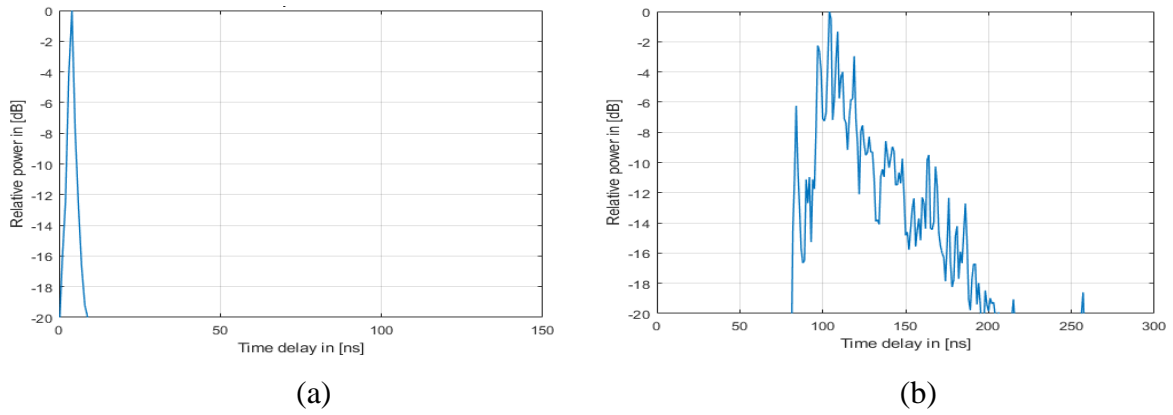
<div align="center">**Figure 2-9 Delay spread from an impulse signal**</div>

It can be seen from the figure 2-9 an example of delay spread. The transmitted signal is shown in figure 2-9a and the replicated components at the receiver in figure 2-9b due to the multipath effect, where the arrival time to the receiver differs from one signal to another according to their paths distance. The first peak is the shortest propagation path.

2.3.3 Coherence bandwidth

The coherence bandwidth is defined as the frequency range over which the channel can be considered a flat to pass all the frequency component in that range with around the same gain and linear phase. The coherence bandwidth can be defined based on the bandwidth over the frequency correlation function at two values 0.5 and 0.9.

2.3.4 Doppler spread

Delay spread and coherence bandwidth are parameters describe the channel time nature. However, they do not provide the channel time variant nature information caused by the relative motion between the transmitter and receiver or the objects movement in the channel. This movement will cause changes in the propagation path lengths either due to the change in the

receiver position or to the doppler effect due to the movement. Where the phase change rate shows as a doppler frequency shift in the propagation path.

2.3.5 Signal strength and path loss

Although the path loss was discussed in section 2.1.4, most of the presented models were for outdoor scenarios and all the conducted path loss measurements in this study were at indoor environments. For the indoor propagation measurements, a different approach was needed for path loss calculation. For that reason, two recommended path loss models were chosen for the indoor measurements which are the close-in (CI) and floating-intercept (FI) path loss model. The CI path loss model is given in equation 2-15

$$PL(f,d)[dB] = FSPL(f,d_0) + 10n \log_{10}(\frac{d}{d_0}) + X_\sigma \quad for \ d \geq d_0 \qquad \textbf{2-15}$$

where n is the path loss exponent, $d_0 = 1m$ for the mmWave and X_σ is a zero mean Gaussian random variable with standard deviation σ in dB [13]

For the CI model a reference distance d_0 is used, where the FSPL is the free space path loss in dB, and it is a function of frequency and is given by: *10log10(4πd₀ λ)²*. The CI path loss model can be calculated by estimating the path loss exponential (PLE = n) using the minimum mean square error (MMSE) method, which is fitting the experimental data with lowest error (by minimizing σ) by using a physical-based d_0 which represents the free space power at this distance.

The second model is the floating-intercept (FI) path loss model, is given in equation 2-16. In this model two parameters are required and the physically based reference to the transmitted power is not considered.

$$PL(d)[dB] = \alpha + 10\beta \log_{10}(d) + X_\sigma \qquad 2\text{-}16$$

where α is the floating-intercept in dB, β is the slope of the fitting line and Xσ the same as in the CI model is a zero mean Gaussian random variable with standard deviation σ in dB which explains the fluctuations of the large-scale signal around the average path loss over distance.

2.3.6 Angular parameters

The power delay profiles of Multipath components are captured for each Tx and Rx orientation angle, which provide the statistics of the received PDPs as a function in azimuth and

elevation angles for both Rx and Tx. Where the received power is calculated from the area under the PDP and can be presented in different ways such as on 3D plot in azimuth and elevation or plotted on polar plots. The adjacent spread of energy departing from the Tx antenna or arriving to the Rx antenna in the azimuth and elevation directions is defined as a lobe, where each individual lobe identifies a propagation direction of multipath [14]. Lobes are representing either AoA arriving at the receiver or AoD departing from the transmitter.

2.3.6.1 Angle of arrival or departure

The AoA or AoD is represented by the power-weighted mean pointing angle ($\bar{\theta}$) of a specific lobe and is obtained from equation 2-17.

$$\bar{\theta} = \frac{\sum_k P(\theta_k)\theta_k}{\sum_k P(\theta_k)} \qquad\qquad \textbf{2-17}$$

where k is a pointing angle index θ_k (degrees) of each angle above a pre-defined threshold level within a lobe and $P(\theta_k)$ is the received power (mW) at θ_k [14, 15].

2.3.6.2 RMS angular spread

The RMS azimuth or elevation angular spread is defined as the second moment of the power angular profile in azimuth or elevation and represent the standard deviation of power-weighted of the azimuth or elevation direction of arrival or departure and is given by equation 2-18.

$$\sigma_\theta = \sqrt{\overline{\theta^2} - (\bar{\theta})^2} \qquad\qquad \textbf{2-18}$$

Where

$$\overline{\theta^2} = \frac{\sum_k P(\theta_k)\theta_k^2}{\sum_k P(\theta_k)} \qquad\qquad \textbf{2-19}$$

where k is a pointing angle index θ_k (degrees) of each angle above a pre-defined threshold level within a lobe and $P(\theta_k)$ is the received power (mW) at θ_k [14, 15].

2.3.6.3 Number of lobes in a polar plot

This defined as the number of spatial directions (above pre-defined threshold) of the incoming energy (AoA) or outgoing energy (AoD) at the receiver or transmitter, respectively.

2.4 Literature review

This project aims to develop a wideband channel characterisation millimetre wave above 6 GHz. The work is dedicated to channel measurements and modelling. To support the deployment of extremely high capacity 5G mm-wave network, the channel model reliability

and accuracy are very important aspects. However, an inclusive and adequately validated model for the above-mentioned frequency range is not yet available. The project aims to close this gap. The frequency dependency of propagation parameters and characteristics in the frequency range of millimetre waves are the main aims of this project. As part of this project, radio channel measurements at several locations and in various propagation environments and multiple frequency bands is conducted. These are used as a basis to investigate new modelling approaches for mm-wave-specific propagation behaviour and to develop a channel model valid over the former frequency range for a large selection of scenarios. A review of the latest channel measurements in mm-wave range is provided.

2.4.1 Wideband measurements:

The channel impulse response is the usual result obtained from such measurements. The other measurement can be made for the channel time-variant characteristics, such as delay spread, angular spread, etc. This survey, will focus mainly on different aspects such as the measurement environments (i.e. indoor and outdoor scenario), the measurement parameters (i.e. path loss models, delay spread, angular spread), the simulation or sounding technique used (i.e. sliding correlator, vector network analyser, FMCW Chirp), and the measurement set up (i.e. measurement procedure, antenna type, antenna height and beamwidth, LoS and NLoS situations).

2.4.1.1 Outdoor environments

3D outdoor measurements at 28 GHz were conducted in urban environments in New York City by M. Samimi et al.[9] to measure Angle of Arrival and Angle of Departure using 10° beamwidth Steerable Antennas, where the Tx was located on the rooftop at about 40 m, 17 m and 7 m above ground. To measure the AoA the receiver antenna was rotated in 10° increments in azimuth to cover full rotation at three different elevation angles (-20°, 0° and 20°) and the Tx antenna was tilted down with -10°. To measure the AoD the Rx antenna was fixed at the azimuth/elevation angle of the strongest received power, while the Tx antenna was tilted down with -10° and rotated in azimuth in 10° increments to cover fill rotation. The paper proposed new lobe statistics, their physical meaning and the procedure to compute them. Theodore S. Rappaport[16] carried out work in an urban cellular and peer to peer RF measurements using a broad sliding correlator channel sounder technique connected to steerable horn antenna with HPBW of 7º at 38 GHz band and 7.3º at 60 GHz band and showed the propagation time delay spread and path loss as a function of separation distance in LoS and NLoS situations and the

effects of different types of scatterers and reflectors such as vehicles, foliage, brick and aluminium-sided buildings were studied. Hao Xu [17] carried out measurements at 38 GHz in an outdoor environment during different weather conditions where the Tx and Rx were located indoors and they were left to run continuously using spread spectrum sliding correlator channel sounder with 200 MHz bandwidth, to estimate worst case multipath channel characteristics involving relative power, time of arrival, angle of arrival, excess delay zone and relative power zone. Youngbin Chang [18] investigated radio channel characteristics using 3D ray- tracing method in an urban environment of Downtown Ottawa at 28 GHz. Important radio channel parameters are provided, such as shadow fading, path loss exponent, delay spread, and angle spread and a proposed dual-slope path loss method for NLoS situation. Jinyi Liang [19] presented a geometrical approach based on measurement data, an estimation of the last hop multipath locations. The measurements were conducted in an urban street environment in Korea at 28 GHz using a wideband channel sounder with 500 MHz bandwidth with 30° HPBW horn antenna at the Tx side and it was fixed. At the Rx side, a 10° HPBW antenna was rotated in azimuth with a 10° step size in horizontal level only. Geoege R. MacCarteny Jr. [20] carried out measurements at 28 and 38 GHz in an urban environment in two different locations. Using a sliding correlator channel sounder with 800MHz bandwidth with directional steerable horn antennas with a 10.9° half power beamwidth for 28 GHz band and 7.8° for the 38 GHz band at 1.5 m Rx height and three Tx antenna heights (i.e. 36 m, 23 m and 8 m) for the 38 GHz band in Austin, Texas and two Tx heights (i.e. 17 m and 7 m) for 28 GHz band in New York City. Non-line of sight path loss using CI and FI path loss models are presented. Geoege R. MacCarteny Jr. [21] provided outdoor propagation measurements and path loss models in Downtown Manhattan in New York City using a broadband sliding correlator channel sounder at 28 and 73 GHz. Using high directive horn antennas with 10.9° HPBW and 7° HPBW for the 28 GHz band and 73 GHz band respectively, path loss models using the close-in path loss model with 1 m free space reference distance are presented for line of sight and non-line of sight situations, and floating-intercept model used for NLoS environment, where the directional received powers summed to synthesize the omnidirectional received powers. Theodore S. Rappaport [22] presented propagation measurements and channel models for frequency bands 28, 38, 60 and 73 GHz collected from different campaigns in an outdoor environment, using wideband sliding correlator channel sounder. Channel characteristics such as multipath delay speared, number of multipath components and path loss models resulted from different measurements. The paper presented by X. Raimundo, S. El-Faitori, Y. Cao, and S. Salous [23]

was dedicated to measure path loss, delay spread, and the angular spread statistics in azimuth for the 51-57 GHz 67-73 GHz frequency bands at street canyon scenario. The measurements were conducted using 2x2 MIMO dual polarized chirp sounder with horn antennas with a beamwidth (Tx = 53° and Rx=19°) for the 51-57 GHz band and (Tx=39° and Rx=15°) for the 67-73 GHz band. The measurements were conducted by rotating the antennas at the receiver with 5° step size to cover full rotation in azimuth. The collected data were analysed with 2 GHz bandwidth for both bands. The log-distance path loss model was used where the received power of all angles were summed to synthesise omnidirectional antennas for each measurement location. Y. Azar et al. [24] presented outdoor in downtown Manhattan measurement results conducted at 28 GHz band using Steerable Beam Antennas with the same setup in [14] to measure path loss using CI path loss model. G. R. MacCartney and T. S. Rappaport [25] presented outdoor propagation measurements for mobile communication channels and backhaul using a sliding correlator channel sounder with 7° half-power beamwidth directional steerable antennas in an urban environment in New York City at 73 GHz band. The Tx antenna was on two rooftop heights 7 m and 17 m above the ground. To measure the path loss using the CI path loss model, the Rx antenna was rotated in half-power beamwidth to cover full rotation in azimuth at three different elevation angles. E. Ben-Dor, T. S. Rappaport [26] presented wideband propagation measurements at 60 GHz frequency band in two different outdoor environments, the in-vehicle and peer-to-peer cellular scenarios. The measurements were conducted using sliding correlator channel sounder with 1.9 GHz bandwidth and rotating directional antennas to measure the AoA, delay spread and path loss using CI path loss model. T. S. Rappaport et al.[27] presented outdoor urban measurements campaigns were conducted around New York University at 28 GHz and the University of Texas at Austin at 38 GHz. The measurements were conducted using sliding correlator channel sounder with rotatable directional antennas with 10° and 30° beamwidths were used for both Tx and Rx at the 28 GHz band, and with 7.8° half-power beamwidth for Tx and 49.4° beamwidth for Rx at the 38 GHz band. The AoA, AoD, path loss, RMS delay spread and building penetration and reflection characteristics were estimated. G. R. Maccartney, T. S. Rappaport [28] presented the measurement campings were conducted in dense urban environment in New York City at 28 GHz and 73 GHz bands [22, 27] and in the urban environment in Austin at 38 GHz band [22] to measure the omnidirectional path loss using the close-in path loss model by summing the received powers of all angles. A. I. Sulyman, A. T. Nassar [29] presented path loss models for 5G based on outdoor directional empirical measurements in urban environments at 28 GHz

band in New York City and 38 GHz band in Austin, Texas. The measurements were performed using sliding correlator channel sounder with steerable antennas for two different antennas beamwiths (i.e 10.9^o and 28.8^o for the 28 GHz band, and 7.8^o and 49.4^o for the 38 GHz band). A. I. Sulyman, A. Alwarafy [30] presented the results of previous measurements at 28 and 73 GHz bands in different environments [22, 25, 27-29] and at 60 GHz frequency band [13, 16, 22, 26] to study directional path loss models in urban environments in LoS and NLoS situations. A new close-in path loss beam combining model was proposed based on 28 GHz and 73 GHz bands measurements. M. K. Samimi, T. S. Rappaport [31] presented a letter of probabilistic omnidirectional propagation path models based on measurements conducted in LoS and NLoS outdoor measurements in New York City at 28 GHz and 73 GHz bands, using the CI and FI path loss models. M. K. Samimi and T. S. Rappaport [32] proposed joint temporal and spatial omnidirectional statistical channel model in dense urban NLoS environments for 28 GHz band based on directional emperical measurements in Manhattan. A statistical simulator was presented, can be used for system-wide simulations to recreate reliable and accurate PDPs and channel statistics. M. K. Samimi and T. S. Rappaport [2] presented a comparison study between the empirical measurement and statistical simulation at 28 GHz band in dense urban outdoor environment in Manhattan. The measurement was conducted using directional antennas at both the Tx and Rx with 10° half power beamwidth. The Rx was rotating in 10° step size to cover full rotation in azimuth for three elevation angles. An omnidirectional path loss estimated using the CI path loss model by synthesize the directional collected data. S. Sun *et al.*[33] presented a comparison between two path loss models (CI and ABG) in urban outdoor environments using data collected in propagation measurement campaigns or using ray-tracing simulation tool in the frequency range between 2 GHz band and 73.5 GHz band. The study suggested that the CI model and ABG model showed very comparable results and the CI model offering a physical basis and simplicity. T. S. Rappaport, F. Gutierrez [34] provided measurement results in outdoor urban environment at 38 GHz band to measure different parameters such as the effect of the Tx antennas height of mobile base station on coverage (where different Tx heights were used from two to eight stories), path loss and delay spread. The measurements were conducted using a sliding correlator channel sounder connected to steerable horn antennas at both sides with a 7.8^o HPWB at Tx and two HPWB values were used at Rx (i.e. 49.4^o, 7.8^o). J. N. Murdock, E. Ben-Dor [35] presented measurement results conducted at 38 GHz band in an outdoor urban cellular environment in University of Texas at Austin using sliding correlator channel sounder connected to steerable horn antenna at both sides. The Tx antenna was located on rooftop at

two different heights (i.e. 18 m, 36 m) and the Rx at 1.5 m above the ground. The outage characteristics for the outdoor cellular channel and effect of the reflection and diffraction paths on the obstructed links were studied. T. S. Rappaport and S. Deng [36] presented outdoor measurements at 73 GHz band at New York University to study ground reflection and foliage attenuation using sliding correlator channel sounder connected to rotatable horn antenna with HPBW of 7 degrees at both sides at heights of 4 metres at Tx and 2 meters at Rx above ground. G. R. MacCartney M. K. Samimi [37] carried out at different measurements in outdoor environments at 28 GHz and 73 GHz bands in New York City using sliding correlator channel sounder connected to directional horn antenna with HPBW 10.9 degrees at 28 GHz band and 7 degrees at 73 GHz band. The measurements were conducted to measure the statistics of directional RMS delay spread, and the omnidirectional RMS delay spreads were synthesized using MATLAB-based 3-D ray-tracing. S. Sun and T. A. Thomas [38] provided a study of the line-of-sight probability and single- and dual-slope omnidirectional path loss models (i.e. ABG, CI and FI path loss models) using data collected in urban outdoor measurements conducted in Austin, USA and Aalborg, Denmark at different frequency bands.

S. Salous, X. Raimundo, and A. Cheema [39] presented measurement results conducted at two frequency bands 51-57 GHz and 67-73 GHz in different outdoor environments such as an open square, a car park, road side, and street canyon. The measurements were conducted using wideband chirp channel sounder connected to two horn antennas with HPBW 56.3º at Tx for the first band and 40º at the second band for dual polarization measurements. At the receiver rotatable horn antennas were rotated in 5 degrees step size in the horizontal level to cover full rotation. The measurements were performed to estimate the omnidirectional path loss parameters. D. Dupleich and R. Müller [40] presented the measurements results of Double-directional line-of-sight in outdoor scenario in Germany at three different frequency bands 6.75 GHz, 30 GHz, and 60 GHz. The measurements were performed using a wideband channel sounder connected to directional horn antennas with 30 degrees HPBW at both sides where the Tx antennas were fixed at rooftop at 17 metres above the ground and the Rx antenna at 1.6 metres. The measurements were conducted to measure the synthesized omnidirectional path loss, delay spread and angular spread. A. M. Al-Samman, T. A. Rahman [41] presented a line-of-sight measurement results conducted at different frequency bands 10.5 GHz, 15 GHz, 19 GHz, 28 GHz and 38 GHz in outdoor corridor environment using customised channel sounder connected to different horn antennas HPBW for each frequency band. The measurements were

performed to compare three different path loss models (i.e. ABG, CI and FI) and to measure the time despersion parameters.

2.4.1.2 Indoor environments

G. R. Maccartney, T. S. Rappaport [13] presented LoS and NLoS measurements conducted in closed-plan indoor scenario that included a corridor, adjacent-rooms, a cubicle farm, and a hallway at 28 GHz and 73 GHz bands. The measurements were conducted using sliding correlator channel sounder, using rotatable horn antennas for dual polarized antenna configurations. The omnidirectional path loss was estimated using CI and FI path loss models by synthesizing the directional measurements, and the delay spread statistics were presented. The work done by Byungchul Kim [42] to measure radio propagation characteristics such as reflections, diffractions and penetration in NLoS situation at 28 GHz in office environment and compared with 3D ray tracing simulation results. The measurements were conducted using a vector signal generator connected to a horn antenna at the Tx at a height of 2 m above the floor and a spectrum analyser connected to a dipole antenna at the Rx at a height of 1.5 m above the floor. The paper presented by Mikko Kyro [43] for radio channel measurements and modelling at 60 GHz in hospital environments in Japan with 500MHz bandwidth using VNA sounding method with biconical antenna at Rx and unidirectional open-ended waveguide at Tx. Path loss and multipath characteristics channel modelling was performed. The path loss and delay spread were compared with a regular indoor office. Dajana Cassioli and Nikola rendevski [44] presented a work to measure the channel impulse response in an office environment that includes one, two and three individuals at the 60 GHz frequency band using PN-sequence channel sounder technique with a directional horn antenna at Tx with a 9° beamwidth, and omni-directional at the reciver. To obtain an accurate model for human-induced shadowing in both proximity and blockage situations, regression fits were applied to the collected data responses. Suiyan Geng [45] reports measurements made at 60 GHz in various indoor environments such as corridor and hall using broadband channel sounder method for continuous route and direction of arrival measurements. The propagation channel statistical parameters such as, the path loss, the shadowing, the RMS delay spread and the number of paths, are investigated. The measurements were conducted using a horn antenna at the Tx in the corridor scenario whereas a horn and biconical antenna at the Rx in the corridor and at both Tx and Rx in the hall scenario and the antennas heights of Tx and Rx were the same. Hirokazu Sawada, Kazuya Fujita and Shuzo Kato [46] carried out measurements at 60 GHz using vector network analyser sounding method with a very high bandwidth 3 GHz and ray tracing simulation

technique in a cubicle office scenario. To obtain an impulse response model, two scenarios for near and far locations from the access point are conducted and statistical channel models were proposed. Jing Wang [47] defined and presented an analytical model at 60 GHz for indoor environment and developed a ray-based model for shadowing loss calculation caused by humans present around the communication link. Chanez Lounis [48] presented a first result of the path loss characterization at 60 GHz in underground mining environment in LoS situation. The model is used to characterize large scale fading. The method of sounding was vector network analyser connected to a horn antenna at both the Tx and Rx. Andreas G. Siamarou [49] conducted measurements in an indoor corridor environment at 63.4 to 64.4 GHz using vector network analyser sounding method with 1 GHz bandwidth, to estimate instantaneous coherence bandwidth and measure transfer function and channel frequency response. M. Fryziel [50] conducted measurements for indoor multipath radio channel in a medium size computer room at 60 GHz. The sounding method used is vector network analyser. A statistical propagation model was presented including large scale fading, small scale fading and path loss exponent and compared between circular and linear polarization, where circular polarization showed better robustness. Sijia Deng [51] presented indoor propagation measurements and path loss models in a large office environment using a broadband sliding correlator channel sounder at 28 and 73 GHz. Using high directive horn antennas with $30°$ HPBW and $15°$ HPBW for the 28 GHz band and 73 GHz band respectively, the RMS delay statistics and path loss models using the close-in path loss model with 1 m free space reference distance are presented for line of sight and non-line of sight situations, where the directional received powers summing to synthesize the omnidirectional received powers. George R. [52] presented the measurements result for the same scenario in [24] where the scenario in this paper divide the large office into corridor, open plan and close plane Jacqueline Ryan [53] presented the results of measurements were conducted using wideband sliding correlator channel sounder to study the penetration loss in an indoor office at 73 GHz band for different materials such as glass doors and windows, whiteboard writing walls, closet doors and steel doors. X. Raimundo, S. Salous [54, 55] presented wideband measurements for two frequency bands (51-57 GHz band and 67-73 GHz band) in different indoor environments such as small office, classroom, factory and corridor. The measurements were conducted using 2x2 MIMO dual polarized chirp sounder with horn antennas with a beamwidth (Tx = $56.3°$ and Rx=$18.4°$) for the 51-57 GHz band and (Tx=$51.4°$ and Rx=$14.4°$) for the 67-73 GHz band. To measure the path loss, RMS delay spread and angular spread. The antennas at the receiver were rotated with $5°$ step size in azimuth to cover

360° at zero elevation angle only and the received power of all angles were summed to synthesis omnidirectional antennas for each measurement location, where the log-distance path loss model was used. K. Haneda *et al.* [56] presented the new channel model requirements which should support 5G operating over frequency bands up to 100 GHz which are as follows: It should preferably be based on the current used 3GPP 3D model with adding the 5G requirements and scenarios. It should cover a wider frequency range up to 100 GHz. For multi-band operation, the evaluation of joint propagation characteristics is needed over different frequency bands. Large channel bandwidths must be supported up to 2 GHz. Large antenna arrays range must be supported, with very high directivity. Different array types are needed for 5G with arbitrary polarization. The mobility up to 350 km/hr must be structured in the new model even for small-scale mobility and rotation of both ends to support different scenarios such as device to device and vehicle to vehicle. Spatial/temporal/frequency consistency must be supported in the new model. It should ensure different indoor/outdoor channel states, such as line-of-sight and non-line-of-sight. Also, presented results of different measurements over range of selected frequency bands between 6 GHz and 100 GHz band, at office [51, 52] (including open areas, corridor and close area) and shopping mall environments. The measurements were conducted to study different channel characteristics such as path loss, delay spread, penetration loss. A propagation analyses of the reflection coefficient and transmission loss in indoor environment based on measurements at 28 and 38 GHz were reported by A. Fagiani, M. Vogel, and S. Cerqueira Jr [57]. In Addition, material characterization of common buildings materials in Brazil was presented such as brick, plaster walls, glass and wooden doors based on numerical simulations and measurements. N. Zhang, X. Yin [58] introduced indoor channel measurements in LoS and NLoS situations at 72 GHz band with 2 GHz bandwidth. The measurements were conducted in a canteen using Agilent signal generator adopted as the Tx and signal analyzer as the Rx, each was controlled by a computer. A rotatable horn antenna with 10° beamwith was used at both Tx and Rx. To measure the AoA the Rx antenna was rotated in 10° step size in azimuth to cove full rotaion at three different elevation angles (-10°, 0°, 10°). The cluster angular spreads statistics in the azimuth and elevation of arrival was extracted and the variation in angular spread against the Tx-Rx separation distance was investegated. Y. Xing and T. S. Rappaport [59] presented propagation measurements at D-band and provides the wideband channel sounder design of a 139-145 GHz band, and suggests wideband propagation measurements in indoor environments and penetration loss measurements for common building materials at 140 GHz band. The measurements were

conducted using rotatable horn antennas with a 8° half power beamwidth. M. B. Majed, T. A. Rahman [60] presented indoor carridor measurements at 4.5 GHz, 28 GHz, and 38GHz in LoS and NLoS situations using Series Synthesized Signal Generator at the Tx connected to horn antenna and spectrum analyzer at Rx connected to two antenna type (i.e. horn and omnidirectional antennas). The measurements were conducted in University Teknologi Malaysia to study well-known channel models and proposing a new path loss model. A comparison between the new proposed path loss model and the well known models for directional and omnidirectional path loss was provided. F. Qamar, M. H. S. Siddiqui [61] presented simulation study carried out at 28 GHz band and 38 GHz band using the CI and AGB path loss models. The results show that the performance is significantly higher for the CI path loss models compared to the ABG for both 28 GHz band and 38 GHz band. E. M. Vitucci *et al.* [62] provided a study in a medium size lecture room in the Technical University at 10 GHz band and 60 GHz band and Ray Tracing tool is used to interpret the empirical results. The measurements were conducted using a custom wideband channel sounder connected to rotatable directional horn antennas at both sides. The Tx antenna can scan 180°, whereas the Rx antenna can scan 360° in azimuth, the dual directional measurements were conducted with step size of 20° in horizontal level only at both sides. A. Al-Samman *et al.*[63] presented measurement results conducted in indoor corridor environment in the University Teknologi Malaysia at 3.5 GHz band and 28 GHz band using channel sounder connected to horn antennas with HPBW 58.97^o at Tx and 44.8^o at Rx, where the Rx antenna was pointing to zero degres in both azimuth and elevation, whereas the Tx was pointing in two angles in azimuth (0° and 45°) for LoS and NLoS respectively and zero degrees in elevation for both and the Tx and Rx antennas height were at 1.5 m. The measurments were conducted to measre the path loss using different path loss models and delay spread parameters. J. Huang, Y. Liu, J. Sun, W. Zhang, and C. Wang [64] conducted measuremnts in an indoor office to study the effect of the antenna height and directivity on the channel propagation characteristics at 60 GHz band with 3 GHz band width. The measurements conducted using a signal generator and vector network analyzer connected to an omnidirectional antenna at the Tx at two different heights (1.6 m and 2 m) and two direcional antennas at the Rx with HPBW 10° and 55°. A. M. Al-Samman, T. Abd Rahman, and M. H. Azmi [65] peresented measurements resluts indoor carridor environmnt in the University Teknologi Malaysia at 19 GHz band , 28 GHz band , and 38 GHz band for LoS and NLoS scenarios. Different path loss models, the delay spread and azimuth angular spread were studied. The measurements were conducted using wideband channel sounder connected to horn

antannas at a height of 1.7 m at Tx and 1.5 m at Rx and with HPBW 46.4^o at the 19 GHz band, 44.8^o at 28 GHz band and 28.3^o at 38 GHz band. In the LoS measurement the Tx and Rx antennas were stationary at zero degrees in both azimuth and elevation, whreas in the NLoS the Rx antenna was rotated in step sze of 90° to cover full rotaion at horizontal level only. D. Dupleich *et al.*[66] provided simultaneous directional measurements in indoor large corridor in the Zusebau at the TU Ilmenau at 6.75 GHz band, 30 GHz band, and 60 GHz band where the antennas were mounted above each other at the Tx, whereas the antennas were at the same height at the Rx, but they were pointing to different angles. The Rx antenna was rotated in azimuth from −150° to 180° in 30° step size, and in elevation from −30° to 30°, with step size of 30°. The characteristics of the used antennas were similar in the measured bands. However, the results were influenced by them since they were not de-embedded from the measurements. The study investigated synthetic omni-directional the power delay profile and delay and angular spread results. Q. Wang, S. Li, X. Zhao, M. Wang, and S. Sun [67] carried out measurements in indoor open office at KeySight Beijing, China at 26 GHz band with 1GHz bandwidth using an omnidirectional antenna at Tx at a height 1.98 m and a horn antenna at Rx with 10° beam-width at a height of 1.87 m. The Rx antenna was rotated in azimuth with a step size of 5° to cover full rotation and in elevation with a step size of 10° from -10° to -30°. The directional path loss using CI path loss model and delay spread and angular spread were studied. P. F. M. Smulders [68] provided indoor radio channels statistical characterization review at 60 GHz band. The measurements were performed in different indoor environments included offices, laboratories, conference rooms and corridors using antennas with different HPBWs ranging from 8 to 360 degrees at both Tx and Rx side for LoS and NLoS scenarios. The path loss parameters were measured using log-distance path-loss model using various reference distances. S. Geng, J. Kivinen, and P. Vainikainen [69] presented indoor propagation measurements results conducted in LoS in a corridor and in LoS and NLoS in a hall environments at 60 GHz band. The path loss, RMS delay spread, and shadowing were studied by using wideband channel sounder.

2.4.1.3 Indoor and Outdoor environments

Hang Zhao [70] presented reflection and penetration loss measurements procedure and results for common building materials at 28 GHz band for outdoor and indoor materials such as concrete, brick, tinted and clear glass, and drywall. The measurements were conducted using sliding correlator channel sounder connected to steerable horn antennas with 10o HPBW using

two incident angles (10o and 45o). The outdoor materials such as tinted glass showed high penetration loss and large reflection coefficient values, whereas the indoor clear glass showed low values for the penetration loss and reflection coefficient at the 28 GHz band. Shu Sun [71] provided results of five different path loss models at 28 GHz and 73 GHz bands using the data collected in [24] and [27] including the close-in and floating-intercept models. According to the results it was concluded for the single-frequency path loss that due to its physical basis and simplicity, the CI model is preferable compared to the FI model for both outdoor and indoor environments. S. Salous Y. Gao, [72] presented results of measurements performed in 30 GHz and 60 GHz frequency bands in indoor and outdoor environments using directional horn antenna rotated in azimuth with step of 5o to cover full rotation at zero elevation angle only to measure the RMS delay spread for both bands with 2.2 GHz and 4.4 GHz bandwidth for 30 GHz band and 60 GHz band respectively. S. Nie, M. K. Samimi [73] reporting the results of different camping measurements at 73 GHz band in an office [51, 52] (indoor) and some outdoor scenarios such as foliage attenuation, free space, and ground bounce. The report presented the indoor path loss exponent results compared with free space in LoS and NLoS situations. The omnidirectional LoS path loss exponent was lower than free space due to ground bounces. The outdoor measurements were conducted to study the foliage attenuation rates and ground bounce reflection coefficients at outdoor courtyard in Downtown Brooklyn. The free space and foliage measurements were conducted in dual antenna polarizations where directional horn antennas with 7° HPBW were used. The receivers and transmitter heights were at 2 meters and 4 meters above the ground respectively. The receiver antenna was rotated in step size of 10o in azimuth to cover full rotation and at three different elevation angles (0o, +7o, -7o). S. Sun et al.[74] presented a comparison study of three different path loss models (i.e. ABG model, CI model, and the CIF model with a frequency-weighted path loss) using data collected from different measurements conducted in various indoor and outdoor environments in microwave and mmWave bands.

It can be seen from this review that the channel characterization research is still active in both indoor and outdoor environments, especially in the frequency bands above 6 GHz. For instance, the sounding systems which used in most of the experimental work have the maximum null to null bandwidth about 3 GHz, and the spatial resolution was in most of the indoor studies around 10 nanoseconds, whereas the sounding bandwidth used in this project reached up to 6 GHz and the spatial resolution up to 0.5 nanoseconds or 15 cm. Moreover, most of the available measurements in the range above 6 GHz were conducted for various bands using different

measurement set up (different channel sounding techniques, different antenna beamwidth and different measurement procedure) at different environments which make the comparison between them is not accurate. While, the measurements in this work were conducted at different frequency bands with the same set up and in the same environments to study the frequency dependence. In addition, in most of the previous work, the omnidirectional path loss was estimated by synthesise the directional measurements and most of the measurements conducted at horizontal level only and for few positions. Whereas, in this study the path loss was estimated from the collected data using an omnidirectional antenna at the receiver at a large number of positions for all measured bands and scenarios. The measurement results of the path loss and the delay spread parameters in LoS in chapter 3 and in NLoS in chapter 4 have been accepted in the ITU recommendation ITU-R P.1238-10.

Table 2-1 Partial summary of channel propagation modelling

Ref. No.	Carrier frequency [GHz]	Sounding method	Measured parameters	Measurements scenario	Simulation method	Research outcome	Antenna type	
							Tx	Rx
[63]	3.5	correlation channel	path loss models and delay spread	Indoor corridor	Not mentioned	Different path loss models and delay spread	Horn	Horn
[60]	4.5	VNA	Path loss	Indoor carridor	Not mentioned	directional and omnidirectional path loss	Horn	Horn+Omni
[66]	6.75	Custom channel sounder	power delay profile	Indoor large corridor	Not mentioned	Delay and angular spread	Directive	Directive
[62]	10	Custom channel sounder	double-directional	Lecture room	Ray-tracing	Departure, arrival angles	Steerable Horn	Steerable Horn

Ref. No.	Carrier frequency [GHz]	Sounding method	Measured parameters	Measurements scenario	Simulation method	Research outcome	Antenna type	
							Tx	Rx
[65]	19	Custom channel sounder	Channel impulse response	Indoor carridor	Not mentioned	Different path loss, angular spread, and RMS delay spread	Horn	Horn
[67]	26	VNA	path loss, delay and angular spread	Indoor open office	Not mentioned	Directional and mean path loss models, RMS delay and angular spread	Omni	Horn
[63]	28	correlation channel	path loss models and delay spread	Indoor corridor	Not mentioned	Different path loss models and delay spread	Horn	Horn

Ref. No.	Carrier frequency [GHz]	Sounding method	Measured parameters	Measurements scenario	Simulation method	Research outcome	Antenna type	
							Tx	Rx
[42]	28	VNA	Reflections, diffractions and penetration loss	Office	3D Ray-tracing	Passive repeater model	Horn	Dipole
[18]	28	Not mentioned	radio channel parameters	Outdoor urban	3D Ray-tracing	A dual-slope path loss proposed	Not mentioned	Not mentioned
[24]	28	Wideband channel	last hops Statistical characteristics	urban street	Not mentioned	Last hops of multipath estimation	Horn	Horn
[70]	28	Sliding correlator	Penetration loss and reflection coefficient	Indoor and outdoor	Not mentioned	Penetration loss and reflection coefficient	Steerable Horn	Steerable Horn
[24]	28	Sliding correlator	Path loss model	downtown Manhattan	Not mentioned	CI path loss model	Steerable Horn	Steerable Horn

Ref. No.	Carrier frequency [GHz]	Sounding method	Measured parameters	Measurements scenario	Simulation method	Research outcome	Antenna type	
							Tx	Rx
[32]	28	Sliding correlator	Cluster and lobe statistics	Outdoor dense urban	3D ray-tracing	Statistical omnidirectional channel model	Steerable Horn	Steerable Horn
[2]	28	Sliding correlator	CI path loss model	Dense urban outdoor	Ray-tracing	Omnidirectional path loss	Steerable Horn	Steerable Horn
[51]	28	Sliding correlator	Path loss and delay spread	Large office	Not mentioned	Path loss and delay spread	Horn	Horn
[52]	28	Sliding correlator	Path loss, delay spread,	corridor, open and close plane	Not mentioned	path loss models for combined co-cross-polarized	Horn	Horn
[20]	28	Sliding correlator	Path loss models	urban microcellular	Not mentioned	CI, FI path loss models	Horn	Horn

Ref. No.	Carrier frequency [GHz]	Sounding method	Measured parameters	Measurements scenario	Simulation method	Research outcome	Antenna type	
							Tx	Rx
[21]	28	Sliding correlator	Path loss models	Downtown Manhattan	Not mentioned	CI, FI path loss models	Horn	Horn
[22]	28	Sliding correlator	Path loss models, delay spread, number of multipath	Different campaigns in outdoor environments (i.e. backhaul, peer-to-peer, vehicular (V2V) scenarios)	Not mentioned	Directional and omnidirectional path loss models, delay spread, number of multipath	Steerable Horn	Steerable Horn
[71]	28	Sliding correlator	Path loss models	Indoor and outdoor	Not mentioned	Five different path loss models	Steerable Horn	Steerable Horn
[28]	28	Sliding correlator	Path loss	urban environments	Not mentioned	CI path loss model	Steerable Horn	Steerable Horn

Ref. No.	Carrier frequency [GHz]	Sounding method	Measured parameters	Measurements scenario	Simulation method	Research outcome	Antenna type	
							Tx	Rx
[27]	28	Sliding correlator	Angular propagation characteristics	Outdoor urban	Not mentioned	AoA, AoD, path loss,delay spread, penetration and reflection characteristics	Steerable Horn	Steerable Horn
[29]	28	Sliding correlator	Path loss models	Different outdoor environments	commercial planning tools	Path loss models proposed	Steerable Horn	Steerable Horn
[30]	28	Not mentioned	Path loss model	Different outdoor environments	Not mentioned	CI path loss model	Steerable Horn	Steerable Horn
[57]	28	VNA	Reflection coefficient and transmission loss	Indoor environments	Altair WinProp software	Penetration loss, propagation coefficient	Horn	Horn

Ref. No.	Carrier frequency [GHz]	Sounding method	Measured parameters	Measurements scenario	Simulation method	Research outcome	Antenna type	
							Tx	Rx
[31]	28	Sliding correlator	CI and FI path loss models	Downtown Manhattan	Ray-tracing	Probabilistic omnidirectional path loss	Steerable Horn	Steerable Horn
[13]	28	Sliding correlator	Omnidirectional CI and FI path loss, delay spread	Closed-plan indoor	Not mentioned	Path loss, RMS delay spread	Horn	Horn
[60]	28	VNA	Path loss	Indoor carridor	Not mentioned	directional and omnidirectional path loss	Horn	Horn+Omni
[61]	28	Not mentioned	CI and AGB path loss models	Indoor network scenario	MATLAB-based Vienna LTE-A	CI performance is significantly higher than AGB	Tri-Sector	Tri-Sector

Ref. No.	Carrier frequency [GHz]	Sounding method	Measured parameters	Measurements scenario	Simulation method	Research outcome	Antenna type	
							Tx	Rx
[65]	28	Custom channel sounder	Channel impulse response	Indoor carridor	Not mentioned	Different path loss, angular spread, and RMS delay spread	Horn	Horn
[72]	30	FMCW Chirp sounder	Power delay profile	Indoor and outdoor	Not mentioned	RMS delay spread	Steerable Horn	Steerable Horn
[66]	30	Custom channel sounder	power delay profile	Indoor large corridor	Not mentioned	Delay and angular spread	Directive	Directive
[16]	38	Sliding correlator	Power delay profile	Outdoor urban	Not mentioned	Path loss and delay spread	Horn	Horn
[20]	38	Sliding correlator	Path loss models	urban microcellular	Not mentioned	CI, FI path loss models	Horn	Horn

Ref. No.	Carrier frequency [GHz]	Sounding method	Measured parameters	Measurements scenario	Simulation method	Research outcome	Antenna type	
							Tx	Rx
[22]	38	Sliding correlator	Path loss models, delay spread, number of multipath	Different campaigns in outdoor environments (i.e. backhaul, peer-to-peer, vehicular (V2V) scenarios)	Not mentioned	Directional and omnidirectional path loss models, delay spread, number of multipath	Steerable Horn	Steerable Horn
[27]	38	Sliding correlator	Angular propagation characteristics	Outdoor urban	Not mentioned	AoA, AoD, path loss,delay spread, penetration and reflection characteristics	Steerable Horn	Steerable Horn
[29]	38	Sliding correlator	Path loss models	Different outdoor environments	commercial planning tools	Path loss models proposed	Steerable Horn	Steerable Horn

Ref. No.	Carrier frequency [GHz]	Sounding method	Measured parameters	Measurements scenario	Simulation method	Research outcome	Antenna type	
							Tx	Rx
[57]	38	VNA	Reflection coefficient and transmission loss	Indoor environments	Altair WinProp software	Penetration loss, propagation coefficient	Horn	Horn
[60]	38	VNA	Path loss	Indoor carridor	Not mentioned	directional and omnidirectional path loss	Horn	Horn+Omni
[61]	38	Not mentioned	CI and AGB path loss models	Indoor network scenario	MATLAB-based Vienna LTE-A	CI performance is significantly higher than AGB	Tri-Sector	Tri-Sector
[65]	38	Custom channel sounder	Channel impulse response	Indoor carridor	Not mentioned	Different path loss, angular spread, and RMS delay spread	Horn	Horn

Ref. No.	Carrier frequency [GHz]	Sounding method	Measured parameters	Measurements scenario	Simulation method	Research outcome	Antenna type	
							Tx	Rx
[34]	38	Sliding correlator	path loss, delay spread	urban environment	Not mentioned	pathloss, RMS delay spread, signal coverage	Steerable Horn	Steerable Horn
[36]	54	FMCW Chirp sounder	Path loss, delay spread, cross polarization ratio	Different indoor environments	Not mentioned	Path loss, delay spread, cross polarization ratio	Steerable Horn	Steerable Horn
[37]	54	FMCW Chirp sounder	Path loss, delay spread, angular spread	Different indoor environments	Not mentioned	Omnidirectional path loss, delay spread, angular spread	Steerable Horn	Steerable Horn
[23]	54	FMCW Chirp sounder	path loss, delay spread, angular spread	Outdoor street canyon	Not mentioned	Omnidirectional path loss, delay spread, angular spread	Steerable Horn	Steerable Horn

Ref. No.	Carrier frequency [GHz]	Sounding method	Measured parameters	Measurements scenario	Simulation method	Research outcome	Antenna type	
							Tx	Rx
[39]	54	Wideband chirp channel	Dual polarized path loss	different outdoor environments	Not mentioned	omnidirectional path loss parameters	Two horn	rotatable two horn
[43]	60	VNA	Path loss and delay spread	Hospital	Not mentioned	Path loss and delay spread	Unidirectional open-ended waveguide	Biconical
[16]	60	Sliding correlator	Power delay profile	Outdoor urban	Not mentioned	Path loss and delay spread	Horn	Horn
[47]	60	PN-sequence	Human-induced shadowing	Office	Not mentioned	Derived a statistical model	Horn	Omni
[46]	60	VNA	Impulse response model	Cubicle office	Ray-tracing	statistical channel models	Conical horn	Conical horn

Ref. No.	Carrier frequency [GHz]	Sounding method	Measured parameters	Measurements scenario	Simulation method	Research outcome	Antenna type	
							Tx	Rx
[48]	60	VNA	Path loss	Underground mining	Not mentioned	Large scale fading	Horn	Horn
[50]	60	VNA	Large, small scale fading	computer room	Not mentioned	Path loss	microstrip	microstrip
[22]	60	Sliding correlator	Path loss models, delay spread, number of multipath	Different campaigns in outdoor environments (i.e. backhaul, peer-to-peer, vehicular (V2V) scenarios)	Not mentioned	Directional and omnidirectional path loss models, delay spread, number of multipath	Steerable Horn	Steerable Horn
[26]	60	Sliding correlator	AoA, delay spread and path loss	Outdoor peer-to-peer and in-vehicle	Not mentioned	CI path loss, delay spread, vehicle AoA	Steerable Horn	Steerable Horn

Ref. No.	Carrier frequency [GHz]	Sounding method	Measured parameters	Measurements scenario	Simulation method	Research outcome	Antenna type	
							Tx	Rx
[30]	60	Not mentioned	Path loss model	Different outdoor environments	Not mentioned	CI path loss model	Steerable Horn	Steerable Horn
[62]	60	Custom channel sounder	double-directional	Lecture room	Ray-tracing	Departure, arrival angles	Steerable Horn	Steerable Horn
[64]	60	VNA	power delay profile, delay and angular spread	Indoor office	Not mentioned	Effect of antenna height and directivity	Omni	Direcional
[66]	60	Custom channel sounder	power delay profile	Indoor large corridor	Not mentioned	Delay and angular spread	Directive	Directive
[68]	60	Wideband channel sounder	Large-scale fading, small-scale channel behaviour	Different indoor environments	Not mentioned	Proposed a large-scale fading model	Not mentioned	Not mentioned

Ref. No.	Carrier frequency [GHz]	Sounding method	Measured parameters	Measurements scenario	Simulation method	Research outcome	Antenna type	
							Tx	Rx
[75]	60	VNA	diffuse scattering power and delay spread	shopping mall, railway station	Not mentioned	Initial channel characterization	horn	biconical
[49]	63.4-64.4	VNA	Coherence bandwidth	Corridor	Not mentioned	instantaneous coherence bandwidth	Horn	Horn
[36]	70	FMCW Chirp sounder	Path loss, delay spread, cross polarization ratio	Different indoor environments	Not mentioned	Path loss, delay spread, cross polarization ratio	Steerable Horn	
[37]	70	FMCW Chirp sounder	Path loss, delay spread, angular spread	Different indoor environments	Not mentioned	Omnidirectional path loss, delay spread, angular spread	Steerable Horn	Steerable Horn

Ref. No.	Carrier frequency [GHz]	Sounding method	Measured parameters	Measurements scenario	Simulation method	Research outcome	Antenna type	
							Tx	Rx
[23]	70	FMCW Chirp sounder	path loss, delay spread, angular spread	Outdoor street canyon	Not mentioned	Omnidirectional path loss, delay spread, angular spread	Steerable Horn	Steerable Horn
[39]	70	Wideband chirp channel	Dual polarized path loss	different outdoor environments	Not mentioned	omnidirectional path loss parameters	Two horn	rotatable two horn
[75]	70	VNA	diffuse scattering power and delay spread	shopping mall, railway station	Not mentioned	Initial channel characterization	horn	biconical
[58]	72	VNA	AoA, cluster angular spread	Indoor canteen	Not mentioned	Stochastic model	Steerable Horn	Steerable Horn
[51]	73	Sliding correlator	Path loss and delay spread	Large office	Not mentioned	Path loss and delay spread	Horn	Horn

Ref. No.	Carrier frequency [GHz]	Sounding method	Measured parameters	Measurements scenario	Simulation method	Research outcome	Antenna type	
							Tx	Rx
[52]	73	Sliding correlator	Path loss, delay spread,	corridor, open and close plane	Not mentioned	path loss models for combined co-cross-polarized	Horn	Horn
[21]	73	Sliding correlator	Path loss models	Downtown Manhattan	Not mentioned	CI, FI path loss models	Horn	Horn
[22]	73	Sliding correlator	Path loss models, delay spread, number of multipath	Different campaigns in outdoor environments (i.e. backhaul, peer-to-peer, vehicular (V2V) scenarios)	Not mentioned	Directional and omnidirectional path loss models, delay spread, number of multipath	Steerable Horn	Steerable Horn

Ref. No.	Carrier frequency [GHz]	Sounding method	Measured parameters	Measurements scenario	Simulation method	Research outcome	Antenna type	
							Tx	Rx
[53]	73	Sliding correlator	Penetration loss	Indoor office	Not mentioned	Penetration loss for common building materials	Horn	Horn
[71]	73	Sliding correlator	Path loss models	Indoor and outdoor	Not mentioned	Five different path loss models	Steerable Horn	Steerable Horn
[25]	73	Sliding correlator	Path loss model	urban environment	Not mentioned	CI path loss model	Steerable Horn	Steerable Horn
[73]	73	Sliding correlator	Path loss model, foliage attenuation, free space, ground bounce	Indoor and outdoor	Not mentioned	Path loss models, foliage attenuation	Steerable Horn	Steerable Horn
[28]	73	Sliding correlator	Path loss	urban environments	Not mentioned	CI path loss model	Steerable Horn	Steerable Horn

Ref. No.	Carrier frequency [GHz]	Sounding method	Measured parameters	Measurements scenario	Simulation method	Research outcome	Antenna type	
							Tx	Rx
[30]	73	Not mentioned	Path loss model	Different outdoor environments	Not mentioned	CI path loss model	Steerable Horn	Steerable Horn
[31]	73	Sliding correlator	CI and FI path loss models	Downtown Manhattan	Ray-tracing	Probabilistic omnidirectional path loss	Steerable Horn	Steerable Horn
[36]	73	sliding correlator	foliage-induced scattering, de-polarization effects	outdoor measurements	Not mentioned	ground reflection coefficients and foliage attenuation	rotatable horn	
[13]	73	Sliding correlator	Omnidirectional CI and FI path loss, delay spread	Closed-plan indoor	Not mentioned	Path loss, RMS delay spread	Horn	

Ref. No.	Carrier frequency [GHz]	Sounding method	Measured parameters	Measurements scenario	Simulation method	Research outcome	Antenna type	
							Tx	Rx
[33]	Between 2 and 73.5	Not mentioned	CI and ABG path loss models	Urban outdoor	Ray-tracing	CI offering a physical basis and simplicity	Not mentioned	
[59]	140	Sliding correlator	penetration loss	Indoor environments	Not mentioned	Preliminary penetration loss	Steerable Horn	Steerable Horn

CHAPTER 3

INDOOR LINE-OF-SIGHT MEASUREMENTS

This chapter presents the results of line of sight (LoS) measurements in three typical indoor environments: a large office, a factory like and a small office. To study frequency dependency, measurements at five different frequency bands (12.65 – 14.15GHz, 25.5 – 28.5 GHz, 51.2 – 57.2 GHz, 59.6 – 65.6 GHz and 67 – 73 GHz) were performed using the multiband chirp-based channel sounder developed at Durham University, with in-house built (2x1) Multiple Input Single Output RF heads as shown in figure 3-1. The sounder system consists of four different units: a Rubidium unit, DDFS unit, up-converting unit and the control unit. A brief description of the function of each unit is given in the measurement setup section below. A detailed description of the sounder's architecture and performance is given in [76, 77]. A horn antenna with 20 dBi gain and 18° beamwidth was used at the transmitter side and an omnidirectional antenna at the receiver side for each frequency band. The antennas at both sides were vertically polarized to perform co-polar measurements for all the scenarios. The measurement bandwidth for the first band (12.65 – 14.15GHz) was 1.5 GHz, 3 GHz for the second band (25.5 – 28.5 GHz) and 6 GHz for the last three bands. The data collected were processed and analysed using MATLAB codes to extract several parameters with 1 GHz bandwidth for the first band and 2 GHz for the remaining bands. The power delay profile (PDP) for each point is the first and most important step, where all the other parameters can be calculated from the PDP such as the received power, delay spread and path loss. The data were calibrated using both on-air and back-to-back calibration methods. Two different path loss models were used in this study, which are the close-in (CI) model and the floating intercept (FI) model. The time dispersion parameters such as average delay and RMS delay spread were calculated. The three indoor scenarios mentioned earlier, and their extracted parameters are presented in this chapter. Detailed descriptions of the measurement procedures and conditions for each environment are given as well.

(a)   (b)
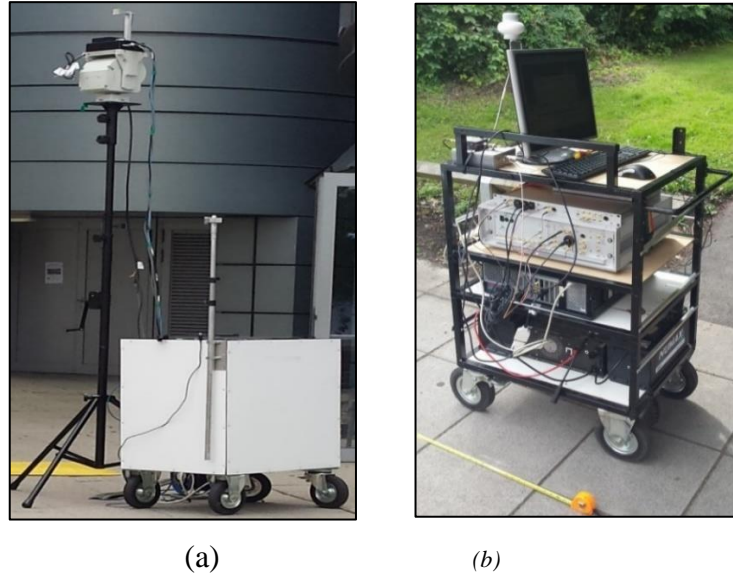
Figure 3-1 Multiband chirp-based channel sounder: (a) transmitter; (b) receiver

3.1 Measurement setup

To set-up the sounding system for measurements, the following procedure was used. At the beginning of each measurement it is necessary to turn the sounder on and to give it enough time to warm up so as to ensure that the frequency references in the Rubidium unit are stable. This indicated by a LED which changes from red to green as shown in figure 3-2. This indicates that the sounder is ready for the programming stage.
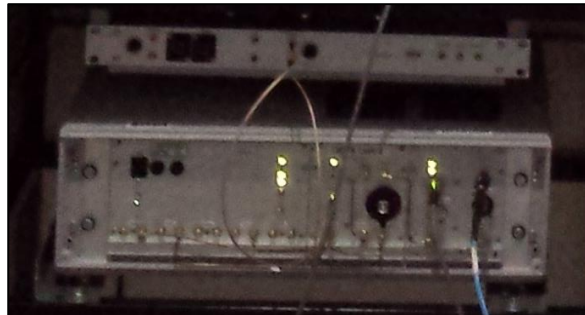
Figure 3-2 Sounder with green LED and the control unit at the top

- The programming of the sounder is started by first programming the DDFS unit, using a C code, offering different options such as modulation type (continuous wave (CW) or frequency modulation continuous wave (FMCW)) in free-run mode or trigger mode. The FMCW and trigger mode were used for all the measurements conducted in this project. The maximum baseband signal bandwidth which can be generated from the

DDFS unit is 0.75 GHz with a sweep repetition frequency equal to 1.22 kHz. Then the output of the DDFS unit is fed into the input of the up-converting unit.

- The second unit which needs to be programmed is the up-converting unit, which up-converts the base band signal bandwidth to 1.5 GHz, this can be anywhere between 12 and 18 GHz at the sounder output, according to the value of the local oscillator (LO) chosen for the unit using another programming code. The selected LO value was 4640 MHz for the frequency bands at 12.65 – 14.15 GHz, 25.5 – 28.5 GHz and 51.2 – 57.2 GHz, 5200 MHz for the band at 59.6 – 65.6 GHz and 5680 MHz for the 67 – 73 GHz band. For frequencies higher than 12 to 18 GHz, there are extra units added to the system for each frequency band, which are the RF heads as shown in figure 3-3.

- There are different RF heads used at the transmitter and receiver side. At the 12.65 – 14.15 GHz band, the output of the up-converting unit is connected directly to the transmitter antenna without adding any RF head on the transmitter side, but at the receiver side an RF head is needed to extract the beat note signal. The RF heads at the receiver side include a heterodyne detector stage to mix down the RF signal to baseband. For the remaining frequency bands there was a need to add RF head units with a multiplication by two for the 25.5 – 28.5 GHz band at both sides, and multiplication by four for the last three bands. The same RF unit is used with different LO values for the up-converting unit as mentioned above.

- After programming the sounder and resetting the control units which generate the clock and the trigger signals for both sides of the sounder (Tx & Rx), the receiver needs to be synchronized with the transmitter. Synchronization can be accomplished in two ways. The first uses a back-to-back connection and the second on-air synchronization. The latter is the preferred way, because in most cases it is not easy to connect the receiver directly to the transmitter. To perform synchronization another code is used to add a delay to the start of the sweep of the receiver so as to bring it close to that of the transmitter. Then a beat note can be obtained with a suitable value normally between 5 and 8 MHz.

- To record the data, a workstation with a 14-bit two channel data acquisition card is used as shown in figure 3-4. A C code has been created to select the desired parameters such as sampling rate and duration of recording time, and to create a folder and save a file for each measured point for further analysis. The sampling rate for all the measurements

was 40 Msamples/sec. The recording time duration was 2 seconds for each point to improve the signal to noise ratio by averaging the collected impulse responses. A switch was used at the transmitter side to clean out the noise by subtracting the received signal from an empty signal, where the switch changes between on and off at a frequency at double the clock rate. When the switch is on the receiver will record the transmitted signal, and when it is off an empty signal is recorded. So, the actual recorded data are for one second and 1220 impulse responses can be averaged for each point.

Figure 3-3 RF heads for all frequency bands at the receiver side

Figure 3-4 Two-channel 14-bit data acquisition card connected to the workstation

Table 3-1 Sounder unit set-up parameters

RF centre freq. (GHz)	13.4	26.8	54.2	62.6	70
RF bandwidth (GHz)	1.5	3	6	6	6
Analysis bandwidth (GHz)	1	2	2	2	2
Sweep repetition frequency	1.22 kHz				

54

3.2 Large office

Figure 3-5(a) shows the layout of the Large office environment. As this scenario represents one of the most common academic environments where a lot of electronic equipment is mounted on top of experimental benches with paths separating them along with common obstructions such as chairs, desks and partitions as shown in figure 3-5(b). At the receiver an omnidirectional antenna was mounted on the top of a trolley at a height of 1.6 m, which is the average height of mobile users. The receiver moved along this path during the recording of data for 2 seconds in steps of one metre at a time. The researchers often use a spatial separation samples of quarter the wavelength or over and no more than two metres in the indoor scenarios[3]. The transmitter was fixed close to the wall at the far end at a height of 2.5 m on the top of a tripod to emulate the hotspot point, and a horn antenna was mounted on the top of a 3D positioner, tilted down at -9 degrees (which is half of the antenna's 3 dB beam-width) to focus the transmitted beam onto the measurement area. The minimum and maximum 2D separation distances between the transmitter and the receiver were 3.55 m and 14.55 m respectively. In order to increase the number of points to give more accurate estimations of path loss, each metre was divided into five sections during the data processing. The whole procedure was repeated five times, once for each frequency band.

(a)   (b)
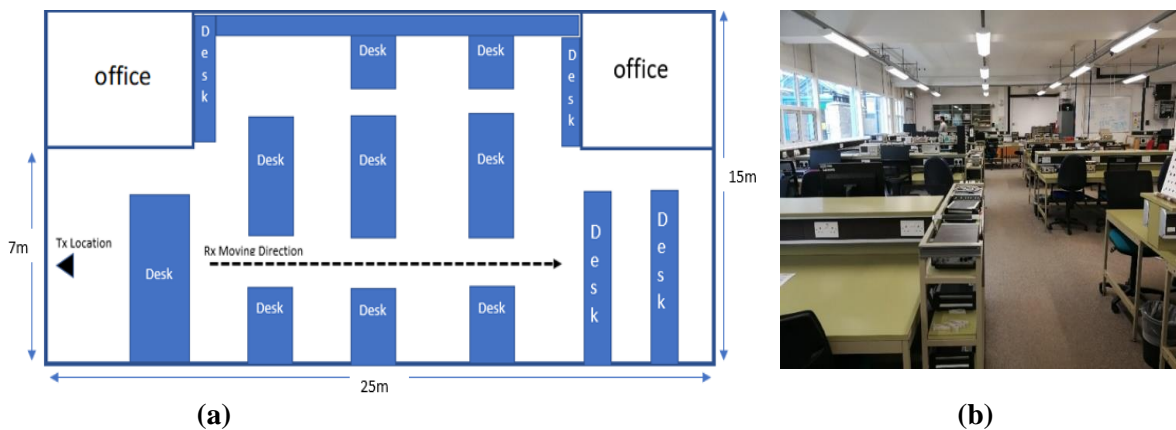
Figure 3-5 Large office: (a) Large officelayout (b) photograph from the Rx point of view

3.2.1 Received power and path loss

From the data collected at each point, a PDP was extracted using a MATLAB code for all the frequency bands. The code converts the raw data to voltage representing the received signal and then it is converted into power in the dB scale in the frequency domain by using a Fourier transformation. To extract a clean impulse response, the following procedure is used. The signal-to-noise ratio is improved by firstly averaging the 1220 impulse responses for both the actual and empty signals, and secondly by subtracting the empty signal from the actual signal. The resulting PDP is saved for each point for use in determining the received power and then for the path loss calculations. Another MATLAB code was created to calculate the received power, and here there are two situations based on the dynamic range (where the dynamic range equal to the difference between the maximum data power level and the average of the noise). In the first, if there is a dynamic range higher than 30 dB, then the received power is calculated by summing all the PDP multipath components within this value from the maximum. The second situation, if the dynamic range is less than 30 dB, then the multipath components that have power levels more than 3 dB above the noise floor are considered as a signal and included in the received power calculation, as shown in figure 3-6. It can be seen from the graphs of received power versus transmitted distance in figure 3-6 that all of the measured frequency bands follow the same general trend where the points closer to the transmitter have the higher power level, then the level starts to decay as the receiver moves away from the transmitter.
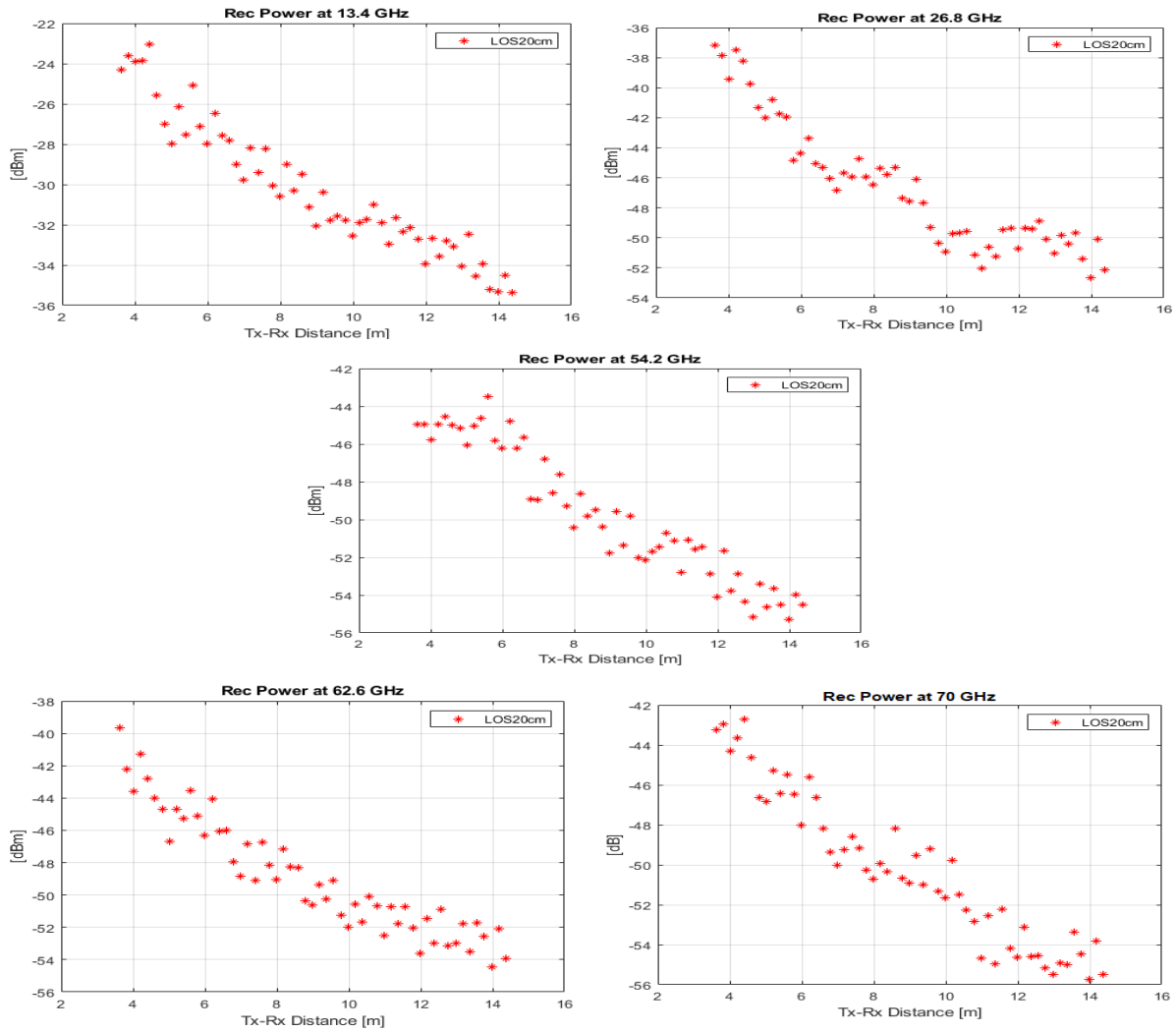
Figure 3-6 Received power for five frequency bands in Large office

Table 3-2 Variation in power levels for each frequency band

Centre Frequency	Power level variation [dBm]	Highest power level [dBm]	Lowest power level [dBm]
13.4 GHz	12	-23	-35
26.8 GHz	16	-37	-53
54.2 GHz	13	-43	-56
62.6 GHz	15	-39	-54
70 GHz	13	-43	-56

Table 3-2 shows the variation in power level for each frequency band, where the difference between the highest and lowest variation was within 4 dB. The lowest variation was 12 dB at the centre frequency of 13.4 GHz and the highest was 16 dB at the 26.8 GHz centre frequency. These values were as expected, where the lowest attenuation over the range was at the lower frequency band of 13.4 GHz and it increases as the frequency band increases. However, the

attenuation at 26.8 GHz was high, which might be due to absorptive carpeted floor [68] and ceiling, as the power drop can be seen clearly at certain distances such as between 6 and 8 metres and between 9 and 12 metres in the received power for 26.8 GHz in figure 3-6. At the other frequency bands the reflection effect was not as high as at 26.8 GHz. There are several factors controlling reflected multipath components, such as wavelength, surface texture and incidence angle.

Two path loss models were used to calculate path loss. These are the CI model and the FI model as shown in figure 3-7 (a) and (b) respectively. The parameters of both models are presented in table 3-3. The two models show very similar values in this scenario in terms of the PLE (n) for the CI model compared with the slope (β) for the FI model, where the maximum difference between them over the five frequency bands is less than 0.5 dB, with a maximum difference of 0.3 dB in the standard deviation (σ) between the two models. The PLE for 13.4 GHz was slightly less than the theoretical free space value (n=2), where it was 1.83. For the higher frequencies it was slightly more than 2, which might be due to the effect of diffusion, where the carpeted floors are likely to contribute to greater attenuation for the higher frequency bands [13]. The two pathloss models effected mainly by the environment contents and the results were similar in both models which give an advantage to the CI over FI model based on the number of measured parameters for each model.
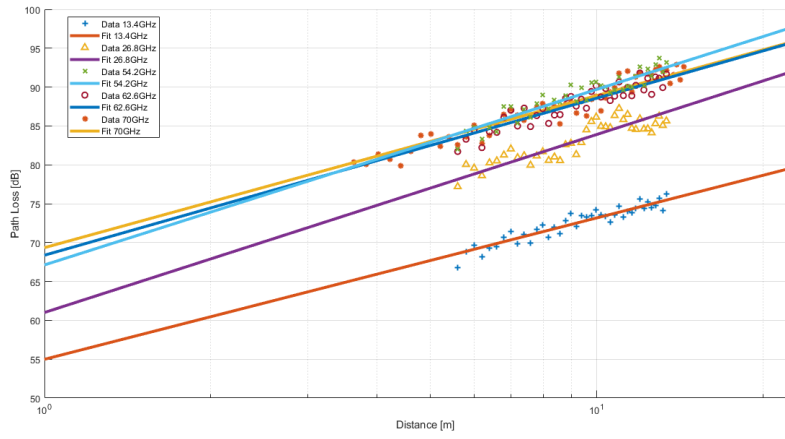
(a)
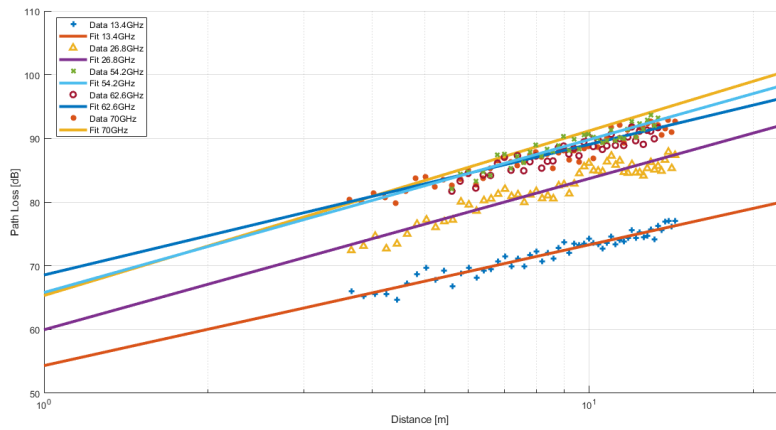
(b)

Figure 3-7 LOS Path loss for two different models: (a) CI model; (b) FI model

Table 3-3 Parameters of the two path loss models

Path loss Model		13.4 GHz	26.8 GHz	54.2 GHZ	62.6 GHz	70 GHz
CI	n	1.83	2.22	2.26	2.06	2.16
	σ	0.83	1.25	0.98	1.03	0.97
FI	α	54.33	59.96	65.8	68.55	65.33
	β	1.89	2.37	2.39	2.05	2.58
	σ	0.82	1.22	0.97	1.03	0.67
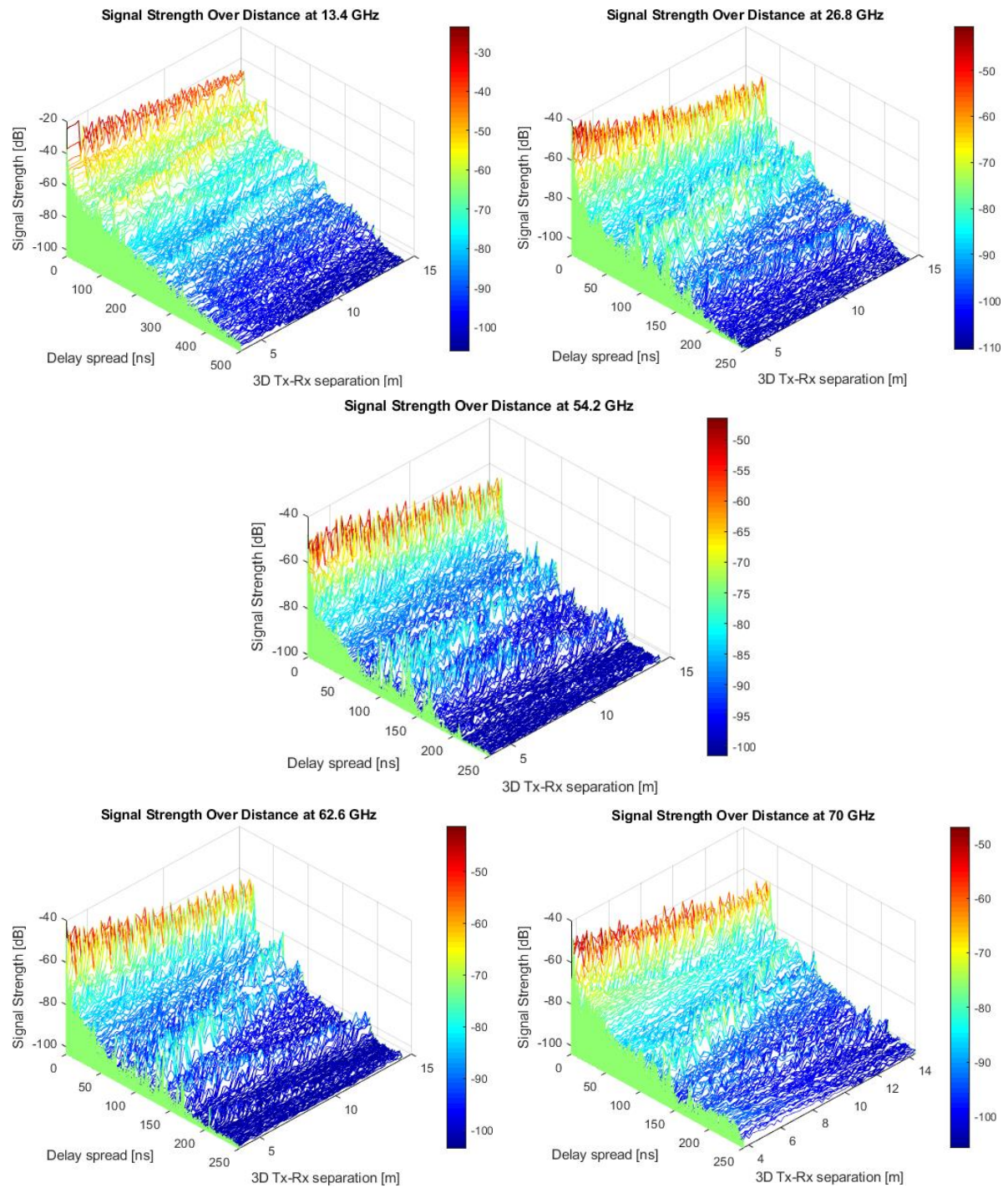
Figure 3-8 Signal strength against range for five frequency bands

Figure 3-8 shows the decay in signal strength against delay spread for all the measured frequencies. As can be seen in the figure, there was a decay in the signal strength as the distance between the transmitter and the receiver increased over all the measured bands. However, there is a fluctuation in the signal strength at 26.8 GHz which as mentioned earlier might be due to absorptive carpeted floor and the ceiling at certain distances.

3.2.2 Time dispersion parameters

3.2.2.1 Power delay profile

Three PDP examples (each normalized to its maximum) from all the measured frequency bands at the beginning, middle and the end are shown in figure 3-9. It can be seen from these PDP examples that, the multipath components are very close to each other, especially for the higher frequencies, where the time resolution of the sounder is about 0.5 nanoseconds for the last four bands and 1 nanosecond for the first frequency band. This means that the environment is largely dispersive, and the scatterers are very close to each other. The excess time delay for this environment with respect to the main component (LoS) and within a 20 dB threshold from the maximum is between 1 and 109 nanoseconds in the 12.65 – 14.15 GHz band, between 3 and 94 nanoseconds in the 25.5 – 28.5 GHz band, between 3 and 49.5 nanoseconds in the 51.2 – 57.2 GHz band, between 0.5 and 51 nanoseconds in the 59.6 – 65.6 GHz band, and between 1.5 and 112 nanoseconds in the 67 – 73 GHz band. The delay spread ranges were in general as expected in this environment, where the dimensions of the laboratory are about 25 m in length while the width varies between 7 m at the front and back and 15 m in the middle. For the LoS measurements, only about 15 m can be used including the front and the middle parts, and the back part was excluded because of barriers and partitions. The lower frequency band has a longer delay spread compared with those of the higher frequency bands due to the increase in the attenuation ratio with distance as the frequency increase. However, the 67 – 73 GHz band shows the highest value of the excess time delay compared with the other frequency bands. This is because the power level difference between the main component and the multipath components at this band was not as high as in the other frequency bands, as can be observed from the PDP samples shown in figure 3-9. It is noticeable that, despite it being a LoS measurement, there are reflection components very close to the main component and even in some cases their level is higher than the LoS component, as clearly seen in figure 3-9 (e) at point 1. Also, the minimum excess time delay for the 12.65 – 14.15 GHz and the 59.6 – 65.6 GHz bands was equal to the sounder time resolution. The far filed for all the used antennas is less than one metre.

a) for 12.65 – 14.15 GHz at points 1, 30, 50

b) for 25.5 – 28.5 GHz at points 1, 30, 55

c) for 51.2 – 57.2 GHz at points 1,30,50

d) for 59.6 – 65.6 GHz at points 1,47, 55

e) for 67 – 73 GHz at points 1, 21, 55
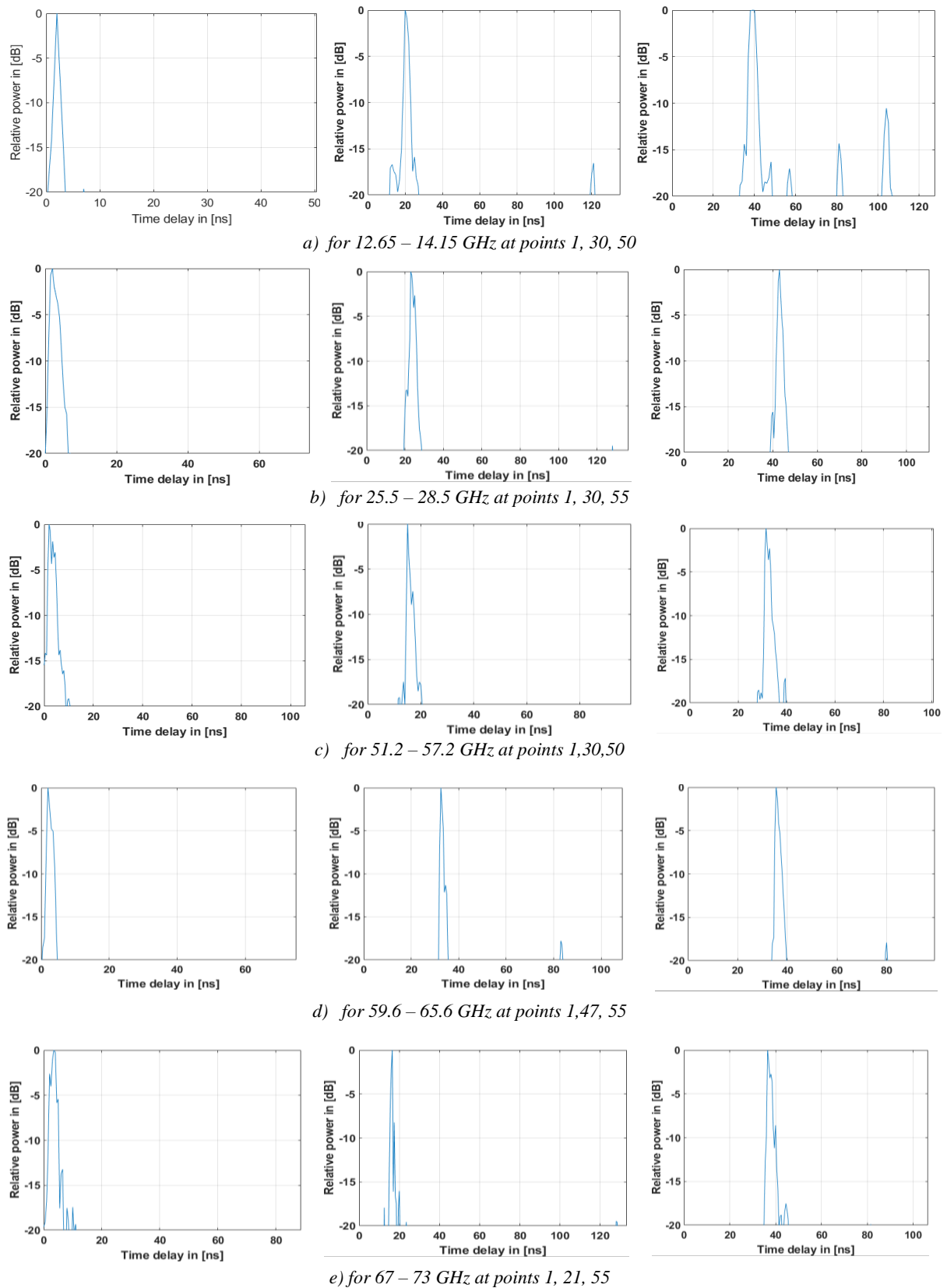
Figure 3-9 Three different PDP samples from all measured frequency bands

Figure 3-10 presents the normalized PDPs to their maximum for each frequency band within a 20 dB threshold from the maximum. This figure shows that the delay spread for all measured bands in this scenario is less than 120 nanoseconds, and the delay spread decreases as the receiver moves away from the transmitter. It can be seen from the images below that the delay spread at 13.4 GHz is higher than those for the other frequency bands at most of the points, as expected. Also, there were two reflected waves, the first one reflected from a partition about 1.5 metres from last point and it is about 2 metres high and the second reflection from the wall at the end of the room.
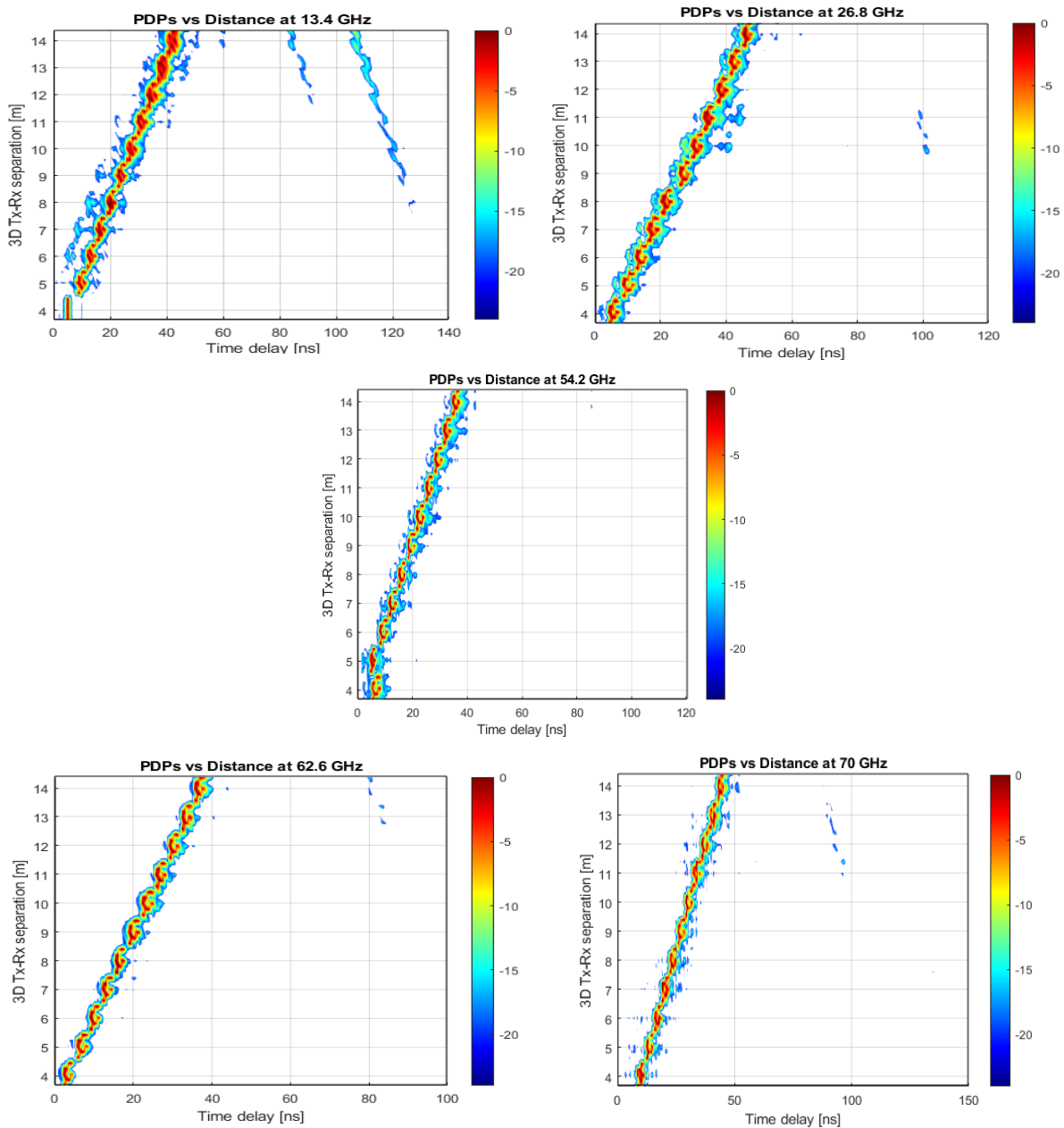
Figure 3-10 PDPs against distance for all measured frequency bands

3.2.2.2 Average and RMS delay spread

A MATLAB program was used to calculate these parameters. The first step in this program is to check the dynamic range for all PDPs. If there are components higher than a certain value, which in this project is 20 dB from the maximum. Only the multipath components satisfying this condition are used to calculate the average and RMS delay, and all the others below this level are discarded. The second step is to calculate these two parameters at the chosen threshold value of 20 dB, as shown in figures 3-11 and 3-12 for all the measured bands in this scenario. The average delay spread over all bands was within 13 nanoseconds, as shown in figure 3-11. The values of average delay spread fluctuate around a certain level with some spikes and dips at some distances, which is an indication of the number and power level of the multipath components at these distances as can be seen in figure 3-10.
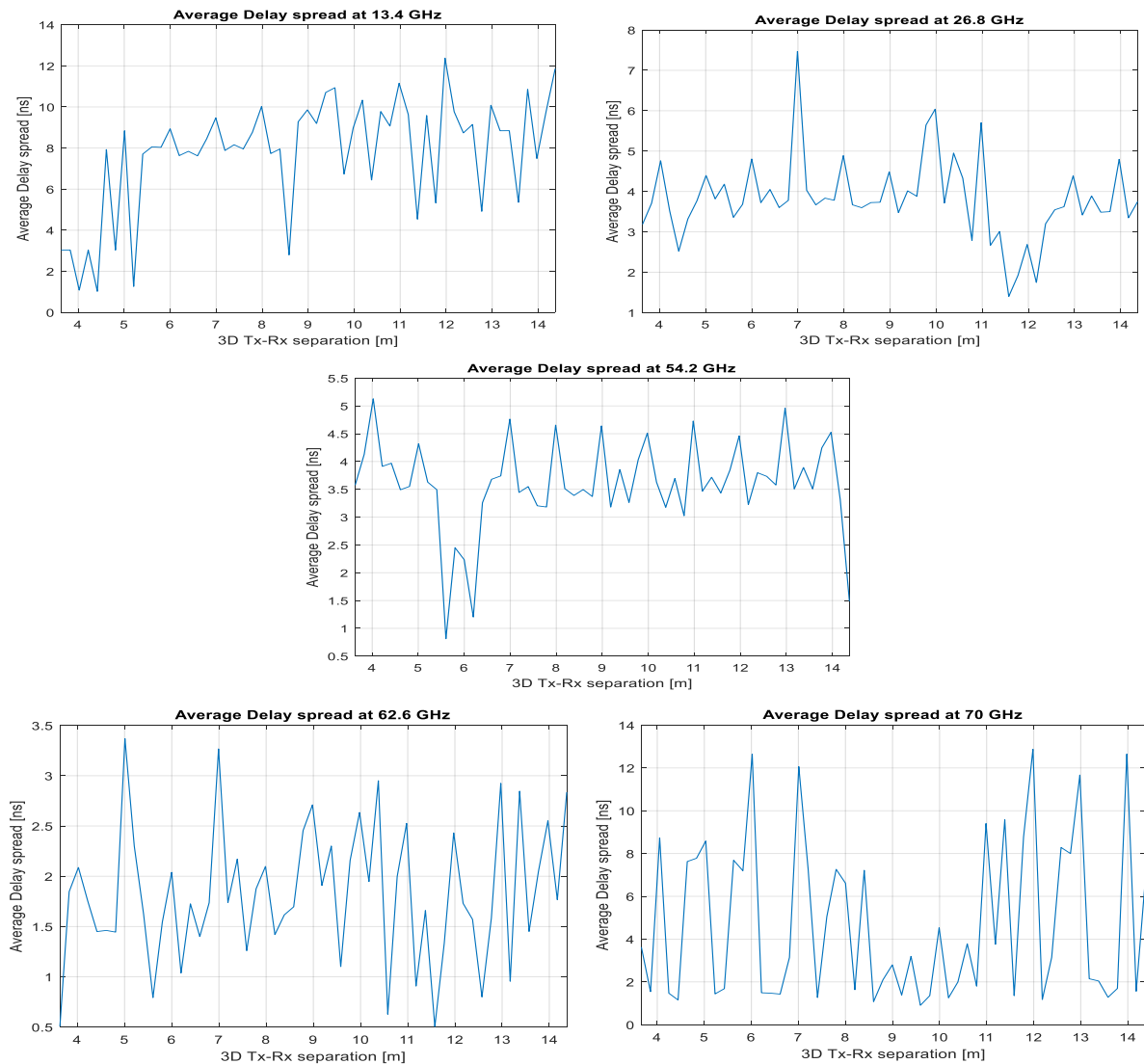
Figure 3-11 Average delay spread against distance for all measured frequency bands
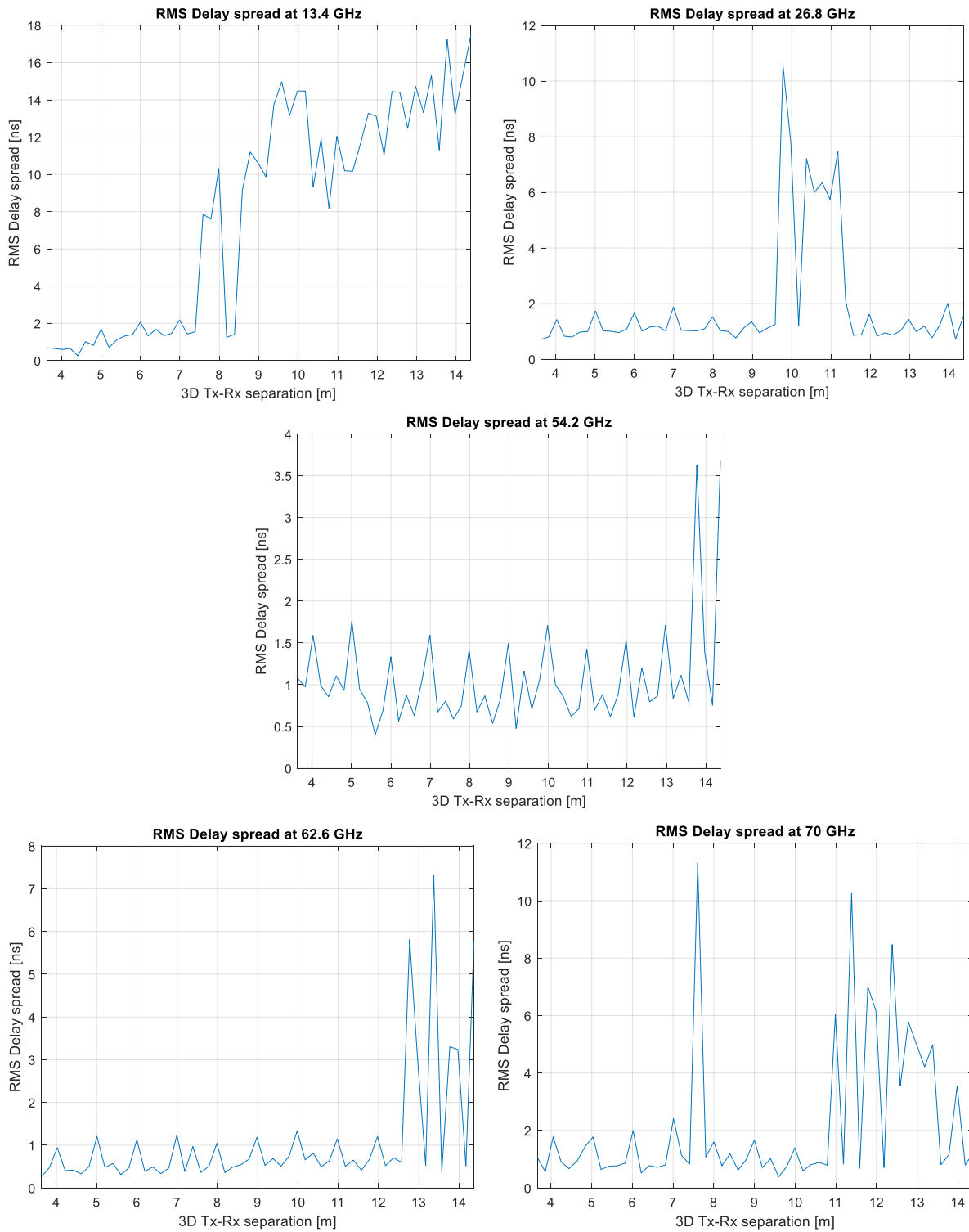
Figure 3-12 RMS delay spread against distance for all measured frequency bands

Figure 3-12 presents the calculated values for the RMS delay spread over all measured frequencies. This figure shows sudden increases at some distances, which indicate the existence of multipath components far from the main component at these distances, as is noticeable from the colormap in figure 3-10. The effect of these components is shown in the RMS delay spread,

even if their power level is very low (close or equal to -20 dB). This is seen in the 54.2 GHz and 70 GHz images in figure 3-10 where the components producing the high excess time delay were at around -19.63 dB for the 70 GHz.

Figure 3-13 shows the cumulative distribution function (CDF) for the RMS delay spread over all of the measured frequency bands. This figure shows that the lower frequencies as expected, have longer delay spreads than higher ones, where 13.4 GHz has the largest RMS delay spread, which was less than 20 nanoseconds for this environment. Table 3-4 presents the RMS delay spread values for indoor environments. In table 3-4, 50% represents the median value, the 10% and 90% values of cumulative distribution are also presented in this table for all the measured frequency bands. The table shows a decrease in the CDF of the RMS delay spread as the frequency increases. However, there is similarity between the two frequency bands at 54.2 GHz and 70 GHz, as can be noticed in table 3-4 and also in figure 3-13.

Figure 3-13 CDF of RMS delay spread for all measured frequency bands

Table 3-4 The CDF values of the RMS delay spread

CDF	13.4 GHz	26.8 GHz	54.2 GHz	62.6 GHz	70 GHz
10%	0.67	0.8	0.6	0.36	0.61
50%	1.41	1.06	0.87	0.54	0.87
90%	9.69	5.87	1.56	1.18	1.57

3.3 Factory like environment

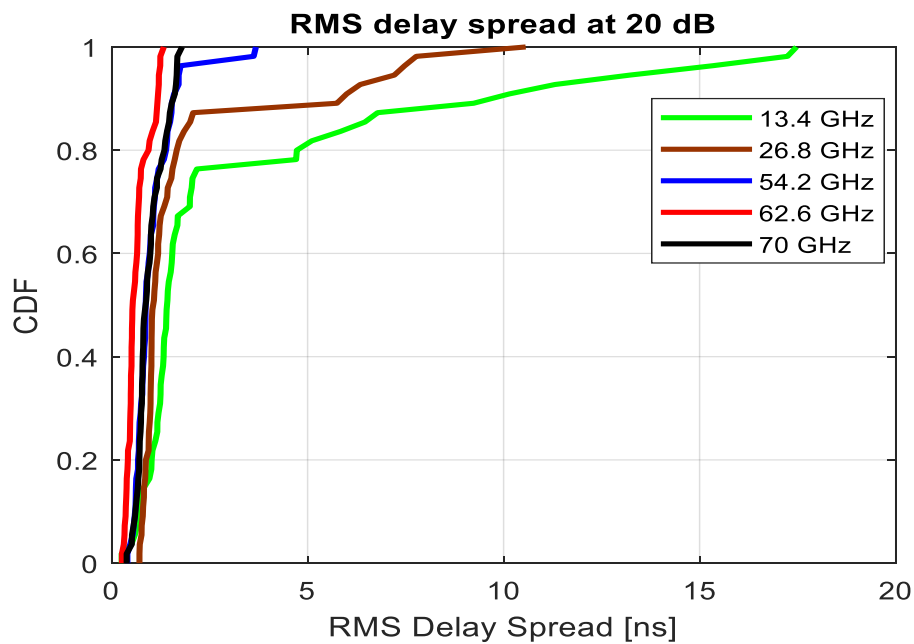The second scenario in this study is the factory like environment. Figure 3-14 (a) shows the layout of the laboratory and figure 3-14 (b) presents a photograph taken from the receiver side on the second floor to give a good sense of the laboratory's contents, where the transmitter is located at the far end of the picture. The laboratory is formed of two floors with a total height about 6 metres, the width is about 14 metres and it is around 34 metres long. The laboratory is a very reflective environment, being full of metallic surfaces of different sizes and shapes that might generate a long delay spread in this environment. The surrounding wall of the second floor is mainly made of wired glass for protection, where the wind tunnel produces high level of noise and vibration, and all of the machines shown in the layout are part of the wind tunnel system. The transmitter antenna was fixed during the measurement at a height of 3 metres above the ground in the location shown in the layout and the receiver antenna was placed at a height of 1.6 metres. The receiver was moving in the direction shown by the black dashed arrow in the figure, where it was 6 metres away from the receiver to start with. The experimental set-up was the same as that described in section 1.1.

<div align="center">(a)   (b)</div>
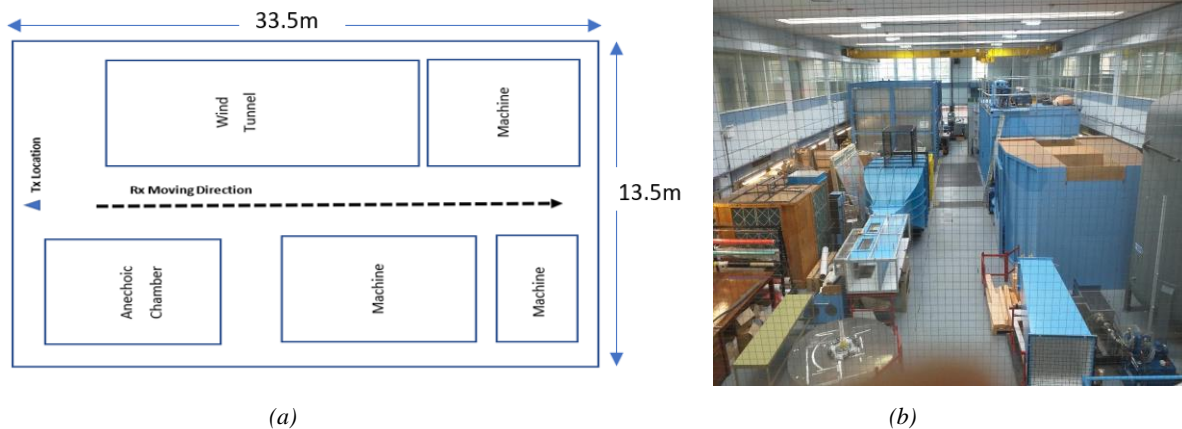
Figure 3-14 Factory like : (a) layout; (b) photograph from the Rx point of view

3.3.1 Received power and path loss

Figure 3-15 shows the received power versus separation distance between the transmitter and receiver for each frequency band. The general trend was the same over all bands, where the power level descends with increasing the separation distance between the transmitter and the receiver with variations in power level at some distances and varying from one frequency to another. Table 3-5 presents the values of power level variation over distance for each frequency band. The table shows some similarity in variations between most of the bands. It is noticeable

that the 26.8 GHz shows the highest variation between the near and far points, which was 20 dB. The variations for the remaining frequencies were very close to each other, within 1 dB.
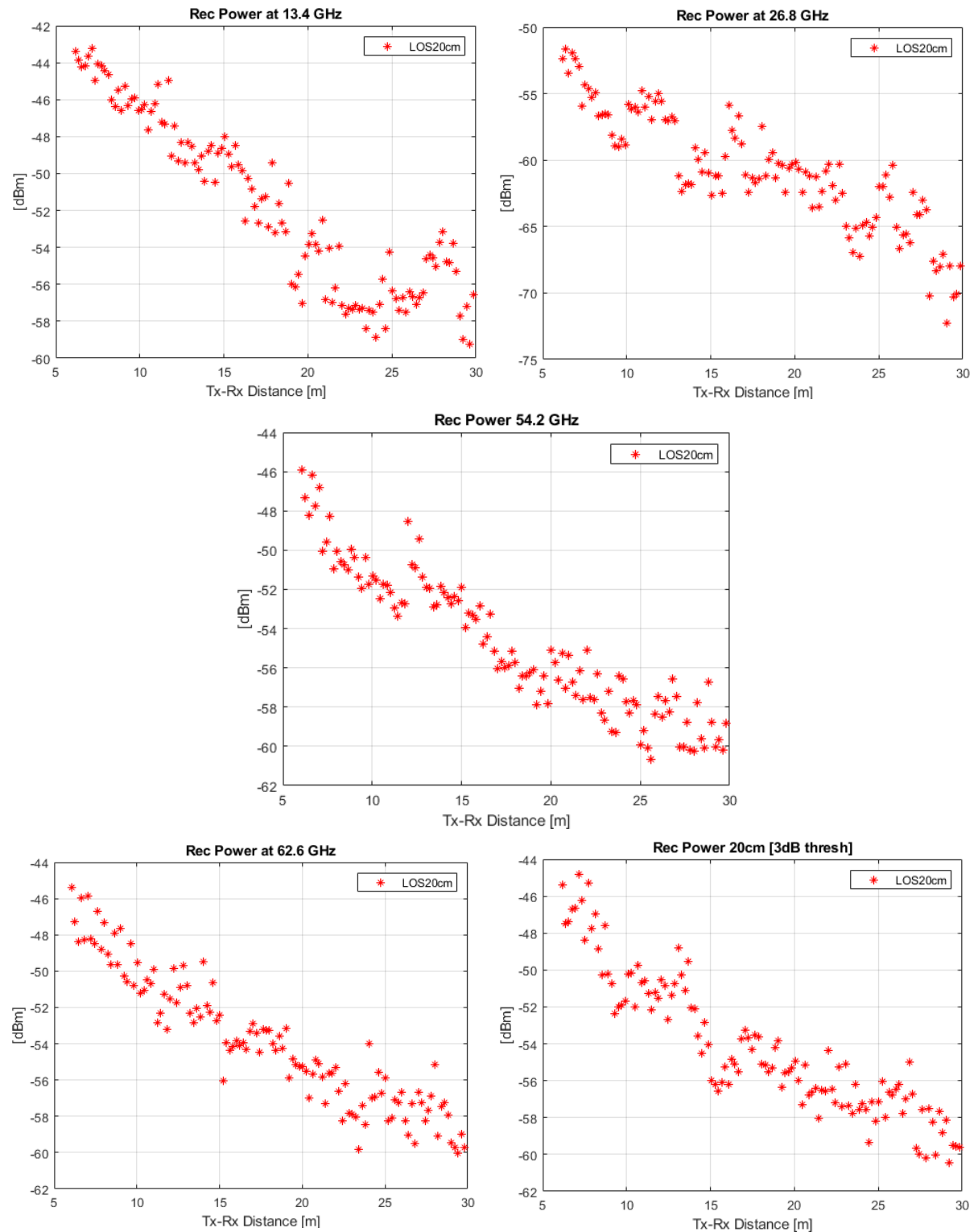
Figure 3-15 Received power for five frequency bands in the factory like

Table 3-5 Variations in power level for each frequency band

Centre Frequency	Power level variation [dBm]	Highest power level [dBm]	Lowest power level [dBm]
13.4 GHz	16	-43	-59
26.8 GHz	20	-52	-72
54.2 GHz	15	-46	-61
62.6 GHz	15	-45	-60
70 GHz	16	-44	-60

(a)

(b)
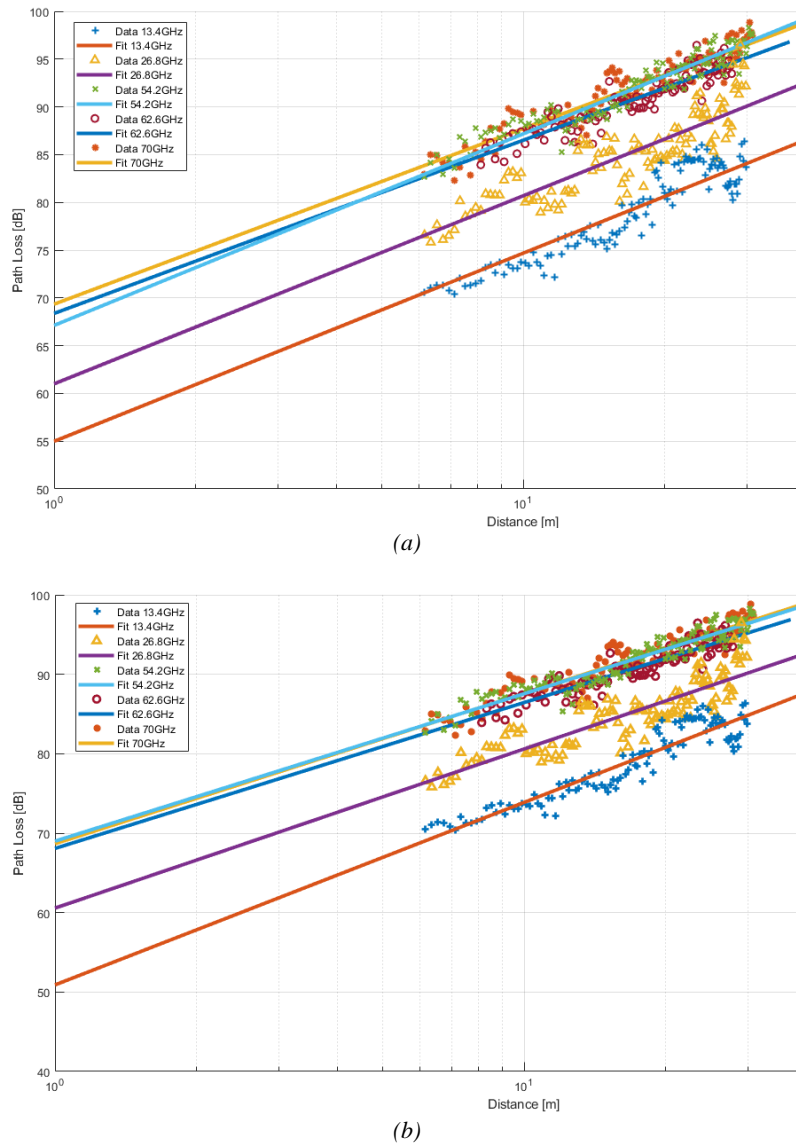
Figure 3-16 LOS Path loss for: (a) CI model. (b) FI model

The CI path loss model and the FI path loss model for the measured bands are shown in figure 3-16 (a) and (b) respectively. The parameters for both models are presented in table 3-6. There was a similarity in the parameters between the two models over all bands. The maximum

difference between the PLE(n) for the CI model compared with the slope (β) for the FI model for all the five frequency bands was less than 0.4 dB. The maximum difference in the standard deviation (σ) between the two models was 0.11 dB in this environment.

The PLE for all bands was less than or equal to the theoretical free space value (n=2), which can be explained by the fact that, this environment is highly reflective and the measured path was bounded by metallic surfaces on both sides, which might work as a wave guide at most of the measurement points. It can be noticeable that, the standard deviation at the 26.8 GHz was higher than the other bands for both models which shows the dispersion effect of this environment was higher at this band than the others.

Table 3-6 Parameters of the two path loss models

Path loss Model		13.4 GHz	26.8 GHz	54.2 GHZ	62.6 GHz	70 GHz
CI	n	1.97	1.97	2	1.81	1.84
	σ	1.76	2.12	1.21	1.12	1.29
FI	α	50.89	60.56	68.99	68.1	68.67
	β	2.29	2	1.86	1.84	1.89
	σ	1.65	2.12	1.18	1.12	1.29

Figure 3-17 illustrates the signal strength decay against delay spread for the five bands. The figure shows a general trend of a decay in signal strength as the separation distance between the transmitter and receiver increases. However, there are variations in the signal strength level at different distances, where it goes up or down from the average decay slope, probably as a result of the reflected multipath components at each distance for each frequency band. For the 26.8 GHz band there is a noticeable drop in power level at different separation distances especially between 15 to 20 metres, which suggests that this frequency band is affected by the structure of the environment more than the other bands.
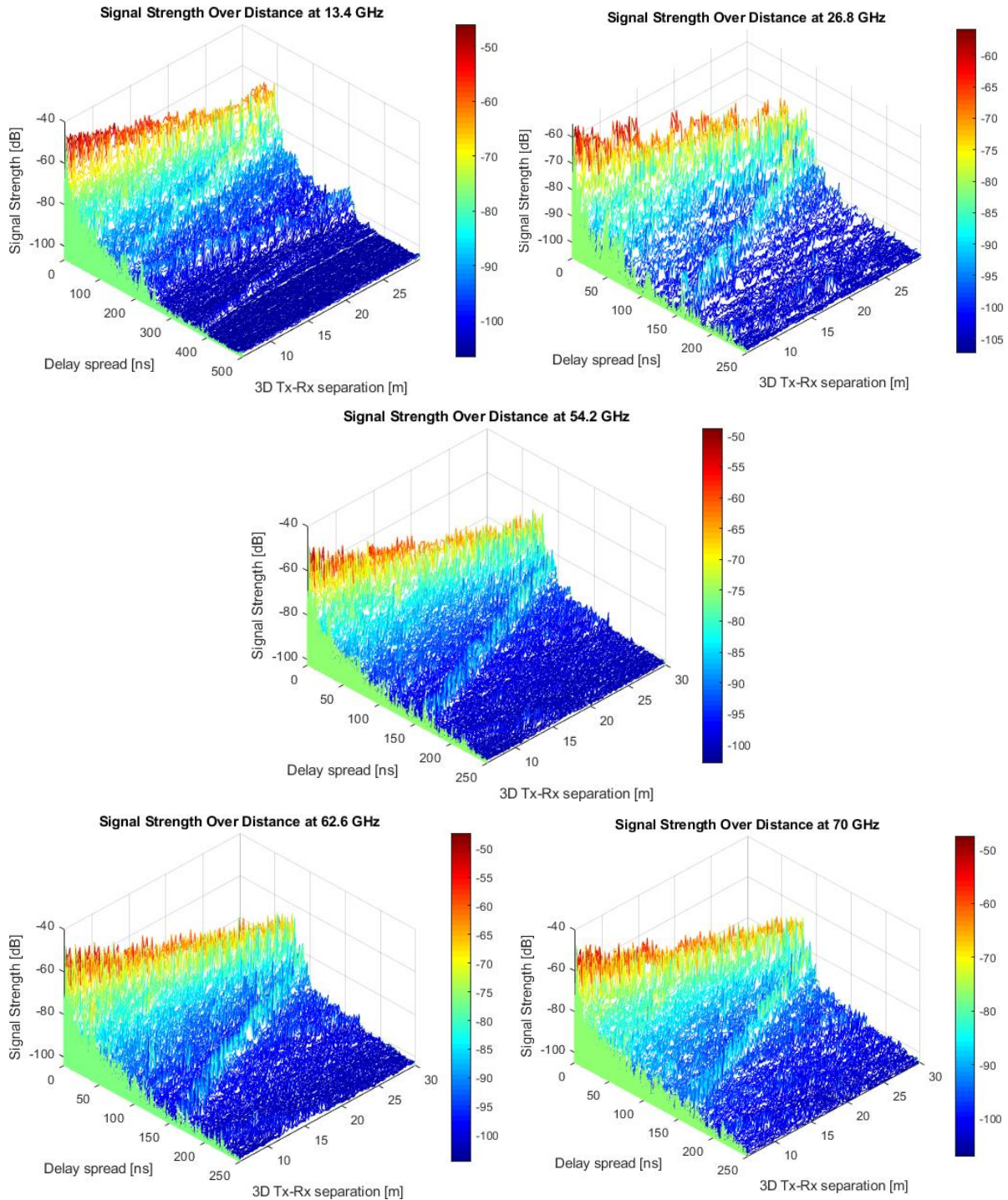
Figure 3-17 Signal strength against range for the frequency bands

3.3.2 Time dispersion parameters

3.3.2.1 Power delay profile

Figure 3-18 shows the normalized PDP samples at three chosen points from each measured frequency band. The PDP examples show large number of multipath components and they are close to each other especially, for the higher frequency bands. That might be because, this environment has high numbers of scatterers, since it is full of metallic surfaces. However, that is not shown in the 12.65 – 14.15 GHz band due to the existence of a very strong single main component compared to the reflected components, especially for the points closest to the transmitter. The excess time delay for this environment with respect to the main component (LoS) and within the 20 dB threshold is between 3 and 100 nanoseconds for the 12.65 – 14.15 GHz band, between 1.5 and 119.5 nanoseconds for the 25.5 – 28.5 GHz band, between 2.5 and 91 nanoseconds for the 51.2 – 57.2 GHz band, between 2.5 and 134 nanoseconds for the 59.6 – 65.6 GHz band and between 1 and 105.5 nanoseconds foe the 67 – 73 GHz band. The delay spread ranges were high for all the bands as predicted earlier in section 1.2, according to the dimensions and contents of this environment. The delay spread for this environment was not normal, where the lower frequencies would be expected to have higher delay spread, but each frequency band responded differently according to wavelength and the shapes and size of scatterers. Therefore, the 59.6 – 65.6 GHz band experienced the longest delay spread, while the delay spread was the shortest at the (51.2 - 57.2 GHz) band in this environment. The longest delay spread was about 1.2 times the laboratory length.

a)   for 12.65 – 14.15 GHz

b)   for 25.5 – 28.5 GHz

c)   for 51.2 – 57.2 GHz

d)   for 59.6 – 65.6 GHz

e)   for 67 – 73 GHz
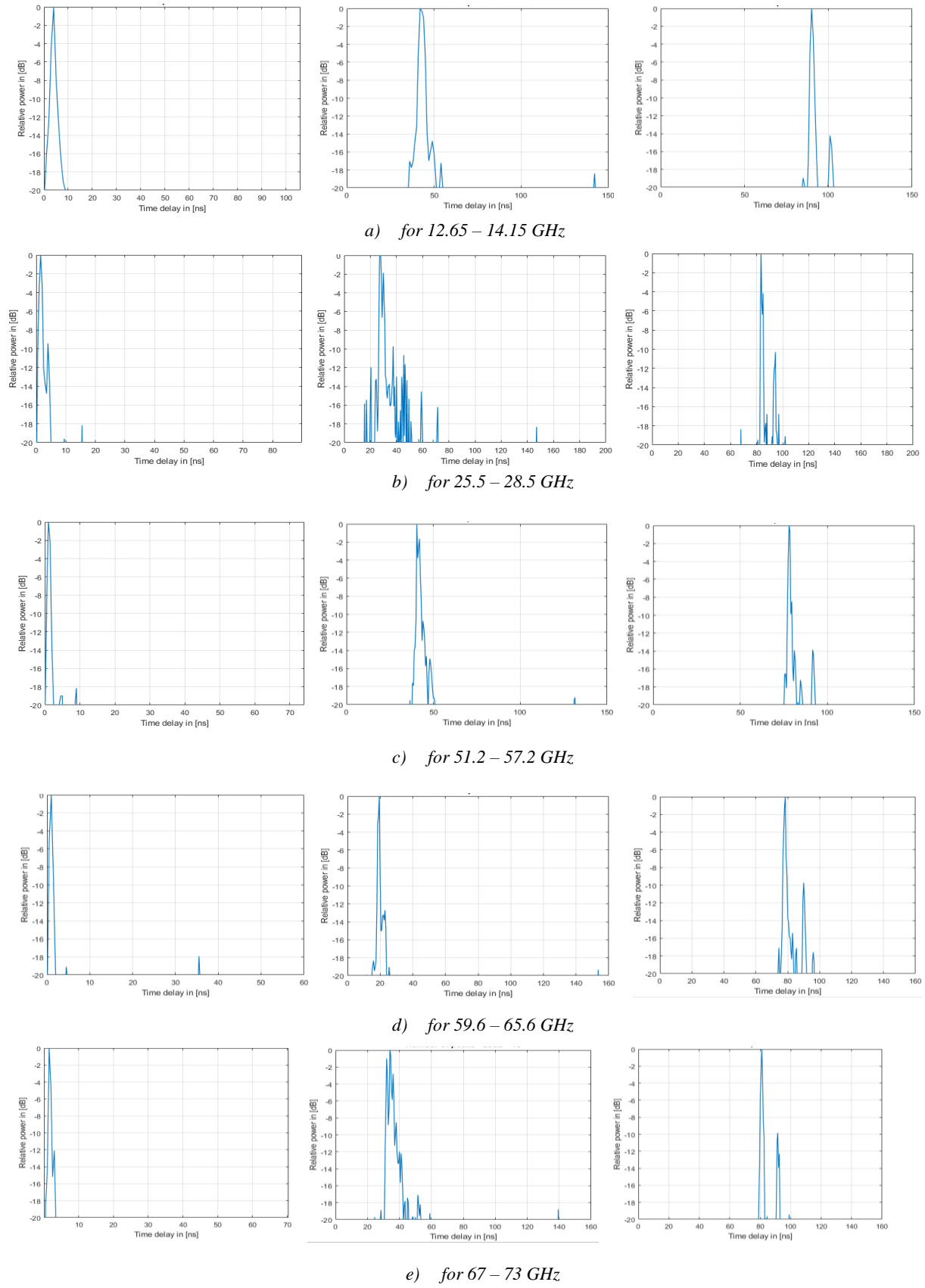
Figure 3-18 PDP samples from all measured frequency bands

73

Figure 3-19 presents the normalized PDPs images to their maximum for each frequency band within a 20 dB threshold from the maximum. This figure shows that the values of delay spread for all bands were less than 120 nanoseconds and decreased as the receiver moved away from the transmitter. It can be seen from the 13.4 GHz image in figure 3-19 that, the difference in power level of the main component between the first point (which is the closest to the transmitter) and the far points increased as the separation distance increased to become more than 10 dB at about half of the points. This might be explained by the absence of multipath components in the 13.4 GHz image, despite the excess time delay being about 100 nanoseconds at this frequency band.
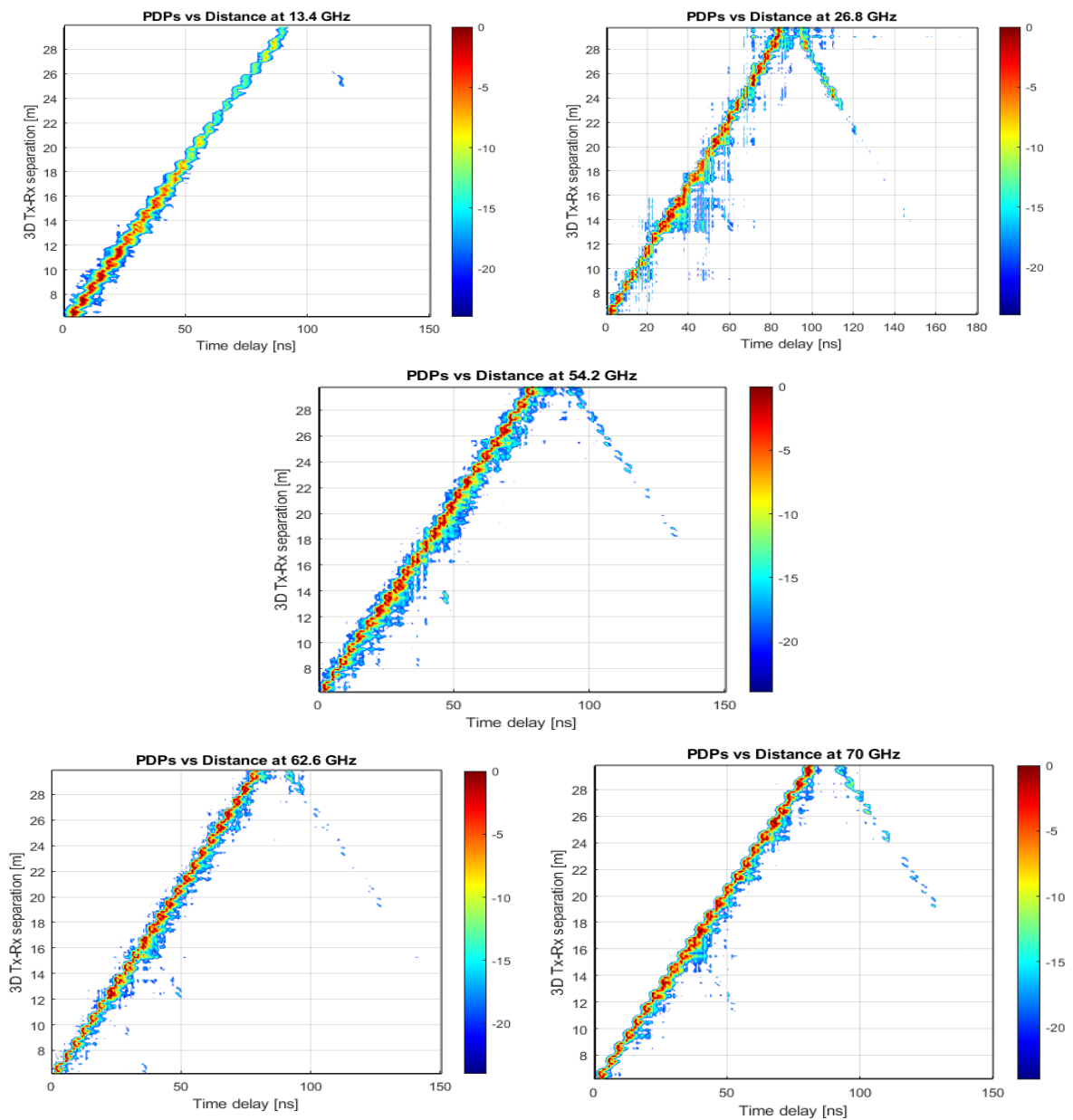
Figure 3-19 PDPs against distance for all measured frequency bands

3.3.2.2 Average and RMS delay spread

Figure 3-20 shows that the average delay spread was less than 30 nanoseconds for all bands. The average delay spread for 13.4 GHz shows a small variation within 4 nanoseconds up to about 20 metres separation distance, and then there is a sudden increase after that to reach about 16 nanoseconds for the last few points, which shows the effect of the difference in the power level of the main component between the close and far points. For 26.8 GHz, the average delay spread dropped at the distance intervals between 10 to 12 and 16 to 20 metres due to reductions in the number and power level of multipath components, and it reached a maximum value at 24 metres which reflects the power level and number of multipath components at this distance, as shown in figure 3-19. In general, there is sudden change which may be up or down in average delay spread between consecutive points. This is a clear indication of the nature of this environment, as mentioned earlier, is dispersive and frequency sensitive.

Figure 3-20 Average delay spread against distance for all measured frequency bands

The value of RMS delay spread for all measured frequencies are presented in figure 3-21. This figure shows a noticeable increase in RMS delay spread in all the bands after a certain distance, indicating the existence of multipath components at these distances.
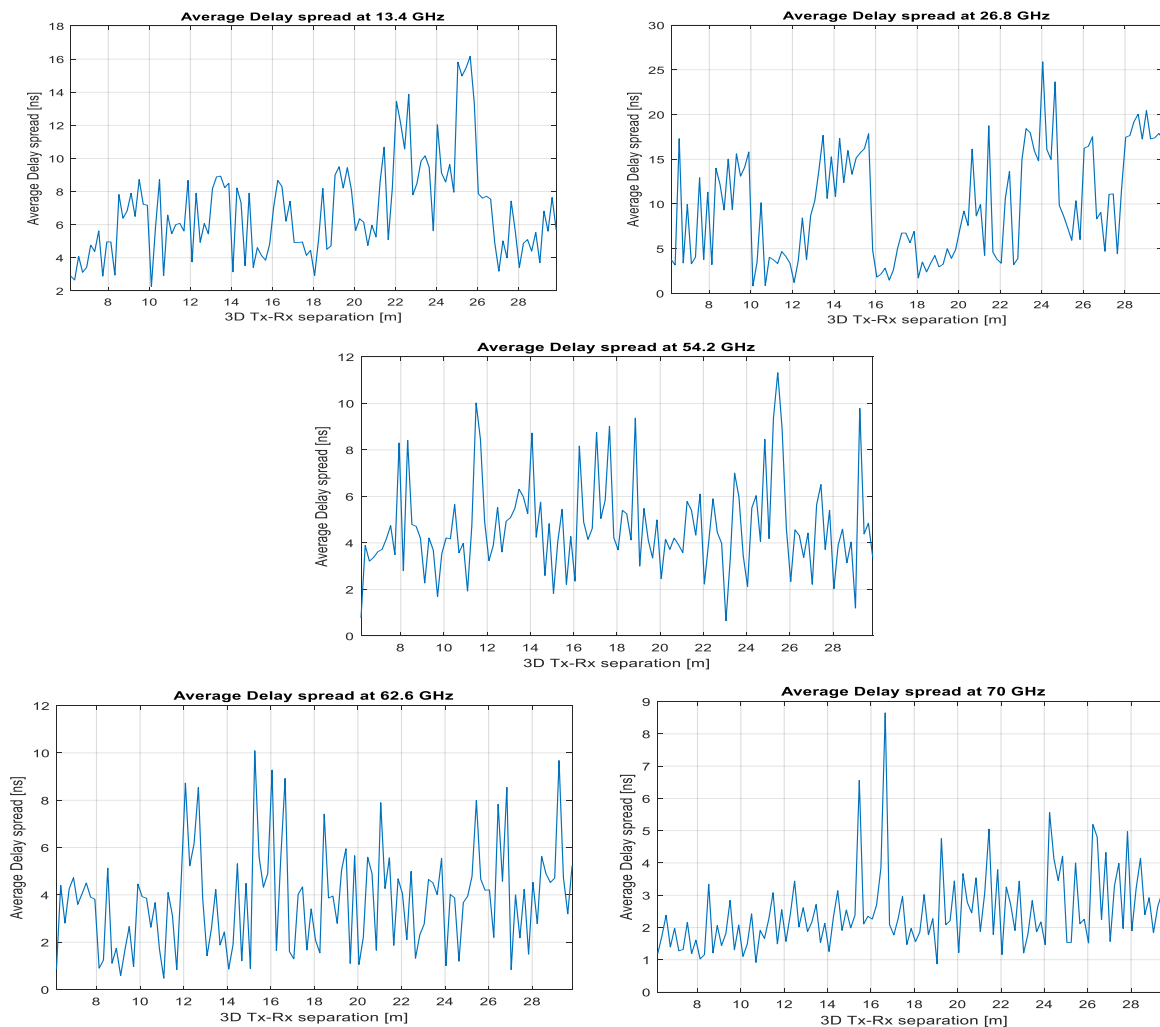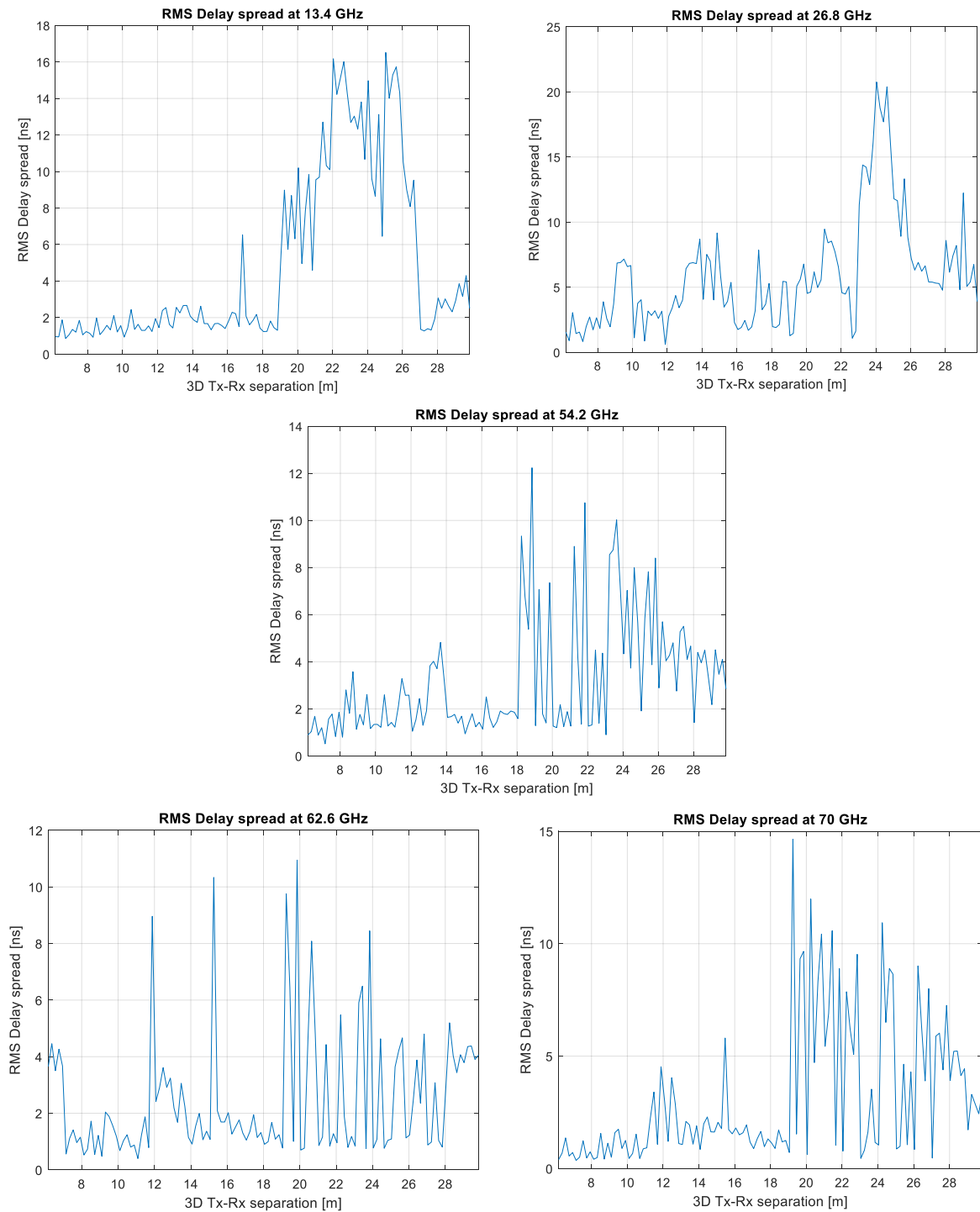

Figure 3-21 RMS delay spread against distance for all measured frequency bands

The RMS delay spread values represent the number and power level of such components. This can be checked by comparing figure 3-21 to the colormap in figure 3-19. However, for the 13.4 GHz image, most of these components are not shown because the image was normalized to the strongest main component over all the PDPs and the difference between the first and far points was more than 10 dB and the threshold was 20 dB from the maximum. Therefore, the multipath components with power level differences greater than 10 dB from their main components will not appear in this image.

The CDF of the RMS delay spread for all the measured frequency bands are shown in figure 3-22, which was less than 25 nanoseconds for this environment. The RMS delay spread values for indoor environments are presented in table 3-7. The figure and the extracted values in the table show, as expected, a longer RMS delay spread for the lower frequency bands than those for the higher ones, especially at 90% for the first four bands. However, the CDF for the RMS delay spread at 70 GHz was close to that at 54.2 GHz, as in the previous scenario. For the 10% and the median values, all the frequency bands follow the same trend of the CDF value decreasing as frequency increases, except for 26.8 GHz where the RMS delay spread gave the highest values compared with those of the other bands.

Figure 3-22 CDF of RMS delay spread for all measured frequency bands

Table 3-7 The CDF values of RMS delay spread

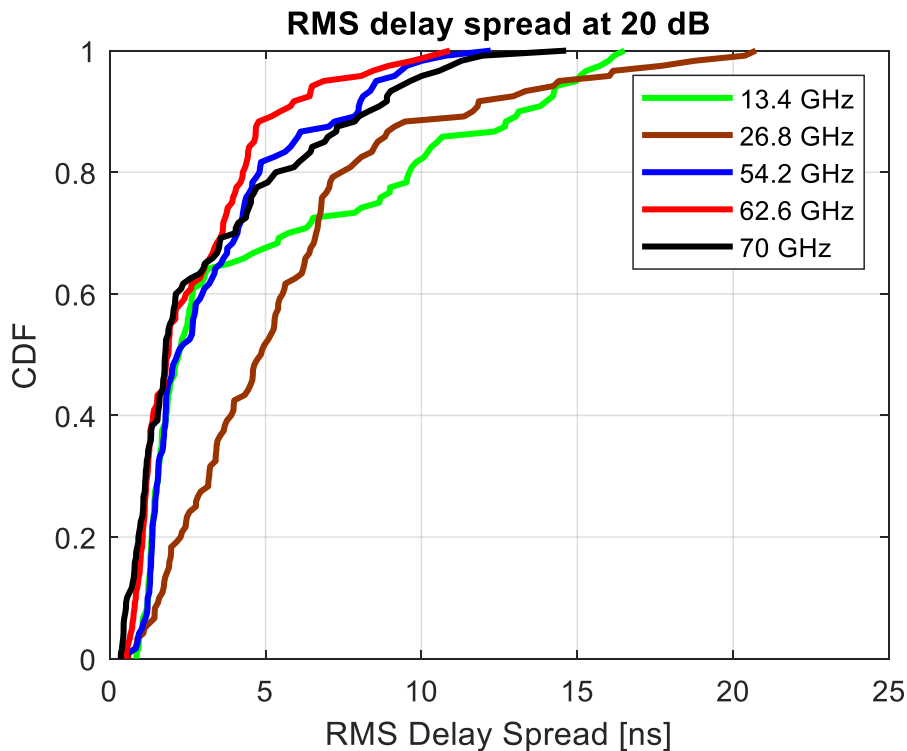| CDF	13.4 GHz	26.8 GHz	54.2 GHz	62.6 GHz	70 GHz
10%	1.23	1.62	1.22	0.84	0.56
50%	2.22	4.85	2.17	1.88	1.78
90%	13.12	11.65	7.98	5.47	8.29

3.4 Small office

The third environment involved in this study is the small office scenario. This environment has the characteristics of a wide corridor, as shown in the layout in figure 3-23 (a) and the photo from the receiver point of view 3-23 (b). Its width is about 6 metres and about 30 metres long, and the ceiling height in the measurement area is less than 2.5 metres. The wall on one side is a glass window, and on the other side the final 10 metres are also made of glass, as seen in the photograph in figure 3-23 (b). The wall at the opposite end to location of the transmitter is made completely of glass with metallic frames. The experimental set-up and the procedure were the same as that in the previous scenarios described in section 3.1 except for the height of the transmitter antenna which was 2.3 metres above the ground and the receiver was 5 metres away from the transmitter at the first point.
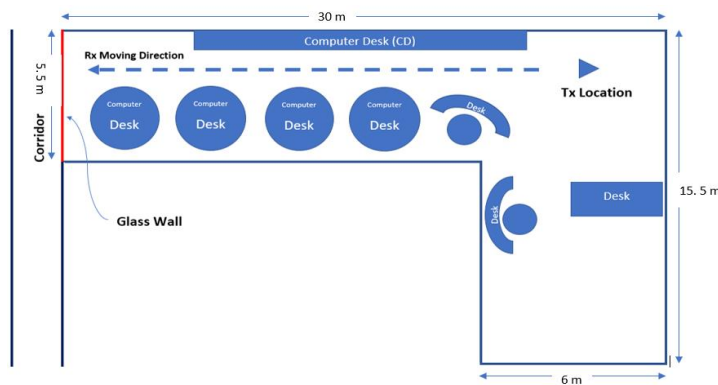
(a)   *(b)*

Figure 3-23 Small office: (a) layout (b) photograph from the Rx point of view

3.4.1 Received power and path loss

Figure 3-24 presents the received power versus separation distance between the transmitter and receiver for each frequency band calculated using the same MATLAB codes as in the previous scenarios. The general trend shows a large variation for all the bands at different distances, which gives some idea of the level of reflected signals from the surroundings, including glass

walls and windows, the carpeted floor and the low ceiling. Thus, the power level drops considerably at certain intervals of distance for each band according to their wavelengths. In general, the received power decreases as the Tx-Rx separation distance increases. The minimum, maximum and variation in power levels for each frequency band are given in table 3-8. The difference between the highest and the lowest variation was 9 dB in this environment. It is noticeable that the 26.8 GHz shows the highest variation between the near and far points in all three study scenarios.
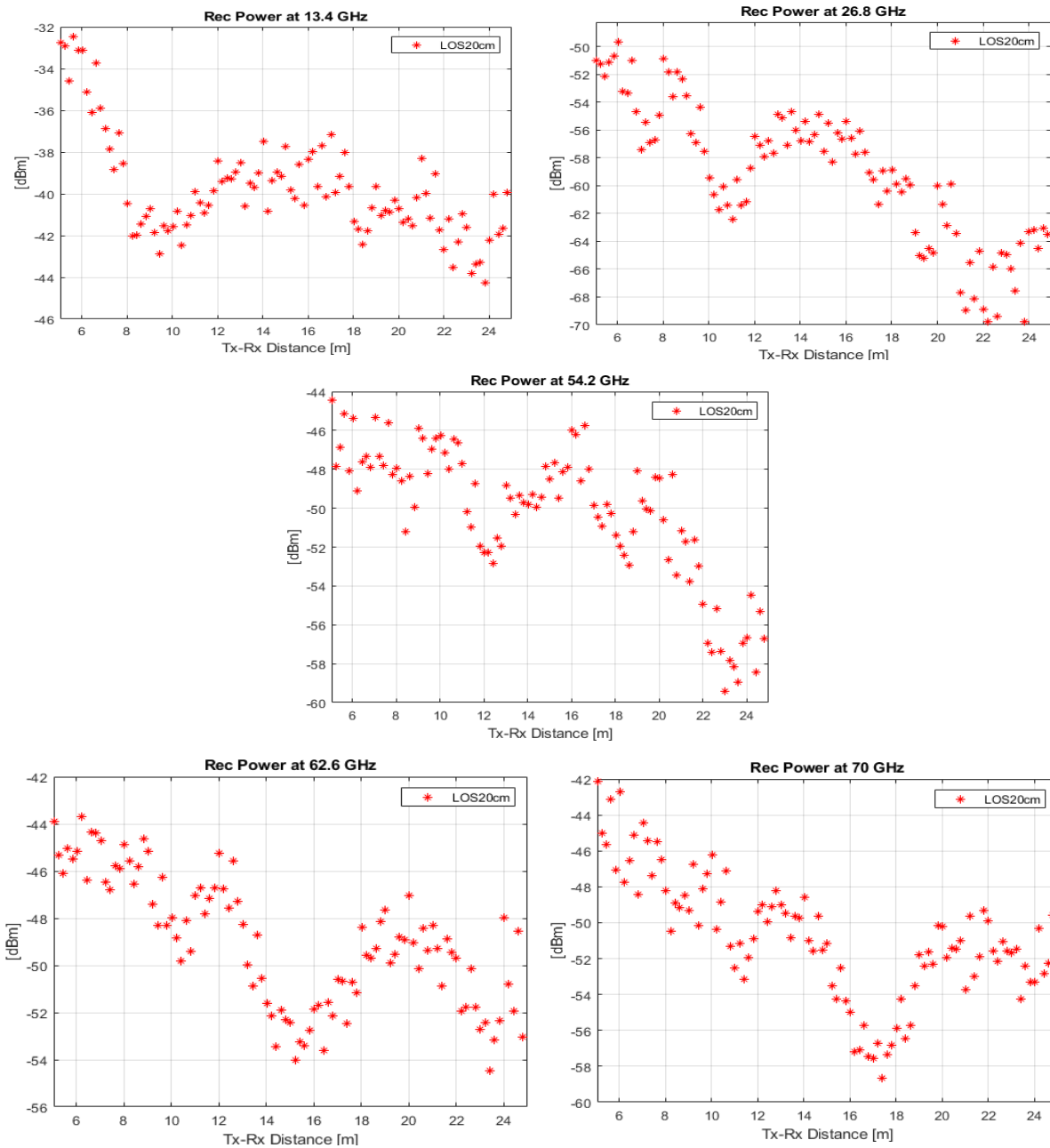
Figure 3-24 Received power for five frequency bands in small office

Table 3-8 Variation in power level for each frequency band

Centre Frequency	Power level variation [dBm]	Highest power level [dBm]	Lowest power level [dBm]
13.4 GHz	12	-32	-44
26.8 GHz	20	-50	-70
54.2 GHz	15	-44	-59
62.6 GHz	11	-44	-55
70 GHz	17	-42	-59
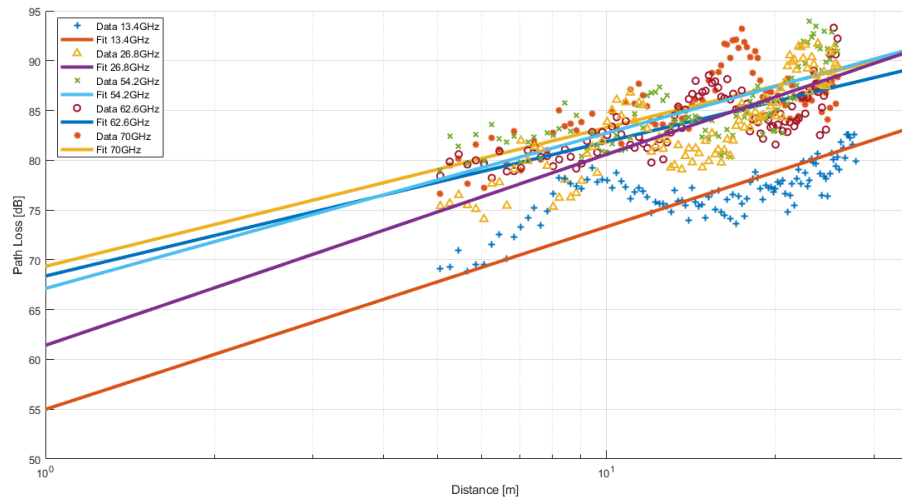
(a)
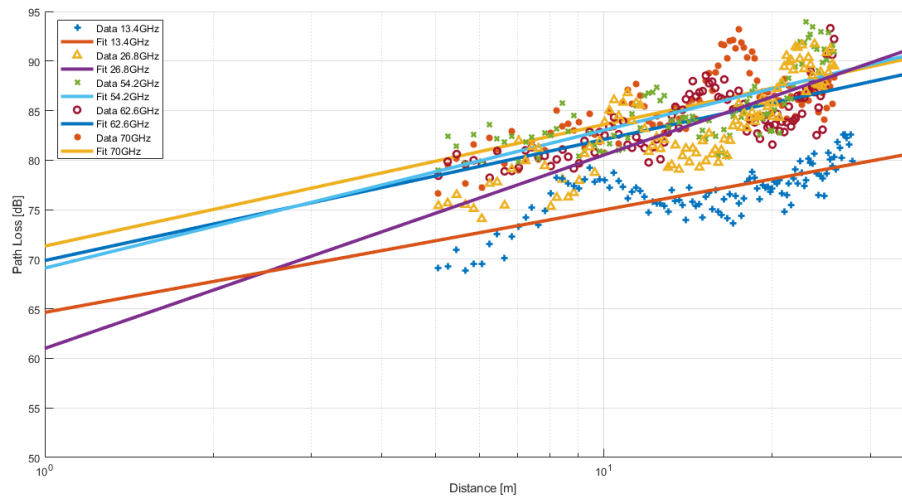
(b)

Figure 3-25 LOS path loss for: (a) CI model; (b) FI model

Figure 3-25 (a) and (b) illustrate the path loss models for the CI and FI models respectively for the measured bands. Table 3-9 gives the parameters of the two models. The equivalent parameters for both models were close with only a small difference of about 0.17 dB between

(n) & (β) and 0.02 dB for (σ) for all the bands except 13.4 GHz where the difference between (n) & (β) was about 0.8 dB, as can be observed by comparing figure 3-25 (a) and (b) for that band. The difference in the standard deviation (σ) between the two models for this band was 0.59 dB. This difference in the equivalent parameter between the two models at this band might be due to the large drop in the received power at Tx-Rx separation distances between 7 and 12 metres as shown in figure 3-24 for 13.4 GHz. The PLE values for all bands were lower than the theoretical free space value (n=2), especially for the last three bands where it was more than 0.4 dB lower than the theoretical free space value. This shows the effect of the reflected signals from the glass wall at the end of the corridor, which have more effect on the lower bands than the higher ones. The corridor scenarios are generally expected to have low PLE values due to the wave guide effect.

Table 3-9 Parameters of the two path loss models

Path loss Model		13.4 GHz	26.8 GHz	54.2 GHZ	62.6 GHz	70 GHz
CI	n	1.83	1.92	1.56	1.35	1.39
	σ	2.52	2.54	2.56	2.13	2.45
FI	α	64.64	61	69.11	69.87	71.33
	β	1.03	1.95	1.39	1.22	1.23
	σ	1.93	2.54	2.54	2.11	2.43

Figure 3-26 shows a decay in signal strength with delay spread for all bands. Also, there was a decay in the signal strength in general as the Tx-Rx separation distance increased. However, there was a change in the signal strength level, either up or down from the mean slope of decay at different distances as a result of the reflected multipath components at each distance for each frequency band according to their phase and amplitude. The variation in the power level was more noticeable at 26.8 GHz, where the power drop from the strongest power level reached more than 15 dB at Tx-Rx separation distances between 20 and 24 metres. This means that this environment has a higher effect at this frequency band than at other bands.
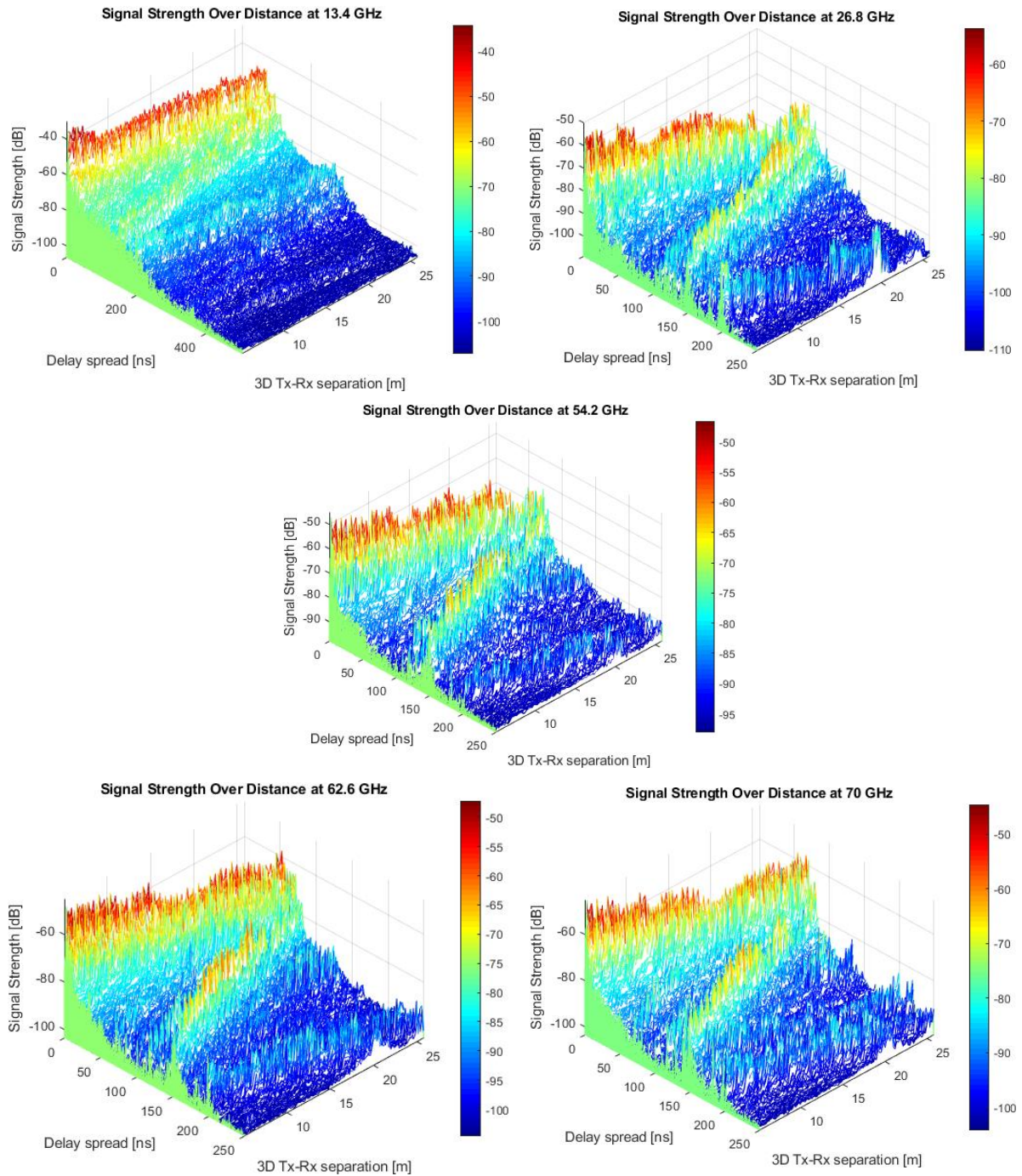
Figure 3-26 Signal strength against range for five frequency bands

3.4.2 Time dispersion parameters

3.4.2.1 Power delay profile

The PDP samples normalized to their maximum at three selected points from each frequency band are given in figure 3-27. These examples show high numbers of multipath components close to each other, particularly at the higher frequency bands. The sounder time resolution is 0.5 nanoseconds for the last four bands. This gives an indication of the large number of

reflectors in this environment and how close they are to each other. For the 12.65 – 14.15 GHz band, the sounder time resolution is 1 nanosecond, which may be because there are fewer multipath components at this band. In addition to existence of a strong dominant component at this band, specifically in the closer points to the transmitter. In this environment, the excess time delay with respect to the main component (LoS) and within the 20 dB threshold is between 1 and 123 nanoseconds for the 12.65 – 14.15 GHz band, between 2.5 and 139 nanoseconds for the 25.5 – 28.5 GHz band, between 4 and 147 nanoseconds for the 51.2 – 57.2 GHz band, between 4 and 133.5 nanoseconds for the 59.6 – 65.6 GHz band and between 2 and 144.5 nanoseconds for the 67 – 73 GHz band. The excess time delay for all bands was less than 150 nanoseconds in this environment. The values were very close to each other especially for the last three bands. However, the 51.2 – 57.2 GHz band shows the longest excess time delay compared with the other bands, that might be due to the dynamic range was low at this band. This increases the likelihood of more multipath components being included in the excess time delay calculation than for the other bands. Meanwhile the shortest excess delay was at the 12.65 – 14.15 GHz band, which shows the effect of a strong single dominant component. In addition, the destructive reflected components from the glass wall on the 12.65 – 14.15 GHz band had a larger effect than on the other bands as seen in the received power graph, where it was expected that there would be longer excess time delays for the lower bands than the higher bands. It is conspicuous that, despite it being as LoS measurement, some components were very close to the main component, and in addition, their level was higher than the LoS component in some cases, as shown in figure 3-27 (b) and (c).
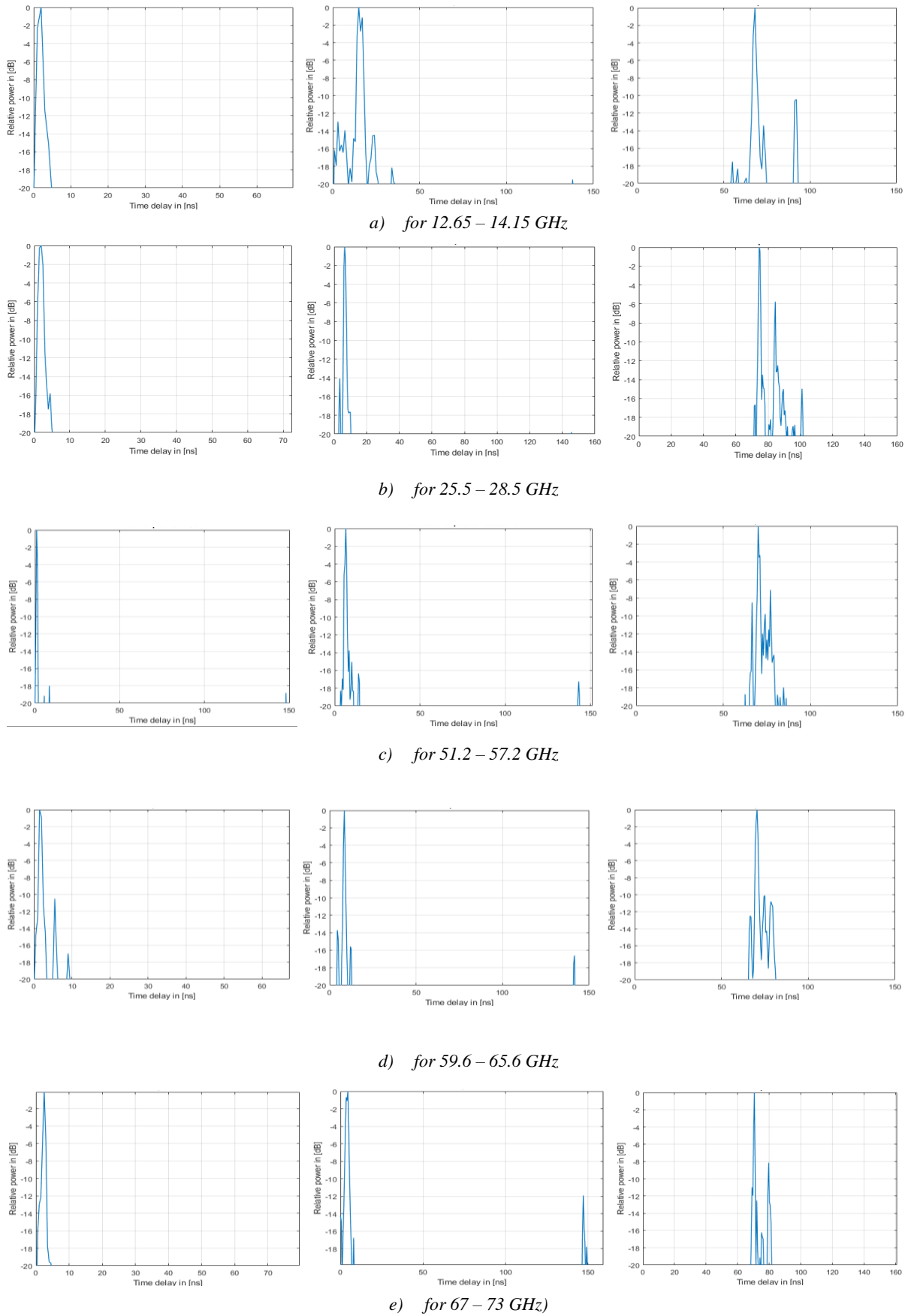
a)   for 12.65 – 14.15 GHz

b)   for 25.5 – 28.5 GHz

c)   for 51.2 – 57.2 GHz

d)   for 59.6 – 65.6 GHz

e)   for 67 – 73 GHz)

Figure 3-27 PDP samples from all measured frequency bands

The PDP images for each frequency band, normalized to their maximum within 20 dB from the maximum, are presented in figure 3-28. The delay spread in this environment was within 150 nanoseconds for the points closer to the transmitter for all bands, and it decreased as the Tx-Rx separation distance increased. The images show more components around the main component for the 51.2 – 57.2 GHz band, as a result of the low dynamic range in this band. For the first three bands there was a second wave of reflected multipath components, which is clearer at 26.8 GHz than at 54.2 GHz, and which is very weak at 13.4 GHz. This second multipath wave was reflected from the cross-corridor wall after it had penetrated twice through the glass wall at the end of the small office, as shown in the layout in figure 3-23. The second wave was not shown clearly in the 13.4 GHz image for the same reason mentioned earlier, because the main component has a strong power level compared with the reflected components, and also the first reflected wave was very weak compared to that for 26.8 GHz as shown in the images below. For the 26.8 GHz the signal strength of the first and second reflected waves were high at distances between 18 to 24 metres. For the last three bands the penetration loss was high on the second wave, so it is not shown in the images. However, for the 54.2 GHz there was a weak second wave.

It is noticeable that the reflected multipath components at the last three frequency bands were weak or completely absent when the receiver was moving over the final five metres. Here it would be expected to see stronger multipath components as the receiver became closer to the reflector. A reason for this might be that the receiving antenna for the first two bands was mounted on top of a mast, while for the last three bands it was fixed directly to the RF head and both were mounted on top of a 3D positioner, as shown in figure 3-29, where the Tx-Rx height difference was 0.75 metres and the transmitter was tilted down by 9 degrees. Therefore, this block of metal would reflect most of the transmitted signal back before it reaches the glass wall. In addition, the receiving antenna was covered with only 2 degrees of the transmitted beamwidth over the last five metres.
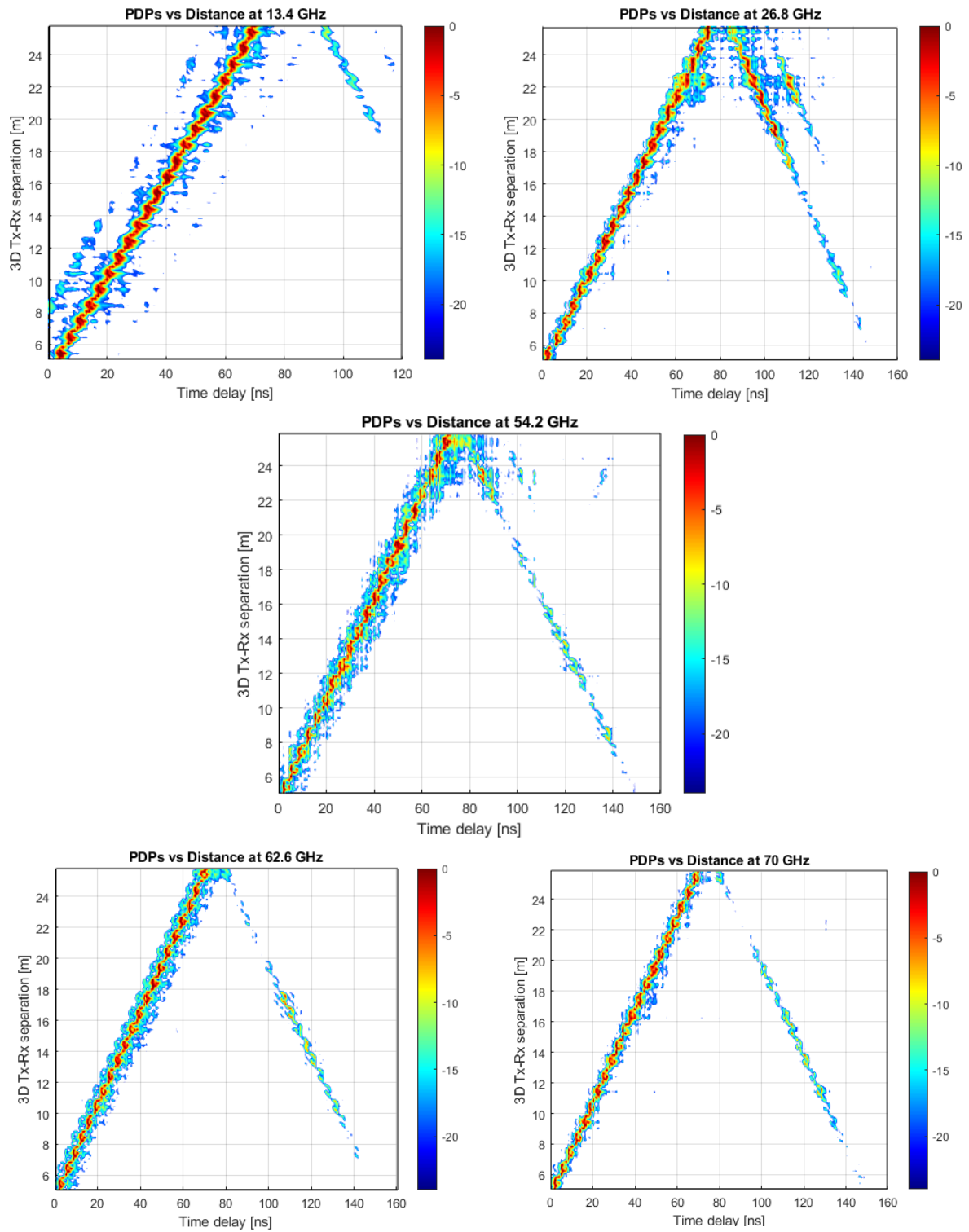
Figure 3-28 Delay spread against distance for all measured frequency bands
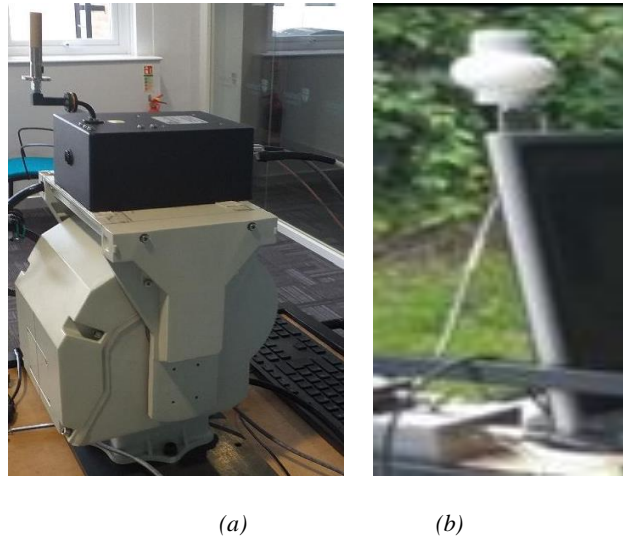
<center>(a)   (b)</center>

Figure 3-29 Omni-directional antennas mounting at the receiver side:

a) for last three bands; b) for the first two bands

3.4.2.2 Average and RMS delay spread

The maximum average delay spread was around 35 nanoseconds over all bands in this scenario, as given in figure 3-30. The average delay spread for the 13.4 GHz shows a small variation of 1 nanosecond around 15 nanoseconds at the separation distance interval from 6.8 to 10.4 metres and a variation of 2 nanoseconds around 16 nanoseconds at the separation distance interval from 21.8 to 24 metres. There was a large variation, either up or down from 2 nanoseconds up to about 16 nanoseconds in the separation interval in between the previous two distance intervals. This shows the drastic change in the number and power level of multipath components between adjacent points. For the 26.8 GHz band, the average delay spread was less than 15 nanoseconds up to the separation distance of 17 metres, and then there was a large increase after that reaching about 30 nanoseconds due to the strong first and second reflected waves when the receiver became closer to the glass wall. The average delay spread at the 54.2 GHz band was between 5 and 15 nanoseconds in most of the points; however, there was a large increase at some distances due to the existence of high power level multipath components at these distances which were about 5 dB lower than the main component, especially at 8.25 and 8.84 metres. For the 62.6 and 70 GHz bands the average delay spread fluctuated between 5 and 25 nanoseconds at the interval from 10 to 18 metres, and for the other points before and after this period the average delay was around 5 nanoseconds.

Figure 3-30 Average delay spread against distance for all measured frequency bands

Figure 3-31 illustrates the RMS delay spread over all measured frequency bands. The values of RMS delay spread give an idea of the existence of multipath components at different distances and how far apart they are, even if their power levels were not particularly high. For the 13.4 GHz the RMS delay spread was less than 8 nanoseconds up to 19 metres separation distance and then the reflected components appear, as in the image in figure 3-28, where the receiver

was closer to the glass wall to reach about 12 nanoseconds at this band. For the 26.8 GHz there were two distances where the RMS delay spread increased. The first was between 9 and 12 metres, reaching about 32 nanoseconds when the receiver was in a good position to receive the signal for all bands; and the second was between 17 and 23 metres where the maximum value was about 27 nanoseconds when the receiver was closer to the glass wall. For the 54.2 GHz the variation in RMS delay was similar to the average delay spread, but on a different scale. For the last two bands the RMS delay spread has higher values in the middle, while it was very low at the beginning and end. It is expected to see a low delay spread at the beginning due to the long distance that the signal needs to travel, and for the last 5 metres.

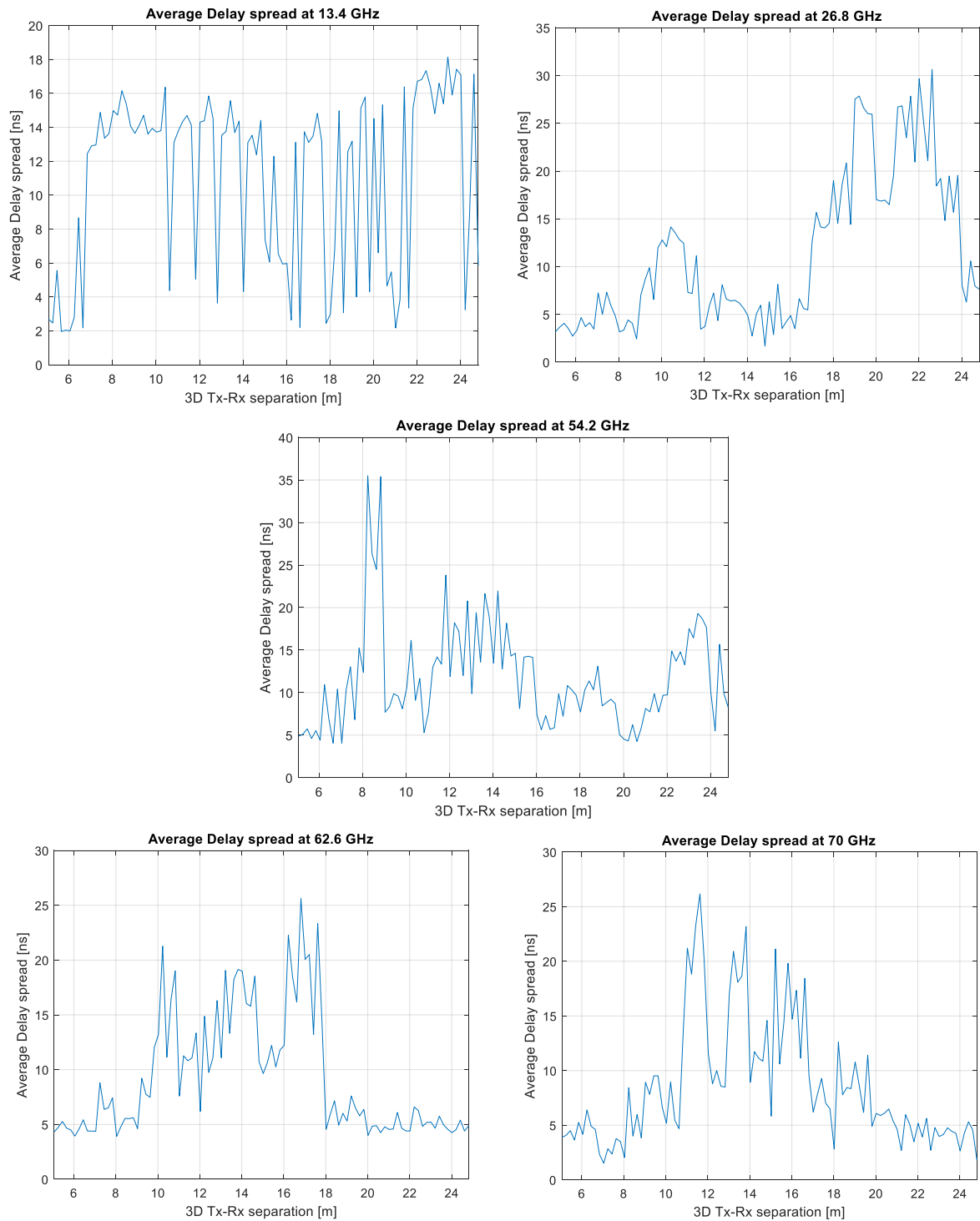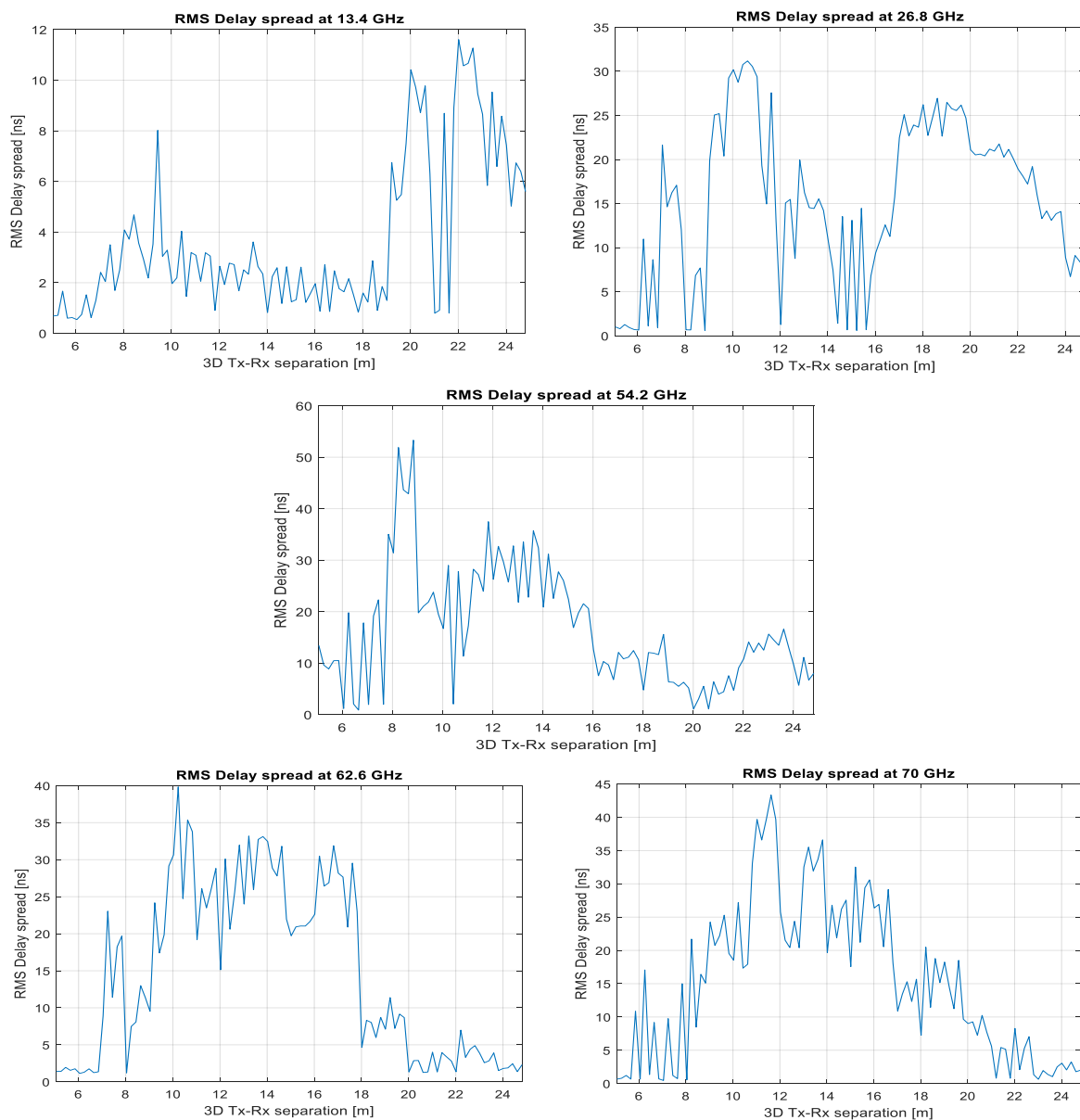**Figure 3-31 RMS delay spread against distance for all measured frequency bands**

The CDFs for the RMS delay spread over all the measured frequency bands are shown in figure 3-32, with values less than 60 nanoseconds for this environment. Table 3-10 presents the indoor recommended RMS delay spread values. The CDF values for 13.4 GHz were very low compared with the other bands especially, at 50% and 90%, which could be due to the large differences in power level between the main component and the reflected multipath components (high dynamic range) which might be caused by the installed power amplifier in the RF head at the receiver side. The last three bands provide the highest CDF values, at 90%, because of the large number of multipath components in the range between 9 and 20 metres. The dynamic range for the last three bands was slightly lower compared with those for the first two bands, as more multipath components were included in the delay spread calculation for the last three bands more than the first two.
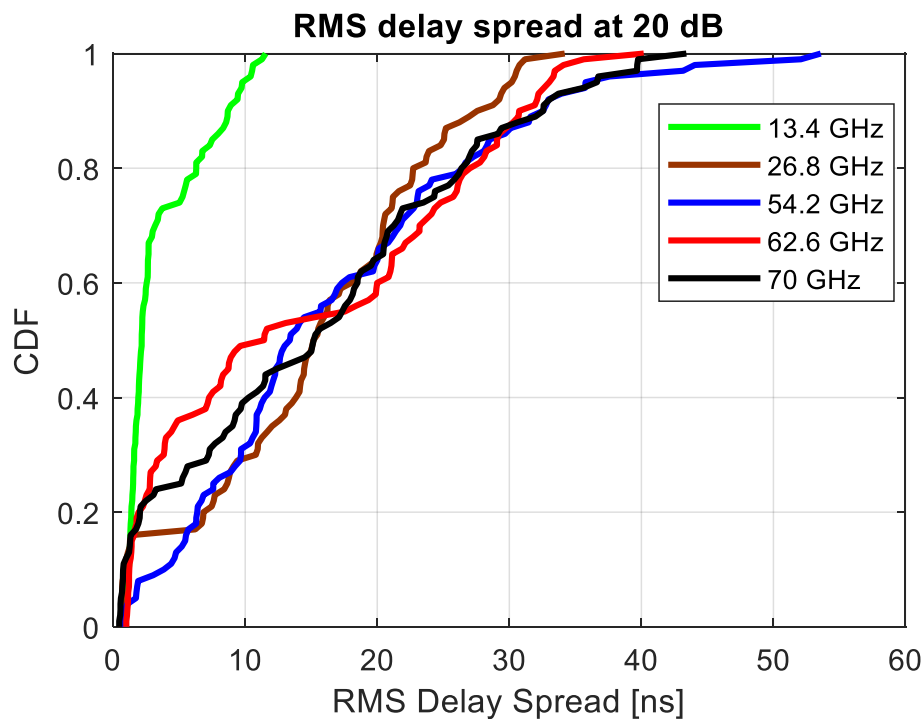

Figure 3-32 CDF of RMS Delay spread for all the measured frequency bands

Table 3-10 The CDF values of RMS delay spread

CDF	13.4 GHz	26.8 GHz	54.2 GHz	62.6 GHz	70 GHz
10%	1.18	0.92	3.83	1.22	0.75
50%	2.16	15.16	13.38	11.43	15.19
90%	8.68	27.57	32.55	30.75	32.57

3.5 Summary and discussion

In these measurements different parameters were calculated such as path loss, average and RMS delay spread. In terms of path loss two models were used in this study, which are the close-in (CI) model and the floating intercept (FI) model. The calculated parameters of both models showed similar values for all scenarios in terms of (n) compared to (β) and the standard deviation (σ) in both models. The highest and lowest values for both (n) and (β) at most of the bands were at the large office scenario and small office scenario respectively. Where the values of (n) and (β) were within 2.26 dB and within 2.58 dB respectively, for all bands and at all scenarios. There was a variation in the values of (n) and (β) between the bands at each scenario, where the highest and lowest values of (n) in most of the scenarios were at the 54.2 GHz band and 62.6 GHz band respectively. While for (β) there was no common pattern between the bands over scenarios. For the standard deviation values the highest and lowest values were at the small office and the large office scenarios respectively for both models, where the highest values were at 26.8 GHz band over all scenarios.

For the time dispersion parameters, in terms of the CDF of the RMS delay spread at 90% values, there was a variation in the pattern from one scenario to another, where the highest and lowest values in most of the environments were at the 13.4 GHz band and 62.6 GHz band respectively. It is noticeable that, the 54.2 GHz band and 70 GHz band have shown similar values of the CDF of the RMS delay spread over all the measured environments.

CHAPTER 4

INDOOR NON-LINE-OF-SIGHT AND COMBINED MEAUREMENTS

This chapter presents the results of two sets of non-line-of-sight (NLoS) measurements in indoor environments and one combined LoS and NLoS scenario. The NLoS scenarios are a factory like and a small office. The combined scenario is a large office. The study considers the same five frequency bands (12.65 – 14.15GHz, 25.5 – 28.5 GHz, 51.2 – 57.2 GHz, 59.6 – 65.6 GHz and 67 – 73 GHz) as discussed in chapter 3. The measurements were conducted using the same sounding system with the same procedures and set-up as in chapter 3. However, to improve the signal strength for the three highest frequency bands, a low noise amplifier (LNA) was used in the NLoS measurements. This chapter assesses the same parameters as discussed in chapter 3, which are received power, path loss, excess time delay, average delay and RMS delay spread.

4.1 Factory like environment (NLoS)

Figure 4-1 shows the layout of the factory like environment. The transmitter was moved to the corner and pointed at an angle to illuminate the area between the two dashed lines. To maximize the received signal strength, the angle was calculated according to the antenna's beamwidth so the wind tunnel corner would be the starting point for the beam, as shown in the figure 4-1.The first measurement point was selected to be out of the line-of-sight with the transmitter. The dashed arrow in figure 4-1 shows the receiver's movement route during measurements.
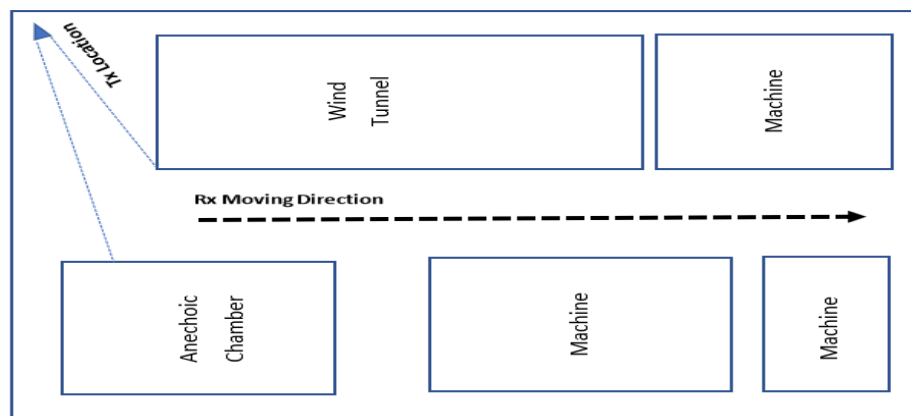

Figure 4-1 Factory like layout NLoS scenario

4.1.1 Received power and path loss

The values of received power versus Tx-Rx separation distance for each frequency band are shown in figure 4-2. The trend in general was similar over all bands due to the waveguide effect of the measured path. The power level fell exponentially as the receiver moved away. However, there was a sudden increase in received power at a distance of around 15 metres, which was caused by the second reflection of the strongest signal from the metallic surface of the wind tunnel. Values of variation in power level against distance are presented in table 4-1 for each frequency band. The table shows larger values of variation for the higher frequency bands, even though the power level of the highest three bands was much higher than that of the first two due to the use of the LNA. This means that the higher frequency bands experienced higher attenuation as the separation distance increased in this environment regardless of their power level.

Table 4-1 Variation in power levels for each frequency band

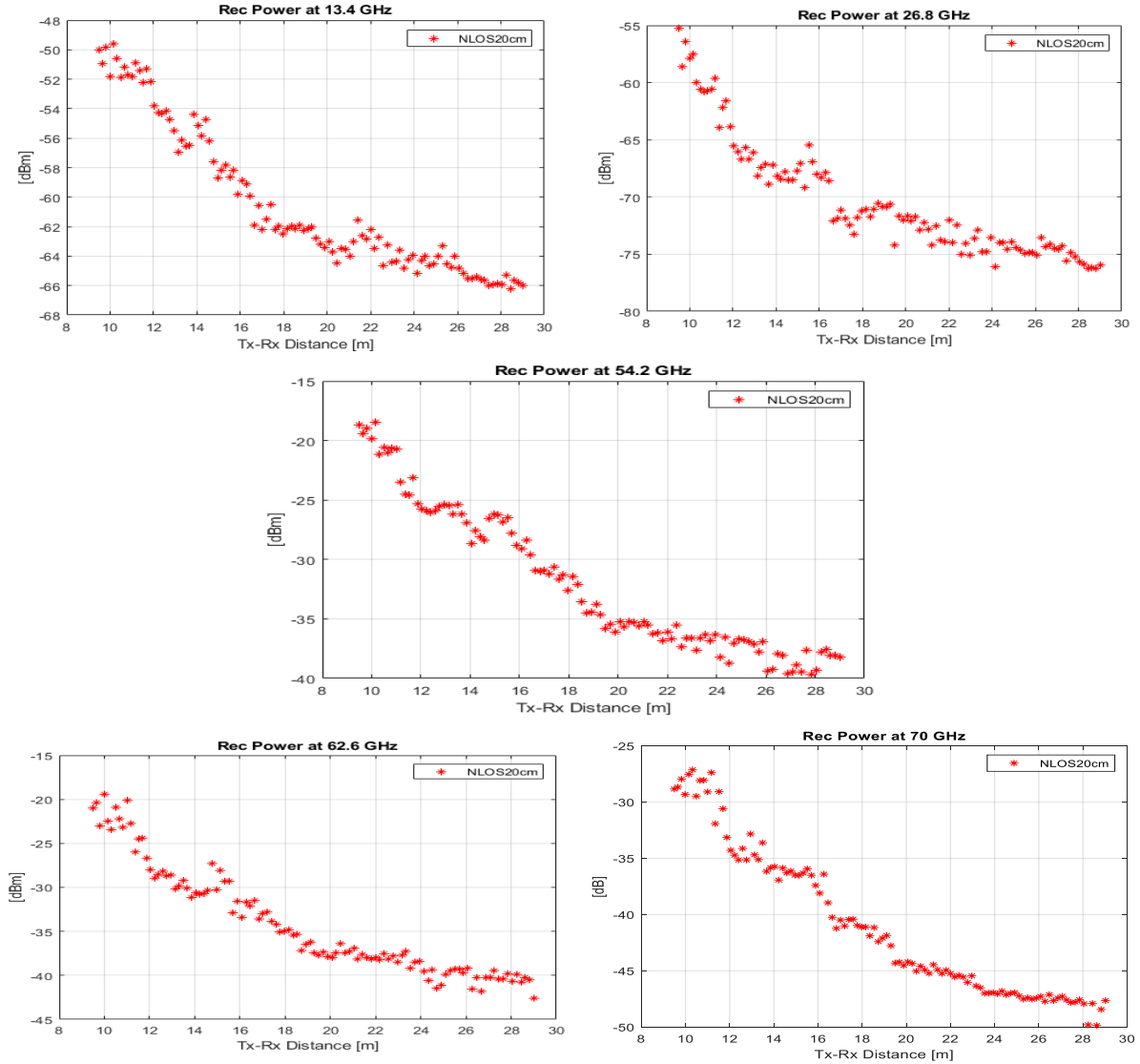| Centre frequency	Power level variation [dBm]	Highest power level [dBm]	Lowest power level [dBm]
13.4 GHz	17	-49	-66
26.8 GHz	22	-55	-77
54.2 GHz	21	-18	-39
62.6 GHz	23	-19	-42
70 GHz	23	-27	-50

Figure 4-2 Received power for five frequency bands in the factory like

The results of the CI and FI path loss models are shown in figure 4-3 (a) and (b) respectively. Table 4-2 presents the parameters of the two models. The two models show closer values in this scenario. For PLE (n) compared with (β) in the first two bands, the difference was within 0.2 dB and within 0.04 for (σ). Meanwhile for the last three bands the difference was higher, at between 0.43 and 0.66 dB for PLE(n) compared with (β) and between 0.12 and 0.3 dB for (σ). The maximum differences over all bands were for (n) 0.24 dB and 0.88 dB for (β), which shows a large variation between bands in the FI model compared with the CI model in NLoS scenario.

(a)

(b)
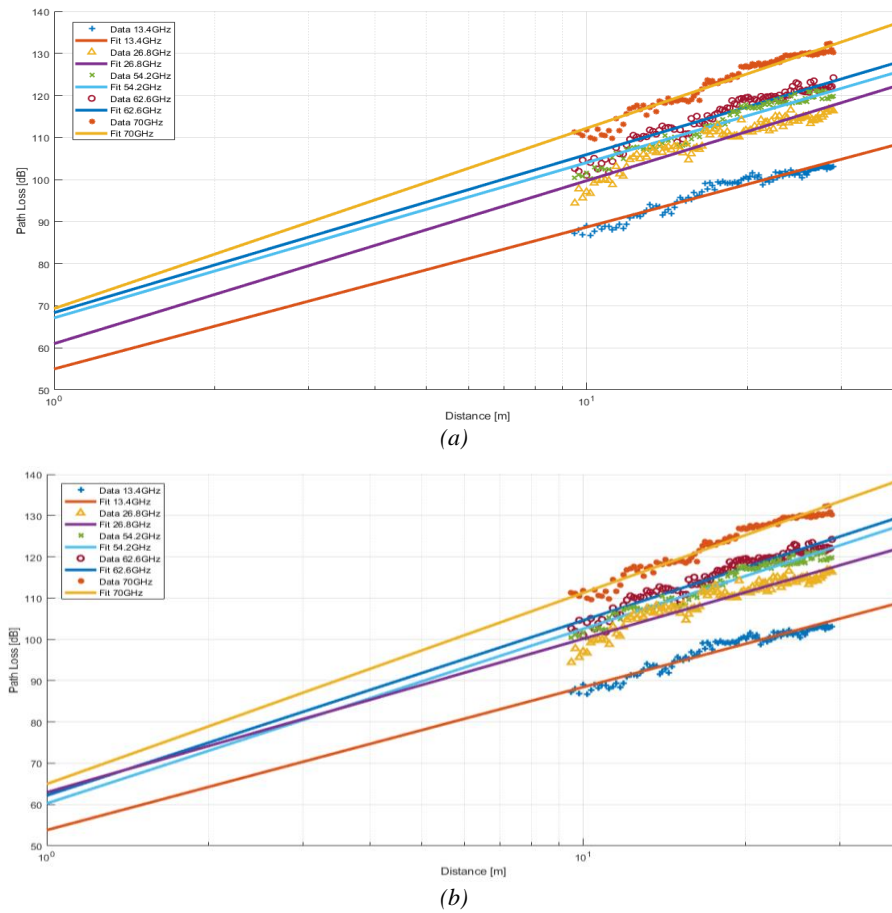
Figure 4-3 NLoS path loss for two different models: (a) CI model; (b) FI model

Table 4-2 Parameters of the two path loss models

Path loss model		13.4 GHz	26.8 GHz	54.2 GHZ	62.6 GHz	70 GHz
CI	n	3.93	3.78	3.69	3.75	3.88
	σ	1.38	1.66	1.46	1.56	1.59
FI	α	57.53	62.89	59.93	62.95	60.87
	β	3.73	3.66	4.26	4.18	4.54
	σ	1.34	1.65	1.24	1.44	1.29
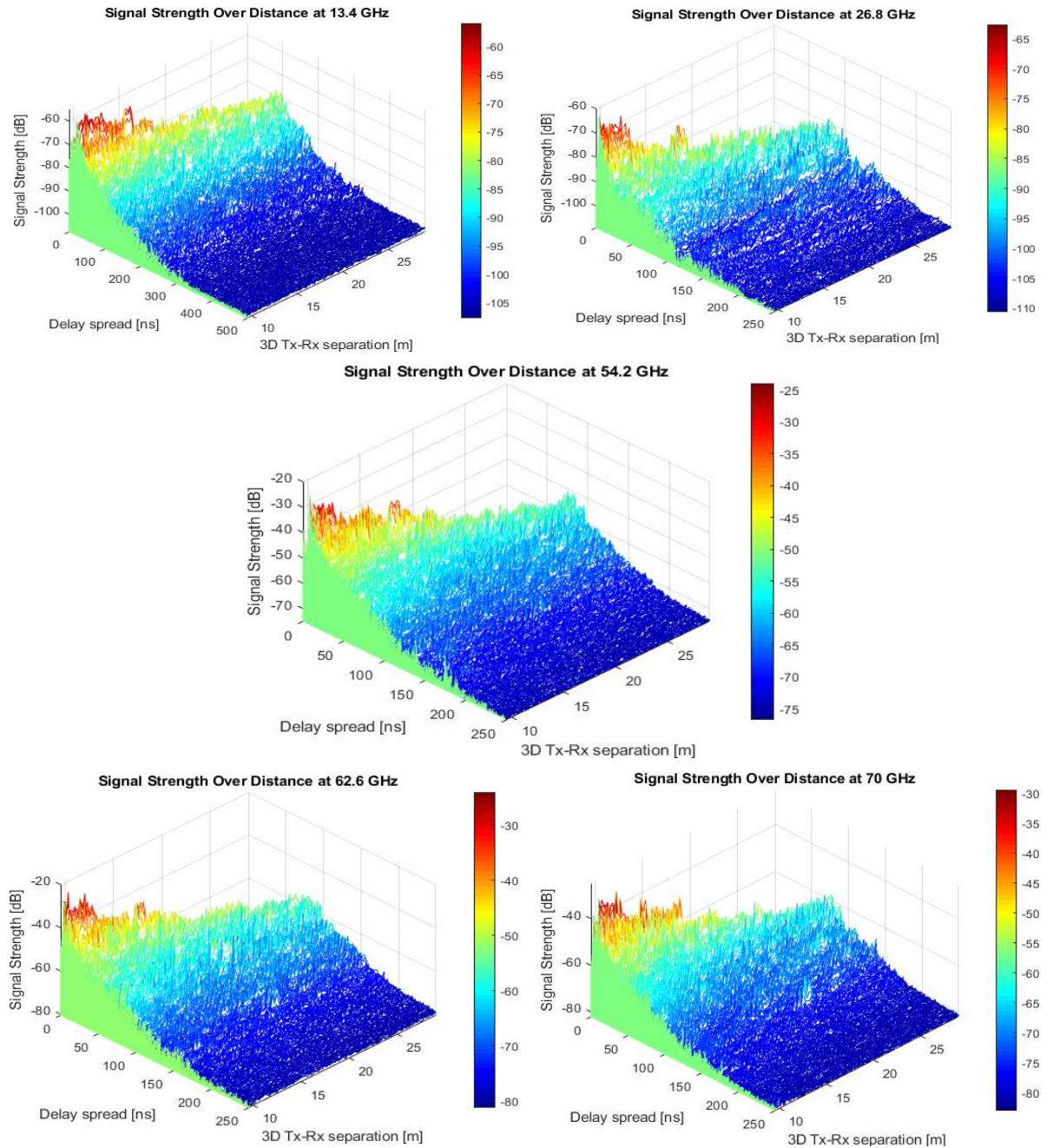
Figure 4-4 Signal strength against range for five frequency bands

Figure 4-4 illustrates the exponential decay in signal strength against both delay spread and separation distance for all measured frequencies. It is noticeable that there is a large change in the colour map over distance due to the fast decay in signal level. However, there was a sudden increase in the multipath signal's strength around the distance of 15 metres for all bands.

4.1.2 Time dispersion parameters

4.1.2.1 Power delay profile

The normalized PDP samples from each measured frequency band at three selected points are given in figure 4-5. The PDP examples illustrate a large drop in power level with increasing distance for all bands, and the 25.5 – 28.5 GHz band shows the largest drop as shown in figure 4-4. It is noticeable that the number of multipath components increased as the receiver moved away as shown in figure 4-6, where the effect of the strong single component started to disappear. It was expected that a large number of multipath components and a long delay spread would be seen in this scenario where the environment is full of metallic surfaces of different shapes and sizes around the measurement area. The figure shows that for the first band the dispersion was within 250 nanoseconds, while for the remaining bands it was within 200 nanoseconds.
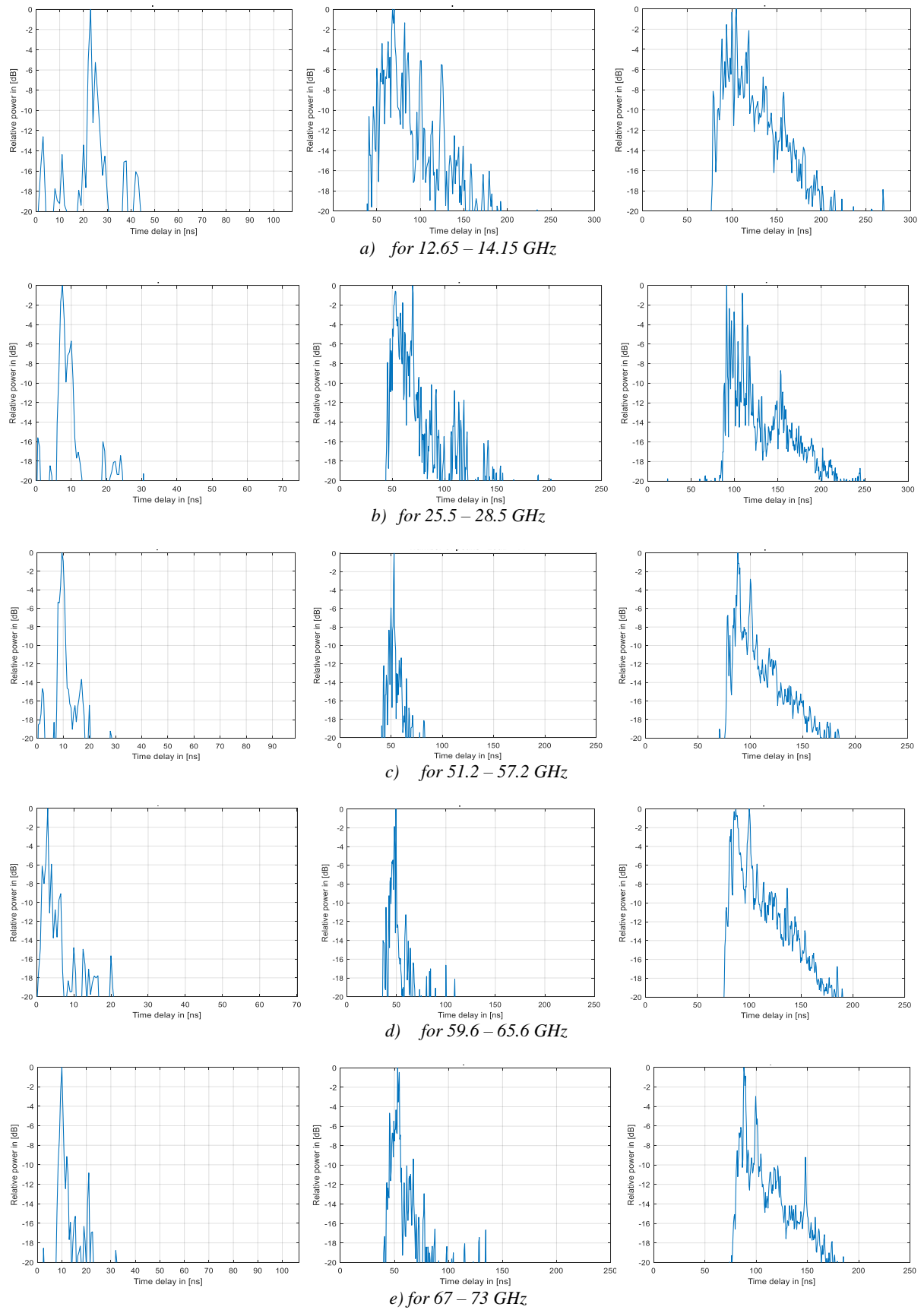
a)   for 12.65 – 14.15 GHz

b)   for 25.5 – 28.5 GHz

c)   for 51.2 – 57.2 GHz

d)   for 59.6 – 65.6 GHz

e) for 67 – 73 GHz

Figure 4-5 PDP samples from all measured frequency bands

98

Figure 4-6 display all of the PDPs at each frequency band normalized to their maximum within a 20 dB threshold from the maximum. This figure shows an increase in the delay spread as the distance increased, where the power level exponentially decays and the effect of the dominant component disappears, as shown in figure 4-4. It can be seen from figure 4-6 the absence of multipath components when distances around 16 metres were reached for all measured bands. This could be due to the gap shown in the layout in figure 4-1 between the anechoic chamber and the machine next to it, where the signals passing through this gap would not return to the measurement area.
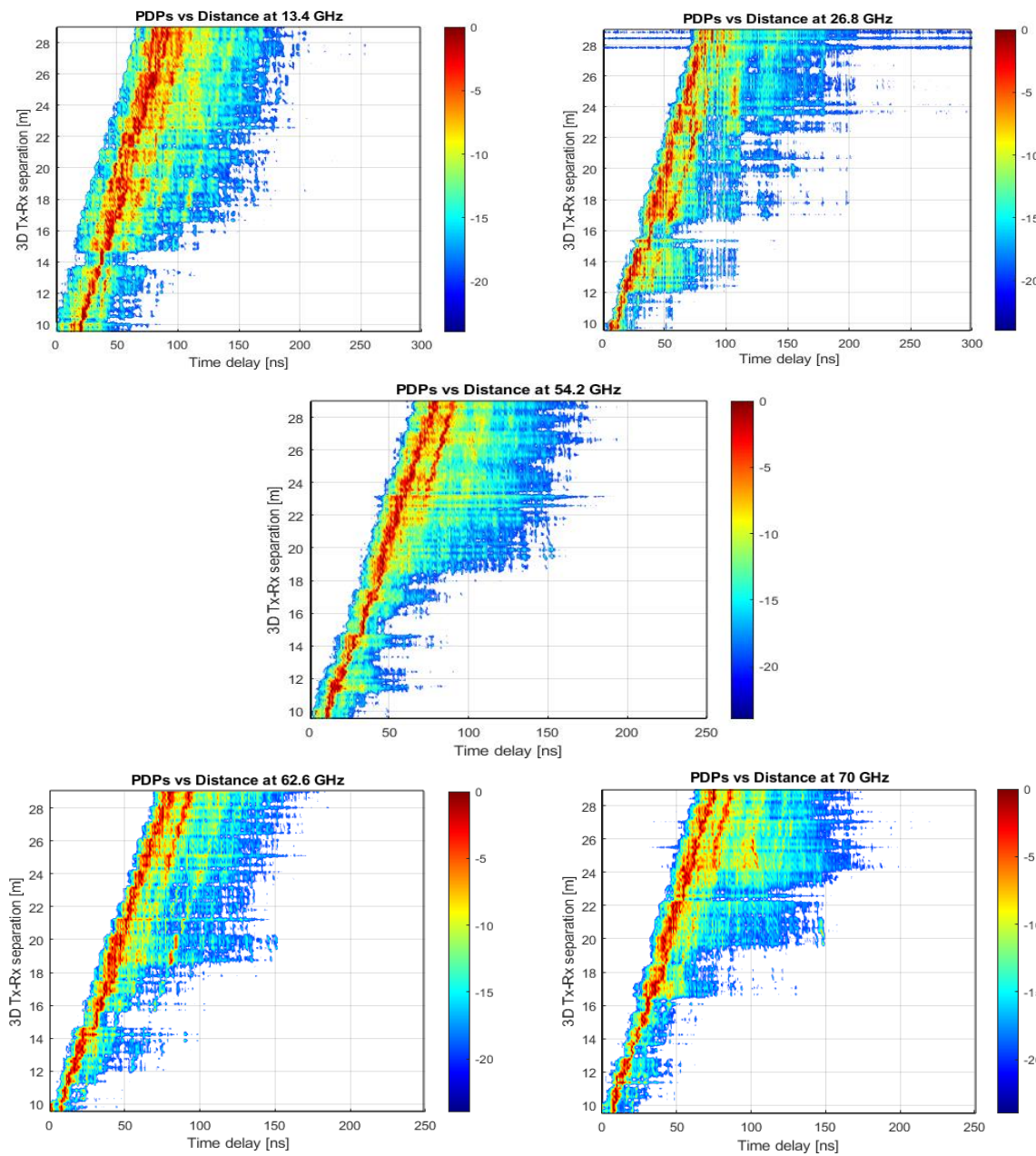

Figure 4-6 PDPs against distance for all measured frequency bands

99

4.1.2.2 Average and RMS delay spread

The average and RMS delay were calculated for 20 dB threshold. In general, there was an increase in the average delay spread for all bands as the separation distance increased, and at these distances the power level of the dominant component is much lower compared with the other reflected signals. However, for the 26.8 GHz and 70 GHz there was a steep drop in average delay values at certain distances, due to the lack of dynamic range which satisfies the condition of 20 dB. This was because of the large drop in power level at these distances for all bands, and especially for these two bands, as shown in figure 4-5. The average delay spread over all bands was within 45 nanoseconds, as shown in figure 4-7.
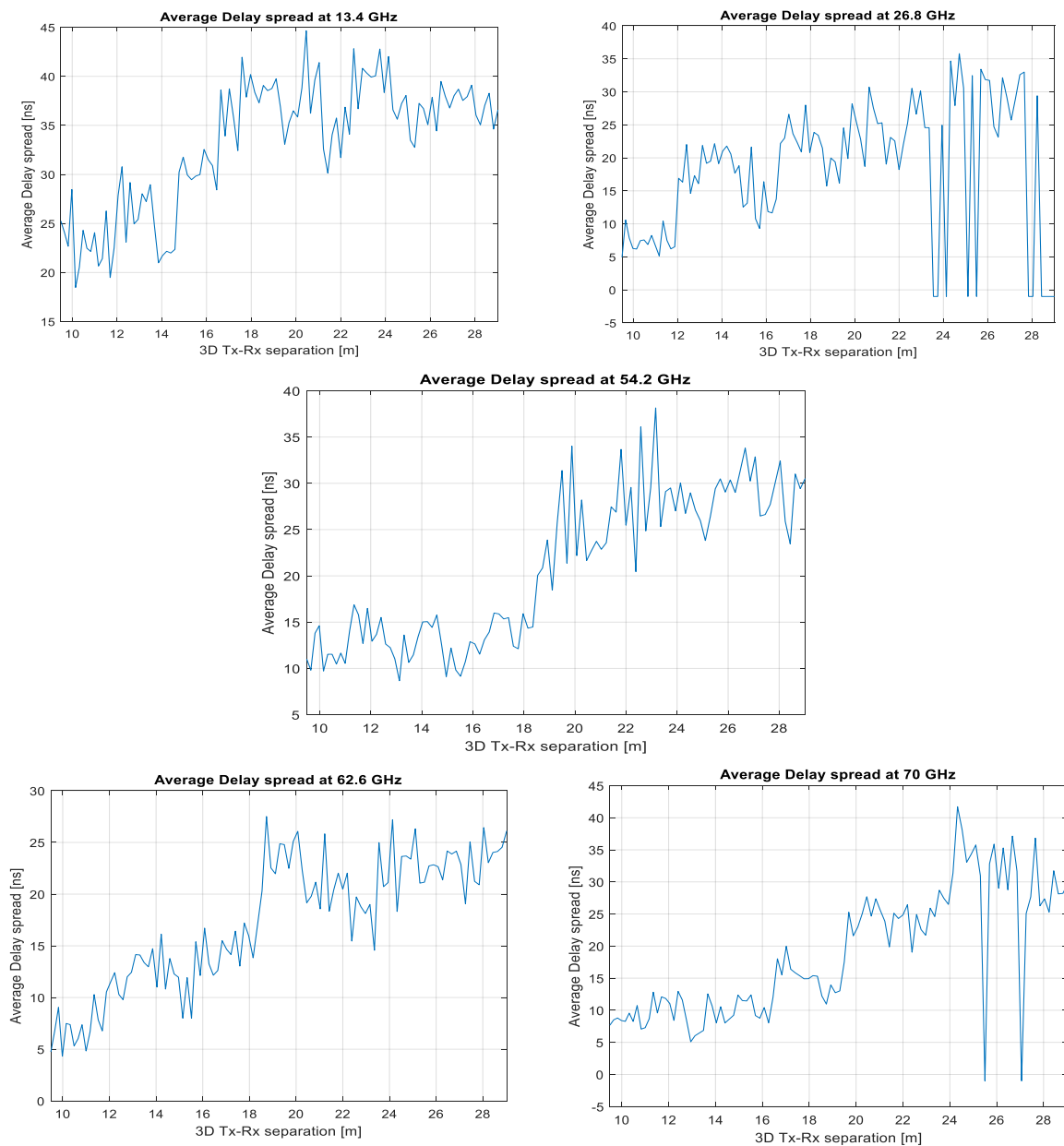

Figure 4-7 Average delay spread against distance for all measured frequency bands

The values of RMS delay spread for each measured frequency band are presented in figure 4-8. They were in general less than 35 nanoseconds, and the highest value was at 26.8 GHz. The same effect of the lack of dynamic range is shown in the 26.8 GHz and 70 GHz graphs. Also, the second reflected wave at a distance of around 15 metres contributed to increasing the power level at these distances, reducing the number of multipath components to be included in the delay spread calculation.
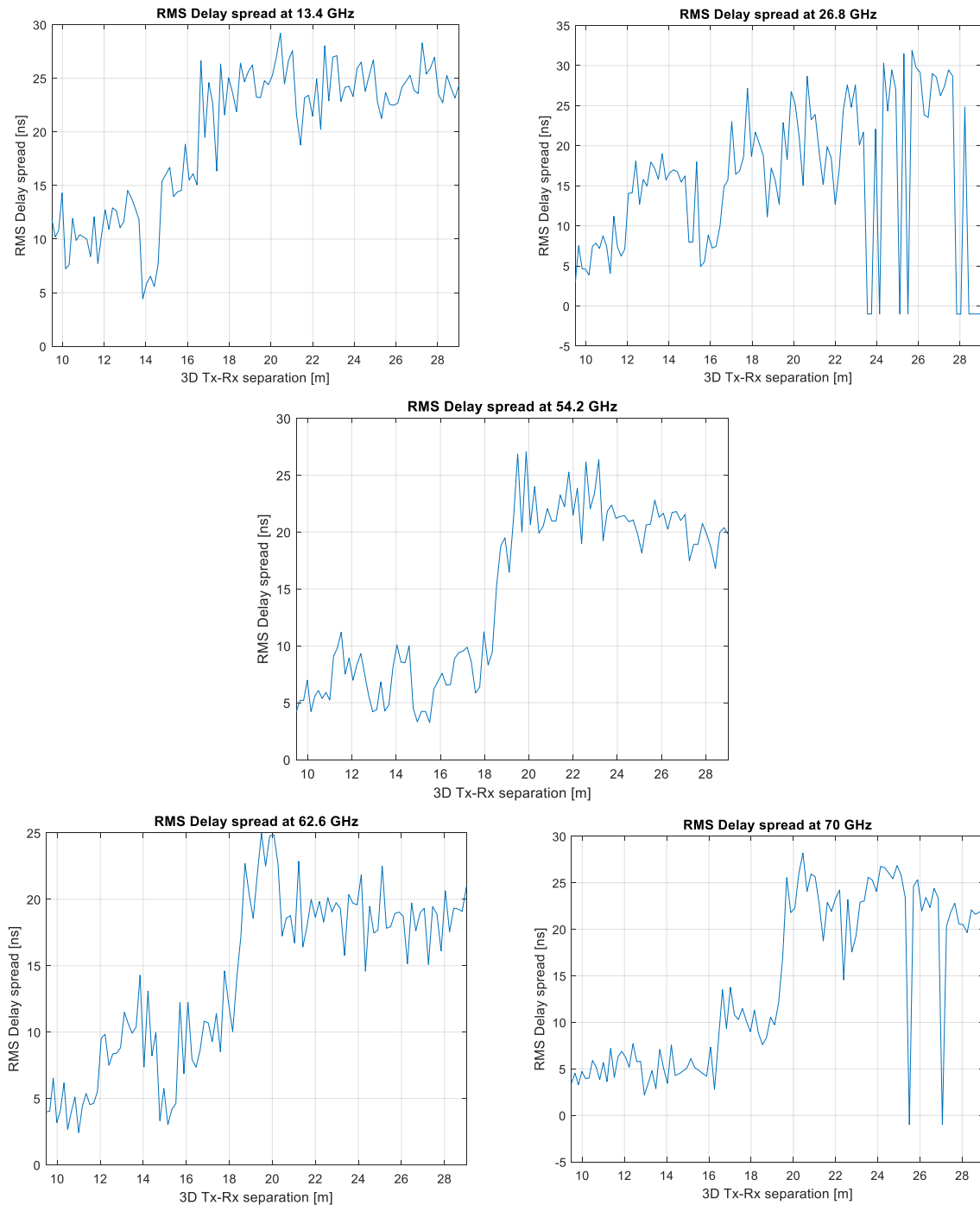

Figure 4-8 RMS delay spread against distance for all measured frequency bands

101

Figure 4-9 shows the CDF of the RMS delay spread for the measured frequency bands. This figure shows that at 10% the delay spread decreases as frequency increases, where the 13.4 GHz has the longest RMS delay spread at less than 5 nanoseconds, as shown in table 4-3. At 50% which is the median value, the curves followed the same trend as in 10% for all bands except for 54.2 GHz, where the value of RMS delay was the lowest. This may be due to the low number of multipath components up to 20 metres (representing half of the measurement points) compared with the other bands, as illustrated in figure 4-6. For 90% the table shows the highest value at 26.8 GHz, despite the large number of points that did not satisfy the conditions. This could be due to the large drop in power level at this band, as given in figure 4-8, and as a result more components were included in the RMS delay calculation especially in the second half of the measurement points.
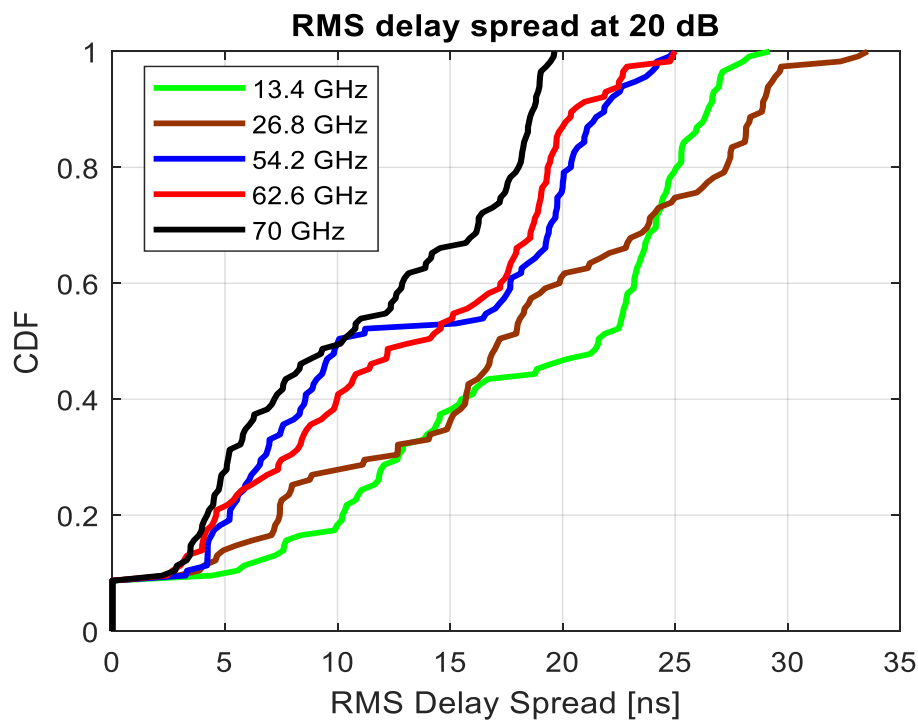

Figure 4-9 CDF of RMS delay spread for all measured frequency bands

Table 4-3 The CDF values of the RMS delay spread

CDF	13.4 GHz	26.8 GHz	54.2 GHz	62.6 GHz	70 GHz
10%	4.99	3.38	3.29	2.55	2.49
50%	21.59	17.16	10.04	13.60	10.22
90%	26.47	28.88	21.85	20.51	18.69

4.2 Small office (NLoS)

The layout for the small office environment is shown in figure 4-10. For the NLoS scenario the transmitter was fixed at the position illustrated in the layout and the transmitter antenna was pointed at an angle which illuminated the area between the two red dashed lines so as to maximize the signal strength in the measurement area, as shown in the layout. The route of the receiver's measurement is indicated by the blue dashed arrow in figure 4-10, where the first point was selected to be out of line-of-sight with the transmitter.
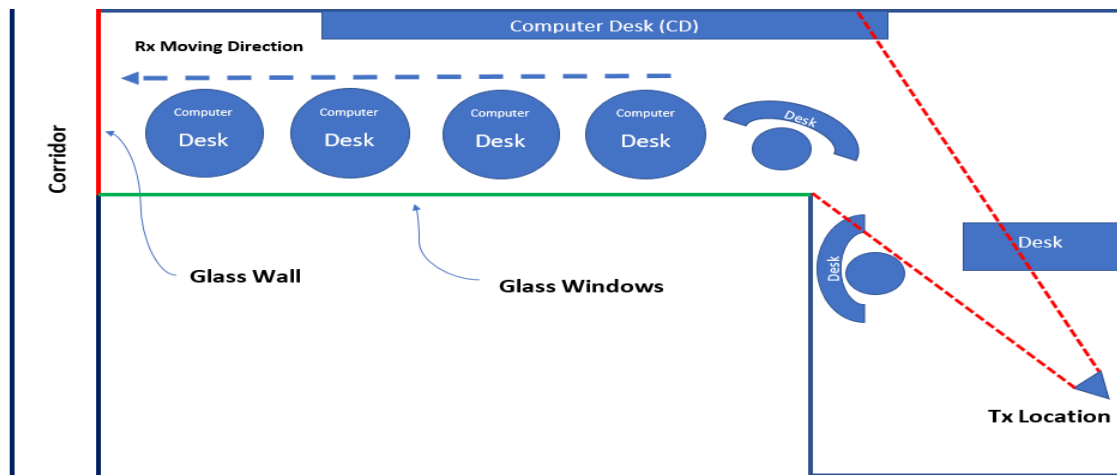

Figure 4-10 Small office layout NLoS scenario

4.2.1 Received power and path loss

The results of received power versus Tx-Rx separation distance for each frequency band are given in figure 4-11. The general trend shows an exponential decay over all bands as the Tx-Rx separation distance increased. However, there was a relatively large drop at distances between 14 and 16 metres, which could be due to the gap between the first and second reflected signals. Then was a sudden increase in power level at around 18 metres, which was clearer at 70 GHz. That might be caused by the second reflection from the glass windows (indicated by the green line in the layout) where it showed that, the glass reflects the higher frequency bands more than the lower bands according to their wavelengths.
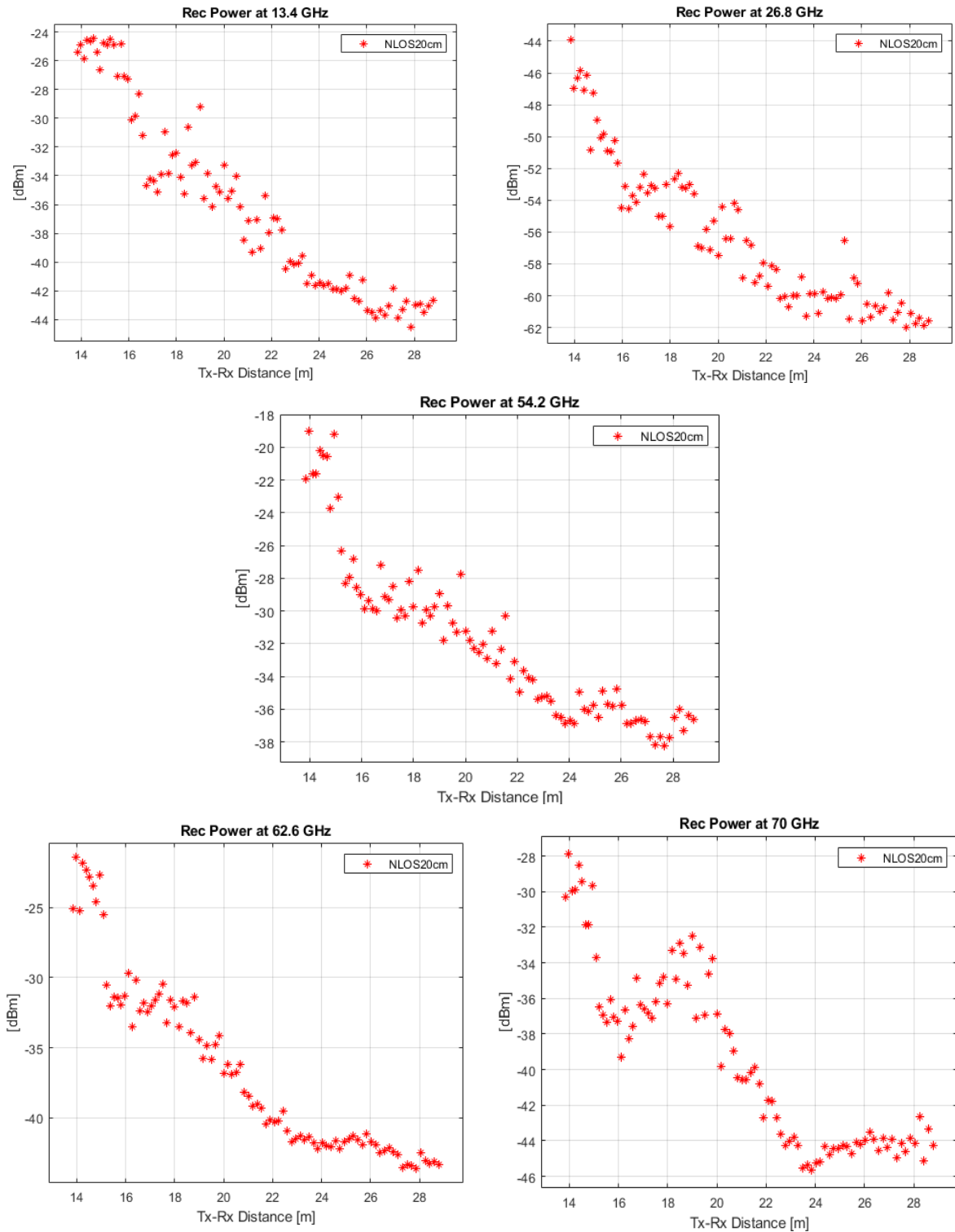
Figure 4-11 Received power for five frequency bands in small office

Table 4-4 presents the calculated values for the minimum, maximum and variation in power levels at each frequency band. The values of variation over bands were similar, and the difference between the highest and lowest variation was only 4 dB in this environment.

Table 4-4 Variations in power level for each frequency band

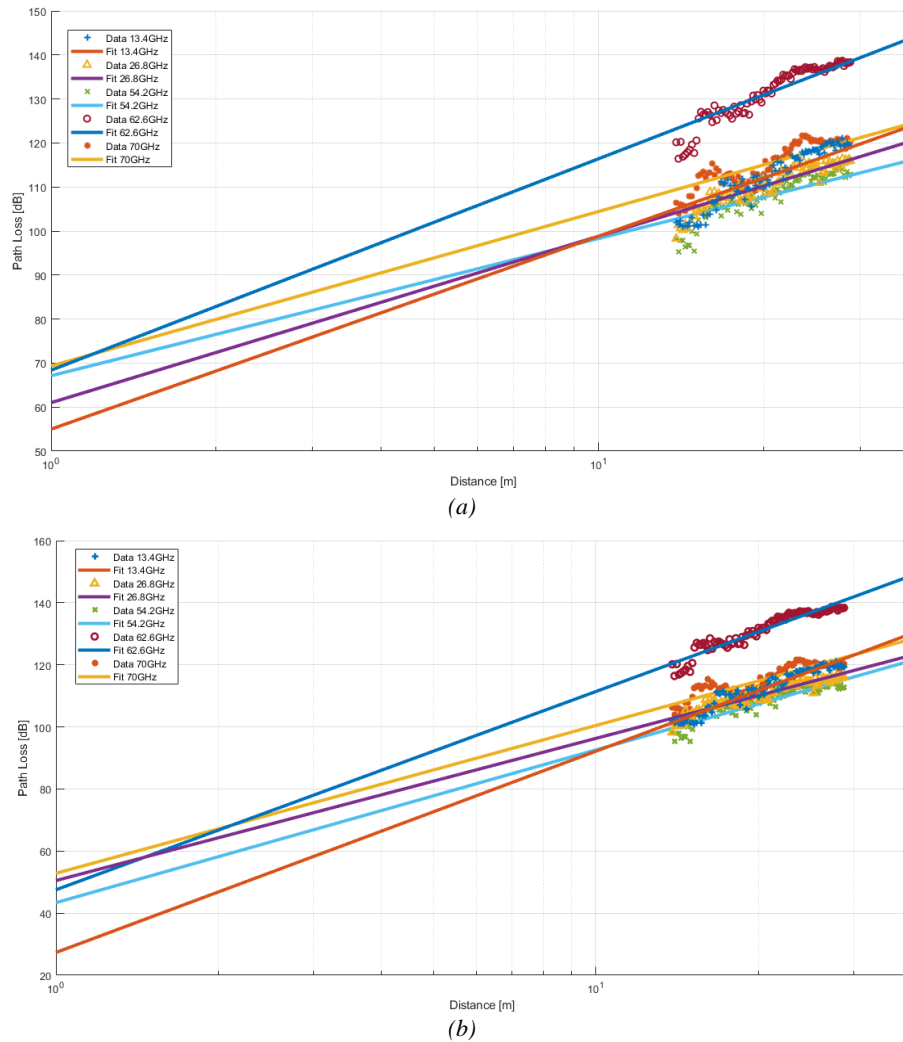| Centre frequency	Power level variation [dBm]	Highest power level [dBm]	Lowest power level [dBm]
13.4 GHz	20	-24	-44
26.8 GHz	18	-44	-62
54.2 GHz	19	-19	-38
62.6 GHz	22	-21	-43
70 GHz	18	-28	-46

(a)

(b)

Figure 4-12 NLoS path loss for two different models. (a) CI model. (b) FI model

Figure 4-12 (a) and (b) provide graphs of the results for the CI and FI path loss models for the measured bands. The 13.4 and 62.6 GHz show higher values of attenuation of the power level compared to the other bands. The parameters of the two models are presented in table 4-5. The results for equivalent parameters for both models were very close at 26.8 GHz, where the difference was only 0.1 dB between (n) and (β) and 0 dB for (σ). The highest difference between (n) and (β) was 1.4 dB at 13.4 GHz, and a difference of 0.28 dB in the standard deviation at 70

GHz. This difference in equivalent parameters between the two models at this band might be due to the large drop in received power at the Tx-Rx separation distances of between 14 and 16 metres, which has less effect on the 26.8 GHz as can be noticed in figure 4-11.

Table 4-5 Parameters of the two path loss models

Path loss model		13.4 GHz	26.8 GHz	54.2 GHZ	62.6 GHz	70 GHz
CI	n	4.46	3.78	3.17	4.85	3.51
	σ	1.75	1.26	1.3	1.51	2.53
FI	α	36.29	60.04	56.90	52.14	52.84
	β	5.86	3.88	3.93	6.07	4.76
	σ	1.53	1.26	1.14	1.27	2.25

Figure 4-13 illustrates the decay in the signal strength with delay spread over all measured frequencies. Also, there was a large drop in the signal strength after a distance of 15 metres, which is clearer in the last three bands. That could result from the low coverage area between the first and second reflected waves. Then there was an increase in power level again over the separation distances between 17 and 21 metres, resulting from the second reflected signals from the glass windows. Then another decline around 24 metres occurred, followed by a slight increase in power level close to the end. These fluctuations in the signal strength against distance might be explained by the fact that the areas fully covered by the reflected signals will show high power levels, while areas in between these zones will show lower levels. There was a large drop in the power level over distance, especially for the last three bands, and the largest drop was for the 59.6 – 65.6 GHz band. This could result from the increase in the number of reflections as the receiver became closer to the final measurement point, where at each reflection the signal will lose part of its strength either due to diffraction, absorption, penetration or diffusion according to wavelength and the surface structure and texture.
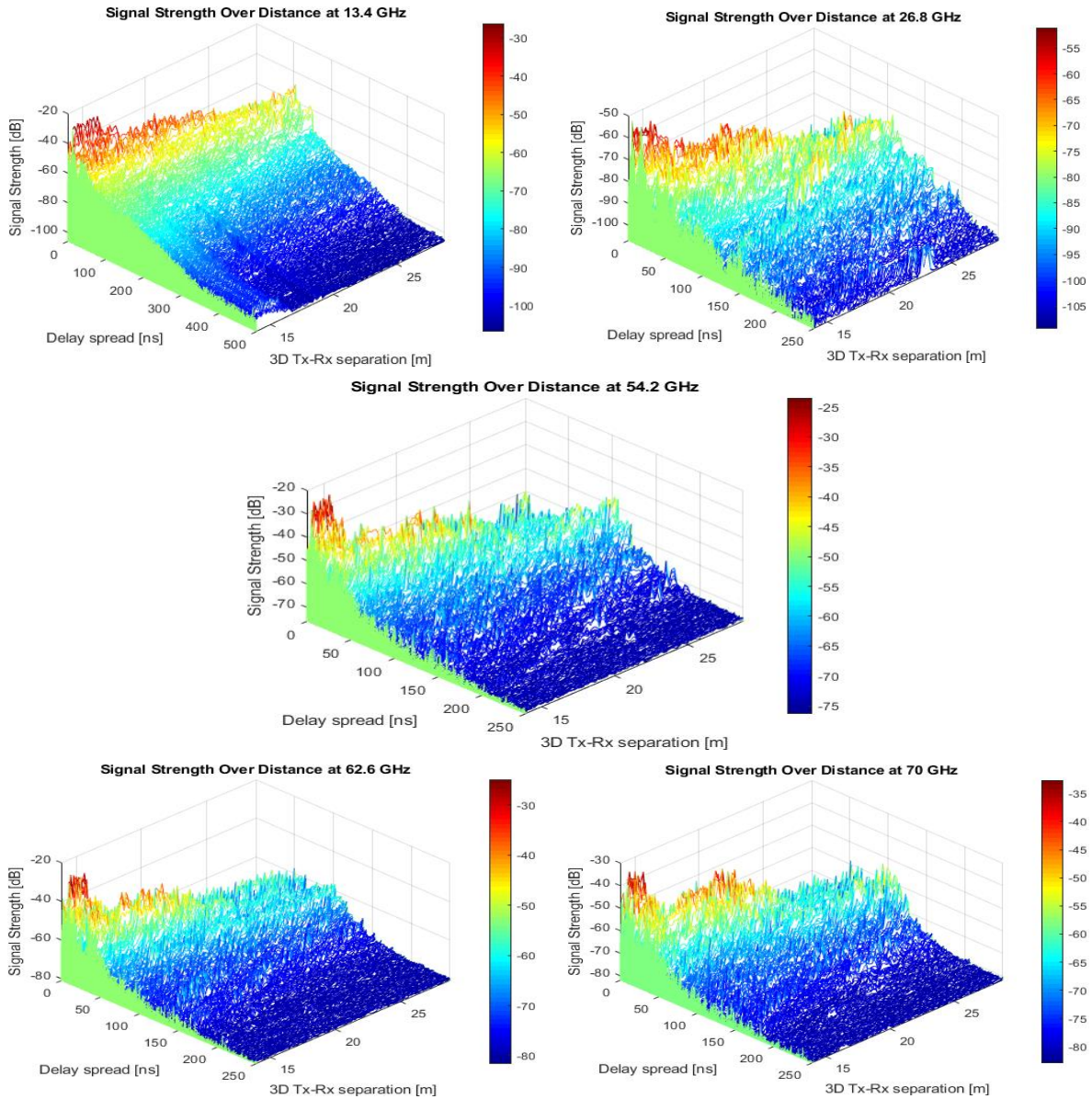
Figure 4-13 Signal strength against range for five frequency bands

4.2.2 Time dispersion parameters

4.2.2.1 Power delay profile

Three selected points for the normalized PDP samples from each measured frequency band are given in figure 4-14. The PDP examples show that the delay spread dispersion is in most cases within 200 nanoseconds. There were large numbers of strong spikes of multipath components in this scenario. Also, the difference between the dominant component and the next strongest one at the first position is shown to be around 15 dB and this decreased as the receiver moved away. It is notable that, in some cases, there were more than one dominant components, including even at the first measurement point as shown in figure 4-14 (b).
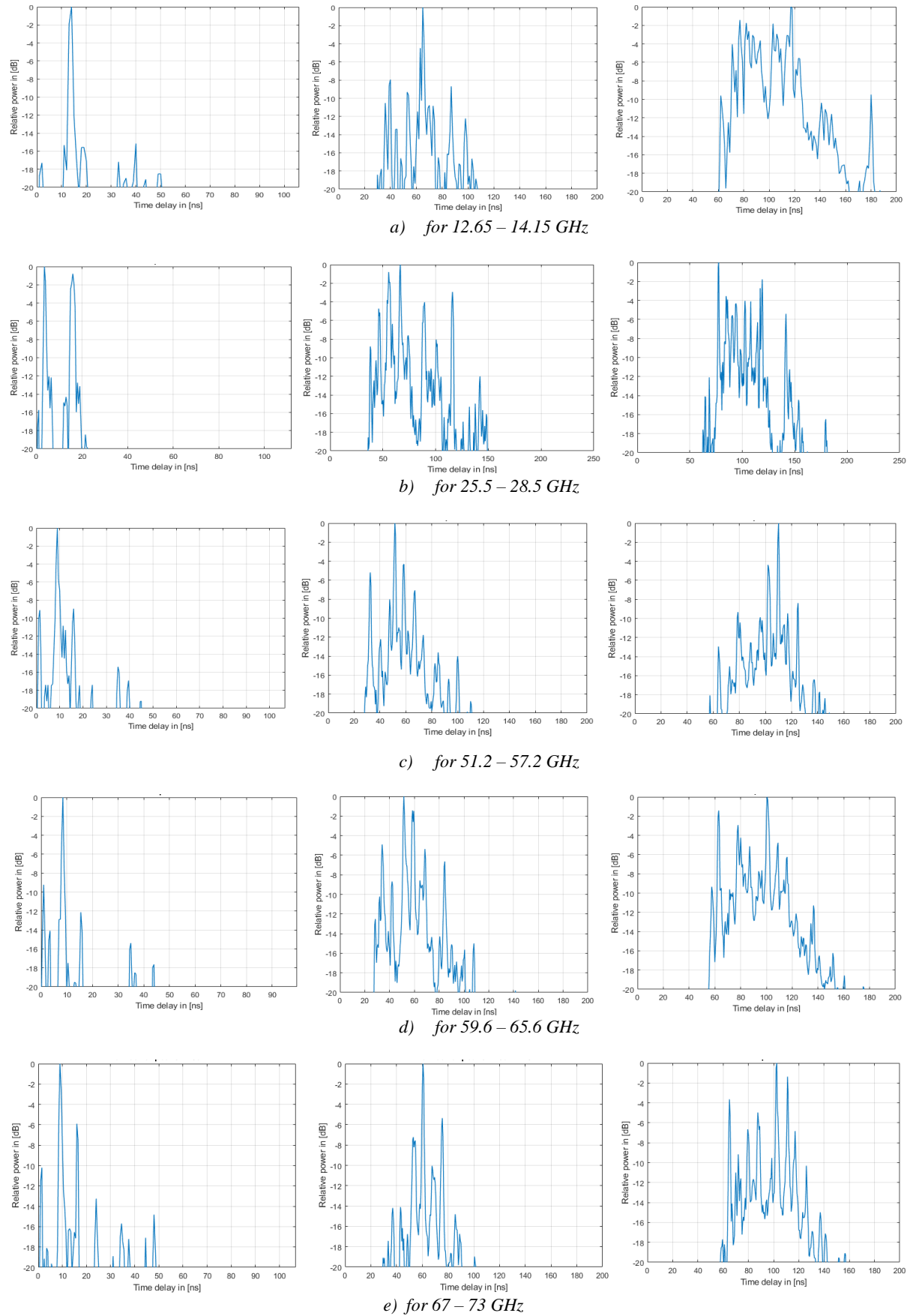
a)   for 12.65 – 14.15 GHz

b)   for 25.5 – 28.5 GHz

c)   for 51.2 – 57.2 GHz

d)   for 59.6 – 65.6 GHz

e) for 67 – 73 GHz

Figure 4-14 PDP samples from all measured frequency bands
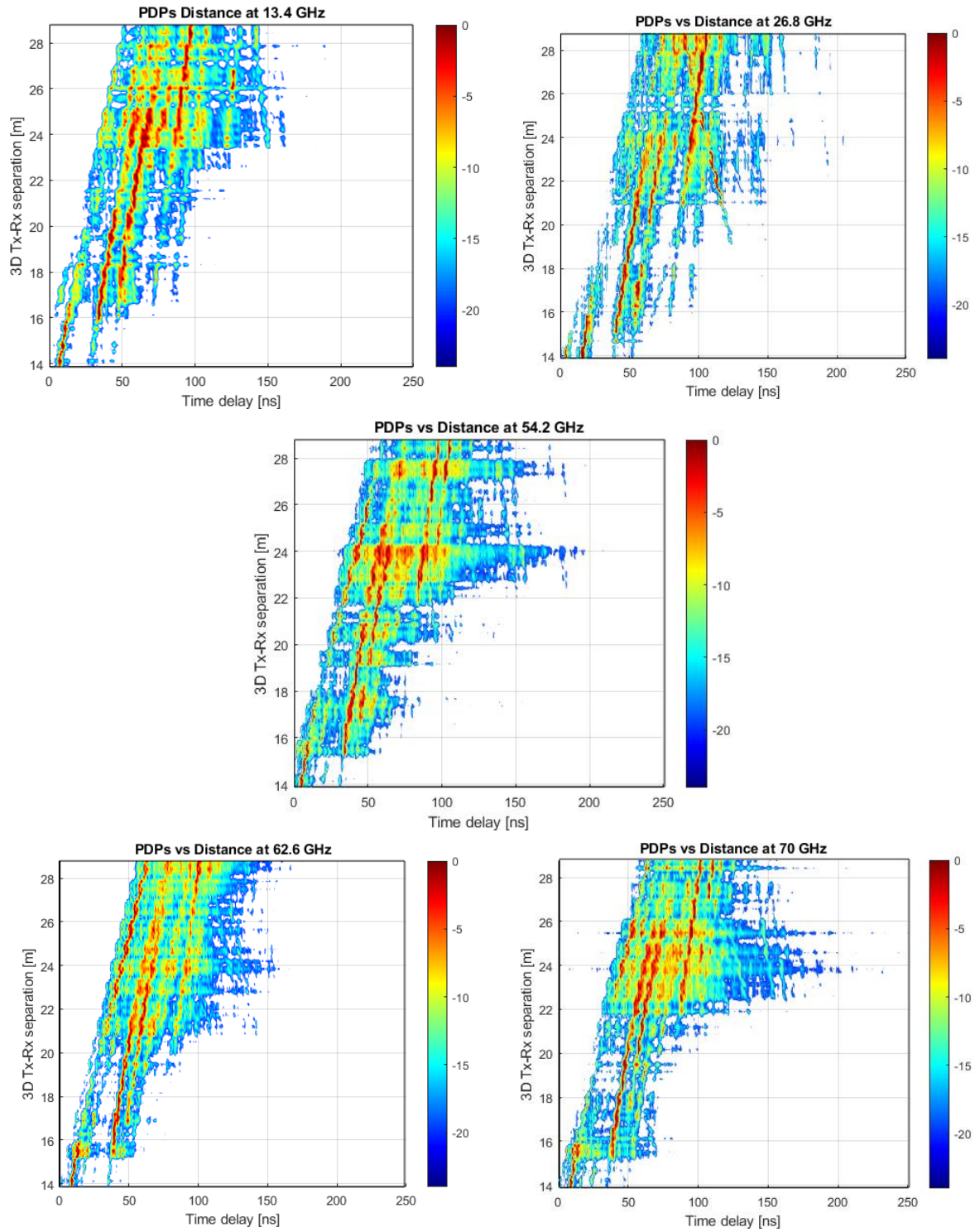
Figure 4-15 PDPs against distance for all measured frequency bands

Figure 4-15 provides PDPs images for each frequency band normalized to their maximum within 20 dB from the maximum. The images show an increase in the delay spread as the Tx-Rx separation distance increases. As the receiver moved away, the power level decayed and the number of reflected waves increased due to the increases in the number of reflection orders, reaching up to 7 reflections as shown in the image for 13.4 GHz. As a result of these reflections, the beam became wider due to the wave guide effect of the scenario. The strength of the power of the first reflection signal had largely decreased at distances between 18 and 22 metres, only to return at a good level for the last three bands, while the effect of the second and third reflected orders started to become apparent at a distance of about 15 metres up to around 27 metres in most of the bands, where the effect of the last reflections started to appear at around 22 metres as the receiver came closer to its final position. The overlap of these reflections at about 18 metres and some other distances resulted in a sudden increase in the received power level, as illustrated in figure 4-11.

4.2.2.2 Average and RMS delay spread

Figure 4-16 presents the average delay spread against the separation distance between Tx and Rx. The figure shows an increase in the average delay spread over all bands starting from a distance of around 15 metres, where the second and third reflected waves are clearly influential as mentioned in the previous section, reaching a maximum at half of the points, where the maximum average delay spread was less than 50 nanoseconds over all bands in this scenario.
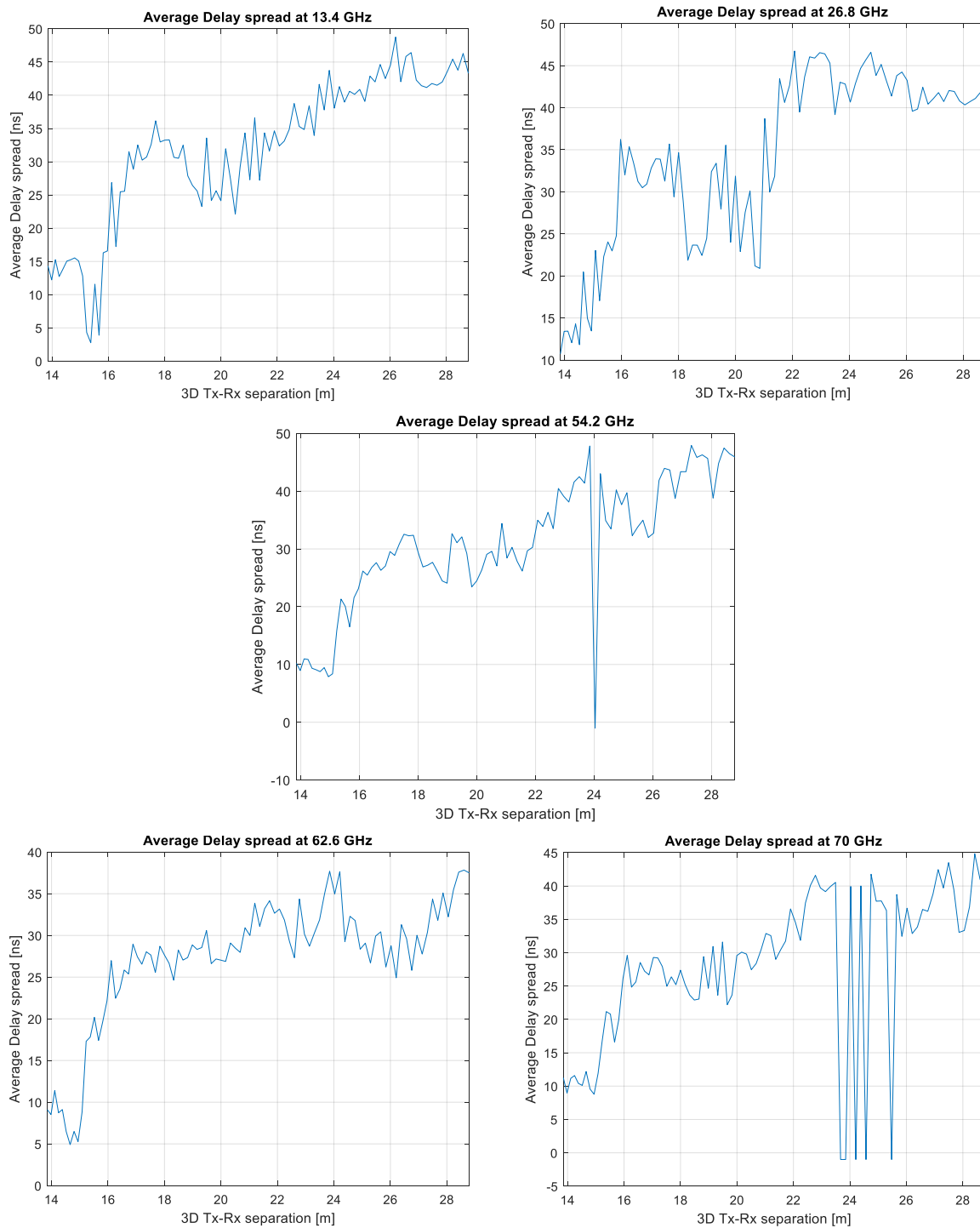
Figure 4-16 Average delay spread against distance for all measured frequency bands

For the 13.4 GHz there was a drop in the average delay in the area between 18 and 19 metres and between 20 and 21 metres due to a reduction in the number of reflected components, as shown in figure 4-15. In addition, there was a steep drop in the average delay, as shown in the figure, for the 54.2 and 70 GHz. The power level generally fell with greater distance, especially

for the last three bands as shown in figure 4-14, which was the result of a lack of dynamic range
to satisfy the pre-set threshold of 20 dB as explained in the previous scenario.
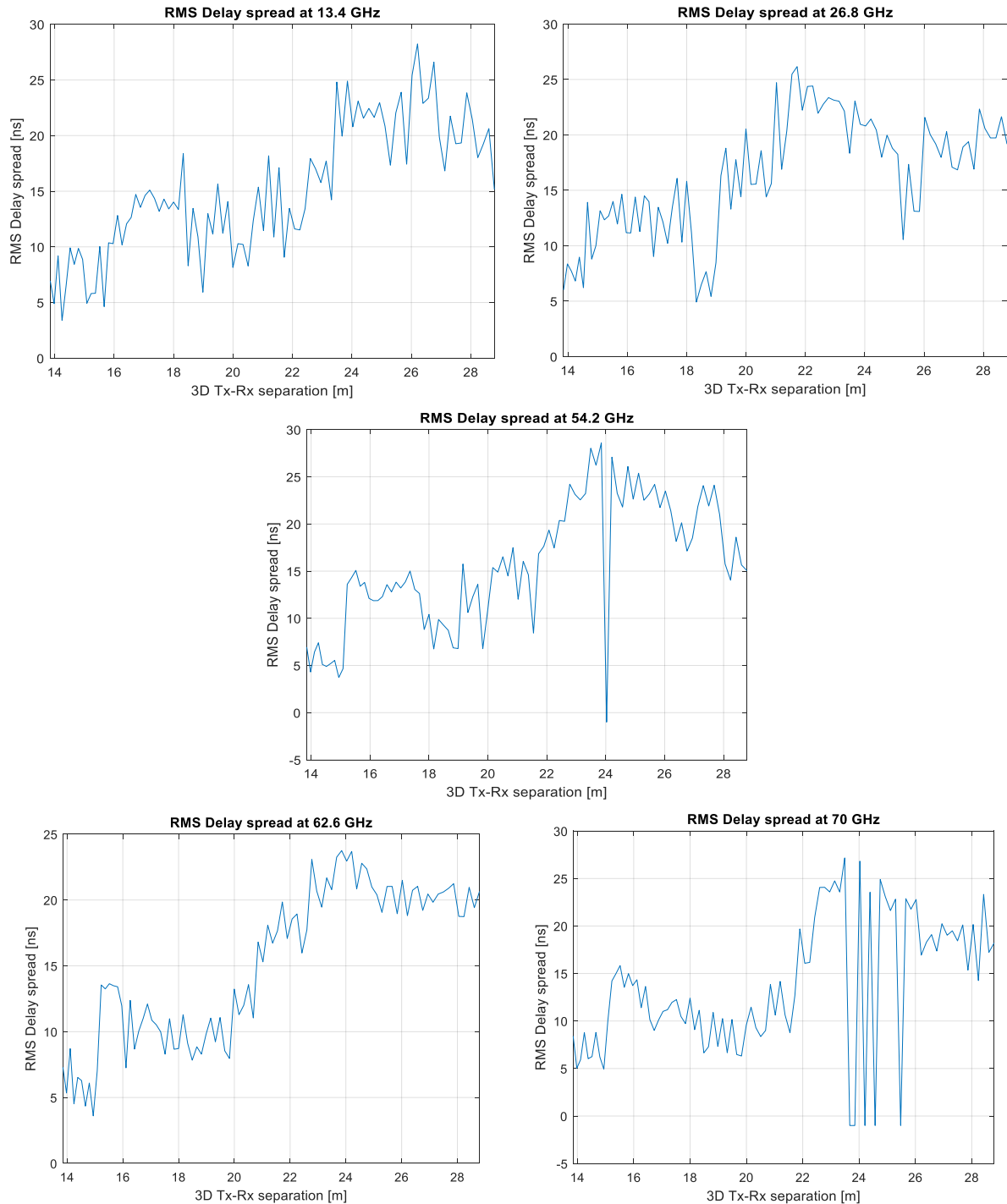

Figure 4-17 RMS delay spread against distance for all measured frequency bands

Figure 4-17 illustrates the calculated values of RMS delay spread for each measured frequency
band. The figure shows similar variations in the RMS graphs as in the average delay spread,
but on a different scale. The 62.6 GHz shows the shortest values of RMS delay spread, which

was less than 25 nanoseconds in this band while it was closer to 30 nanoseconds for the other bands. The lack of dynamic range was shown in the RMS delay spread as well, due to the same reason mentioned above.

The CDFs of the RMS delay spread for the measured frequency bands are given in figure 4-18. The CDF values are presented in table 4-6. The figure and table show similarities for the three values over all bands, and the maximum difference between the bands at 10% was only 1.72 nanoseconds, with the highest and lowest values for 26.8 GHz and 70 GHz respectively. For the median, the maximum difference was 2.68 nanoseconds, and the highest value of CDF was again at 26.8 GHz and the shortest at 62.6 GHz. At 90% the RMS delay spread over all bands was less than 25 nanoseconds and the maximum difference between the bands was 2.87 nanoseconds. The highest value was at 54.2 GHz and the lowest at 62.6 GHz.
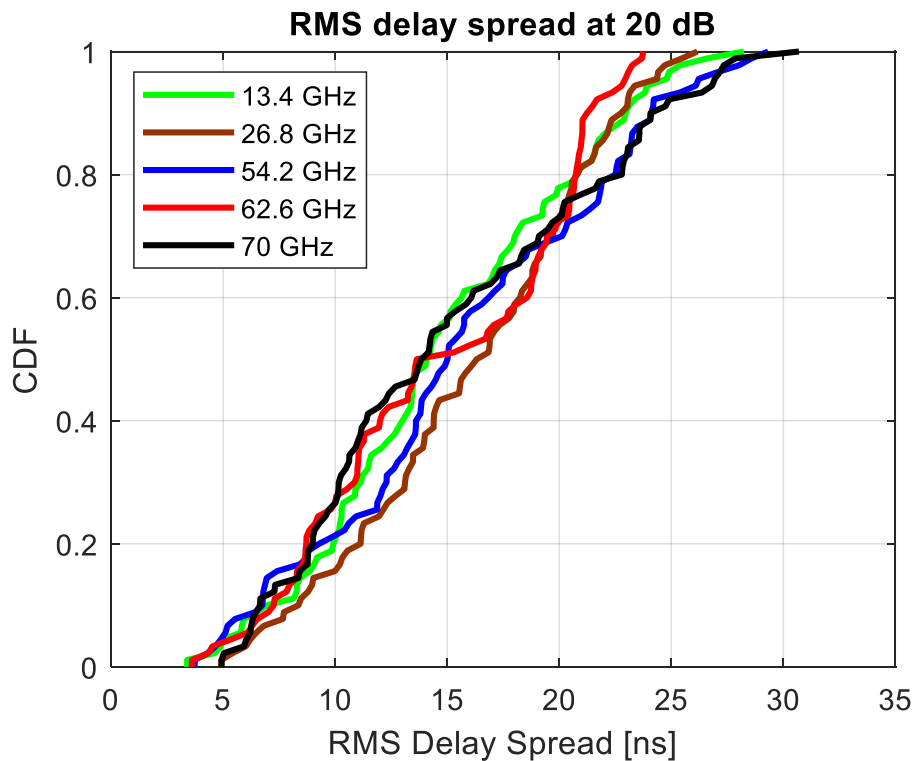

Figure 4-18 CDF of RMS delay spread for all measured frequency bands

Table 4-6 The CDF values of RMS delay spread

CDF	13.4 GHz	26.8 GHz	54.2 GHz	62.6 GHz	70 GHz
10%	6.95	8.36	6.75	7.25	6.64
50%	14.08	16.32	15.01	13.64	13.84
90%	22.96	22.76	24.11	21.24	24.07

4.3 Large office

Figure 4-19 shows the layout of the Large office environment for both LoS and NLoS situation. As shown in the layout, there are two sets of measurements. For the first the transmitter was fixed at position Tx1 and the measurement was conducted in the directions indicated by black dashed arrows, the first showing the measurement points from 1 to 55 which indicated by A and the second points from 56 to 95 indicated by B. In the second set the transmitter was fixed at the location Tx2 and the antenna pointed to the glass windows with aluminium frames indicated by the green colour, with an angle calculated to cover the measured area and the receiver moving in the direction indicated by the red dashed arrow which shows the measurement points from 96 to 150. At the transmitter a horn antenna was mounted on top of a tripod at a height of 2.5 metres above the ground for both sets of measurements, and this was tilted down by -9 degrees for the first set while it was set at zero degrees for the second set. At the receiver, an omnidirectional antenna was mounted on top of a trolley at a height of 1.6 m, which is the average height of the mobile user, for both sets. The measurement procedure and set-up were the same as described in chapter 3.
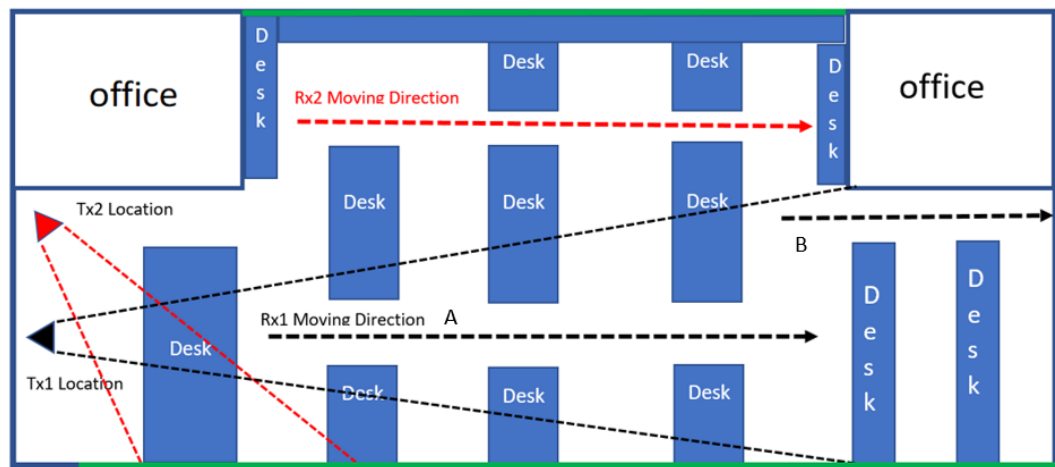

Figure 4-19 Large office layout

4.3.1 Received power and path loss

The received power levels for the measurement points at each frequency band are shown in figure 4-20. The figure shows in general an exponential decay over all bands as the receiver moved away from the transmitter. However, there was a sudden marked drop in received power at point number 96, which is the first point in the second set of measurements (NLoS). This could be due to low signal strength in this area at the edge of the reflected beam. The received power increased gradually after that to reach its highest value at the centre of the reflected beam

and then it decreased slightly again, possibly because of the pillar which blocks part of the reflected signals. The reflected signal strength generally affected by wavelength, transmitted power and type of reflector, which was a glass window in this case.
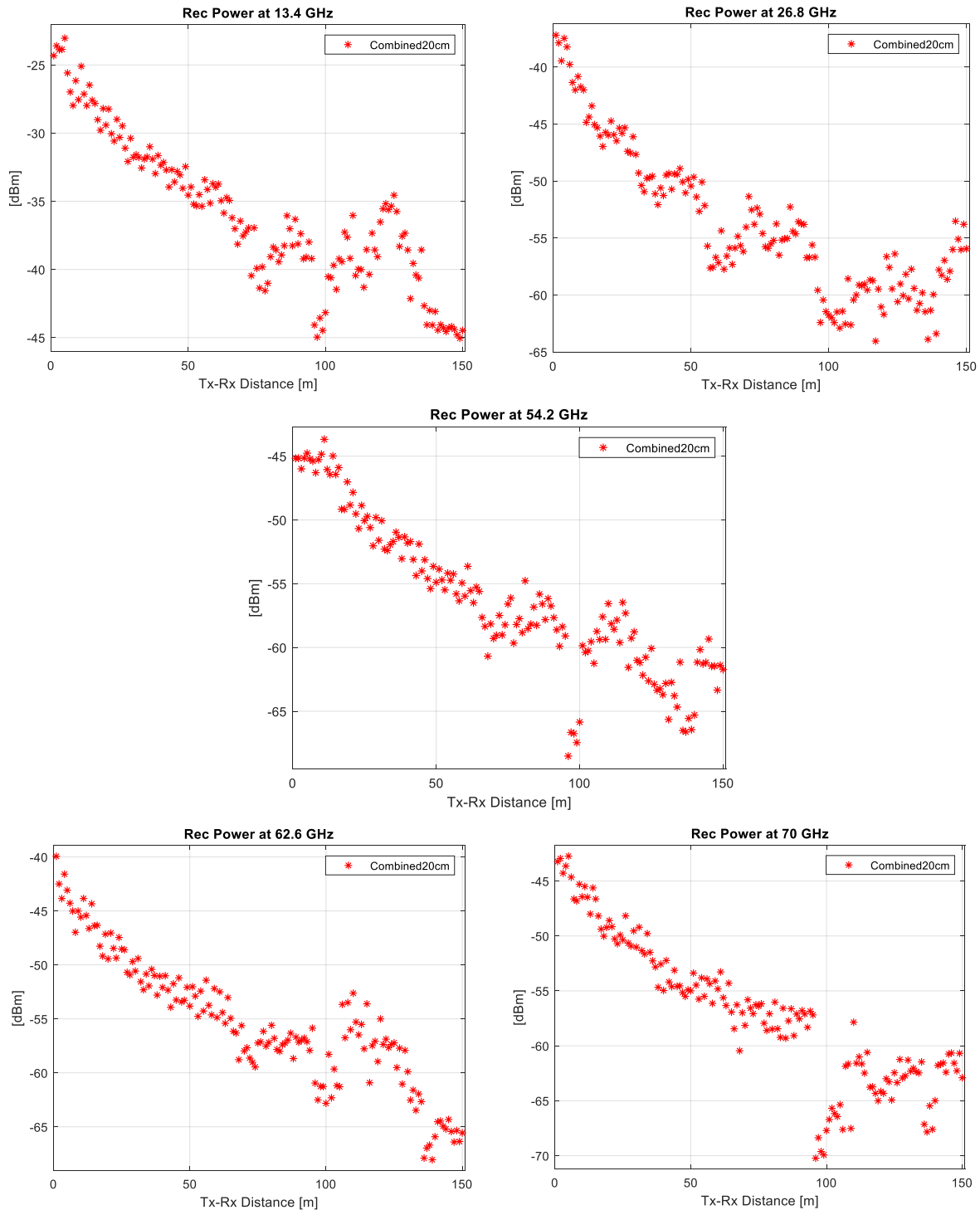

Figure 4-20 Received power for five frequency bands in large office(combined)

Table 4-7 presents the calculated values for the minimum, maximum and variation in power levels at each frequency band. The highest and lowest variations were at 62.6 GHz and 13.4 GHz respectively. The maximum difference in variation between all bands was 6 dB, and the difference was within 3 dB of the 62.6 GHz value for the other three bands.

Table 4-7 Variations in power level for each frequency band

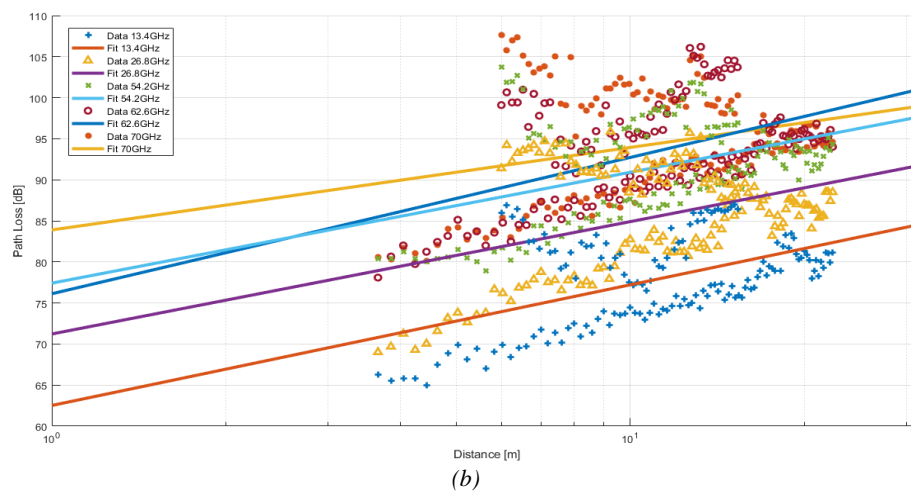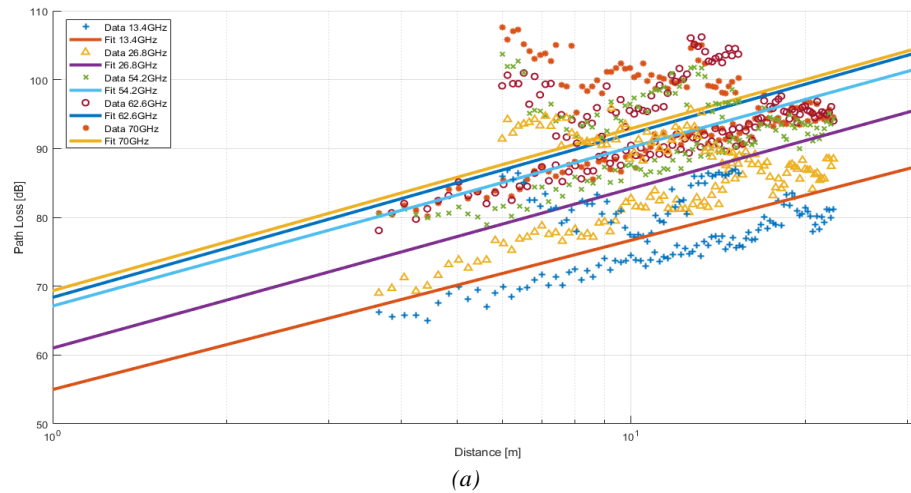| Centre frequency	Power level variation [dBm]	Highest power level [dBm]	Lowest power level [dBm]
13.4 GHz	22	-23	-45
26.8 GHz	27	-37	-64
54.2 GHz	25	-43	-68
62.6 GHz	28	-40	-68
70 GHz	27	-43	-70

(a)

(b)

Figure 4-21 LoS path loss for two different models. (a) CI model. (b) FI model

Figure 4-21 provides graphs of the CI and FI path loss models for the measured bands. The extracted parameters of the two models are presented in table 4-8. There was a large difference between the values from the two models in terms of (n) compared to (β). The FI model shows very low values over distance in the combined compared to the LoS situation described in chapter 3. The PLE values were higher than the free space value (n=2) for all bands and the lowest value was at 13.4 GHz band. It increased as frequency increased, and the higher bands show higher attenuation values compared to the lower bands.

Table 4-8 Parameters of the two path loss models

Path loss Model		13.4 GHz	26.8 GHz	54.2 GHZ	62.6 GHz	70 GHz
CI	n	2.17	2.32	2.31	2.38	2.36
	σ	4.84	6.09	5.59	5.36	6.73
FI	α	62.52	71.22	77.41	76.12	83.89
	β	1.47	1.37	1.35	1.66	1.00
	σ	4.66	5.83	5.29	5.19	6.24

Figure 4-22 provides the results for signal strength decaying with the delay spread over all the measured frequency bands. The figure shows an exponential decay in signal strength up to measurement position 95, which is the last point in the first set of measurements (LoS). Then, there was a large drop in signal strength at the first few points at the edge of the reflected beam, after which it increased gradually to reach the highest value at the centre of the reflected beam. Then another decline followed for the last few measurement points in the second set of measurements (NLoS).
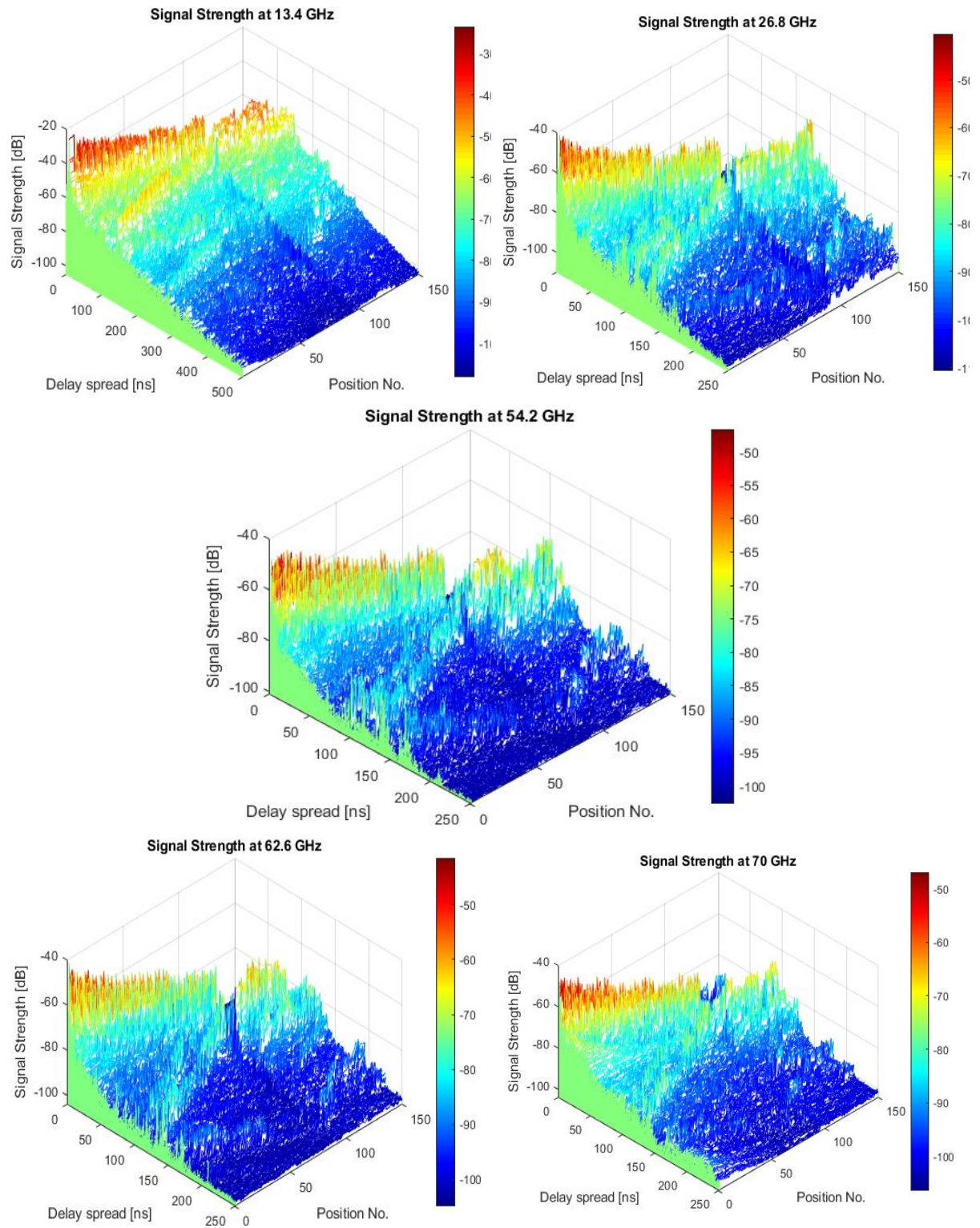
Figure 4-22 Signal strength over measured points for five frequency bands

4.1.2 Time dispersion parameters

4.3.2.1 Power delay profile

Three selected points from the normalized PDP samples for each measured frequency band are presented in figure 4-23. The PDP examples were selected from the points between numbers 56 and 150, where the first part from 1 to 55 were presented in the previous chapter for the LoS scenario. Position 56 shows the first point in the measurement set indicated by the second black dashed arrow (B) in the layout. The second selected sample is the first point of the second set of measurements (position 96) as indicated by the red dashed arrow in the layout graph. Position 96 was selected to show the drop in power level at the first point in the second set as explained above, and the third sample was selected from the points close to the centre of the reflected beam (position 116) to show the resurgence in power level, as shown in figure 4-23 for the 51.2 – 57.2 GHz band and 67 – 73 GHz bands. The samples show high numbers of multipath components which were close to each other, especially in the NLoS situation from points 96 to 150. This shows that the environment has large number of reflectors and they are close to each other, as mentioned earlier in the LoS scenario in chapter 3. The delay spread dispersion for the combined scenario was in most cases within 250 nanoseconds.
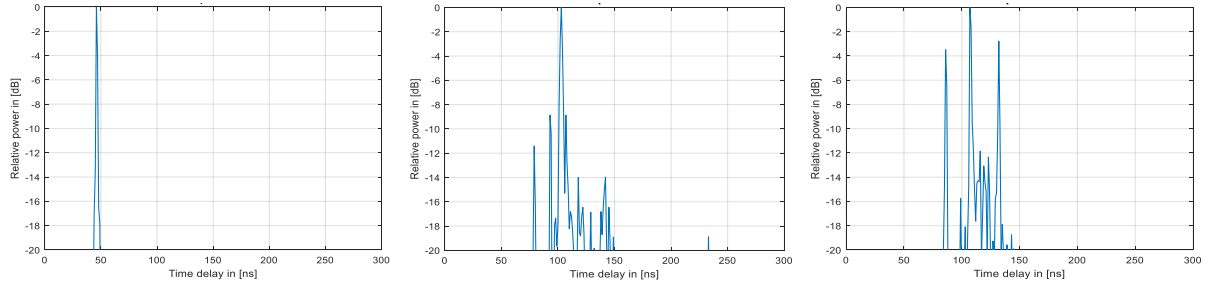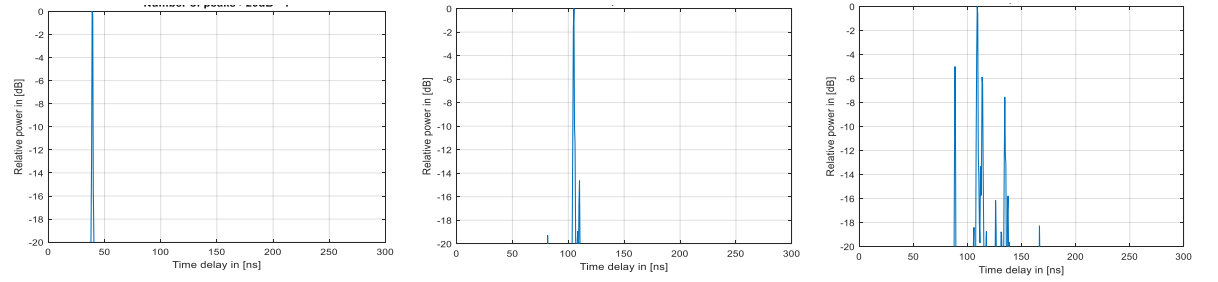
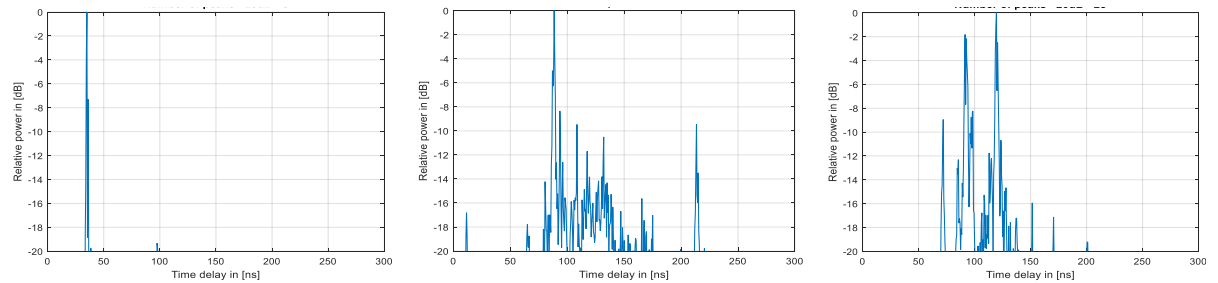*a) for 12.65 – 14.15 GHz at point 56, 96 and 116*
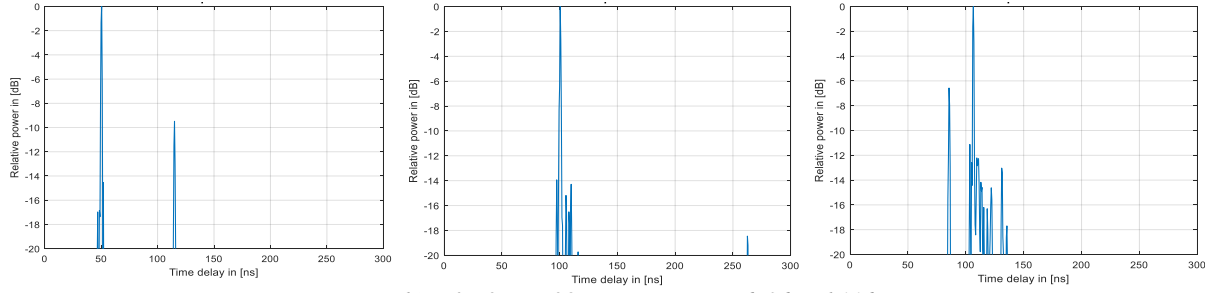
b)   for 25.5 – 28.5 GHz at point 56, 96 and 116
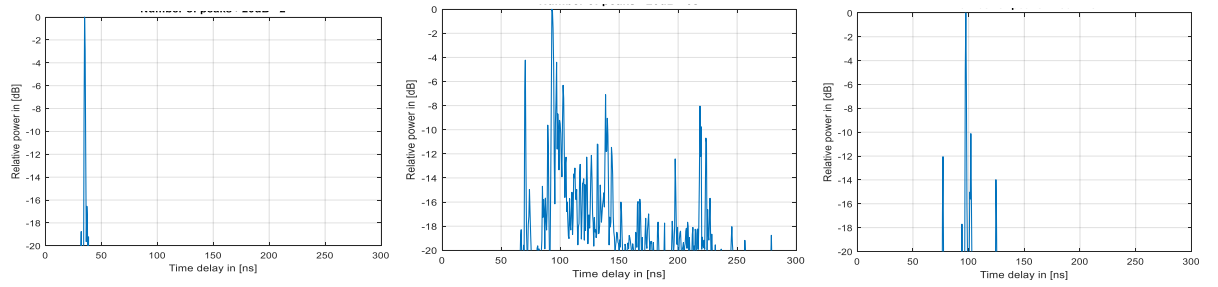
c)   for 51.2 – 57.2 GHz at point 56, 96 and 116

d)   for 59.6 – 65.6 GHz at point 56, 96 and 116

e) for 67 – 73 GHz at point 56, 96 and 116

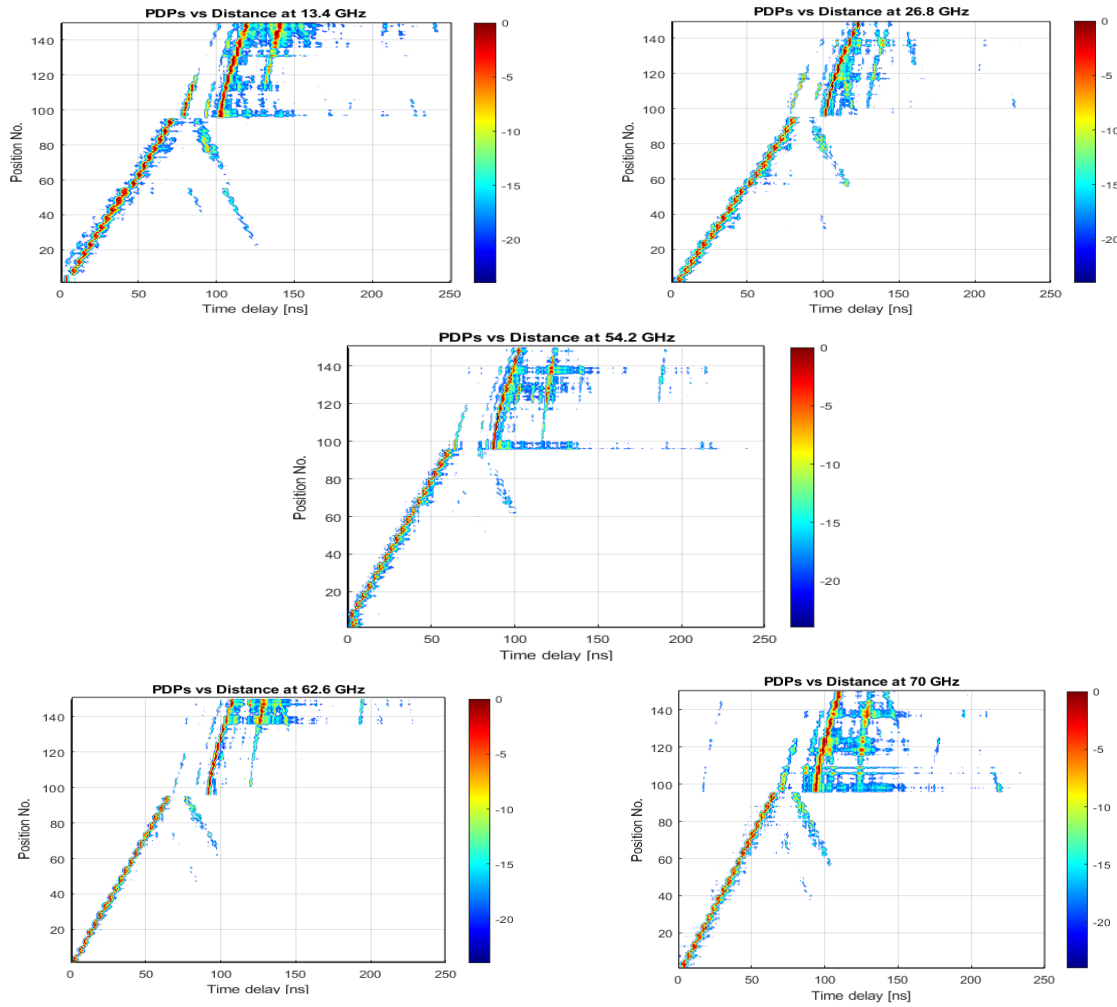**Figure 4-23 PDP samples from all measured frequency bands**

Figure 4-24 PDPs against measured positions for all measured frequency bands

Figure 4-24 provides images of the PDPs normalized to their maximum within 20 dB from the maximum for the measured frequency bands. The images show a decrease in the time delay spread as the measurement point number increases up to position 95, which is the last point in the LoS positions (at the end of the second black dashed arrow (B) in the layout graph). However, there was a slight shift forward in the main components and the reflected signals at position number 56 (it was clear at the 13.4 GHz band), which is the first point in the measurement set indicated by the second black dashed arrow in figure 4-19. For the second set of (NLoS) measurements from positions 96 to 150, there was another larger shift forward for all bands, due to the longer path that the signal travels from the transmitter to the receiver in the NLoS part. In general, the time delay spread for the LoS measurements was less than 150 nanoseconds over all bands, while it was within 250 nanoseconds for the NLoS part. The longest delay spread for the NLoS was at the first points where the power level was at its lowest values, as there were more multipath components as shown in figure 4-23 (c) and (e).

4.3.2.2 Average and RMS delay spread

Figure 4-25 provides the average delay spread versus measurement position. The average delay spread was within 15 nanoseconds up to position 95 over all bands. Then there was a sudden increase in average delay starting from position 96 (NLoS measurements) to reach about 55 nanoseconds at 54.2 GHz. After that, there was a drop in average delay between positions 100 and 120 due to a gradual increase in the power level of the received signals at these positions as shown in figure 4-20.
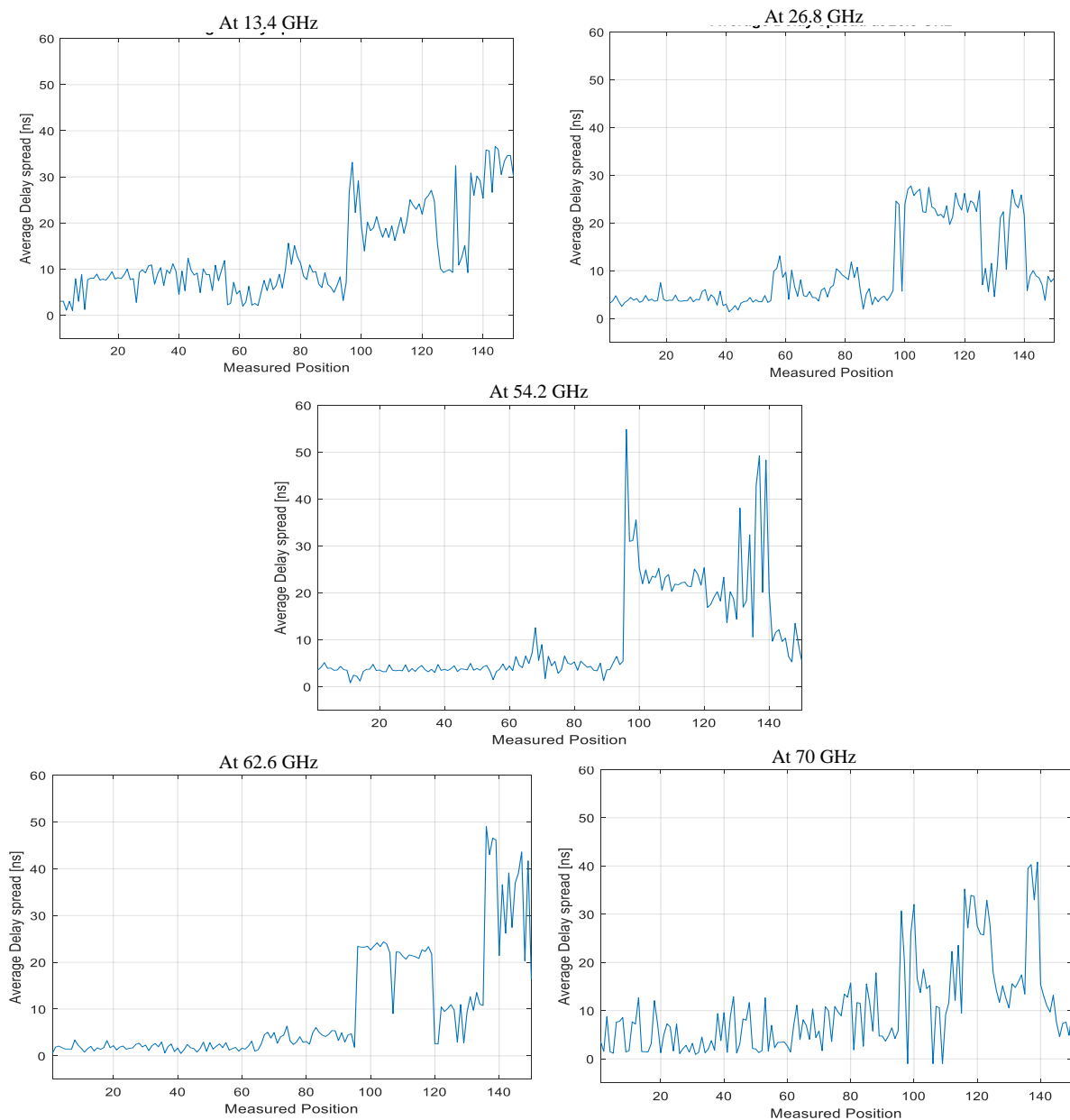

Figure 4-25 Average delay spread over measured positions for all measured frequency bands

The values of RMS delay spread for each measured frequency band are provided in figure 4-26. The figure shows sudden changes at two positions in most of the bands, the first at position 56 which is the starting point of the measurement set indicated by the second black dashed arrow in figure 4-19. The second position is at position 96, which is the first point in the NLoS measurements indicated by the red dashed arrow in the layout in figure 4-19. The maximum RMS delay spread was about 46 nanoseconds at position 96 for 54.2 GHz. The RMS delay spread values at 62.6 GHz were less than 15 nanoseconds for most of the positions and within 20 nanoseconds for the last few positions. The lack in dynamic range at 70 GHz is shown in the RMS delay spread.

Figure 4-26 RMS delay spread over measured positions for all measured frequency bands

123

Figure 4-27 illustrates the CDFs of the RMS delay spread for the measured frequency bands and the values for the indoor environments for each frequency band are presented in table 4-9. The highest and lowest CDF values of the RMS delay spread in all three values were at 13.4 GHz and 62.6 GHz respectively.

Table 4-9 CDF values of the RMS delay spread

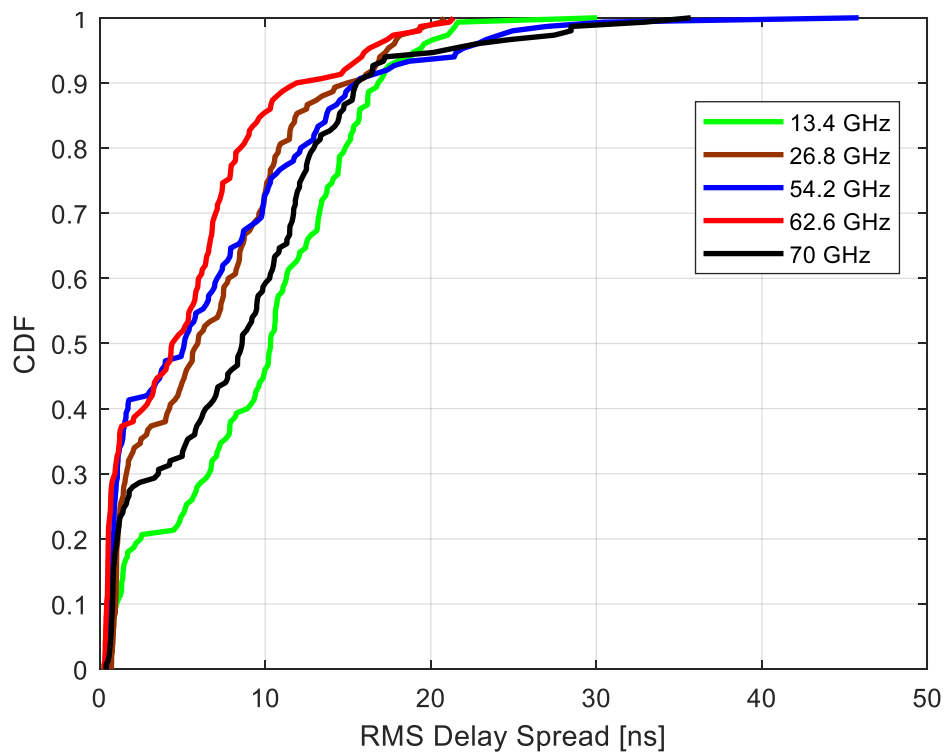| CDF	13.4 GHz	26.8 GHz	54.2 GHz	62.6 GHz	70 GHz
10%	1.01	0.95	0.66	0.42	0.77
50%	10.32	5.93	5.11	4.37	8.60
90%	16.81	14.95	15.52	11.89	15.52

Figure 4-27 RMS delay spread CDFs for all measured frequency bands

4.4 Summary and discussion

In these measurements different parameters were calculated such as path loss, average and RMS delay spread. In terms of path loss two models were used in this study, which are the close-in (CI) model and the floating intercept (FI) model. The calculated parameters of both models showed similar values for all scenarios in terms of (n) compared to (β) and the standard deviation (σ) in both models. The highest and lowest values for both (n) and (β) at most of the

bands were at the small office scenario and large office scenario respectively. There was a variation in the values of (n) and (β) between the bands at each scenario, where the highest values of (n) and (β) in most of the scenarios were at the 62.6 GHz band. While the lowest values of (n) were at 54.2 GHz band and for (β) at the 26.8 GHz band at most of the environments. For the standard deviation values the highest and lowest values at most of the bands were at the large office and small office scenarios respectively for both models, where the highest values were at 70 GHz band at most of the scenarios.

For the time dispersion parameters, in terms of the CDF of the RMS delay spread at 90% values, there was a variation in the pattern from one scenario to another, where the highest and lowest values in most of the bands were at the factory like and large office environments respectively. The lowest values of the CDF at 90% were at the 62.6 GHz band at most of the measured scenarios. It is noticeable that, there was high similarity in the CDF of the RMS delay spread values between the 54.2 GHz band and 70 GHz band at all the measured environments.

CHAPTER 5

DIRECTIONAL MEASUREMENTS

This chapter presents the results of LoS and NLoS wideband measurements in three indoor environments: a large office, a factory like space and a small office, which are the same scenarios as those presented in Chapters 3 and 4, and one outdoor environment (street canyon). To study the frequency dependency, three different frequency bands (12.65 – 14.15 GHz, 25.5 – 28.5 GHz and 59.6 – 65.6 GHz) measurements were conducted using the same multiband chirp-based channel sounder system mentioned in Chapter 3. A horn antenna with 20 dBi gain and around 18° beamwidth mounted on the top of 3D positioner was used at both the transmitter (Tx) and receiver (Rx) side for each frequency band. The positioner can rotate from zero degrees to 360° in azimuth and from -40° to 75° in elevation. The antennas at both sides were vertically polarized to perform a co-polar measurement for all scenarios studied. The measurement bandwidth for the first band (12.65 – 14.15 GHz) was 1.5 GHz, while it was 3 GHz and 6 GHz for the second band (25.5 – 28.5 GHz) and the third band (59.6 – 65.6 GHz), respectively. The plan was to conduct simultaneous measurements for all three frequency bands by using an eight channels data acquisition card (ADC). For that purpose, a C code was written, and some experimental tests were conducted. However, due to the huge data size and the long time required to record this data, an error occurred in the ADC after a few hours. In addition, this challenge is further compounded by the difficulty of mounting the three antennas with their RF heads in the centre of the 3-D positioner at the same height and keeping all of them vertically polarized, especially when the tilt angle is non-zero. Consequently, the plan was changed to conducting a single frequency band measurement each time, and as such, another C code was written to control the positioner azimuth and elevation angles and accordingly record the data using a two-channel 14-bit data acquisition card instead.

At the receiver side, the initial plan was to use a step size equal to half of the beam width (9°) in both azimuth and elevation with five different elevation angles. However, for time saving purposes, after conducting some measurements, the plan was changed, and the measurements were conducted at each position from zero degrees to 360° in azimuth with a step size of 12° for each elevation angle and three different elevation angles with a step size of 15° starting from

-15° to 15°. This was done for all scenarios studied except for the factory like scenario, where there were five different elevation angles due to the height of the ceiling (about 6 meters high), and the first elevation angle was -15° while the last was 45°. There were 30 recorded files for each elevation angle, with each file recorded for 1 second at a 40 MHz sampling rate. Consequently, there were 150 PDPs per point for the factory like scenario, and 90 PDPs per point for the other scenarios. On the other hand, at the transmitter side, the measurements were conducted at each position from zero degrees to 360° in azimuth with a step size of 12° at -9° elevation angle only.

The collected data were processed and analysed using MATLAB to extract several parameters with a 1 GHz bandwidth for the first band and 2 GHz for the other two bands. The power delay profile (PDP) for each angle at each point is the first and the most important step, where all the other parameters can be estimated from the PDP such as the Angle of Arrival (AoA), Angle of Departure (AoD) and the RMS angular spread at both the transmitter and receiver sides. The measured data were calibrated using both the on-air and back-to-back calibration methods. The four scenarios mentioned earlier, and their extracted parameters are presented in this chapter. The same steps and procedures mentioned in Chapter 3 must be followed to set up the sounding system for all measurements conducted. A further description of the measurement procedures and conditions for each environment is provided below.

5.1 Large office environment

Figure 5-1 shows the layout of the Large office environment. This scenario represents one of the most common academic environments with common obstructions such as chairs, desks and partitions. A horn antenna with the specifications mentioned earlier was mounted on top of the 3D positioner at both the Tx and Rx sides. At the receiver, the positioner was mounted on top of a trolley for easier mobility, and the antenna was at a height of 1.6 m from the ground, which is the average height of mobile users. For the LoS situation, the receiver was fixed during the measurements at the positions P1, P2 and P3 (as shown in the layout in figure 5-1) for each frequency band. The transmitter antenna with the 3D positioner were fixed at location Tx1 (as shown in figure 5-1) at a height of 2.5 m from the ground, on top of a tripod to emulate the hotspot point. The antenna was tilted down using the 3D positioner with -9° (which is half of the antenna's 3 dB beam-width) to focus the transmitted beam onto the measurement area. At position P1, the Rx was around 6 metres away from Tx1, and there was about 3 metres

separation distance between the measured points. The whole procedure was repeated three times, once for each frequency band.
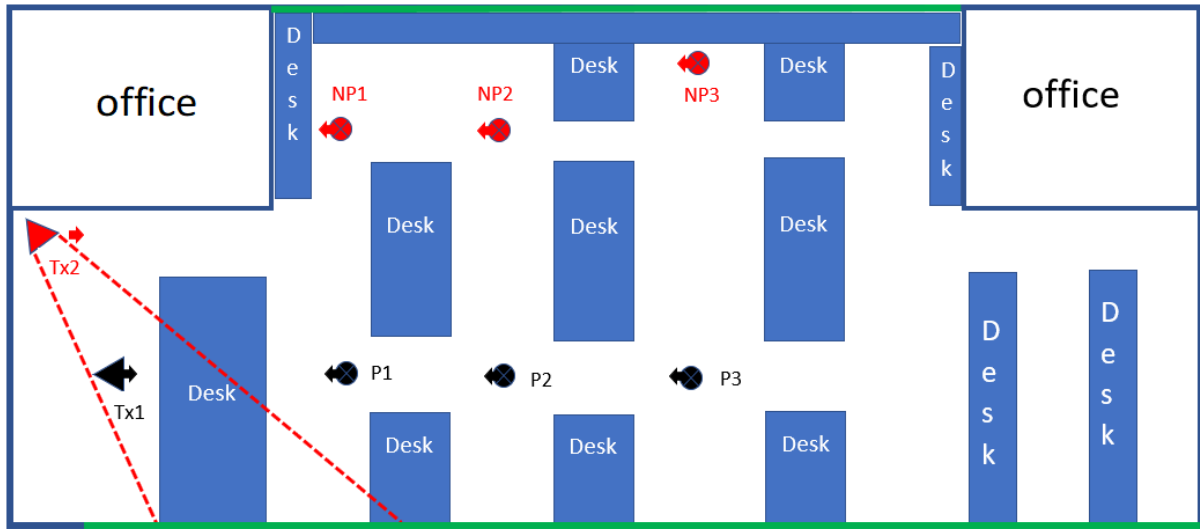

Figure 5-1 Large office layout

5.1.1 Line-of-sight (LoS) measurements

This section presents a description of the measurements carried out in the Large office environment, as well as the results and discussion of the LoS measurements such as the AoA, AoD and RMS angular spread of the three frequency bands mentioned earlier.

5.1.1.1   Angle of arrival (AoA)

For the AoA measurements, the transmitter was fixed at a position pointing towards the receiver, as shown in figure 5-1. The zero azimuth angles for the transmitter and receiver at each point are indicated by a small arrow in the layout in Figure 5-1. The receiver was then rotated clockwise with a step size of 12° in azimuth for the first two bands and 9° for the last band to cover the full rotation for each elevation angle. Three different elevation angles were used with a step size of 15° starting from -15° to 15° in the first two bands, whereas for the last band, five elevation angles were used with 9° starting from -18° to 18°. Figure 5-2 presents the power delay profiles versus the azimuth rotation angle at three different elevation angles when the receiver was at position P1 for all measured bands. The figure shows a strong signal around zero degrees within 25 nanoseconds, which corresponds to the line-of-sight angles where the antennas of the receiver and transmitter were oriented towards each other. Other signals with a lower power level of the reflected waves at different time delays of up to about 200 nanoseconds

were also shown between -50° and +50°. Furthermore, there were also signals that appeared around 180° at different time delays which denote the reflected signals when the receiver was pointing to the opposite direction of the small arrow at each position. It is noticeable that there were more reflected signals at zero degree elevation angle and azimuth angles between 50° and 150° when the antenna of the receiver was pointing to the wide area between the two offices, than when the antenna was pointing to the glass windows between -50° and -150°, as shown in figure 5-1.
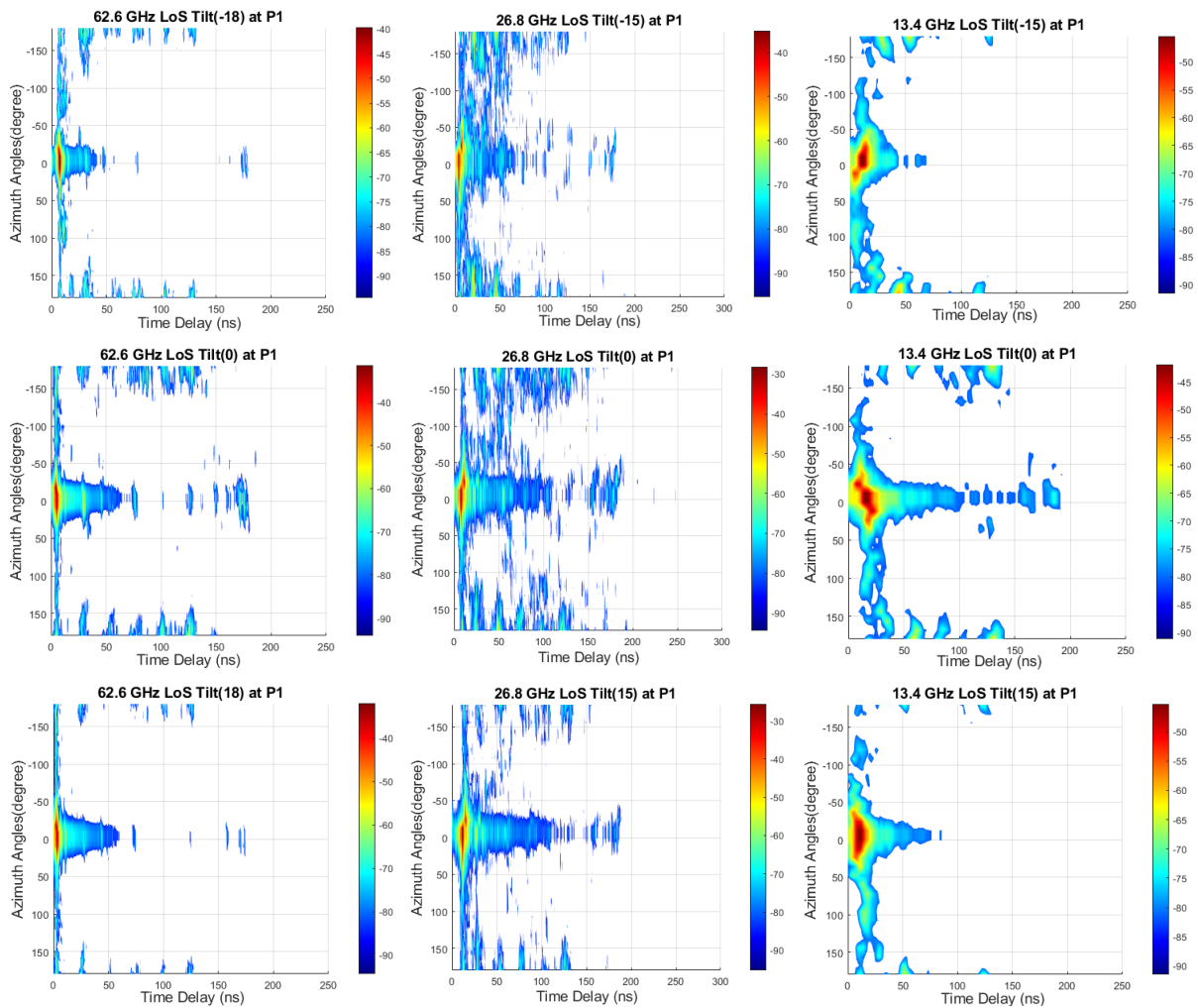

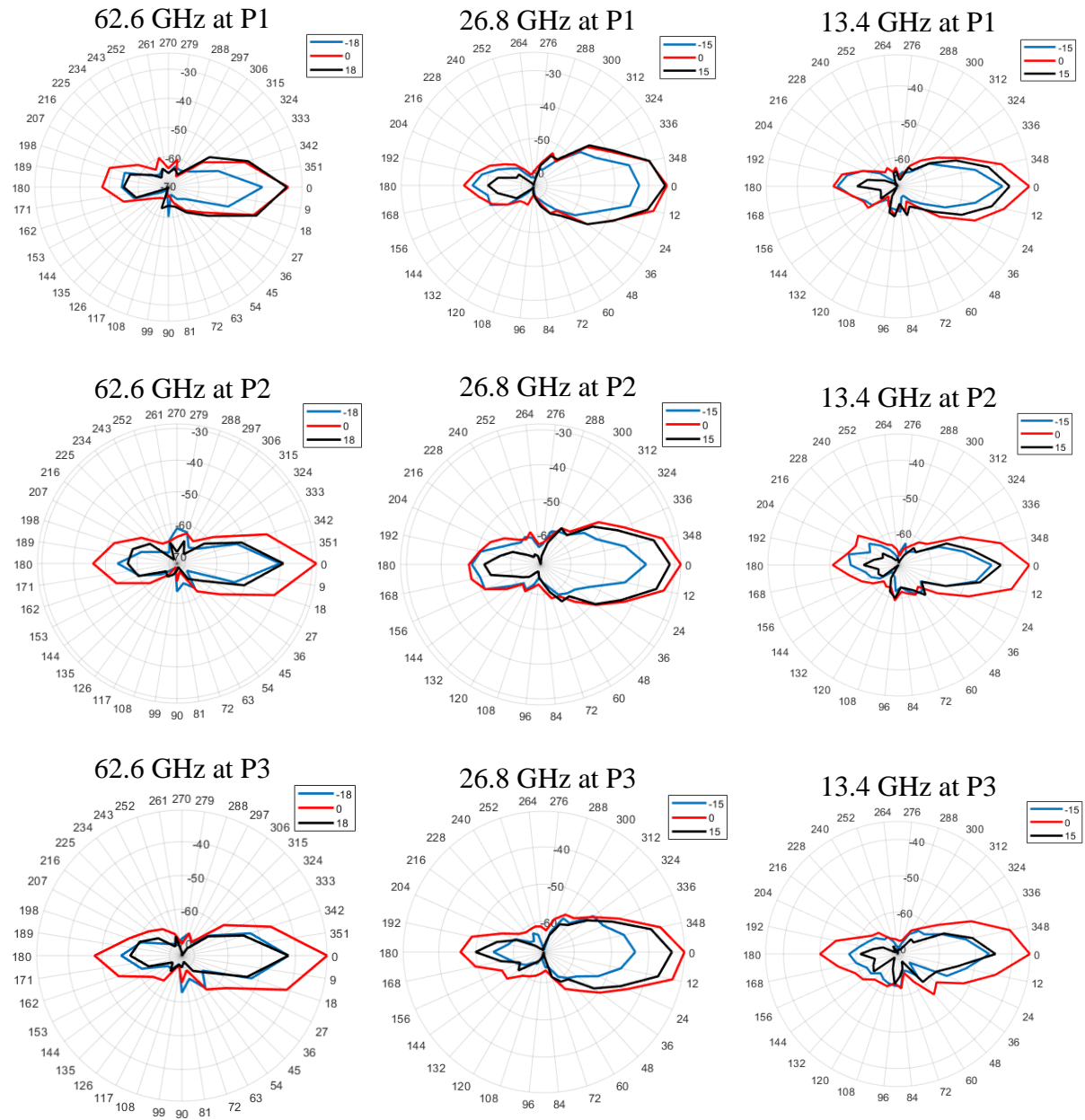**Figure 5-2 PDPs as a function of azimuth angle for three different elevation angles at position P1**

Figure 5-3 Polar plot of the received power versus azimuth angles at the strongest three elevation angles for all bands

Figure 5-3 shows a polar plot of the received power as a function of azimuth angles from 0° to 360° and at three different elevation angles. The figure demonstrates that the strongest signals for all bands and at all points were around zero degrees in azimuth and between $+15^o$ (or $+18^o$ for the 62.6 GHz) and zero degrees elevation angles. The strongest signals approached zero degrees elevation angle and the signal strength decreased for all bands as the distance between the transmitter and receiver increased. There were other signals around the 180° angle in azimuth which were strongest between zero degrees and -15° (or -18° for the 62.6 GHz)

elevation angles. The signal strength of this lobe increased as the receiver moved away from the transmitter and became closer to the reflector (as shown in the polar plot of the received power for each azimuth-elevation combination angle in Figure 5-3). To find out the number of lobes, a threshold of 10 dB was chosen [14, 15, 78] (to remain consistent for all positions at all scenarios) from the strongest received power level over all azimuth angles, where the AoA can then be estimated for each separate lobe accordingly. It is noticeable that the lobe in the 26.6 GHz band is slightly wider than the other two bands, which might be due to the fact that the antennas' 3 dB beam-width was slightly larger than 18° for this band, where the antennas were designed to cover a wide frequency band range (a detailed description of all used antennas is presented in the appendices).
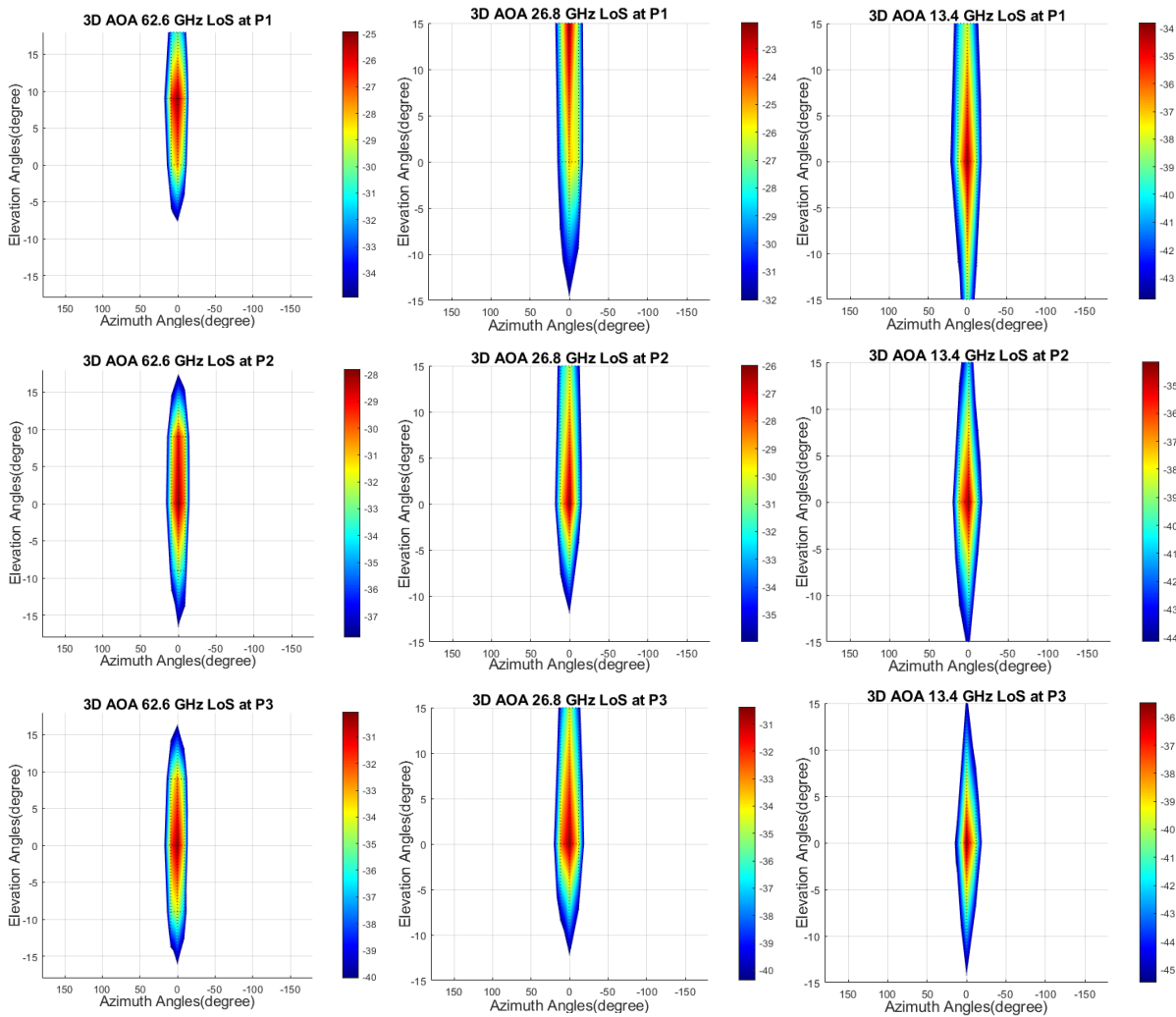

Figure 5-4 3D AoA images for LoS at three measurement positions for all bands

Figure 5-4 shows the 3D images of the AoA in azimuth and elevation within 10 dB from the maximum at three positions for all measured bands. The images show that the strongest AoA in azimuth at all positions was around zero degree for all three bands. For the elevation angle at all positions, the strongest AoA at the 13.4 GHz was very close to zero degree, while it was closer to the positive elevation angle at position P1 for both the 26.8 GHz and 62.6 GHz bands, and became closer to zero elevation angle for all bands when the receiver moved away from the transmitter, as shown in figure 5-4. It is noticeable that the power level was similar at both the positive and negative elevation angles for the 13.4 GHz and 62.6 GHz bands at most of the measured positions, while the power level in the positive elevation angles was stronger at the 26.8 GHz band.

Table 5-1 Estimated AoA in azimuth and elevation and RMS angular spread values

Centre frequency	Position No.	3D Azi. AoA	RMS azimuth angular spread	3D Ele. AoA	RMS elevation angular spread	No. of lobes
13.4 GHz	P1	0.49º	6.52º	1.05º	8.36º	1
	P2	1.27º	7.05º	2.10º	5.21º	1
	P3	358.52º	6.51º	1.53º	4.54º	1
26.8 GHz	P1	0.44º	8.03º	5.38º	9.24º	1
	P2	0.29º	7.81º	3.62º	8.35º	1
	P3	1.74º	7.83º	4.74º	6.97º	1
62.6 GHz	P1	0.63º	6.46º	5.32º	10.52º	1
	P2	359.78º	6.45º	1.85º	6.25º	1
	P3	0.85º	6.43º	0.69º	0.00º	1

Table 5-1 presents the estimated values of the AoA in azimuth and elevation for the strongest lobe and their RMS angular spread for all bands at each measurement position. The table shows the highest and lowest values of the RMS azimuth angular spread at all positions were at the 26.8 GHz and 62.6 GHz bands, respectively. For the 62.6 GHz band, the RMS azimuth angular spread, elevation AoA and RMS elevation angular spread decreased as the transmitter and receiver separation distance increased. On the other hand, for the 13.4 GHz band, the elevation AoA increased and the RMS elevation angular spread decreased as the separation distance between the Tx and Rx increased. For the 26.8 GHz band, the highest and lowest values of the elevation AoA and the RMS azimuth angular spread were at positions P1 and P2, respectively. It is also noticeable that the RMS elevation angular spread for all bands decreased as the position number (i.e. P1 to P3) increased.

5.1.1.2   Angle of departure (AoD)

For the AoD measurements, the received power was investigated for each angle to find the strongest received signal, and the angle of this signal was then selected as a fixed direction at the receiver to measure the AoD. Furthermore, while the receiver was pointing to that angle, the transmitter was then rotated clockwise from zero degree to 360° in azimuth with a step size of 12° in azimuth for the first two bands and 9° for last band to cover the full rotation, and the data were recorded at the receiver side for each Tx angle.

Figure 5-5 plots the PDPs as a function of the Tx azimuth rotation angles with a -9° elevation angle at the transmitter when the receiver was pointing to zero degrees (the angle of the strongest received power) at position P3 for all measured bands. The figure shows strong signals around zero degree within 50 nanoseconds, which corresponds to the line-of-sight angles when the antennas of the receiver and transmitter were oriented towards each other. Other signals with a lower power level of the reflected waves at different time delays of up to about 250 nanoseconds were also observed between -50° and $+50^{\circ}$. Furthermore, there were also signals that appeared around 180° at different time delays which denote the reflected signals when the transmitter was pointing to the wall (i.e. the Tx pointing completely out-of-sight of the receiver). The transmitter was about 2 metres away from the wall.
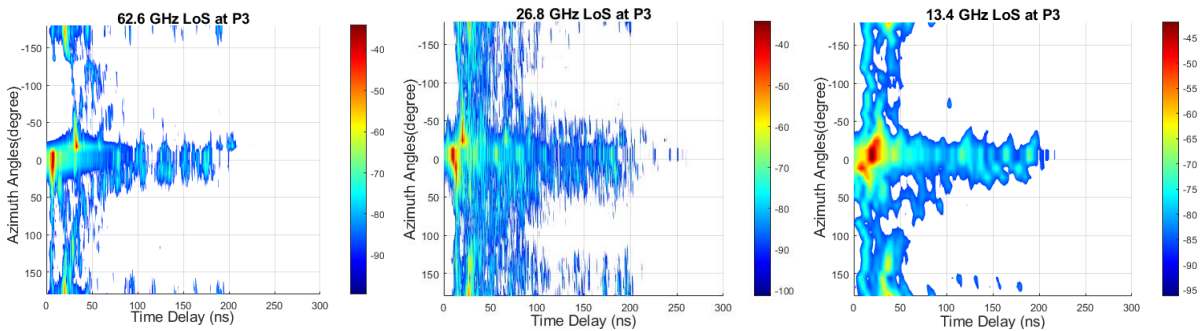

Figure 5-5 PDPs as a function of azimuth angles at -9° elevation angle and position P3 for all bands

Figure 5-6 depicts the polar plots of the received power against the Tx azimuth angles from 0° to 360° (with a step size of 12° for the first two bands and 9° for the last band) for each band at P3 with a 10 dB threshold from the maximum received power. The figure highlights that the strongest signals for all bands were around zero degree in azimuth, which represents the line-of-sight when the Tx and Rx antennas were oriented toward each other, whereas the second strongest lobe was around 180°, which corresponds to the Tx antenna pointing to the wall.
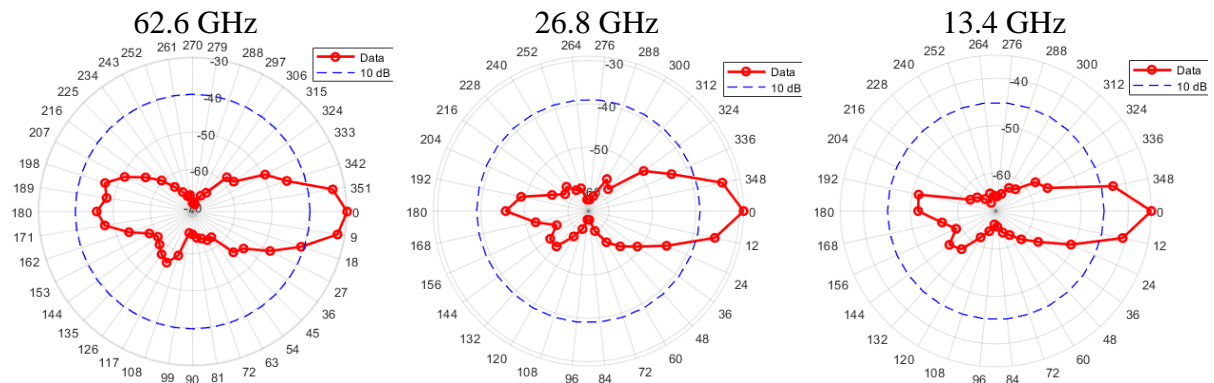
133

Figure 5-6 Polar plot of the received power vs Tx azimuth angles with -9º elevation angle at P3

Table 5-2 presents the estimated values of the AoD in azimuth for the strongest lobe and the RMS angular spread within 10 dB from the maximum for all bands at each measurement position (except position P1 for the 62.6 GHz band, where the data for this position are corrupted). The table shows a decrease in the AoD RMS angular spread values for the first two bands as the separation distance between the Tx and Rx increased, while for the 62.6 GHz band, there was an increase in the AoD RMS angular spread values as the TX-Rx distance increased for the tested positions. The best AoD at all positions and for all bands was around zero degree, which represents the angle when the Tx and Rx antennas were oriented toward each other.

Table 5-2 Estimated AoD in azimuth and RMS angular spread values

Centre frequency	Position No.	AoD	RMS angular spread	No. of lobes
13.4 GHz	P1	358.84º	7.03º	1
	P2	359.87º	6.96º	1
	P3	0.89º	6.66º	1
26.8 GHz	P1	359.73º	7.89º	1
	P2	359.77º	7.84º	1
	P3	359.08º	7.39º	1
62.6 GHz	P1	NA	NA	NA
	P2	0.71º	6.43º	1
	P3	0.74º	6.49º	1

134

5.1.2 Non-line-of-sight (NLoS) measurements

This section presents the results and discussion of the NLoS measurements and provides a detailed description of the measurements in Large office environment, such as the AoA, AoD and the RMS angular spread for the frequency bands mentioned earlier.

5.1.2.1   Angle of arrival (AoA)

For the AoA measurements, the transmitter was fixed at location Tx2 pointing towards the glass windows on the right hand side of Tx2 (indicated by the green line in figure 5-1), with an angle of 66°, which was calculated to cover the NLoS measurements area, as shown in figure 5-1. The zero azimuth angles for the transmitter and receiver at each measured point are indicated by a small arrow in the layout in figure 5-1. The receiver was then rotated clockwise with a step size of 12° in azimuth for the first two bands and 9° for the last band to cover the full rotation of each elevation angle. Three different elevation angles were used with a step size of 15° starting from -15° to 15° for the first two bands, whereas five elevation angles were used with a 9° step size starting from -18° to 18° for the last band.

Figure 5-7 presents the power delay profiles versus the azimuth rotation angle at a zero degrees elevation angle when the receiver was at positions NP1, NP2 and NP3 for all measured bands. The figure shows strong multipath signals between - 40° and -120° at the same time delay for all bands and at all positions, which indicate the reflected multipath signals from the glass windows (indicated by a green line at the right-hand side of Tx2 as shown in figure 5-1). Other multipath signals with lower power levels were observed between 40° and 120° for all bands and at all positions with a slightly longer time delay than the first reflected components. These multipath components were reflected from the windows at the right-hand side of the measured points (second reflection). It is noticeable that the difference in time delay between the first and second reflected multipath components was shorter, and the power level was higher at NP3 than NP1 and NP2 because the receiver at NP3 was closer to the windows, as shown in Figure 5-1.
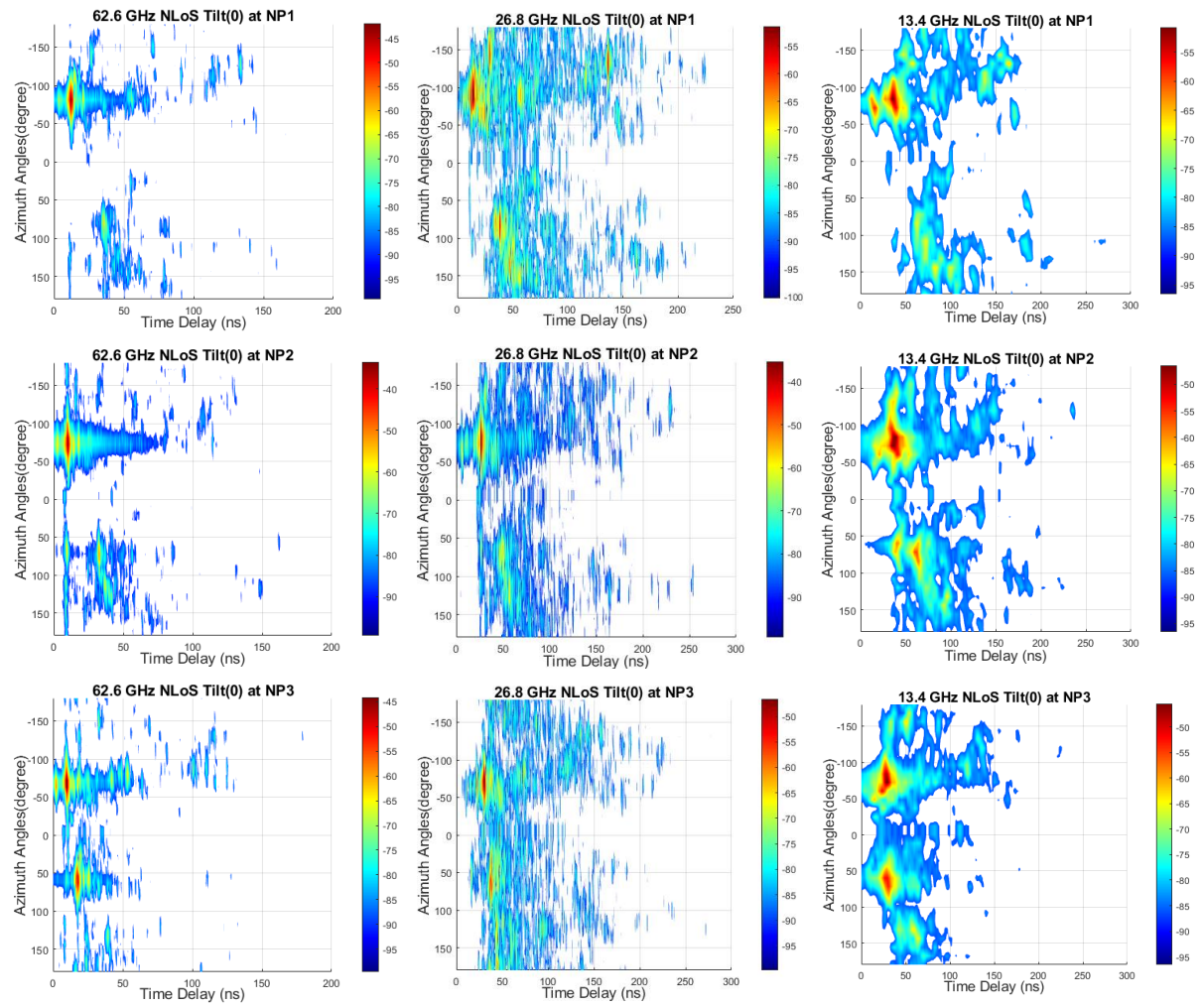
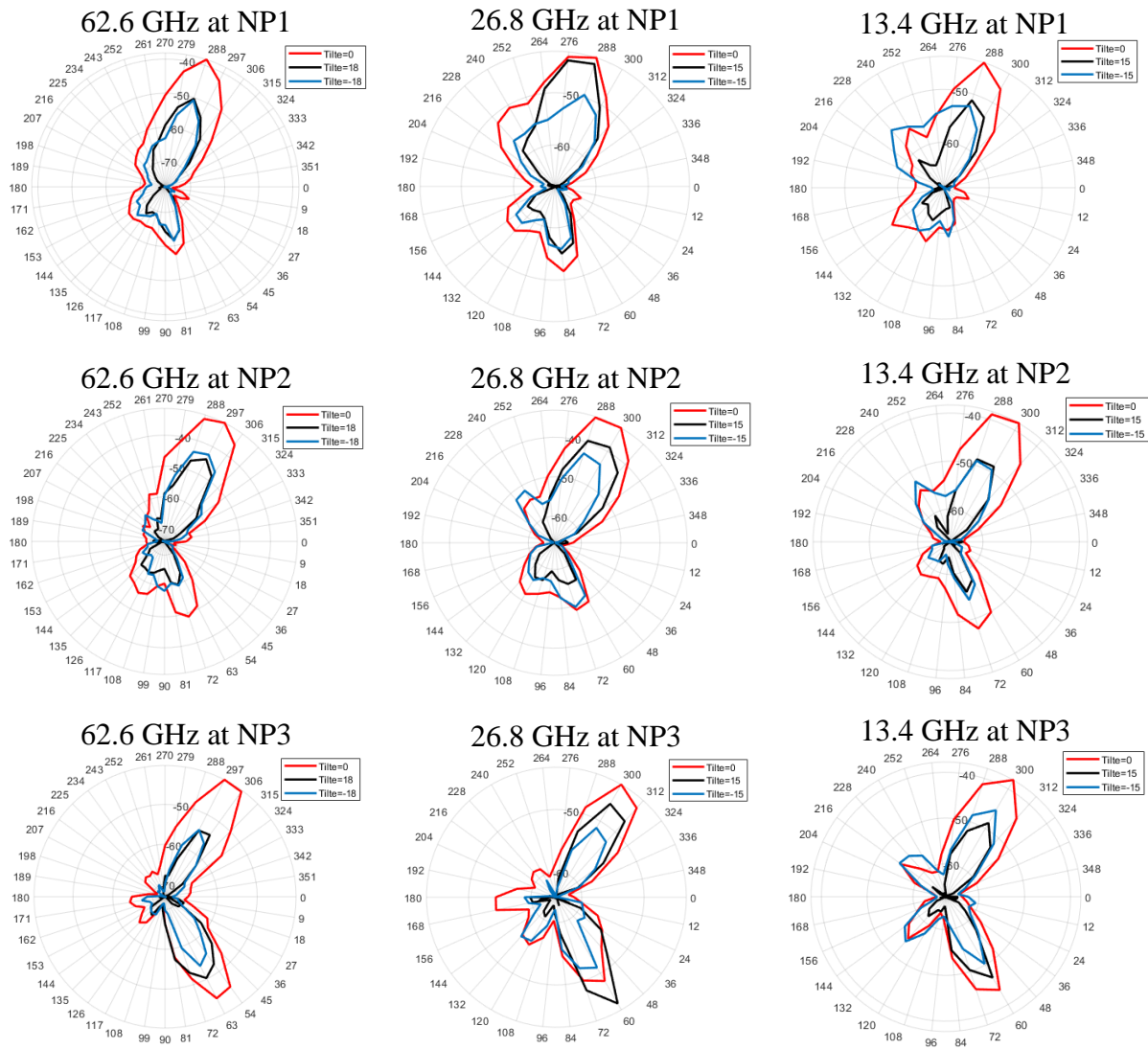**Figure 5-7 PDP as a function of azimuth angles at zero elevation for all measured bands and at all positions**

Figure 5-8 Polar plots of the received power versus azimuth angles at the strongest three elevation angles for all bands and at all three positions
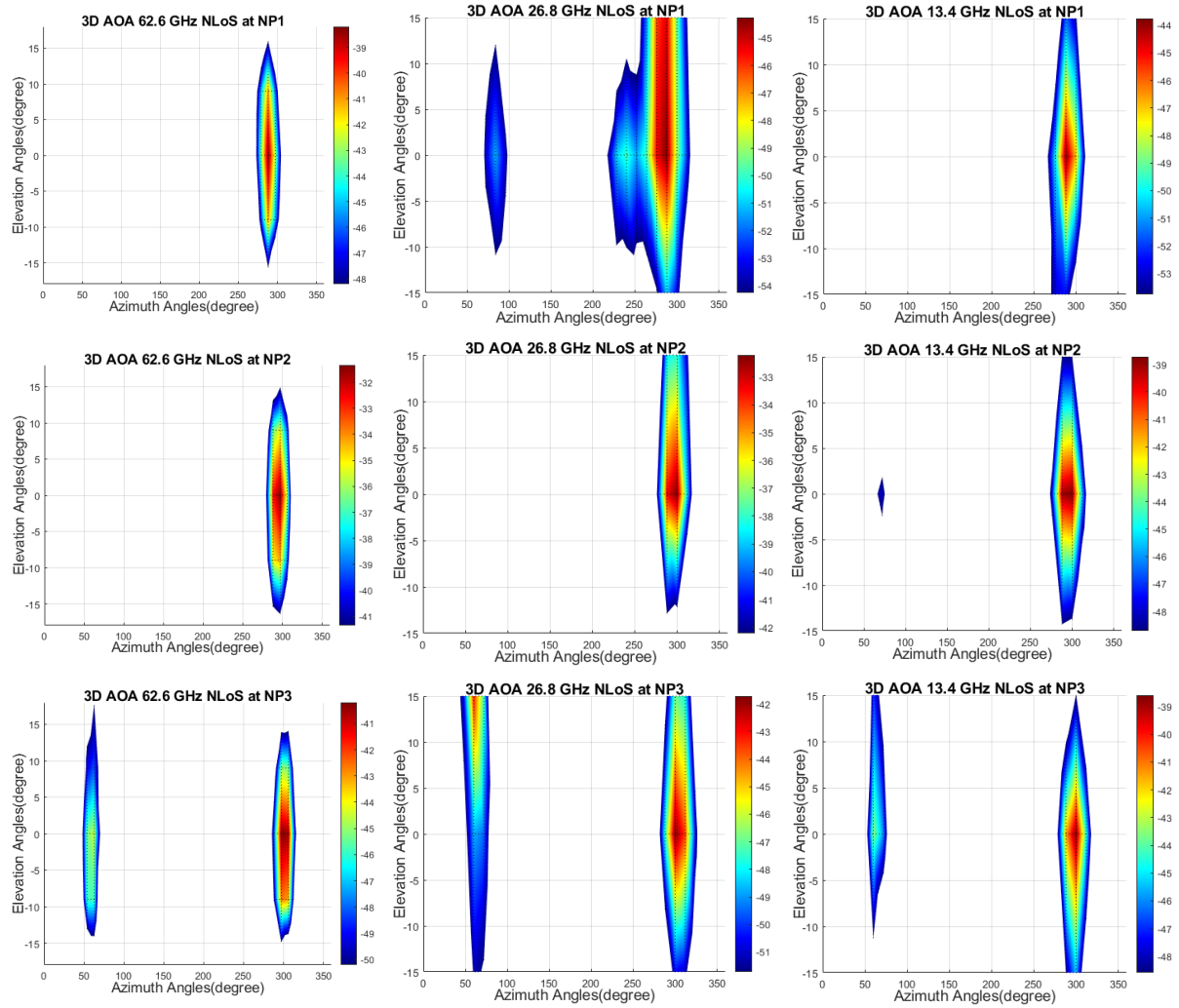
Figure 5-9 3D AoA images for the NLOS scenario at three measurement positions for all bands

Figure 5-9 shows the 3D images of the AoA in azimuth and elevation within 10 dB from the maximum received power at three positions for all measured bands. The images show that at all positions, the strongest AoA in azimuth was between 270° and 320° for all three bands, while the second strongest lobe was between 40° and 90°. In terms of the elevation angles, the strongest AoA were around the zero degrees angle at all positions and in all bands except for the 26.8 GHz at NP1, where the strongest AoA was between +15° and zero degrees, as shown in figure 5-9.

Table 5-3 presents the estimated values of the AoA in azimuth and in elevation for the lobe with the strongest received power and their RMS angular spread within 10 dB from the maximum received power for all bands and at each measurement position in the NLoS scenario. The table shows that the highest and lowest values of the RMS azimuth angular spread at most of the positions occurred at the 26.8 GHz band and 62.6 GHz band, respectively. However, at

position NP2, the largest RMS azimuth angular spread value occurred at the 13.4 GHz band. The elevation angle of the strongest lobe was within 5° form the zero degrees elevation angle in all bands, and the highest values of the RMS elevation angular spread at most of the positions occurred at the 26.8 GHz band. The lowest and highest RMS elevation angular spread values occurred at positions NP2 and NP1 respectively for the first two bands, while the RMS elevation angular spread values decreased as the position number increased for the 62.6 GHz band. It is noticeable that the AoA was negative in elevation at NP3 for the 13.4 GHz band and at NP2 and NP3 for the 62.6 GHz band. The elevation angles at the 62.6 GHz band were closer to or equal to zero elevation angle than the other frequency bands for all measured positions.

Table 5-3 Estimated AoA in azimuth and elevation and RMS angular spread values

Centre frequency	Position No.	3D Azi. AoA	RMS Azimuth angular spread	3D Ele. AoA	RMS elevation angular spread	No. of lobes
13.4 GHz	NP1	289.79º	7.59º	0.42º	7.28º	1
	NP2	294.78º	8.96º	1.38º	4.34º	2
	NP3	298.18º	7.76º	- 1.21º	7.18º	2
26.8 GHz	NP1	278.60º	21.79º	4.99º	10.17º	2
	NP2	296.98º	7.79º	3.13º	6.09º	1
	NP3	304.06º	9.37º	1.79º	8.11º	2
62.6 GHz	NP1	288.26º	5.70º	0.00º	6.45º	1
	NP2	295.39º	6.31º	- 0.49º	6.20º	1
	NP3	300.91º	6.32º	- 1.17º	6.10º	2

5.1.2.2   Angle of departure (AoD)

To find the best receiving angle for the AoD measurements, the procedures used in the LoS scenario (Section 5.1.1.2) were repeated to find the best receiving angle, and the selected angle was chosen according to the best receiving power at each position in azimuth and at the zero degrees angle in elevation for all positions.

Figure 5-10 shows the PDPs as a function of the Tx azimuth rotation angles with a -9° elevation angle at the transmitter and with the receiver pointing to the angle of the strongest received power at position NP2 for all measured bands. The figure shows that the strongest signals occurred between the angles of $+40^{\circ}$ and $+100^{\circ}$ at the same time delay, which correspond to the strongest lobe when the antenna of the transmitter was oriented towards the glass windows at the right-hand side of the transmitter (the area between the two red dashed lines shown in Figure 5-1). Other signals with lower power level of the reflected waves were observed between $+100^{\circ}$

and +150º, and these signals were stronger at the 13.4 GHz band than the other two bands. In addition, there were other signals that appeared between -50º and -150º whose power level decreased as the frequency band increased. These received signals corresponded to the case when the transmitter was pointing to the opposite direction of the strongest lobe (to the corner next to Tx2), as shown in figure 5-1.
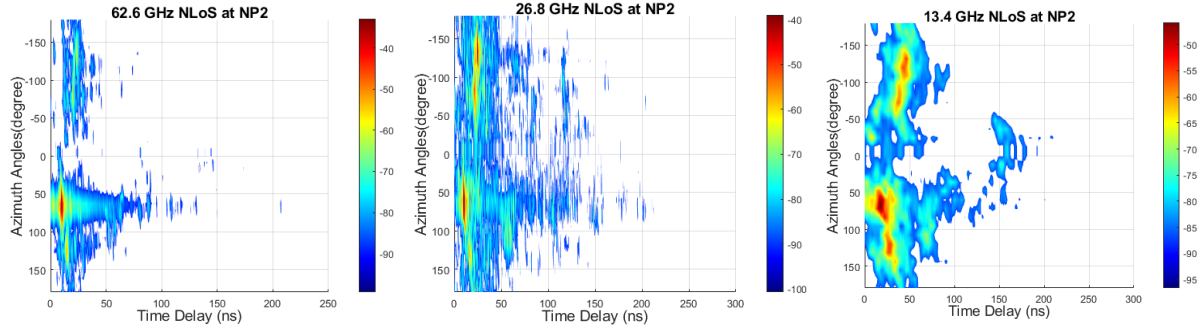

Figure 5-10 Tx PDPs as a function of azimuth angles at -9º elevation angle and position NP2 for all bands

Figure 5-11 shows polar plots of the received power as a function of the Tx azimuth angle from 0º to 360º (with a step size of 12º for the first two bands and 9º for the last band) for each band at NP2 with 10 dB threshold from the maximum power when the receiver was fixed at the azimuth angle of the strongest received power. The figure shows that the strongest received power was between 60º and 72º in azimuth for all bands when the Tx antenna was pointing to the direction indicated by the two red dashed lines in Figure 5-1. The second strongest lobe occurred in the first two bands around the 240º angle and was stronger at the 26.8 GHz band than in the 13.4 GHz band. A third lobe can also be seen between 120º and 132º in the 13.4 GHz band only, as it was very weak in the two other bands.
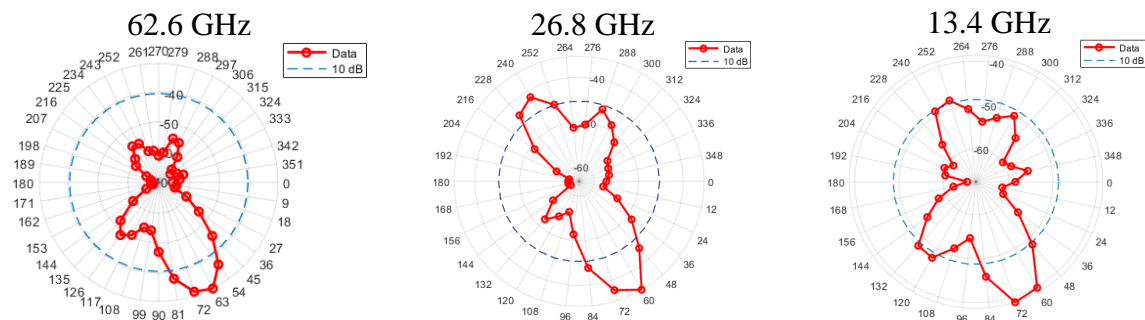
Figure 5-11 Polar plot of the received power vs Tx azimuth angles with -9º elevation angle at NP2

Table 5-4 presents the estimated values of the AoD in azimuth for the strongest lobe and their RMS angular spread within 10 dB from the maximum for all bands at each measurement position. Note that this excludes the results of position NP3 for the 62.6 GHz band because the dedicated time for the measurement finished before completing the measurements at this position, which is why the plan was changed to using fewer azimuth and elevation angles, as seen in the other bands. The table shows a decrease in AoD as the position number increased. Moreover, the number of lobes for the 62.6 GHz band was equal to 1 at the two measured positions, while it was at least 2 for the other bands. This means that the power in this band experienced higher attenuation compared with the other lower frequency bands in this environment.

Table 5-4 Estimated AoD in azimuth and RMS angular spread values

Centre frequency	Position No.	AoD	RMS angular spread	No. of lobes
13.4 GHz	NP1	81.95º	8.34º	2
	NP2	68.37º	7.65º	3
	NP3	63.24º	6.99º	3
26.8 GHz	NP1	74.17º	8.34º	2
	NP2	62.85º	7.29º	2
	NP3	60.39º	7.88º	3
62.6 GHz	NP1	73.74º	6.33º	1
	NP2	66.51º	7.26º	1
	NP3	NA	NA	NA

5.2 Factory like environment

Figure 5-12 shows the layout of the factory like environment. For the LoS scenario, the receiver was fixed during the measurements at positions P1, P2 and P3 for each frequency band, as shown in the layout in figure 5-12. The transmitter antenna with the 3D positioner were fixed at location Tx1 at a height of 3 m from the ground, on top of a tripod to emulate the hotspot point. The antenna was tilted down at -9º (which is the half of the antenna's 3 dB beam-width) to focus the transmitted beam onto the measurement area. The position P1 was about 6 metres away from Tx1 and there was about 6 metres separation distance between the measured positions. The detailed description of the environment is presented in Section 3.3 of Chapter 3. The whole procedure was repeated three times, once for each frequency band.
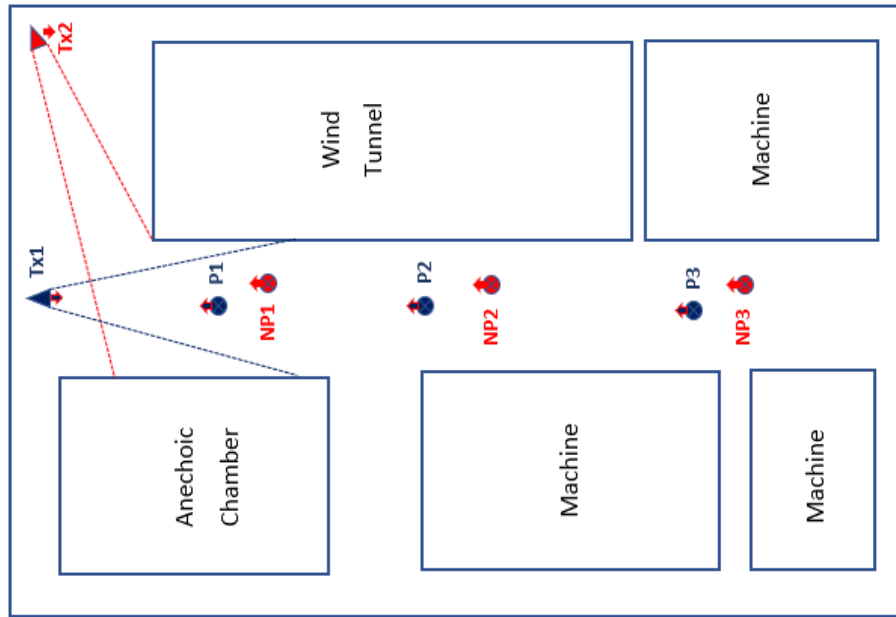
Figure 5-12 Factory like layout

5.2.1 Line-of-sight (LoS) measurements

This section describes the measurements conducted in factory like environment and presents the results and a discussion of the LoS measurements such as the AoA, AoD and the RMS angular spread for the three frequency bands mentioned earlier.

5.2.1.1 Angle of arrival (AoA)

For the AoA measurements, the transmitter was fixed at a position pointing towards the receiver, as shown in figure 5-12. The zero azimuth angles for the transmitter and receiver at each point are indicated by a small arrow in the layout in Figure 5-12. The receiver was then rotated clockwise with a step size of 12° in azimuth for the first two bands and 9° for the last band to cover the full rotation for each elevation angle. Five different elevation angles were used with a step size of 15° starting from -15° to 45° for the first two bands, whereas five elevation angles were used with a 9° step size starting from -18° to 18° for the last band.

Figure 5-13 presents the power delay profiles versus the azimuth rotation angle for three selected elevation angles with the receiver at position P3 for all measured bands. The figure shows a strong signal around zero degrees within 25 nanoseconds, which corresponds to the line-of-sight angles where the antennas of the receiver and the transmitter were oriented towards each other. Other signals with a lower power level of the reflected waves at different time delays

of up to about 250 nanoseconds were also observed between -50º and +50º. In addition, there were also signals that appeared around 180º at time delays of around 110 nanoseconds, which denote the reflected signals when the receiver was pointing to the opposite direction of its zero azimuth. It is noticeable that there were reflected signals with different power levels at all azimuth angles within a time delay of 50 nanoseconds for all bands, which highlights the reflective nature of this environment, where it is full of metallic surfaces.
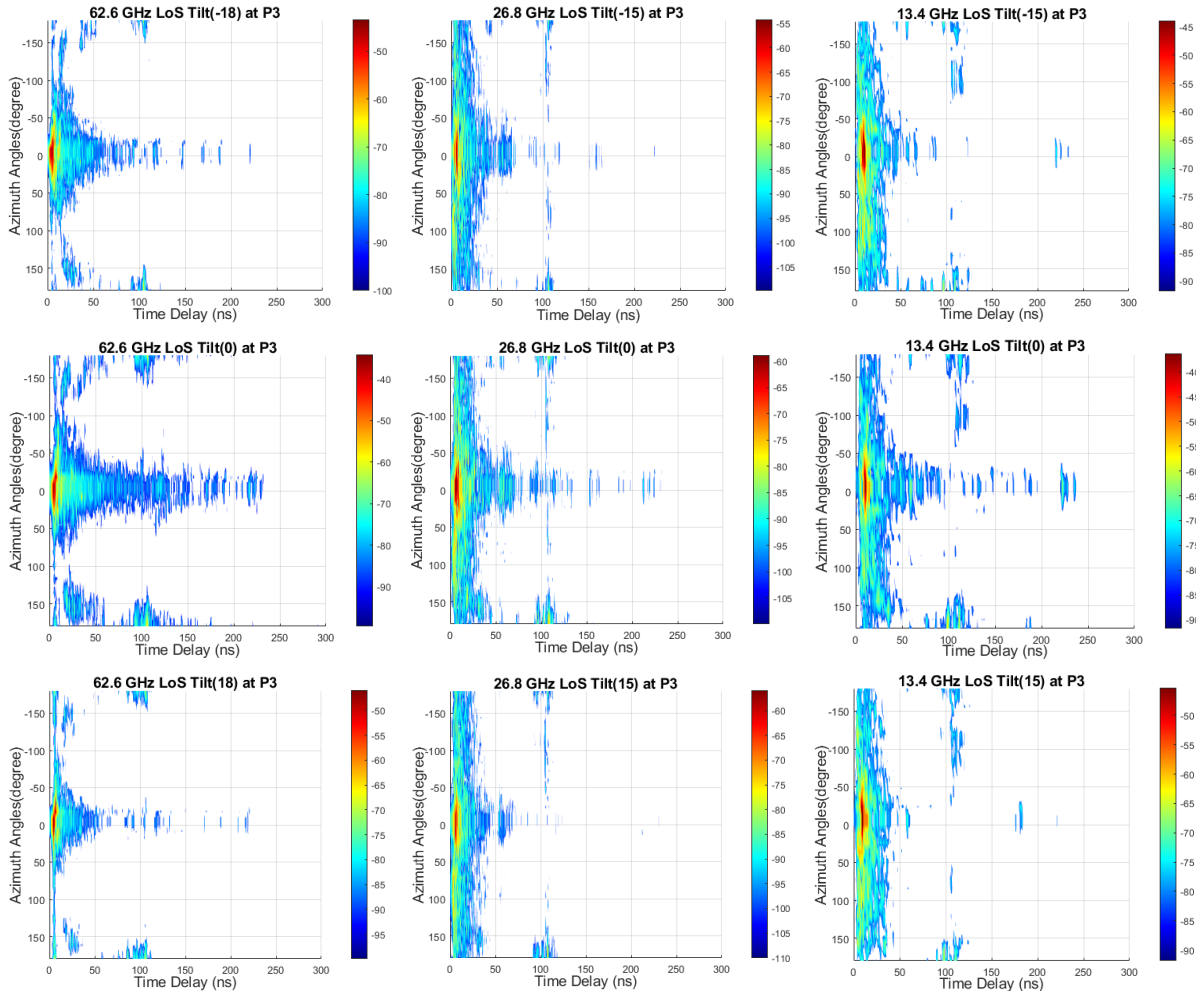
Figure 5-13 PDPs as a function of azimuth angles for three different elevation angles at position P3

Figure 5-14 shows polar plots of the received power as a function of the azimuth angles from 0º to 360º at three different elevation angles. The figure shows that the strongest signals for all bands and at all points were around the zero degrees angle in azimuth. For P1, the strongest signals in elevation were at +15º for the first two bands and +18º for the 62.6 GHz band, which is due to the height of the transmitter antenna. The elevation angle of the strongest received

power approached the zero degrees elevation angle and the signal strength of this lobe decreased compared with the previous position for all bands as the distance between the transmitter and receiver increased. There was another lobe around 180° in azimuth which was stronger at a zero degree elevation angle for all bands and at all positions.
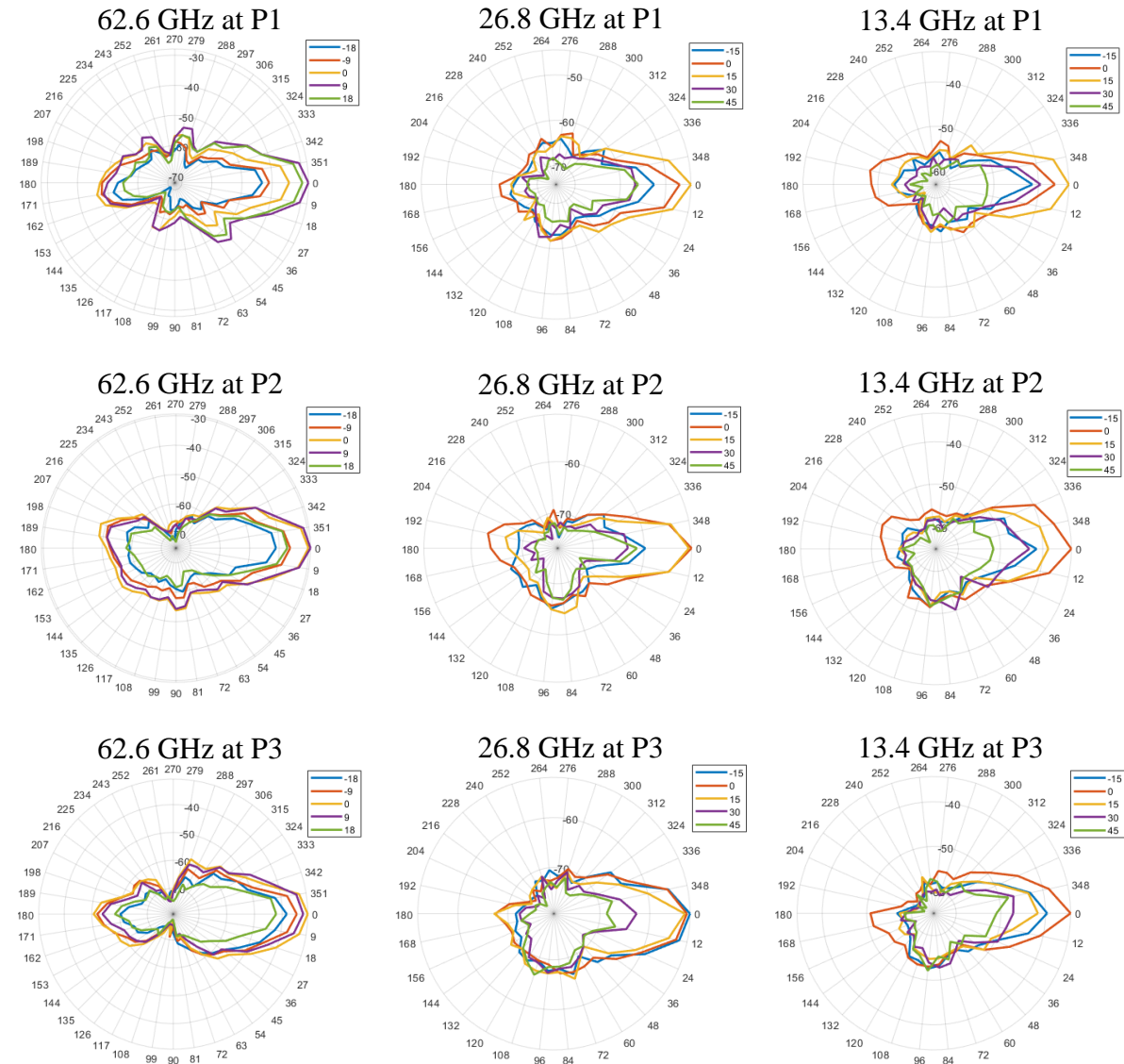
Figure 5-14 Polar plots of the received power versus azimuth angles at five different elevation angles and three positions for all bands

Figure 5-15 shows the 3D images of the AoA in azimuth and elevation within 10 dB from the maximum at three positions and for all measured bands. The images show that at all positions, the strongest AoA in azimuth was around zero degrees for all three bands. For the elevation at position P1, the strongest AoA for the first two bands was around +15°, while it was around 9° for the 62.6 GHz band. This is because the receiver at P1 was close to the transmitter and the

height of the transmitter antenna was 3 m and was tilted down by -9°, thus the strongest elevation angle decreased as the receiver moved away from the transmitter. At P2, the strongest elevation angle occurred between zero degrees and +9° for the 62.6 GHz band, and between zero degrees and +15° for the 26.8 GHz band, while it was closer to the zero elevation angle for the 13.4 GHz band. Finally, at P3, the strongest AoA in elevation was around zero degrees for all bands and it was slightly stronger in the negative direction for the 26.8 GHz band, as shown in Figure 5-15. It is also noticeable that the effect of the elevation angles +30° and +45° was negligible in terms of the strongest elevation AoA.
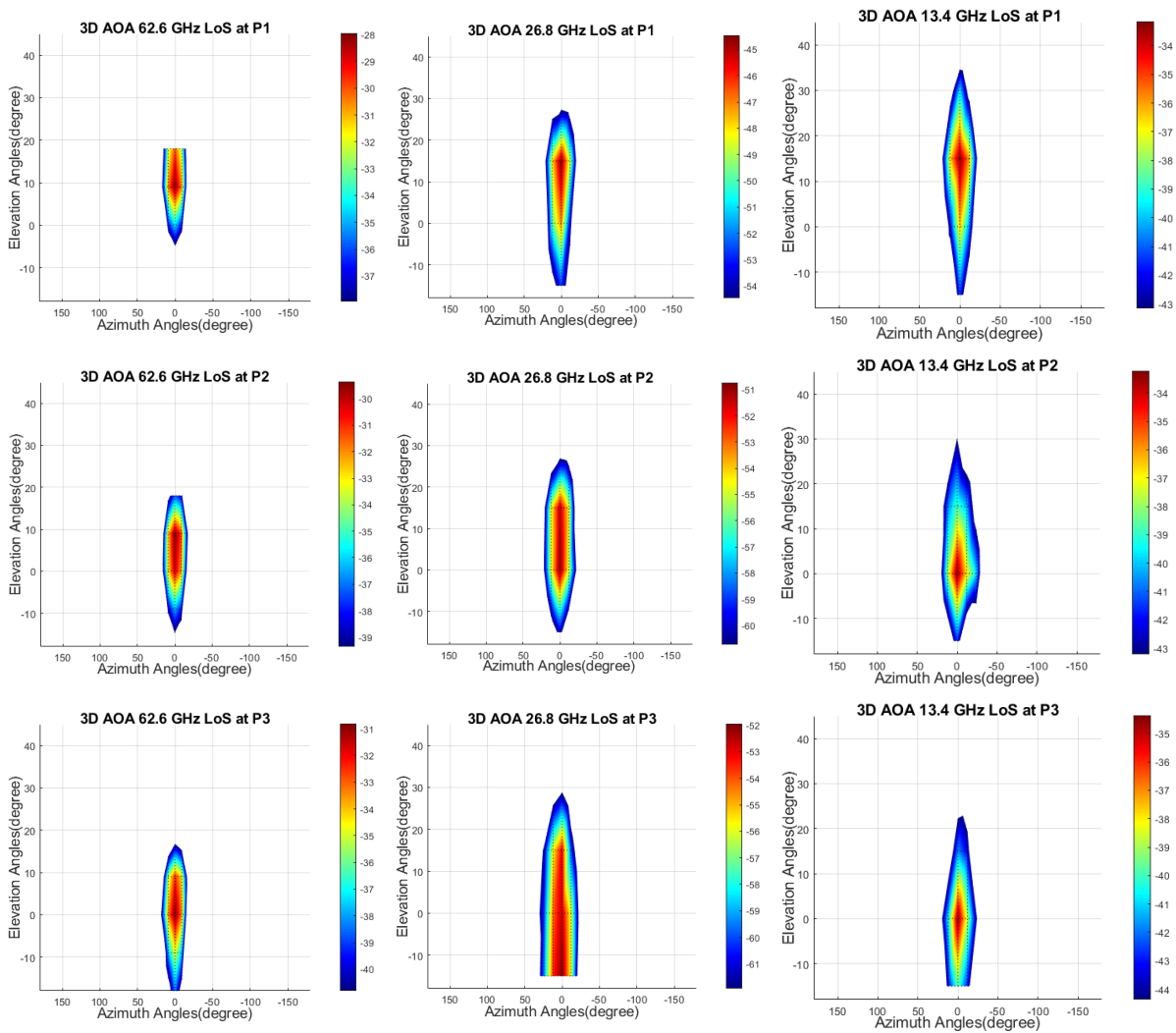
Figure 5-15 3D AoA images for the LoS scenario at three measurement positions for all bands

Table 5-5 presents the estimated values of the AoA in azimuth and elevation for the strongest lobe and their RMS angular spread within 10 dB from the maximum for all bands at each measurement position. The table shows a decrease in the elevation angle of the best AoA as the

separation distance between the transmitter and receiver increased. This what was expected since the difference in height between the Tx and Rx antennas was about 1.4 m and the Tx antenna was tilted down at -9°. The number of lobes was 1 in all positions and for all bands, which shows that the difference between the received power of the line-of-sight signals compared to the reflected signals from other directions was more than 10 dB. It is also noticeable that the value of the RMS azimuth angular spread at position P2 was the highest for the 13.4 GHz band, while it was the lowest for the other two bands. Furthermore, the elevation angle at position P3 was negative for the first two bands, which shows that the reflected signals from the ground were stronger than those from the ceiling for these two bands.

Table 5-5 Estimated AoA in azimuth and elevation and RMS angular spread values

Centre frequency	Position No.	3D Azi. AoA	RMS azimuth angular spread	3D Ele. AoA	RMS elevation angular spread	No. of lobes
13.4 GHz	P1	359.56^o	8.38^o	12.77^o	9.43^o	1
	P2	356.99^o	10.47^o	1.40^o	8.13^o	1
	P3	359.04^o	7.29^o	-1.15^o	8.49^o	1
26.8 GHz	P1	1.71^o	8.96^o	7.38^o	9.83^o	1
	P2	359.88^o	8.00^o	5.68^o	8.99^o	1
	P3	3.05^o	10.29^o	-1.21^o	12.26^o	1
62.6 GHz	P1	0.44^o	7.62^o	10.95^o	5.80^o	1
	P2	359.12^o	6.54^o	3.49^o	5.95^o	1
	P3	0.72^o	7.47^o	1.22^o	6.39^o	1

5.2.1.2   Angle of departure (AoD)

For the AoD measurements, the received power was investigated for each angle to find the strongest received signal, and the angle of this signal was then selected as a fixed direction at the receiver to measure the AoD. With the receiver was pointing at that angle, the transmitter was then rotated clockwise from zero degrees to 360° in azimuth with a step size of 12° in azimuth for the first two bands and 9° for the 62.6 GHz band to cover the full rotation. The data were then recorded at the receiver side for each Tx angle.

Figure 5-16 presents the PDPs as a function of the Tx azimuth rotation angle at a -9° elevation angle at the transmitter, with the receiver pointing to zero degrees (the angle of the strongest received power) at position P3 for all measured bands. The figure shows strong signals around zero degrees within about 20 nanoseconds, which correspond to the line-of-sight angles when

the antennas of the receiver and transmitter were oriented towards each other. Other signals with a lower power level of the reflected waves at different time delays of up to about 250 nanoseconds were also observed between -50° and +50°. There were also signals that appeared around the 180° angle at different time delays, where they had the strongest power level at about 25 nanoseconds, which denoted the reflected signals when the transmitter was pointing to the wall behind Tx1, where the wall consisted of glass windows with metallic frames. The transmitter was about 2 metres away from the wall.
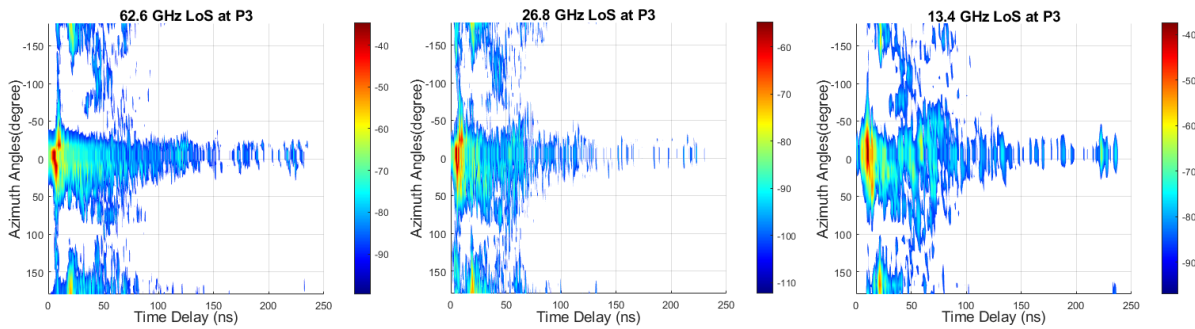
Figure 5-16 PDPs as a function of azimuth angles at -9° elevation angle and position P3 for all bands

Figure 5-17 shows polar plots of the received power as a function of Tx azimuth angles from 0° to 360° (with a step size of 12° for the first two bands and 9° for the last band) for each band at position P3 with a 10 dB threshold from the maximum received power. The figure demonstrates that the strongest signal for all bands was around the zero degrees angle in azimuth which represents the line-of-sight when the Tx and Rx antennas were oriented towards each other, while the second strongest lobe was around 180° when the Tx antenna was pointing to the wall. The received power in the second lobe for all bands was less than the threshold.
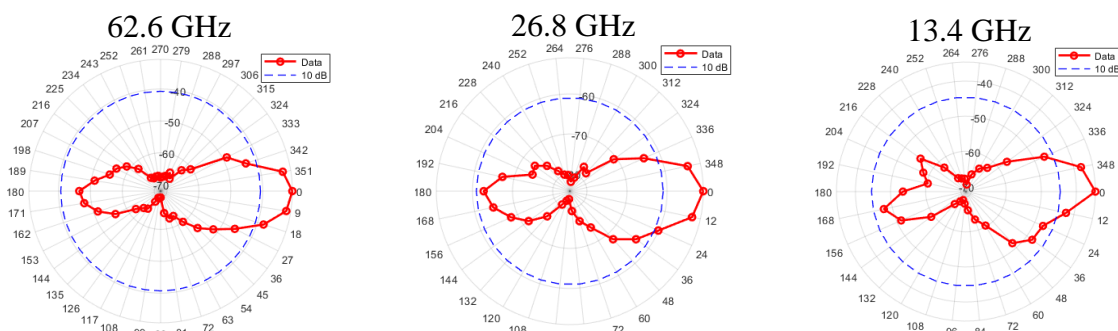
Figure 5-17 Polar plots of the received power vs Tx azimuth angles at -9° elevation angle and position P3

Table 5-6 presents the estimated values of the AoD in azimuth for the strongest lobe and their RMS angular spread within 10 dB from the maximum for all bands at each measurement position. The table shows a decrease in the RMS angular spread for the first two bands as the separation distance between the transmitter and receiver increased. The 26.8 GHz band showed the highest value of the RMS angular spread at positions P1 and P3 compared to the other bands, while it showed the lowest value at position P2.

Table 5-6 Estimated AoD in azimuth and the RMS angular spread values

Centre frequency	Position No.	AoD	RMS angular spread	No. of lobes
13.4 GHz	P1	359.97°	7.39°	1
	P2	0.83°	7.77°	2
	P3	357.85°	7.13°	1
26.8 GHz	P1	0.35°	8.33°	1
	P2	2.18°	7.64°	1
	P3	0.79°	8.62°	1
62.6 GHz	P1	359.11°	6.45°	2
	P2	0.74°	7.98°	1
	P3	1.94°	7.89°	1

5.2.2 Non-line-of-sight (NLoS) measurements

This section presents the results and discussion of the NLoS measurements, as well as a detailed description of the measurements in the factory like environment, such as the AoA, AoD and their RMS angular spread for the same frequency bands.

5.2.2.1 Angle of arrival (AoA)

For the AoA measurements, the transmitter was fixed at location Tx2 pointing towards the anechoic chamber (the direction indicated by two red dashed lines in figure 5-12) with an angle of 36° from the zero-azimuth angle in clockwise direction. The angle was calculated to maximize the signal strength in the measurement area for the NLoS measurements, as shown in figure 5-12. The zero-azimuth angles for the transmitter and receiver at each point are indicated by a small arrow in the layout in Figure 5-12. The receiver was then rotated clockwise with a step size of 12° in azimuth starting from zero degrees for all measured bands to cover

the full rotation for each elevation angle. Five different elevation angles were used with a step size of 15$^{\text{o}}$ starting from -15$^{\text{o}}$ to 15$^{\text{o}}$ for all bands.
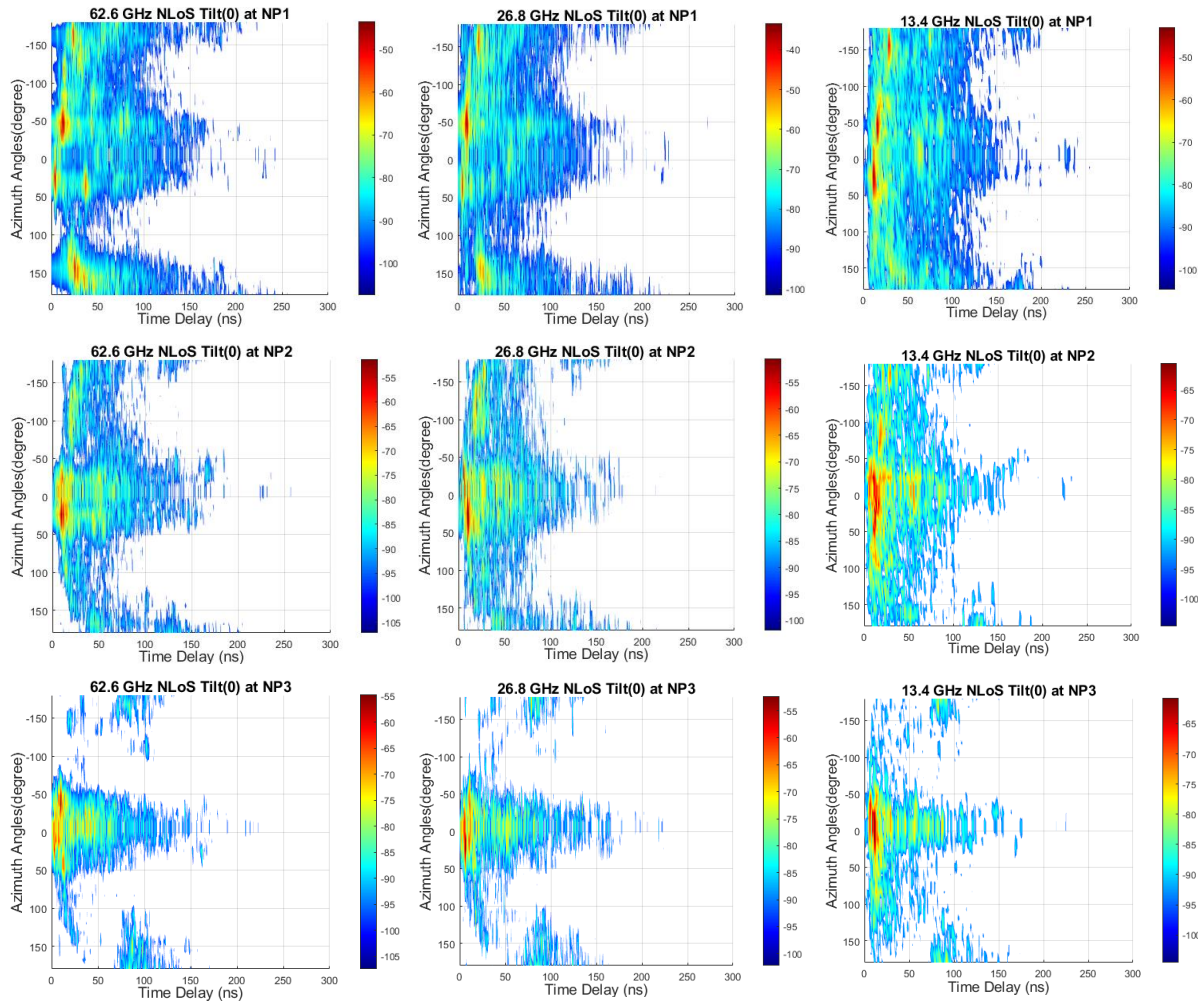
Figure 5-18 PDP versus azimuth angles at zero elevation for all measured bands and positions

Figure 5-18 presents the power delay profiles versus azimuth rotation angle at a zero degrees elevation angle when the receiver was at positions NP1, NP2 and NP3 for all measured bands. The figure shows several strong multipath signals spots at different angles and different time delays in position NP1, which shows the reflective nature of this environment where it is full of metallic surfaces. The strongest signals for the last two bands were between -10$^{\text{o}}$ and -70$^{\text{o}}$ angles at the same time delay, which represent the second order reflected signals from the wind tunnel surface, where the first order signals were reflected from the anechoic chamber surface. Furthermore, for the 13.4 GHz band, the strongest signals occurred between zero degrees and +60$^{\text{o}}$ angles, as shown in figure 5-18. At positions NP2 and NP3, the strongest received signal

became concatenated around zero degrees angle with a wide range of angles at position NP2, especially for the 13.4 GHz band, and the range decreased at position NP3 to become within around 100° between -50° and +50° angles. This might be because surfaces at both sides of the measurements area worked as a wave guide to focus the signals around the zero degrees angle in azimuth at the receiver.

Figure 5-19 Polar plots of the received power versus azimuth angles at the strongest three elevation angles for all bands

Figure 5-19 shows polar plots of the received power as a function of azimuth angles from 0° to 360° at the three elevation angles of the strongest received power in the NLoS scenario. At position NP1, the figure shows mainly four different lobes with different power levels for all bands, which again highlights the nature of this environment. At position NP2, they became

two lobes with a wider beam, where the second order reflected signals from the surface of the wind tunnel became dominant and the first order reflected signals from the surface of the anechoic chamber almost disappeared. At position NP3, the number of reflection orders increased as shown in Figure 5-18, and the signals focused around zero degrees in azimuth due to the waveguide effect of the measured path. There was another lobe around 180° with a lower power level, which represents the reflected signals from the back wall at the end of the measured path. It is also noticeable that the strongest received power for most of the lobes was at the zero degrees elevation angle for all bands and at all positions.
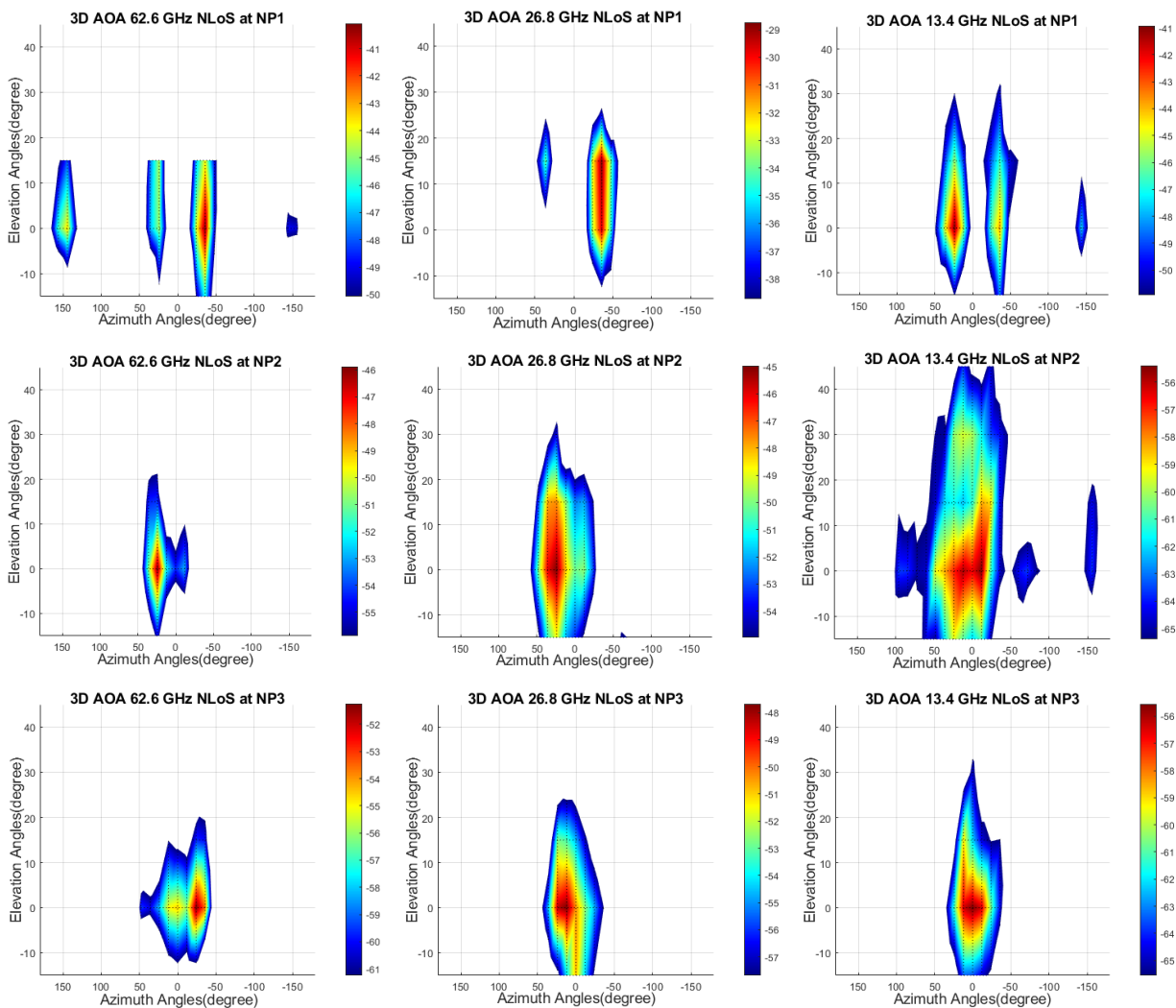
Figure 5-20 3D AoA images for NLoS at three measurement positions for all bands

Figure 5-20 shows the 3D images of the AoA in azimuth and elevation within 10 dB from the maximum at three positions for all measured bands. The images show several lobes at position NP1 for all bands, with the strongest lobe between -20° and -50° in azimuth for the last two

bands, and between 0º and +50º for the 13.4 GHz band. At position NP2, the lobes combined into one broad lobe around the 0º angle, therefore forming the strongest lobe; whereas the second lobe only occurred in the 13.4 GHz band around the 180º angle. The lobe at the 13.4 GHz band was the widest in both azimuth and elevation, while the narrowest lobe in azimuth and elevation was at the 62.6 GHz band. At position NP3, the lobes became more focused around the 0º angle in both azimuth and elevation due to the waveguide effect of the measurement path, where metallic surfaces were present at both sides of the path, and the location of position NP3 was close to the end of the path, as shown in figure 5-12.

Table 5-7 Estimated AoA in azimuth and elevation and RMS angular spread values

Centre frequency	Position No.	3D Azi. AoA	RMS azimuth angular spread	3D Ele. AoA	RMS elevation angular spread	No. of lobes
13.4 GHz	NP1	25.75º	9.52º	2.41º	7.92º	3
	NP2	16.09º	29.89º	- 0.31º	9.21º	3
	NP3	358.68º	14.79º	0.62º	7.83º	1
26.8 GHz	NP1	324.75º	7.73º	8.19º	7.47º	2
	NP2	19.33º	19.31º	0.99º	10.45º	2
	NP3	7.48º	17.25º	- 1.82º	9.75º	1
62.6 GHz	NP1	325.86º	6.66º	1.49º	9.37º	4
	NP2	19.08º	13.99º	0.25º	6.97º	1
	NP3	348.85º	23.67º	2.01º	9.19º	2

Table 5-7 presents the estimated values of the AoA in azimuth and elevation for the lobe of the strongest received power and their RMS angular spread within 10 dB from the maximum for all bands and at each measurement position in the NLoS scenario. The table shows that the RMS azimuth angular spread at position NP2 was the highest for the first two bands, while for the 62.6 GHz band, the RMS azimuth angular spread increased as the receiver moved away from the receiver. The elevation angle of the strongest lobe at position NP2 was closer to zero elevation angle compared to the other positions for all bands. It is noticeable that the elevation angle of the strongest lobe for all bands and at all positions was smaller than the half beam-width of the antenna (9º) despite the transmitter antenna's height and the factory like 's ceiling height. In addition, the elevation angle of the strongest lobe was negative at position NP2 for the 13.4 GHz band and at position NP3 for the 26.8 GHz band. Furthermore, the AoA of the strongest lobe was closer to the zero degrees angle in azimuth at position NP3 for all bands.

5.2.2.2   Angle of departure (AoD)

To find the best receiving angle for the AoD measurements, the procedures used in the LoS scenario (Section 5.1.1.2) were repeated to find the best receiving angle, and the selected angle was chosen according to the best receiving power at each position in azimuth and at the zero degrees angle in elevation for all positions.
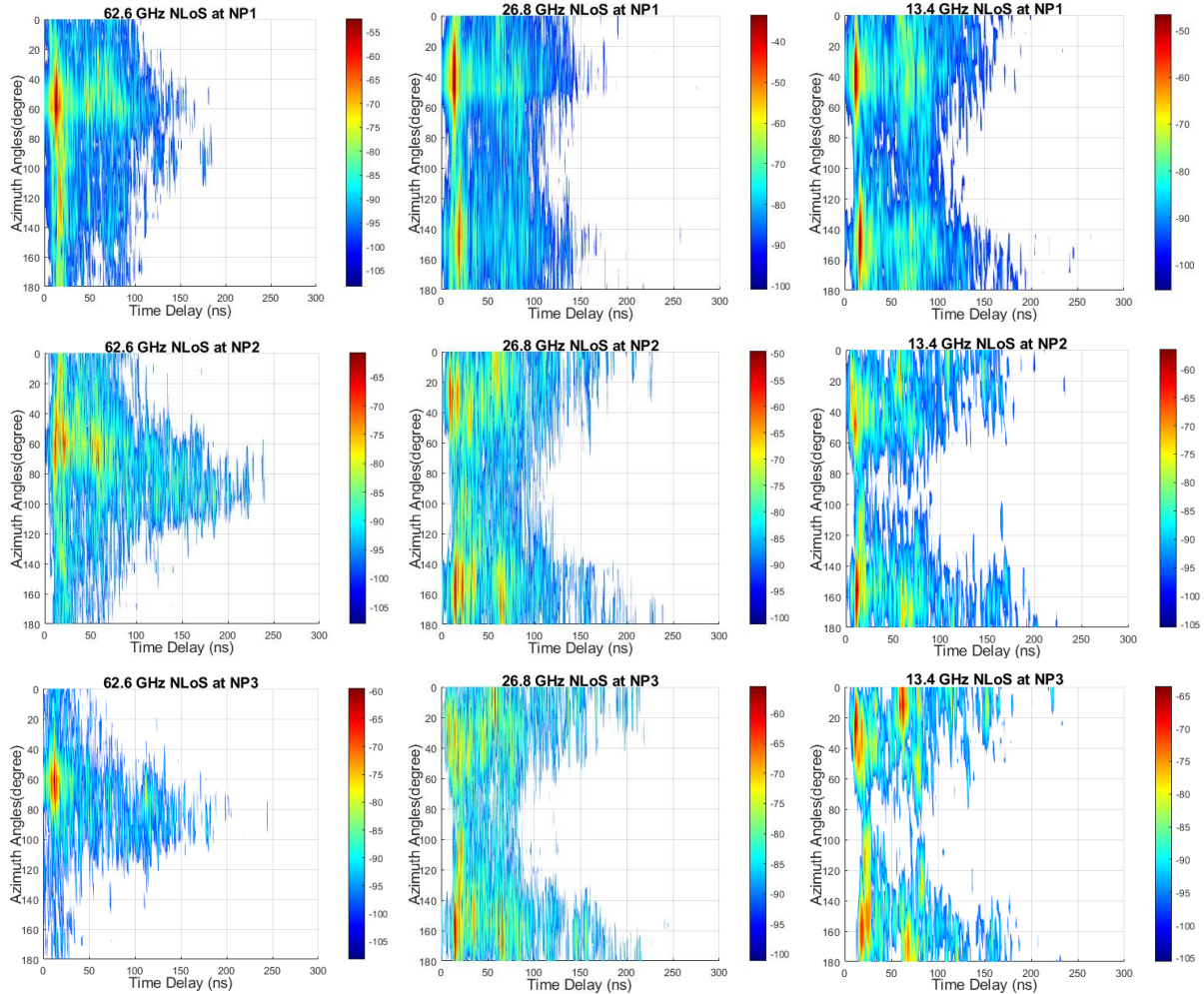
Figure 5-21 Tx PDPs as a function of azimuth angles at 0° elevation angle for all positions and bands

Figure 5-21 presents the PDPs as a function of the Tx azimuth rotation angle from zero degrees to 180° in clockwise direction (the zero angle of Tx is indicated by the small red arrow shown in figure 5-12). The transmitter was close to the wall to emulate the hotspot situation with a 0° elevation angle at the transmitter. The receiver was pointing to the azimuth angle of the strongest received power at all positions and for all measured bands. For the first two bands, the figure shows that the strongest signals came from two different directions, the first between 0° and 70° angles at two different time delays, which corresponds to the lobe when the antenna

of the transmitter was oriented towards the area between the two red dashed lines shown in Figure 5-12. On the other hand, the second lobe occurred between 110° and 180° angles, and the two lobes were wider at position NP1 but shrunk and moved towards the zero and 180° angles as the receiver moved away. For the 62.6 GHz band, there was one main direction of the strong signals that appeared between 20° and 80° at position NP1, and other weak signals between 110° and 150°. The second lobe declined at position NP2 and disappeared completely at NP3. This might be because the Tx antenna at this band was not at the centre of the 3D positioner, as in this measurement, two different antenna types were used next to one another.

Figure 5-22 shows polar plots of the received power as a function of the Tx azimuth angle from 0° to 180° with step size of 12° for all bands and at each position with a 10 dB threshold from the maximum power when the receiver was fixed at the azimuth angle of the strongest received power. The figure shows that at position NP1, the strongest received power was between 24° and 60° angles in azimuth for all bands when the Tx antenna was pointing to the direction indicated by two red dashed lines in Figure 5-12. The second strongest lobe occurred in the first two bands around the 144° angle and was stronger at the 13.4 GHz band than at the 26.8 GHz band, whereas it was very weak at the 62.6 GHz band. For the first two bands, the lobes were closer to zero and 180° angles when the receiver moved away, while for the 62.6 GHz band, there was only one lobe that was almost fixed around the 60° angle.

Table 5-8 presents the estimated values of the AoD in azimuth for the strongest lobe and their RMS angular spread within 10 dB from the maximum for all bands and at each measurement position. The table indicates that the AoD at position NP3 for the first two bands was closer to either the zero or 180° angles, which highlights the waveguide effect of this environment as mentioned earlier. The number of lobes at the first two bands was higher than that at the 62.6 GHz band at most of the positions.
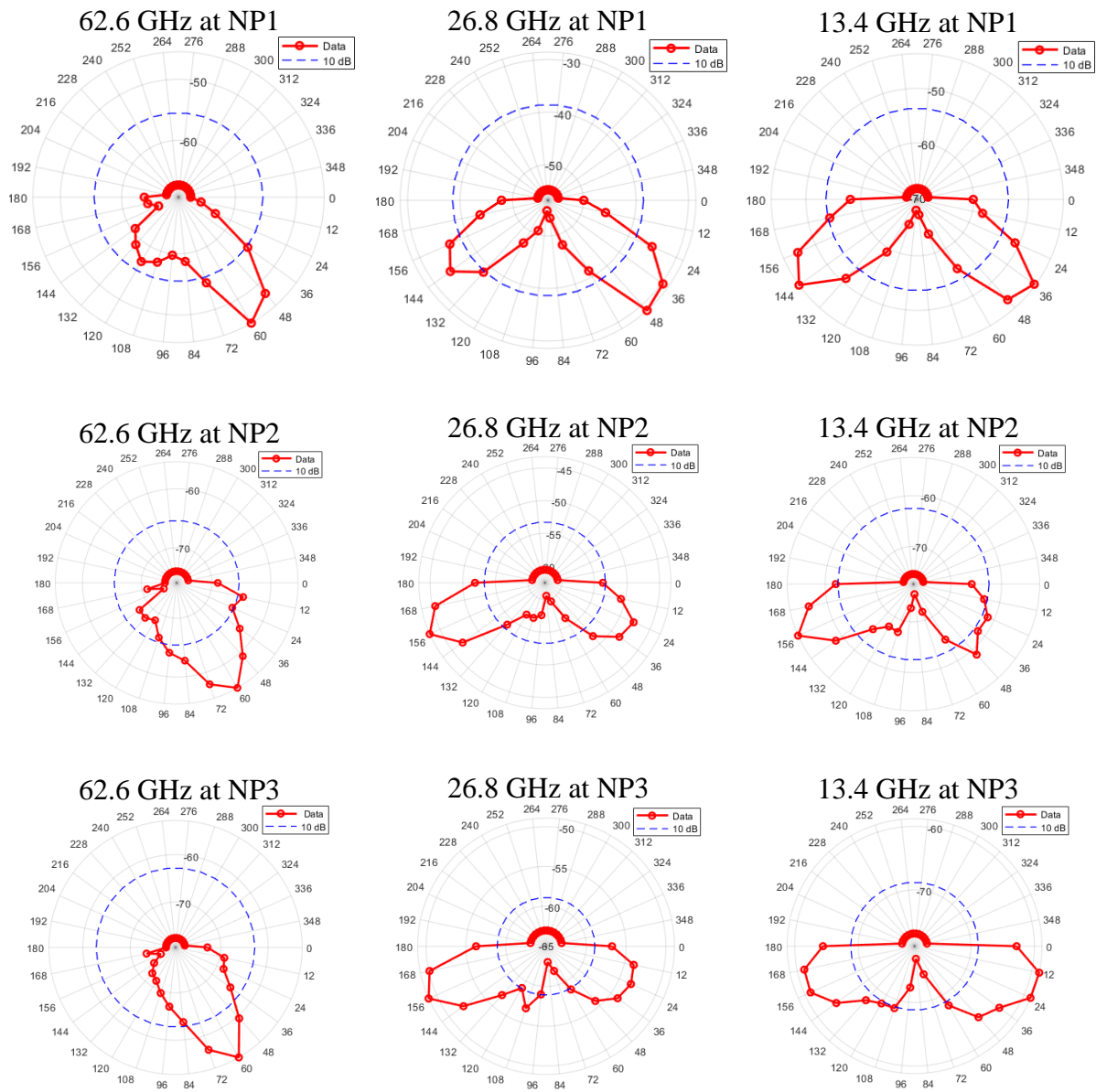
Figure 5-22 Polar plots of the received power vs Tx azimuth angles at 0º elevation angle for all positions and bands

Table 5-8 Estimated AoD in azimuth and RMS angular spread values

Centre frequency	Position No.	AoD	RMS angular spread	No. of lobes
13.4 GHz	NP1	38.99º	7.65º	2
	NP2	158.59º	9.09º	2
	NP3	19.38º	18.26º	2
26.8 GHz	NP1	40.67º	8.16º	2
	NP2	158.57º	9.93º	2
	NP3	157.58º	11.99º	3
62.6 GHz	NP1	55.72º	8.37º	1
	NP2	60.80º	12.23º	2
	NP3	61.31º	7.26º	1

5.3 Small office environment

Figure 5-23 shows the layout of the small office environment used for both the LoS and NLoS scenarios. For the LoS scenario, the receiver was fixed at positions P1, P2 and P3 during the measurements for each frequency band, as shown in the layout in figure 5-23. Furthermore, the transmitter antenna with the 3D positioner was fixed at location Tx1 at a height of 2.35 m from the ground, on top of a tripod to emulate the hotspot point. Using the 3D positioner, the antenna was tilted down at -9° (which is half of the antenna's 3 dB beam-width) to focus the transmitted beam onto the measurement area. Position P1 was about 6.5 metres away from Tx1 and there was about 3 metres separation distance between the measured positions. A detailed description of this environment was presented in Section 3.4 of Chapter 3. The whole procedure was repeated three times, once for each frequency band.
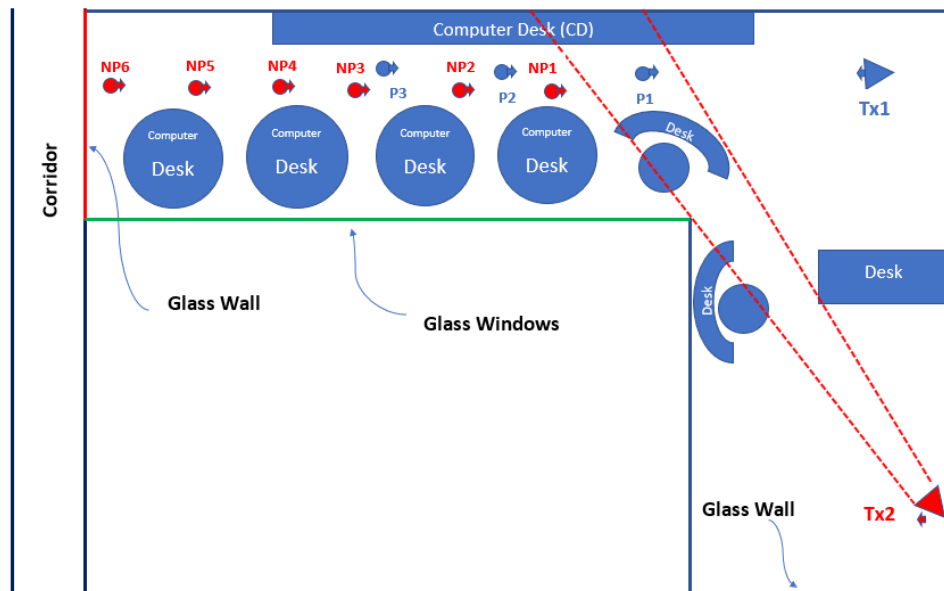
Figure 5-23 Small office layout

5.3.1 Line-of-sight (LoS) measurements

This section describes the measurements carried out in the small office environment and presents and discusses the results of the LoS measurements such as the AoA, AoD and their RMS angular spread at the three frequency bands used.

5.3.1.1   Angle of arrival (AoA)

For the AoA measurements, the transmitter was fixed pointing towards the receiver as shown in figure 5-23. The zero azimuth angles for the transmitter and receiver at each position are indicated by a small arrow in figure 5-23. The receiver was then rotated clockwise with a step size of 12° in azimuth for the first two bands and 9° for the last band to cover the full rotation for each elevation angle. Three different elevation angles were used with a step size of 15° starting from -15° to 15° for the first two bands, while five elevation angles were used with 9° step size starting from -18° to 18° for the last band.
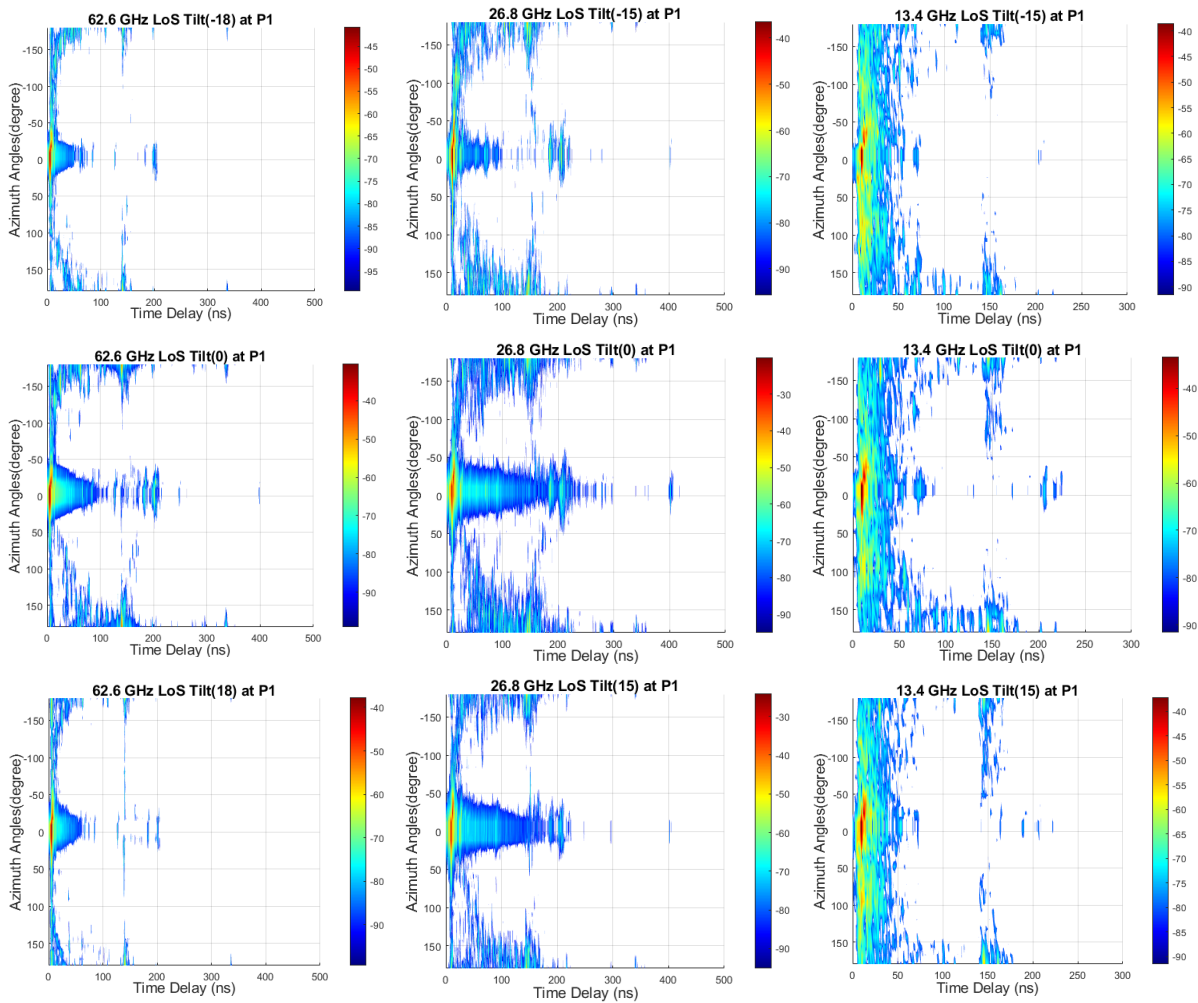
Figure 5-24 PDPs versus azimuth angles for three different elevation angles at position P1

Figure 5-24 presents the power delay profiles as a function of the azimuth rotation angles at three different elevation angles, with the receiver at position P1 for all measured bands. The figure shows strong signals around the zero degrees angle within 25 nanoseconds, which correspond to the line-of-sight angles where the antennas of the receiver and transmitter were

oriented towards each other. Other signals with a lower power level of the reflected waves at different time delays of up to about 400 nanoseconds were also detected between the -50° and +50° angles. There were also signals that appeared around the 180° angle at different time delays, which denote the reflected signals when the receiver was pointing towards the glass wall at the end of the measurement path, as shown in figure 5-23. Furthermore, one can also notice the existence of reflected signals at most azimuth angles around 150 nanoseconds (which might be due to the reflected signals from the glass wall), with most of the signals occurring between the azimuth angles of 100° and 260°.
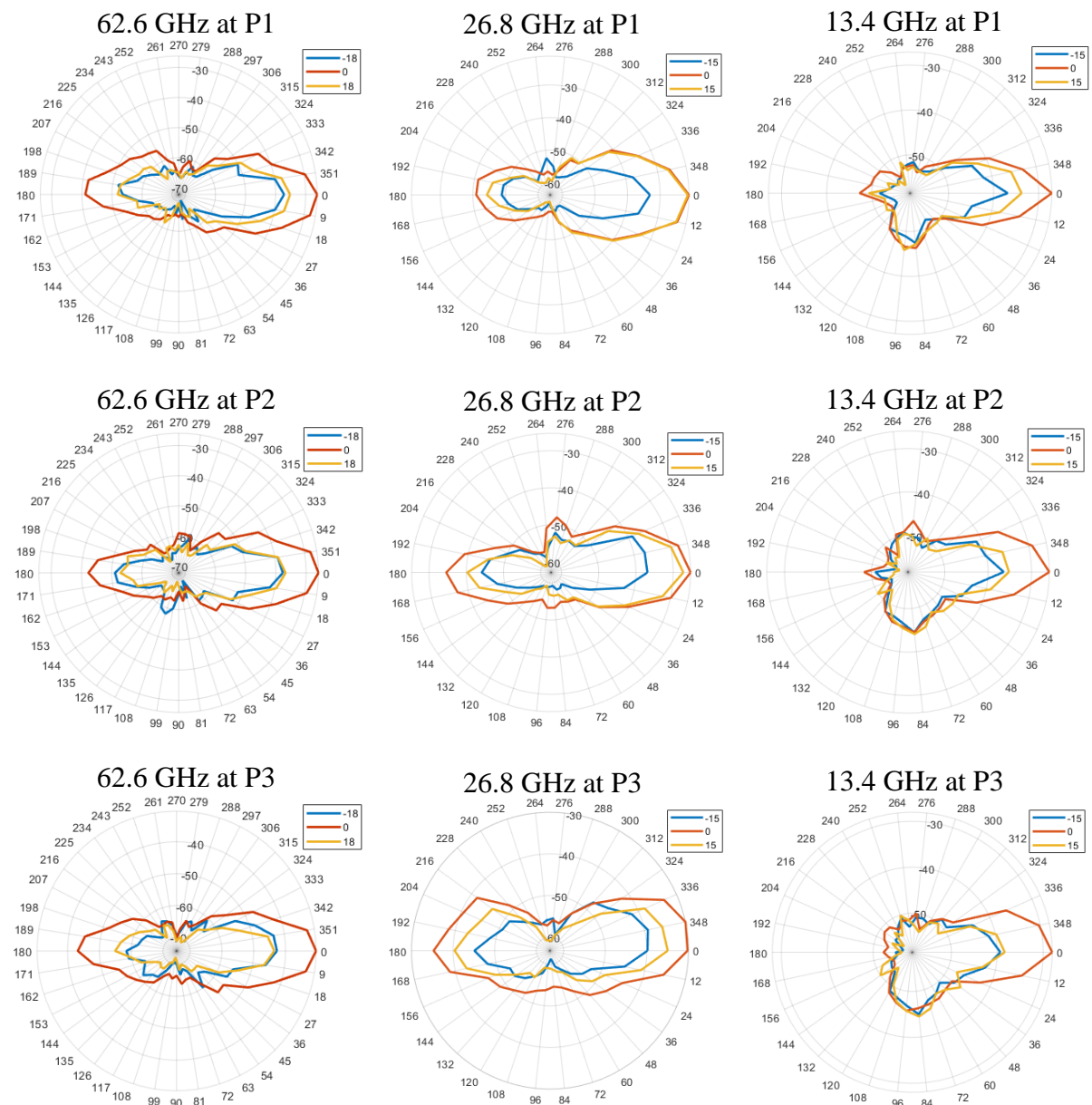
Figure 5-25 Polar plots of the received power versus azimuth angles at the strongest three elevation angles for all bands

Figure 5-25 shows a polar plot of the received power as a function of azimuth angles from 0° to 360° at three elevation angles. The figure demonstrates that the strongest received power for all bands and at all points was around the angle of zero degrees in azimuth and between $+15^o$ (or $+18^o$ for the 62.6 GHz band) and zero degrees elevation angles. The elevation angle of the strongest lobe became closer to the zero degrees and the power level of this lobe decreased for all bands as the distance between the transmitter and receiver increased. There was also another lobe around the 180° angle in azimuth for the last two bands, and the power level of this lobe increased as the receiver moved away from the transmitter and became closer to the glass wall, as shown in figure 5-23. For the 13.4 GHz band, the back lobe at the 180° angle was very weak, which might be due to the ability of this frequency band to penetrate through the glass wall being higher than that of the other two bands. For the 26.8 GHz band, the received power at the negative elevation angle was very low compared to the zero and positive elevation angles, while for the other two bands, the received power at the positive and negative elevation angles were close to each other, as shown in figure 5-25.

Figure 5-26 shows the 3D images of the AoA in azimuth and elevation within 10 dB from the maximum at three positions and for all measured bands. The images show that at all measured positions, the strongest AoA in azimuth was around the zero degrees angle for all three bands. For the elevation angle, the strongest AoA at position P1 for the first two bands was close to zero degrees angle, while it was around 5° for the 62.6 GHz band, and became closer to the zero elevation angle for all bands when the receiver was at positions P2 and P3, as shown in figure 5-26. Furthermore, a second lobe at the 180° azimuth angle can be seen only for the 26.8 GHz band at position P3. The back lobe at 180° occurred between the 0° and $+15^o$ angles in elevation. Table 5-9 presents the estimated values of the AoA in azimuth and elevation for the strongest lobe and their RMS angular spread for all bands and at each measurement position. The table shows a decrease in the elevation angle of the best AoA as the Tx-Rx separation distance increased, except for the 26.8 GHz band at position P2, where the elevation angle had the highest value at this band. In addition, the RMS azimuth angular spread at position P3 was the highest for all bands.
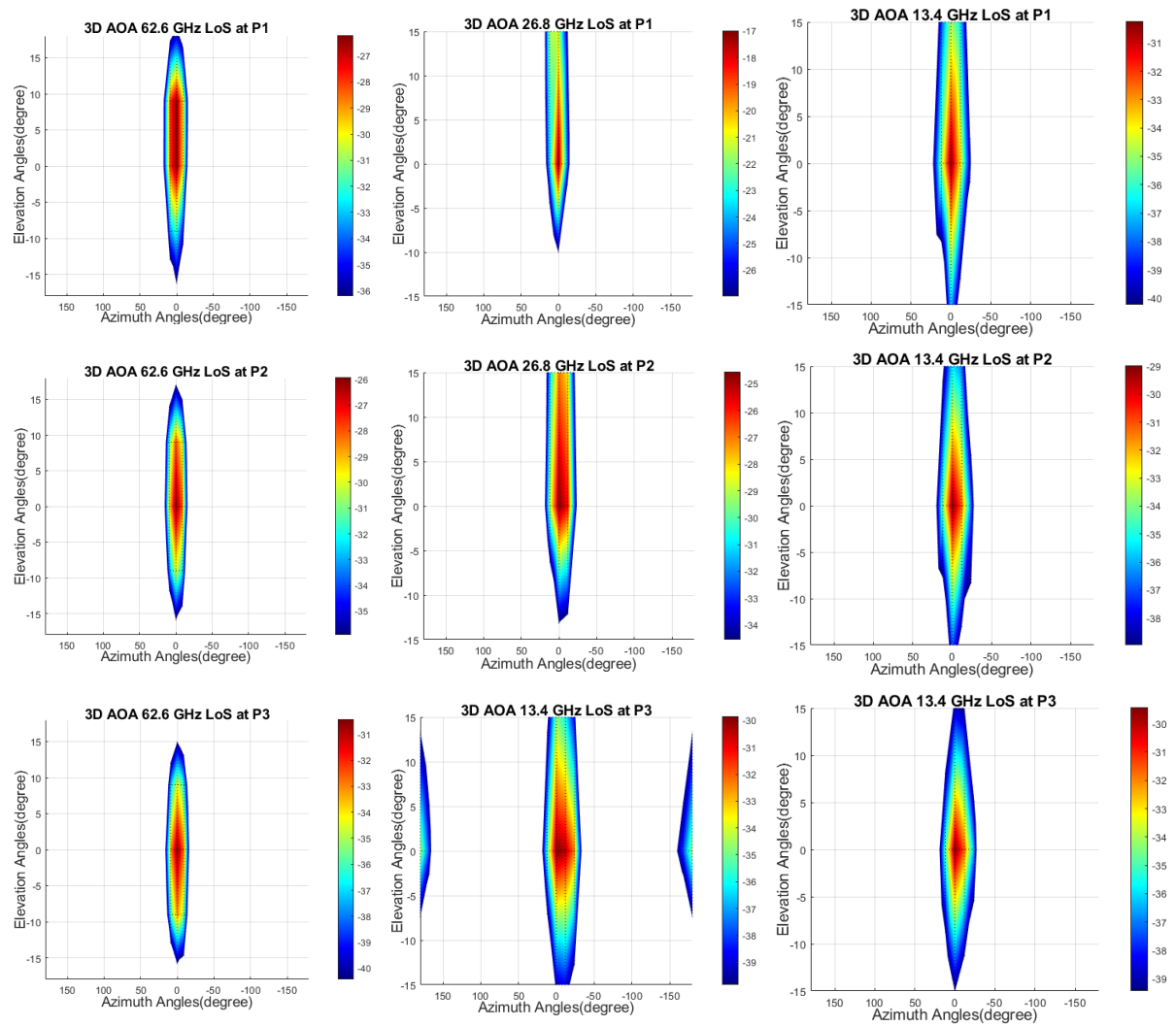
Figure 5-26 3D AoA images for the LoS scenario at three measurement positions and all bands

Table 5-9 Estimated AoA in azimuth and elevation and RMS angular spread values

Centre frequency	Position No.	3D Azi. AoA	RMS azimuth angular spread	3D Ele. AoA	RMS elevation angular spread	No. of lobes
13.4 GHz	P1	357.93º	9.44º	1.32º	8.92º	1
	P2	356.19º	9.82º	0.72º	7.97º	1
	P3	356.00º	9.89º	0.21º	6.36º	1
26.8 GHz	P1	1.29º	6.34º	4.17º	6.72º	1
	P2	357.82º	8.42º	5.46º	7.22º	1
	P3	352.34º	11.09º	1.36º	8.07º	2
62.6 GHz	P1	0.89º	6.45º	2.90º	6.06º	1
	P2	359.33º	6.43º	1.05º	6.33º	1
	P3	359.76º	6.52º	- 0.61º	6.25º	1

5.3.1.2   Angle of departure (AoD)

For the AoD measurements, the received power was measured at each angle to find the strongest received signal, and the angle of this signal was then selected as a fixed direction at the receiver to measure the AoD. While the receiver was pointing to that angle, the transmitter was then rotated direction from 0° to 360° in azimuth with a step size of 12° in azimuth for the first two bands and 9° for last band to cover the full rotation. The data were then recorded at the receiver side for each Tx angle.
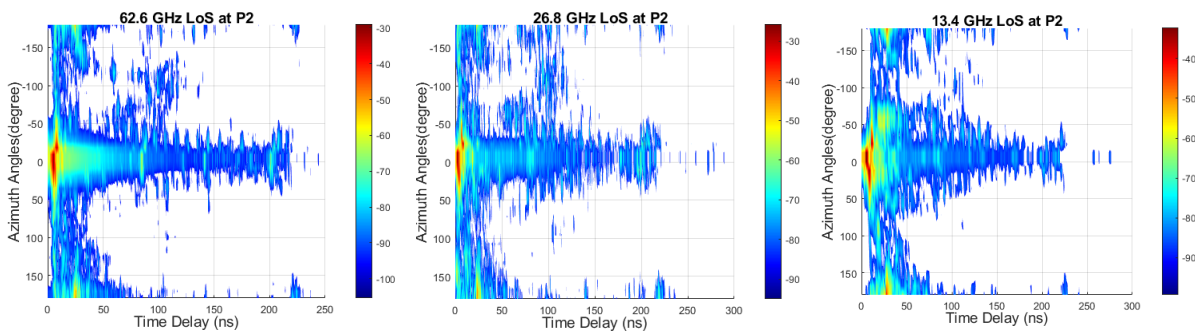
Figure 5-27 PDPs as a function of azimuth angles at -9° elevation angle and position P2 for all bands

Figure 5-27 presents the PDPs for all measured bands as a function of the Tx azimuth rotation angles at a -9° elevation angle at the transmitter, with the receiver pointing to the zero degrees angle (the angle of the strongest received power) at position P2. The figure shows a strong signal around the angle of zero degrees within 25 nanoseconds, which corresponds to the line-of-sight angles where the antennas of the receiver and transmitter were oriented towards each other. Other signals with a lower power level of the reflected signals and at different time delays of up to about 250 nanoseconds were also detected between the -50° and +50° angles. Furthermore, there were also signals that appeared around the 180° angle at different time delays, which denote the reflected signals when the transmitter was pointing to the wall behind Tx1 (the transmitter was about 2.7 metres away from the wall). It is also noticeable that there were more signals reflected at azimuth angles between -50° and -150°, when the Tx1 antenna was pointing to the open area at the left-hand side of the Tx1, than there were at between +50° and +150°, when the Tx1 antenna was pointing to the wall at the right hand side of Tx1, as shown in figure 5-23.

Figure 5-28 depicts the polar plots of the received power as a function the Tx1 azimuth angles from 0° to 360° (with step size of 12° for the first two bands and 9° for the third band) for each

band at position P2 with a 10 dB threshold from the maximum received power. The figure shows that the strongest received power for all bands was around the zero degrees angle in azimuth, which represents the case where the line-of-sight when the Tx and Rx antennas were oriented towards each other. On the other hand, the second strongest lobe was around the 180º angle, representing the case where the Tx1 antenna was pointing to the wall behind Tx1. It is also noticeable that the beam width of the strongest lobe at the zero degrees azimuth angle decreased as the frequency band increased.
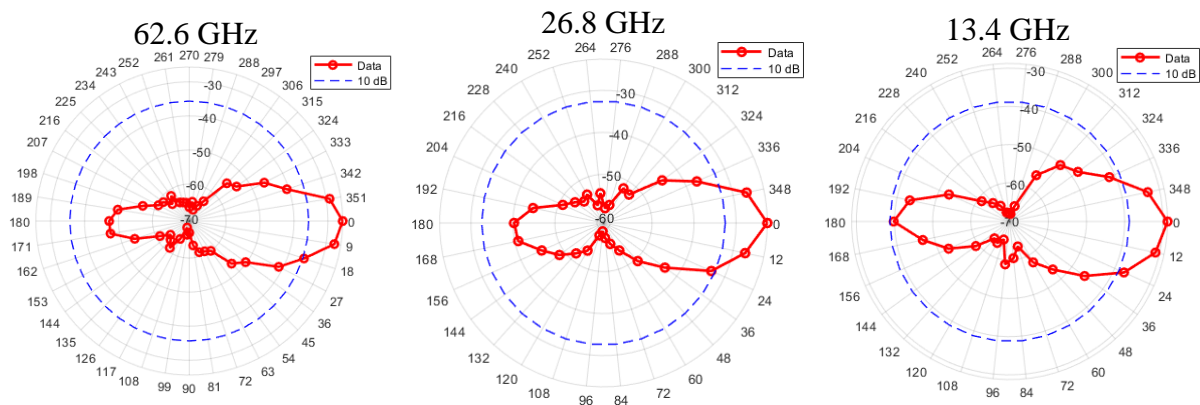
Figure 5-28 Polar plots of the received power vs Tx azimuth angles at -9º elevation angle and P2

Table 5-10 presents the estimated values of the AoD in azimuth for the strongest lobe and their RMS angular spread within 10 dB from the maximum, for all bands and measurement positions. The table indicates that, for the 13.4 GHz and 62.6 GHz bands, the value of the RMS angular spread at position P2 was the highest compared with the other positions, while for the 26.8 GHz band, the value of the RMS angular spread was the lowest at position P2.

Table 5-10 Estimated AoD in azimuth and RMS angular spread values

Centre frequency	Position No.	AoD	RMS angular spread	No. of lobes
13.4 GHz	P1	359.79º	7.25º	1
	P2	1.37º	8.26º	1
	P3	0.95º	8.06º	1
26.8 GHz	P1	1.63º	8.24º	1
	P2	359.79º	7.81º	1
	P3	2.67º	8.55º	1
62.6 GHz	P1	0.34º	6.44º	1
	P2	1.61º	7.32º	1
	P3	1.83º	7.13º	1

5.3.2 Non-line-of-sight (NLoS) measurements

This section presents the results and discussion of the NLoS measurements and provides a detailed description of the measurements in the small office environment, such as the AoA, AoD and their RMS angular spread for the three frequency bands.

5.3.2.1   Angle of arrival (AoA)

For the AoA measurements, the transmitter was fixed at location Tx2 pointing towards the wall (to illuminate the area between the two red dashed lines in figure 5-23) with a 56° angle, which was calculated to cover the measurement area for NLoS measurements at positions NP1, NP2 and NP3, as shown in figure 5-23. The zero azimuth angles for the transmitter and receiver at each point are indicated by a small arrow in the layout in figure 5-23. The receiver was then rotated clockwise with a step size of 12° in azimuth for all bands to cover the full rotation for each elevation angle. Three different elevation angles were used for all bands, with a step size of 15° and starting from -15° to 15°.

Figure 5-29 presents the power delay profiles as a function of the azimuth rotation angles at the zero degrees elevation angle for all receiver positions and all measured bands tested. The figure shows strong multipath signals between the -40° and -120° angles with the same time delay for all bands at positions NP1 and NP2, which correspond to the first order reflected multipath signals from the wall. Other multipath signals with a lower power level were detected between the 40° and 120° angles for all bands and were stronger for the 62.6 GHz band than the other two bands at position NP2. These represent the multipath components reflected from the windows at the right-hand side of NPs (second order reflections). It is also noticeable that starting from position NP3, the strong signals moved towards the zero degrees angle, and the number of reflections increased as the receiver moved away from the transmitter, as shown in figure 5-29.
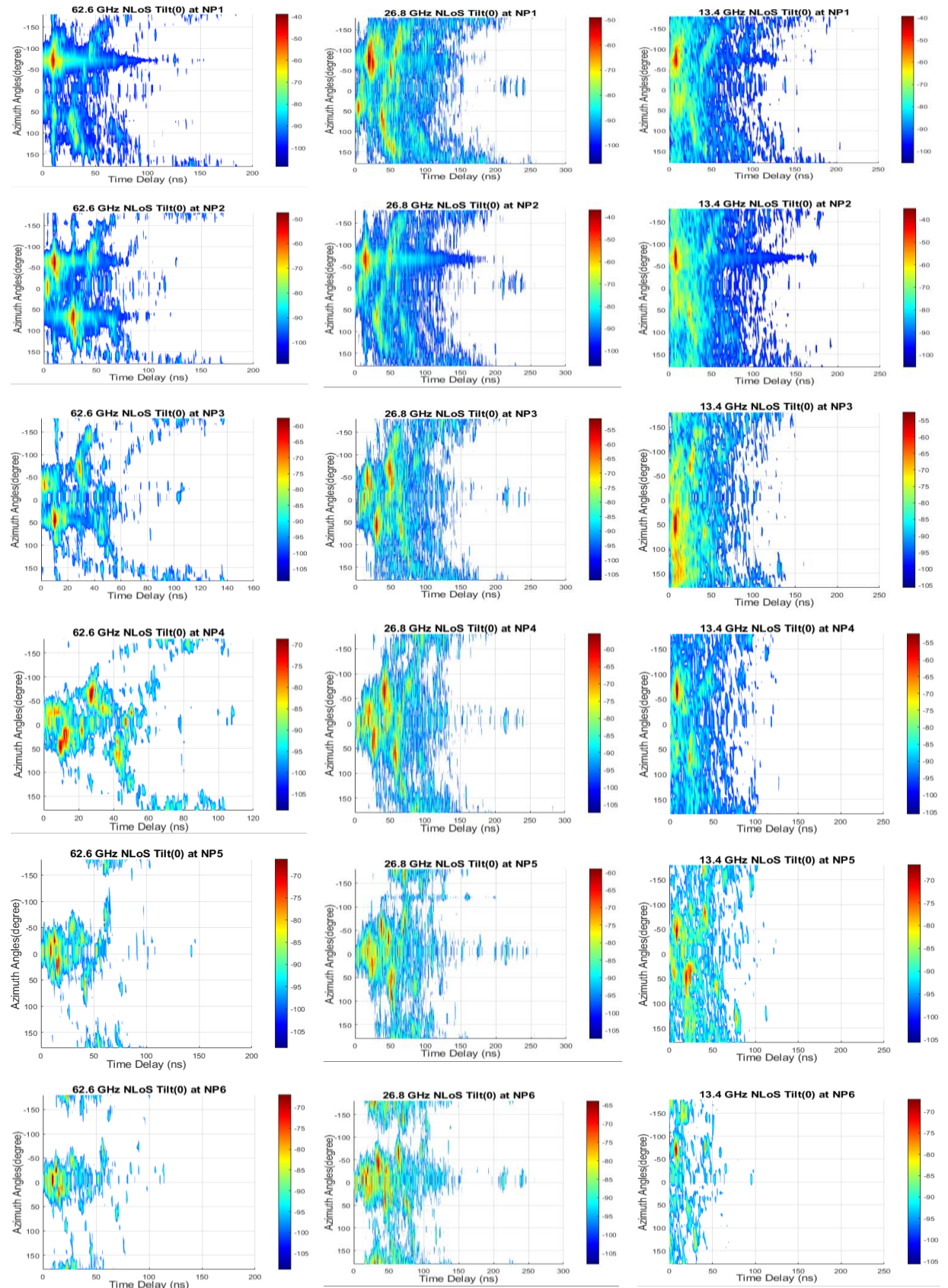
Figure 5-29 PDPs as a function of azimuth angles at zero elevation for all measured bands and all positions

Figure 5-30 shows polar plots of the received power as a function of azimuth angles from 0° to 360° at three elevation angles for the NLoS scenario. The figure shows that the strongest signals for all bands at positions NP1 and NP2 was around the 300° angle in azimuth, and there was another lobe with a lower power level around 48°. At position NP3, the strongest signals switched to the other side (around the angle of 48°) for all bands, and the received power in the lobe around the 300° angle decreased slightly. Then, starting from position NP4, the two lobes combined together to make a wide beam around the zero degrees angle, and another lobe around the 180° angle occurred (as shown in figure 5-30), which might be because the scenario emulated a wide corridor environment. It is also noticeable that the strongest received power for most of the lobes was at the zero degrees elevation angle for all bands and at all positions, which could be due to the low height of the ceiling in this scenario, and consequently, the low Tx antenna height.
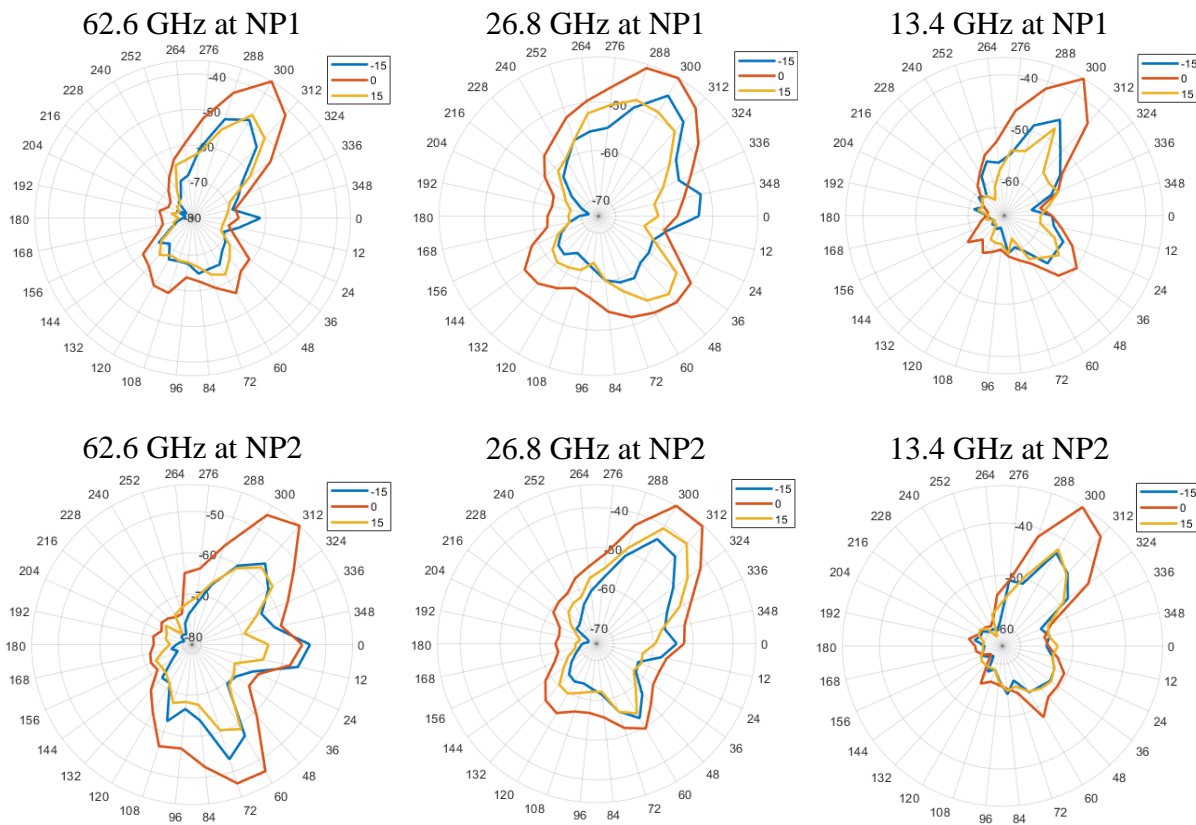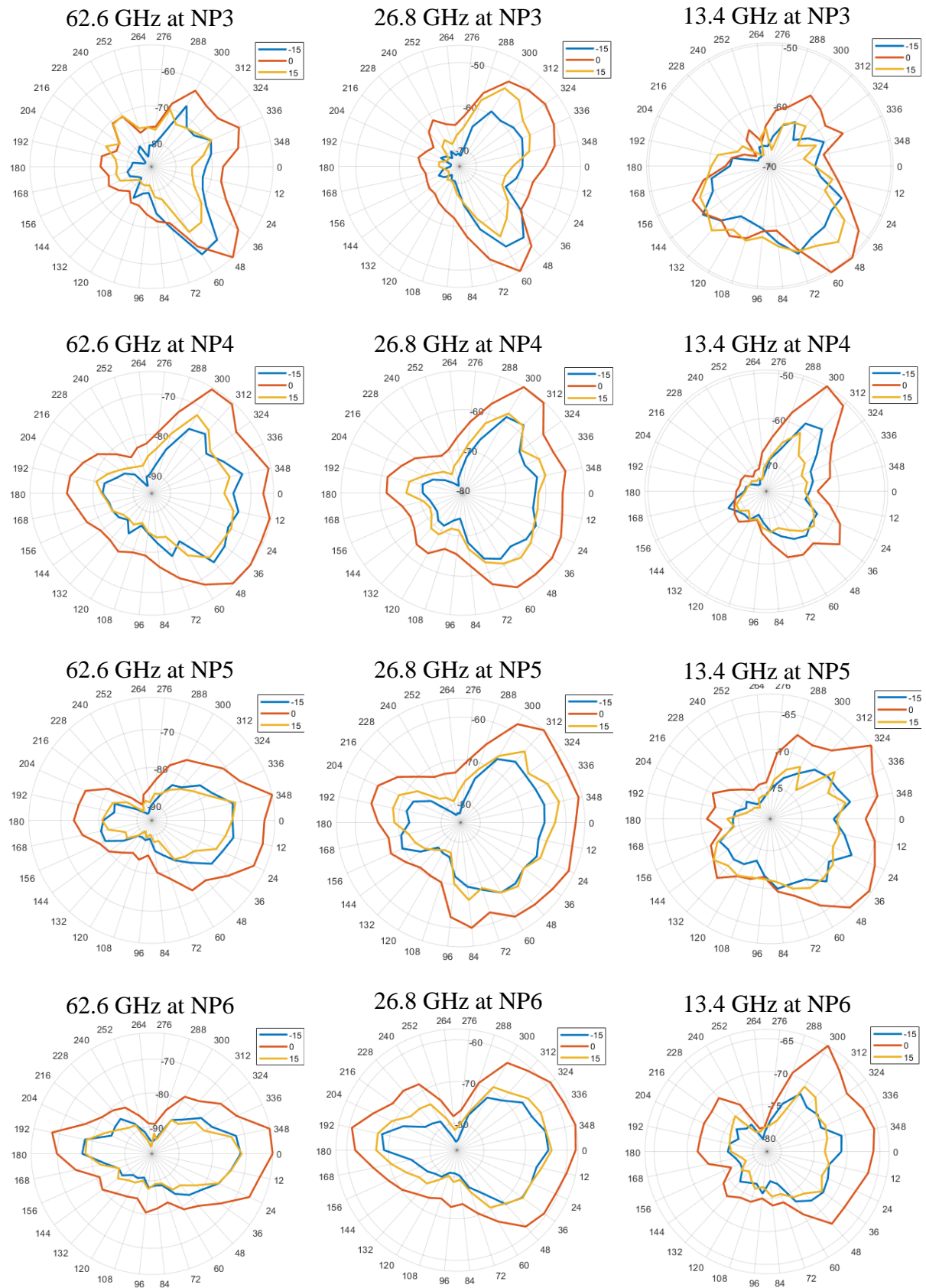
Figure 5-30 Polar plots of the received power versus azimuth angles at the strongest three elevation angles for all bands
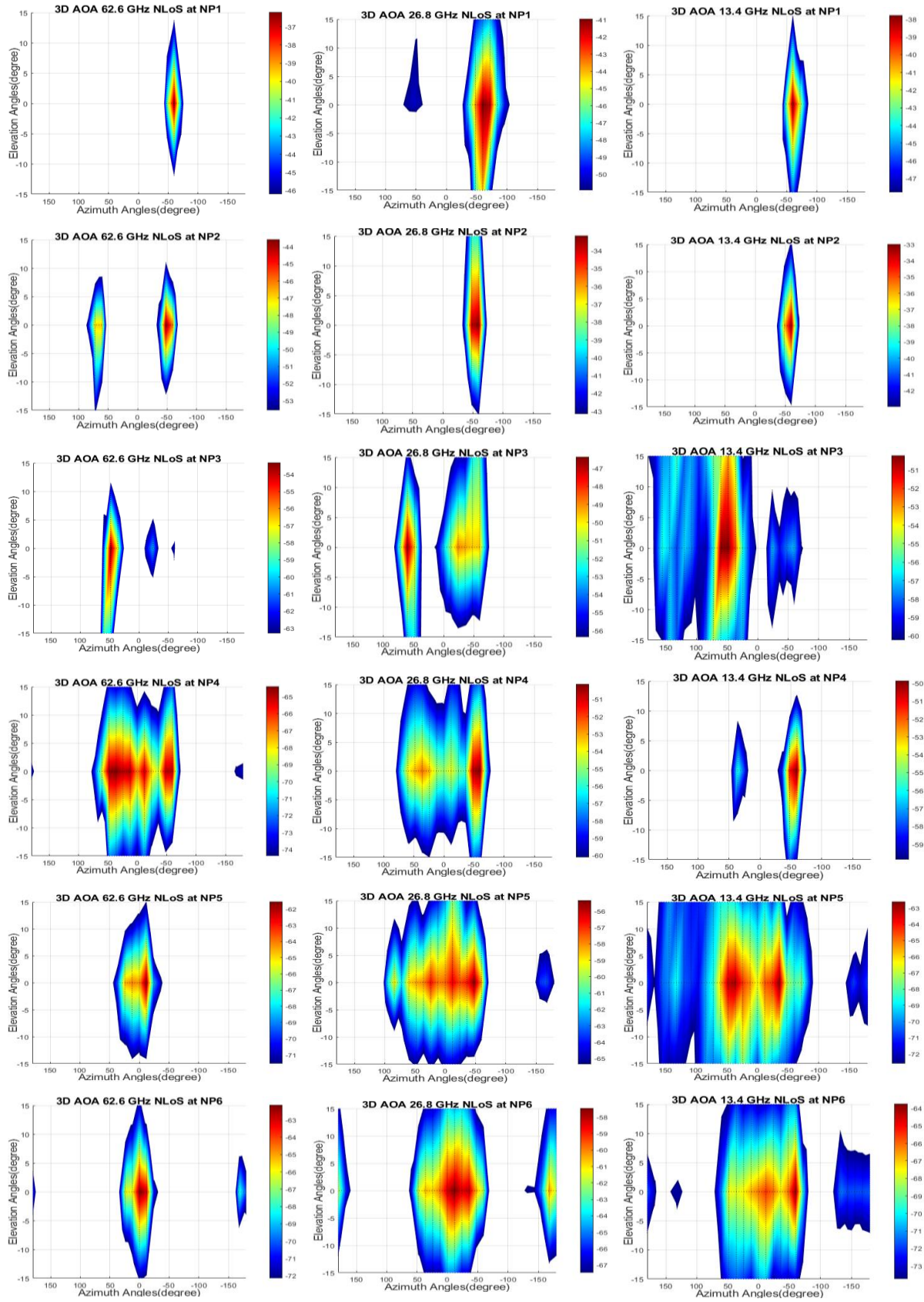
Figure 5-31 3D AoA images for the NLoS scenario at three measurement positions and for all bands

Figure 5-31 shows the 3D AoA images in azimuth and elevation within 10 dB from the maximum at six positions for all measured bands. The images show that at positions NP1 and NP2, the strongest AoA in azimuth was around -60o angle for all three bands, whereas the second strongest lobe was around the 60o angle shown in some bands. At position NP3, the second lobe at the 60o angle became stronger than that at -60o at all bands and more lobes started to appear. Starting from position NP4, the lobes moved from the positive and negative sides toward zero degrees as the distances between the Tx and Rx increased to create one wide lobe around the zero degrees angle at position NP5. At position NP6, the lobe became more focused and its width narrowed as the frequency band increased, while another lobe appeared around the 180o angle at all bands. In terms of the elevation angles, the strongest AoA was around the zero degrees angle at all positions and for all bands, which might be due to the low ceiling height, and accordingly, the low Tx antenna height, at the measurements area.

Table 5-11 Estimated AoA in azimuth and elevation and RMS angular spread values

Centre frequency	Position No.	3D Azi. AoA	RMS azimuth angular spread	3D Ele. AoA	RMS elevation angular spread	No. of lobes
13.4 GHz	NP1	297.52º	9.25º	- 0.85º	6.96º	1
	NP2	302.29º	6.89º	1.52º	4.53º	1
	NP3	51.05º	17.69º	1.15º	9.03º	2
	NP4	305.49º	8.71º	- 2.19º	5.29º	2
	NP5	6.69º	44.29º	- 1.16º	11.42º	2
	NP6	347.39º	37.62º	- 1.10º	8.44º	3
26.8 GHz	NP1	297.57º	14.41º	- 2.89º	9.02º	2
	NP2	305.92º	8.52º	1.69º	7.52º	1
	NP3	58.43º	7.88º	- 1.12º	7.72º	2
	NP4	353.86º	44.56º	0.57º	7.19º	1
	NP5	2.06º	44.44º	3.49º	8.90º	2
	NP6	352.70º	30.95º	0.48º	8.15º	2
62.6 GHz	NP1	300.84º	6.74º	0.00º	0.00º	1
	NP2	309.07º	7.14º	0.00º	0.00º	2
	NP3	47.89º	6.89º	- 3.20º	6.15º	3
	NP4	2.49º	39.36º	- 1.11º	7.27º	2
	NP5	0.77º	18.07º	0.54º	7.54º	1
	NP6	0.43º	13.28º	0.18º	6.50º	2

Table 5-11 presents the estimated AoA values in azimuth and elevation for the lobe of the strongest received power and their RMS angular spread within 10 dB from the maximum for all bands and measurement positions in the NLoS scenario. The table shows that the elevation angle of the strongest lobe was within 3.5° from the zero degrees elevation angle in all bands, which is much lower than the antennas 3 dB half power beam width. It is also noticeable that most of the elevation angles at the 13.4 GHz and 62.6 GHz bands were either zero or negative, which shows that the reflected signals from the ground were stronger than those from the ceiling at most positions for these two bands.
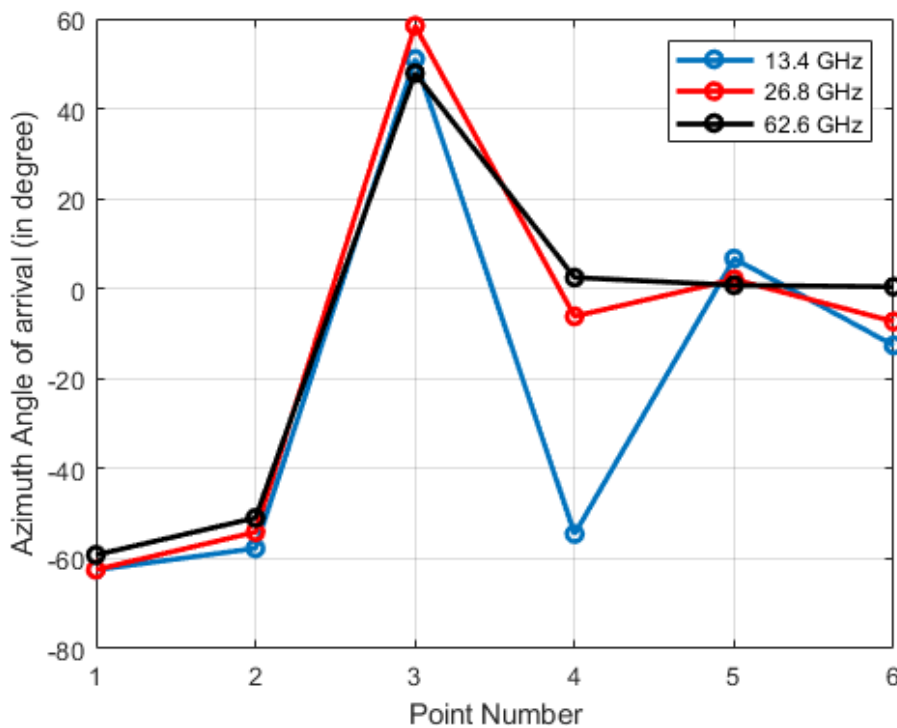
Figure 5-32 Azimuth angles versus position number

Figure 5-32 shows the similarity in azimuth AoA angles versus positions plots for all bands at most positions, a switch from negative to positive angles was shown for all bands around the zero degrees angle at position NP3. At position NP4, the 13.4 GHz band switched back to the negative angles side close to the 60° angle, while the last two bands remained around the zero angle. At positions NP5 and NP6, all the bands were close to the zero azimuth angle.

Figure 5-33 shows the elevation AoA for all bands as a function of measurement position. The figure shows that the elevation angle of arrival was positive at most of the positions for the 26.8 GHz band, was negative for the 13.4 GHz band, and was close to or equal to the zero elevation

angle for the 62.6 GHz band in most of the positions. In general, the 26.8 GHz and 62.6 GHz bands followed the same trend at most positions. At position NP6, the elevation angle became close to zero degrees angle for all bands.
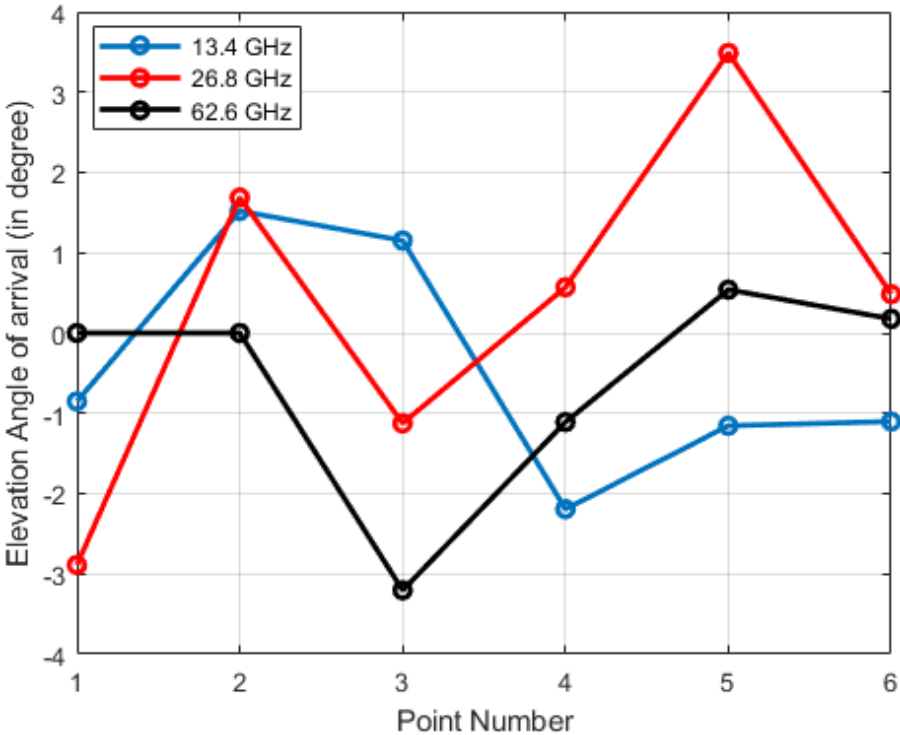
Figure 5-33 Elevation angles versus position number

Figure 5-34 shows the cumulative distribution function (CDF) for the RMS AOA azimuth angular spread for all measured frequency bands. The figure indicates that the 26.8 GHz band had the largest angular spread values, while the 62.6 GHz band had the lowest values at most CDF values. Table 5-12 presents the recommended RMS CDF angular spread values in the indoor environments, where the 10% and 50% and 90% values of the CDF are presented for all measured frequency bands. The table shows that the largest and smallest values of the CDF of the RMS AoA azimuth angular spread at all recommended values occurred at the 26.8 GHz band and 62.6 GHz band, respectively.
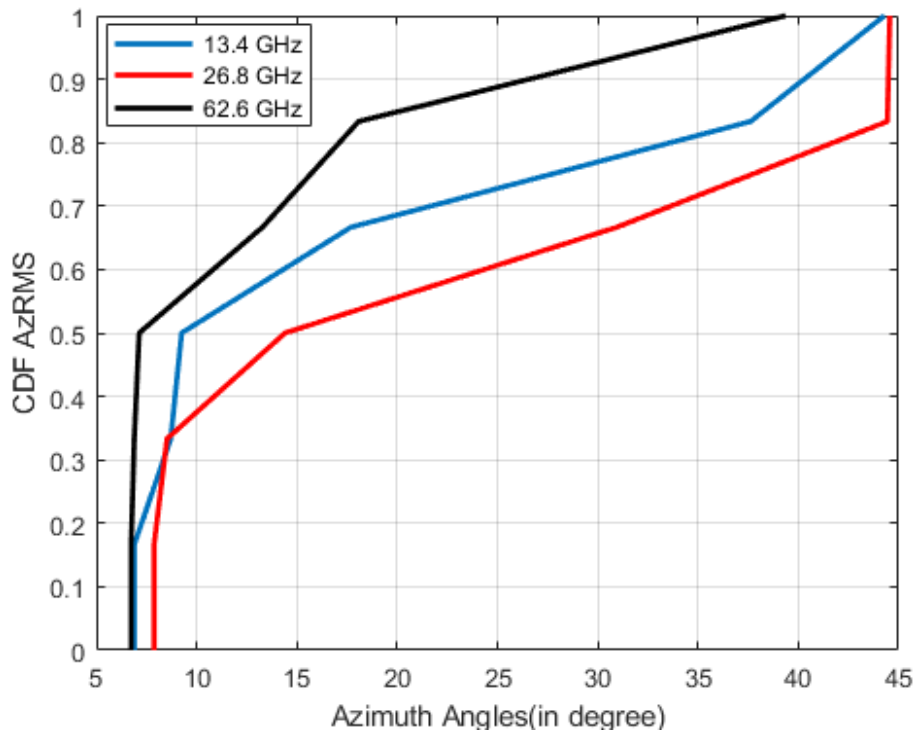
Figure 5-34 CDF of RMS AoA azimuth angular spread for all measured frequency bands

Table 5-12 Values of the RMS AoA azimuth angular spread

CDF	13.4 GHz	26.8 GHz	62.6 GHz
10%	6.89	7.88	6.74
50%	9.25	14.41	7.14
90%	40.29	44.49	26.59
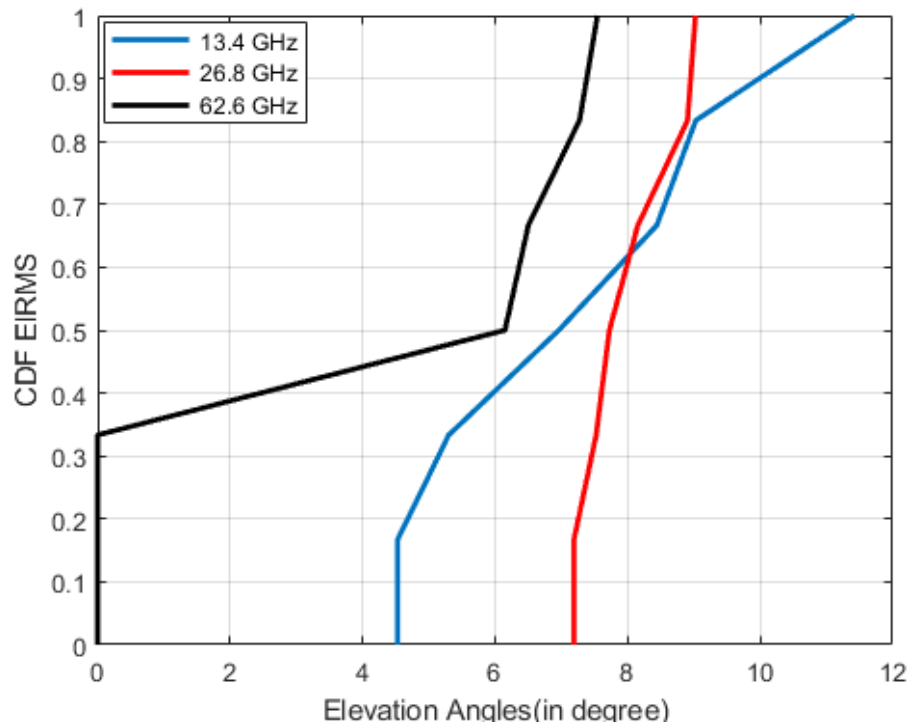
Figure 5-35 CDF of the RMS AoA elevation angular spread for all measured frequency bands

Figure 5-35 shows the CDF for the RMS AOA elevation angular spread for all of measured frequency bands. The figure shows that the CDF of the RMS elevation angular spread of the 62.6 GHz band had the lowest CDF values compared to the other two bands. Table 5-13 presents the CDF values of the RMS elevation angular spread in the indoor environments. The 26.8 GHz band had the largest CDF value at 10% and at the median, while the largest CDF value at 90% was at the 13.4 GHz band. On the other hand, the smallest of all the CDF values occurred at the 62.6 GHz band. The table shows a decrease in the CDF values of the RMS AoA elevation angular spread at 90% as the frequency increased.

Table 5-13 Values of the RMS AoA elevation angular spread

CDF	13.4 GHz	26.8 GHz	62.6 GHz
10%	4.53	7.19	0.00
50%	6.96	7.72	6.15
90%	9.99	8.95	7.38

5.3.2.2 Angle of departure (AoD)

For the AoD measurements, the procedure used in Section 5.1.1.2 was repeated to find the best receiving angle, and the selected angle was chosen according to the best receiving power at each position in azimuth and at the zero degrees angle in elevation for all positions.

Figure 5-36 presents the PDPs as a function of the Tx azimuth rotation angles from -90° to $+90^o$ in clockwise direction (the zero direction of Tx is indicated by the small red arrow in figure 5-23). The transmitter was close to the wall to emulate the hotspot situation with a 0° elevation angle at the transmitter. Furthermore, the receiver was pointing to the azimuth angle of the strongest received power at all positions and for all measured bands. The figure shows that the strongest signals at position NP1 came from the azimuth direction between the $+20^o$ and $+90^o$ angles at the same time delays for all bands, which corresponds to the signals when the antenna of the transmitter was oriented towards the area between the two red dashed lines shown in figure 5-23. Several reflection orders of signals at different transmission angles in the positive direction were detected as the receiver moved away from the transmitter. There were also other signals with a lower power level between the -40° and -90° angles at most of the measured positions for all bands, which corresponded to the reflected signals when the transmitter antenna was oriented towards the glass wall next to Tx2, as shown in figure 5-23.
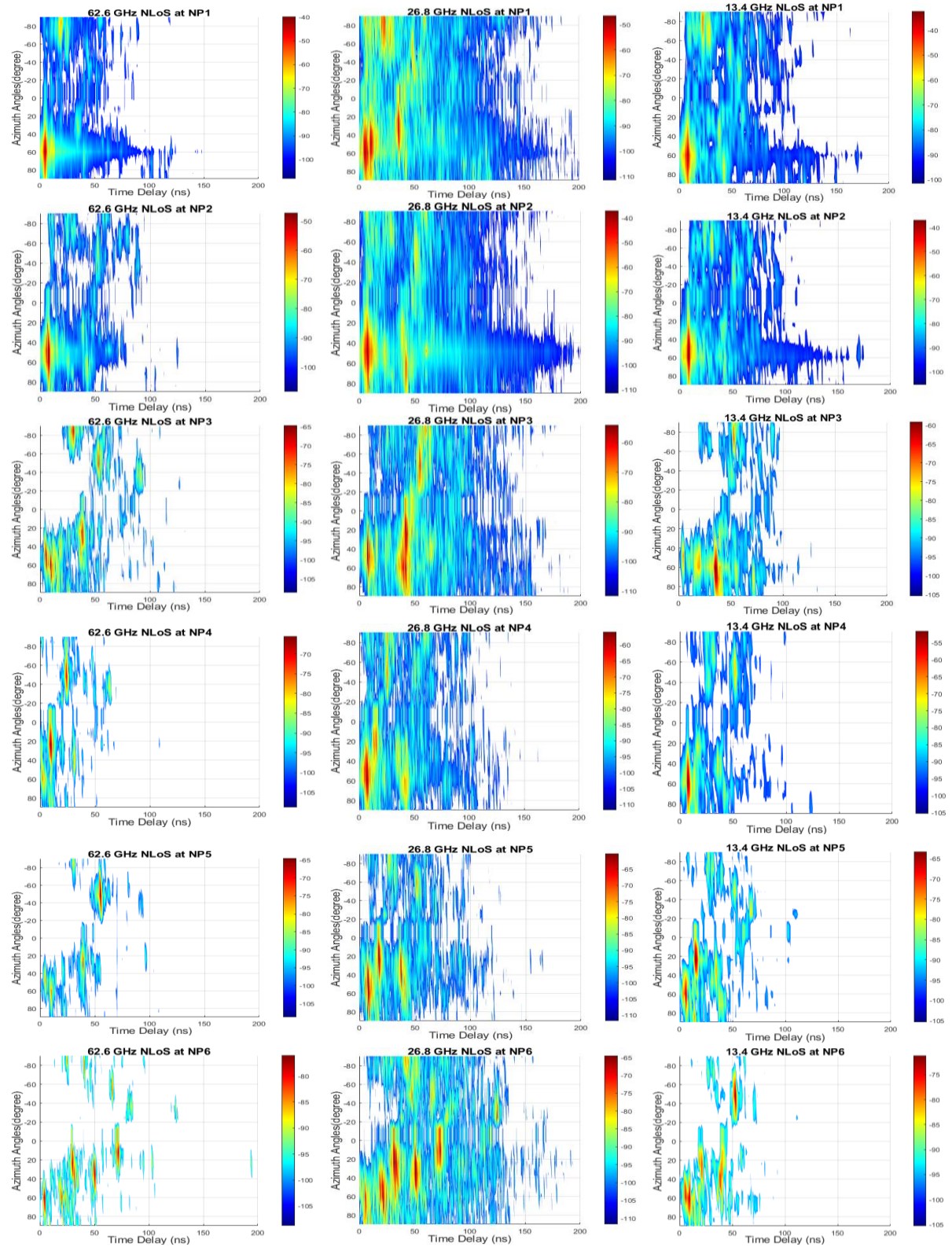
Figure 5-36 Tx PDPs as a function of azimuth angles at 0º elevation angle and for all positions and bands

Figure 5-37 depicts polar plots of the received power against the Tx azimuth angles from -90º to +90º with step size of 12º for the three bands, with a 10 dB threshold from the maximum power when the receiver was fixed at the azimuth angle of the strongest received power. The figure shows that at positions NP1 and NP2, the strongest received power was around the 60º angle in azimuth for all bands when the Tx antenna was pointing to the direction indicated by two red dashed lines in figure 5-23. In addition, another lobe with a low power level can be seen in the figure around the 288º angle. At position NP3, the lobes became wider for the strongest lobe. At position NP4, the strongest lobe was around the 60º angle for the first two bands, and around the 24º angle at the 62.6 GHz band, and there was another lobe around the 324º angle. At position NP5, the strongest lobe was between the 24º and 60º angles for the first two bands, while it switched to the 324º angle for the 62.6 GHz band. Finally, at position NP6, the strongest lobe was between the 24º and 60º angles for all bands, where the reflection order at this position reached up to five reflections, as shown in Figure 5-36.
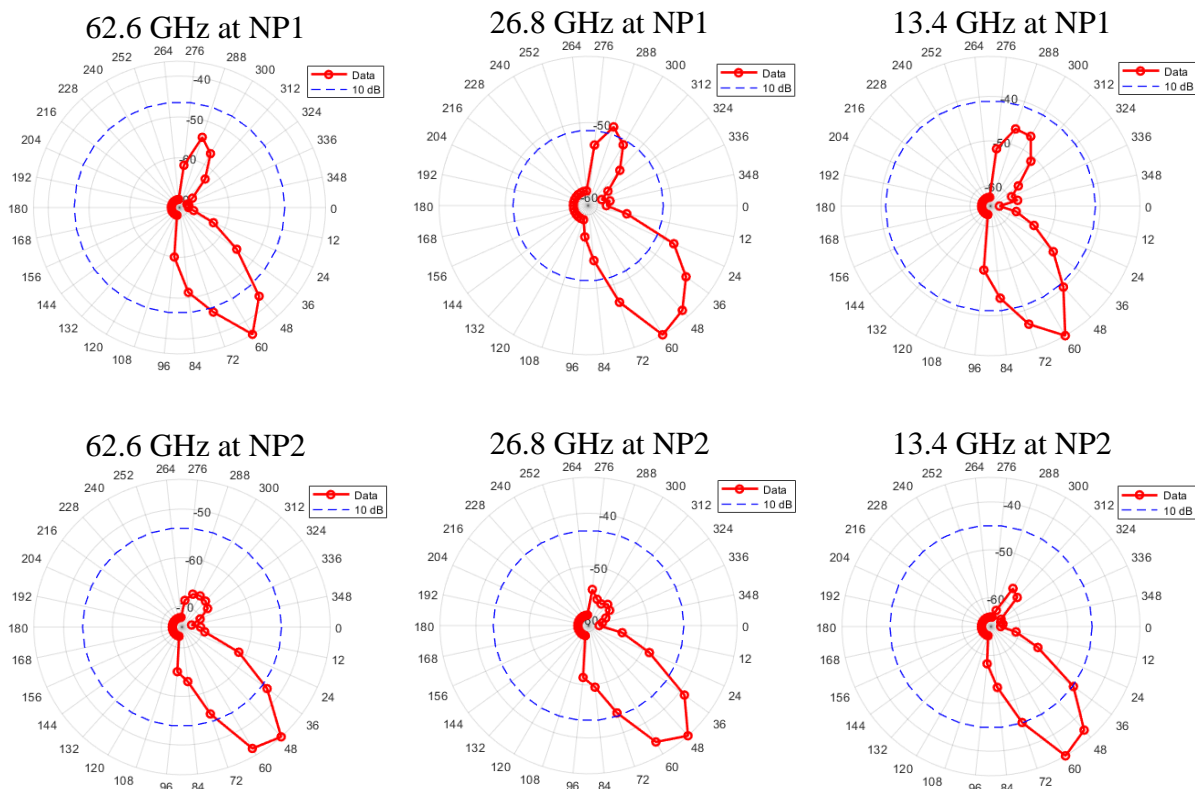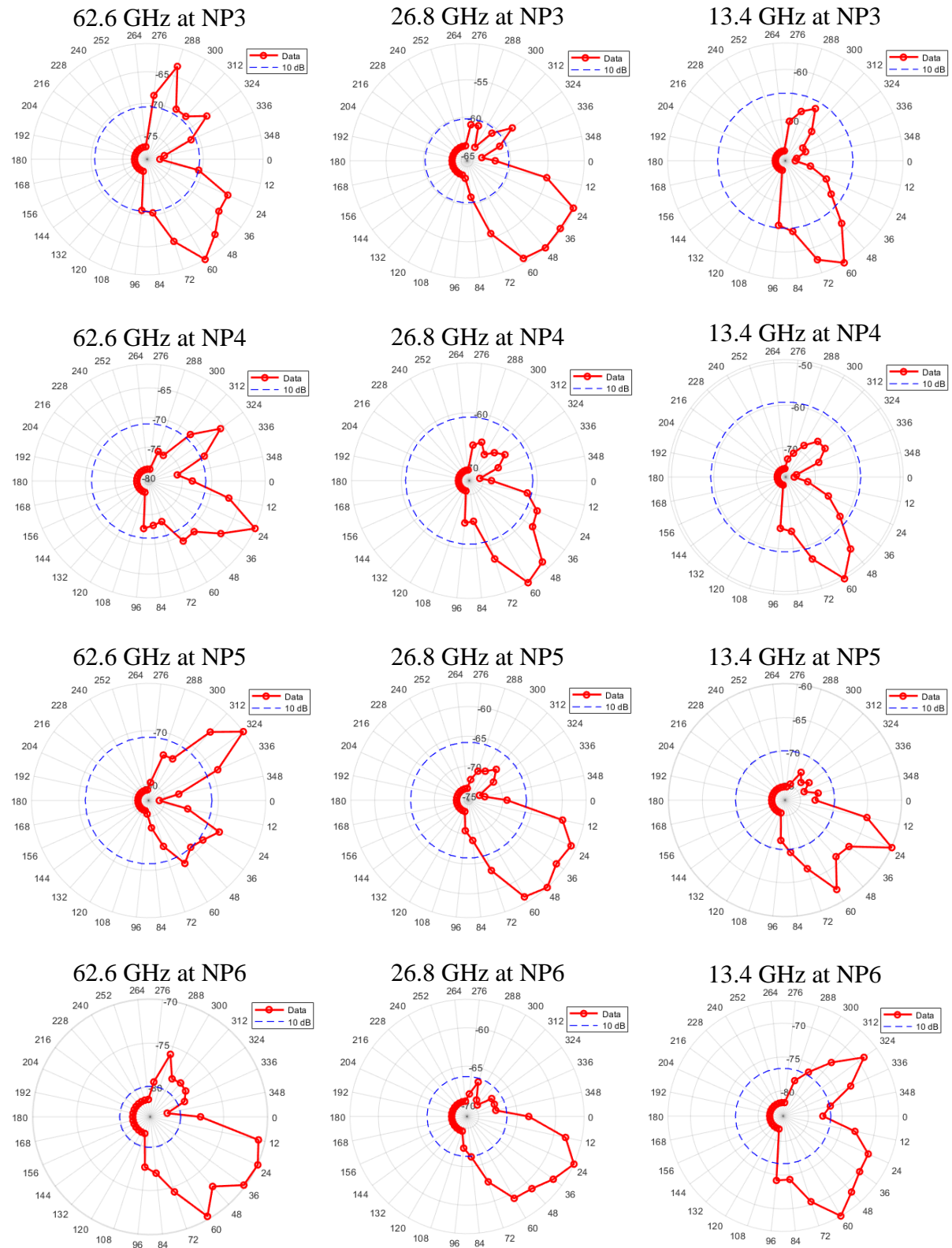
Figure 5-37 Polar plots of the received power vs Tx azimuth angles at 0º elevation angle for all bands and positions

Table 5-14 presents the estimated values of the AoD in azimuth for the strongest lobe and their RMS angular spread within 10 dB from the maximum for all bands and measurement positions. The table shows that the AoD at most of the positions was within the same direction indicated by the two red dashed lines in figure 5-23. However, at position NP5, the strongest transmission lobe for the 62.6 GHz band was around the -37.38° angle at a time delay of about 55 nanoseconds when the Tx2 antenna was pointing towards the glass wall at the left-hand side of Tx2, as shown in figure 5-23. The highest value of the RMS angular spread was at position NP6 for all bands.

Table 5-14 Estimated AoD in azimuth and RMS angular spread values

Centre frequency	Position No.	AoD	RMS angular spread	No. of lobes
13.4 GHz	NP1	61.26°	6.23°	1
	NP2	54.23°	7.29°	1
	NP3	63.54°	8.99°	1
	NP4	58.86°	6.87°	1
	NP5	40.09°	20.84°	1
	NP6	51.06°	21.30°	2
26.8 GHz	NP1	51.15°	12.59°	2
	NP2	49.82°	7.85°	1
	NP3	41.34°	16.68°	2
	NP4	52.99°	12.11°	1
	NP5	40.49°	16.97°	1
	NP6	35.62°	20.52°	1
62.6 GHz	NP1	59.20°	6.03°	1
	NP2	51.73°	7.17°	1
	NP3	50.49°	17.24°	2
	NP4	29.41°	13.01°	2
	NP5	-37.38°	6.85°	3
	NP6	36.67°	20.03°	2
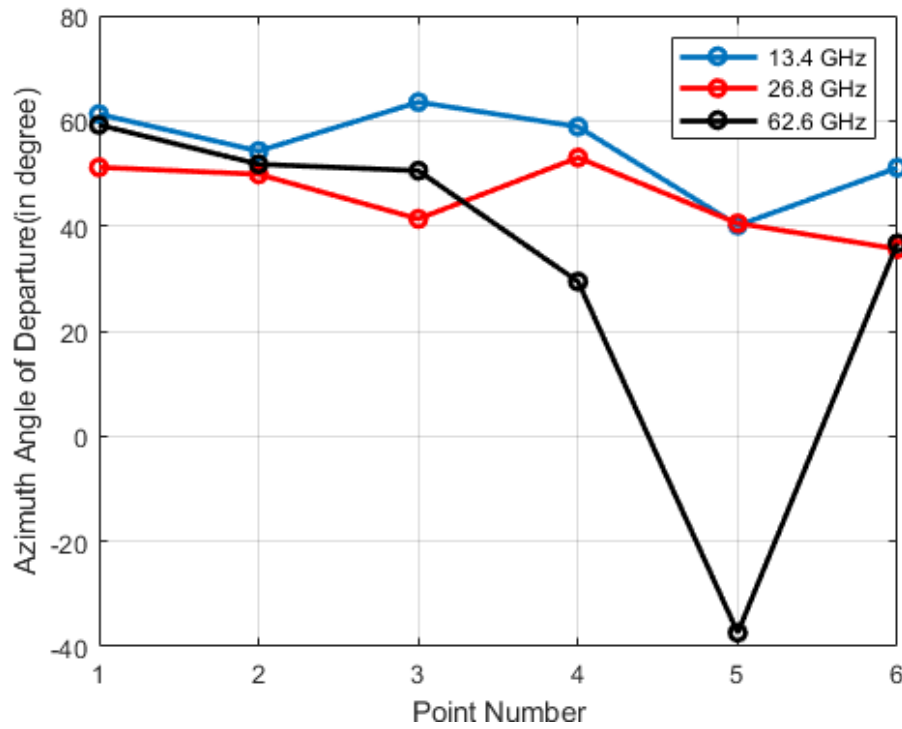
Figure 5-38 Azimuth AoD angles versus position number

Figure 5-38 highlights the similarity in azimuth AoD angles as a function of position for all bands at the first three positions, where the azimuth AoD angles were around the 60° angle. Then, at position NP4, the AoD at the 62.6 GHz band moved to the 29° angle, while the other two bands remained around the same angle for all positions. At position NP5, the AoD at the 62.6 GHz band switched to a negative angle then, at position NP6, reversed back to a positive angle of a similar AoD value as the other two bands. This shows that the 62.6 GHz band was affected differently to the other two bands, especially at position NP5.
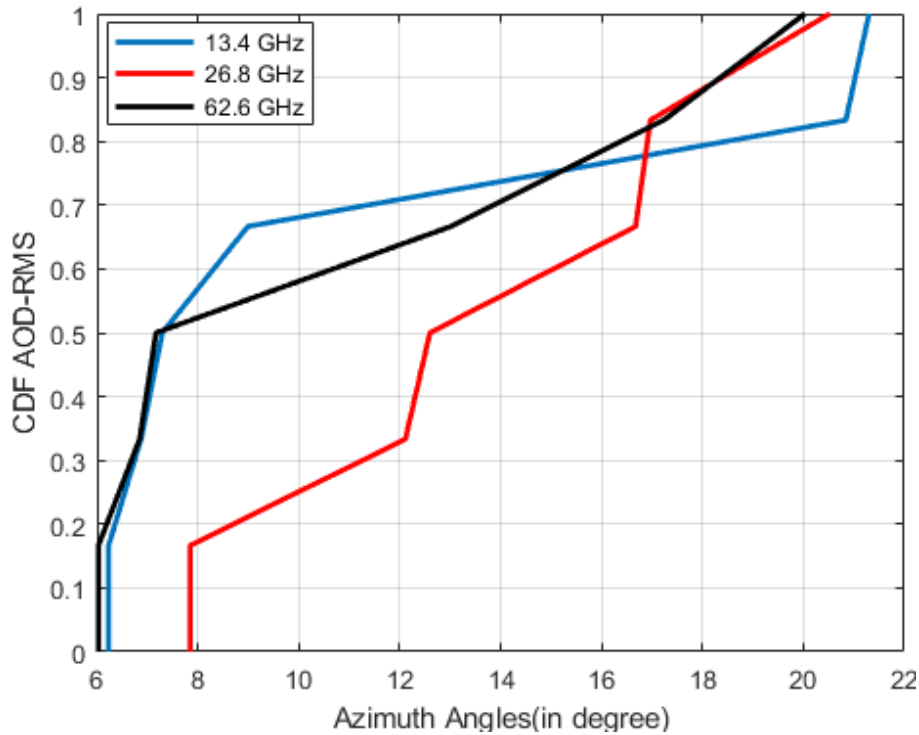
Figure 5-39 CDF of RMS AoD azimuth angular spread for all measured frequency bands

Figure 5-39 shows the CDF for the RMS AoD angular spread for all measured frequency bands. The figure shows that there was a similarity in the CDF values of the RMS angular spread between the 13.4 GHz band and the 62.6 GHz band up to about 75%, where the 26.8 GHz band had larger values than the other bands. Then, it was the 13.4 GHz band that had larger values than the other bands, where the CDF values of the other two bands became very close to each other, as shown in figure 5-39.

Table 5-15 presents the RMS angular spread values in the indoor environments. The table shows that the lowest values of the CDF of the AoD RMS angular spread were at the 62.6 GHz band, the largest values of the CDF at 10% and 50% were at the 26.8 GHz band, and the largest CDF value at the 90% was at the 13.4 GHz band.

Table 5-15 Values of the RMS AoD azimuth angular spread

CDF	13.4 GHz	26.8 GHz	62.6 GHz
10%	6.23	7.85	6.03
50%	7.29	12.59	7.17
90%	21.03	18.39	18.35

179

5.4 Street canyon environment

Figure 5-40 shows the layout of the street canyon environment at Durham University for both the LoS and NLoS scenarios. For the LoS scenario, the receiver was fixed during the measurements at positions P1, P2 and P3 for each frequency band, as shown in figure 5-40. The transmitter antenna with the 3D positioner were fixed at location Tx1 at a 3 m height from the ground, on top of a tripod. Using the 3D positioner, the antenna was tilted down at a -9° angle (which is half of the antenna's 3 dB beam-width) to focus the transmitted beam onto the measurement area. Position P1 was about 24 metres away from Tx1 and there was about 12 metres separation distance between the positions. The whole procedure was repeated three times, once for each frequency band.
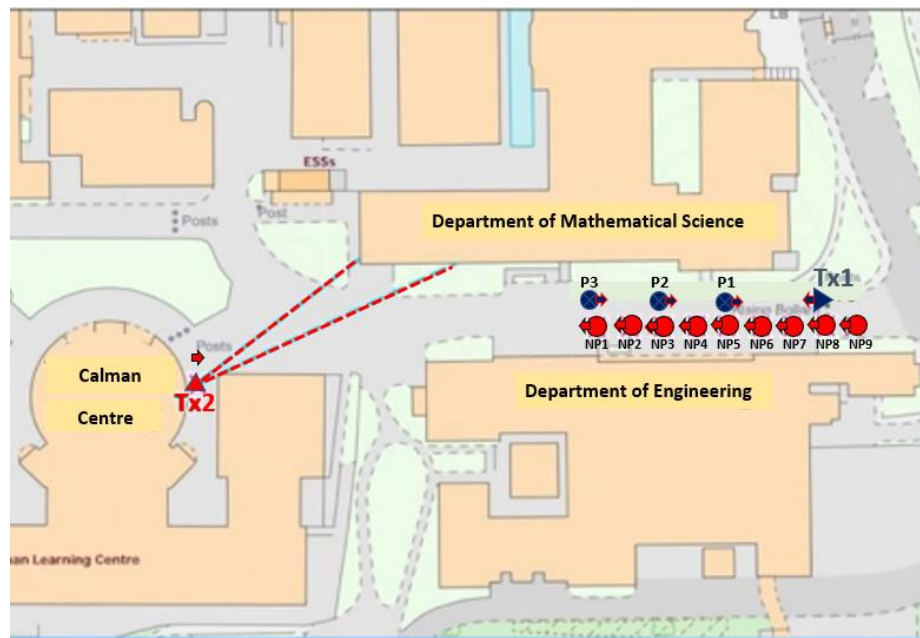
Figure 5-40 Street canyon environment layout

5.4.1 Line-of-sight (LoS) measurements

This section describes the measurements carried out in the street canyon environment at Durham University, and presents the results and discussion of the LoS measurements such as the AoA, AoD and their RMS angular spread for the three frequency bands.

5.4.1.1   Angle of arrival (AoA)

For the AoA measurements, the transmitter was fixed, and the Tx and Rx antennas were pointing towards each other, as shown in figure 5-40. The zero azimuth angles for the transmitter and receiver at each point are indicated by a small arrow in figure 5-40. The receiver antenna was then rotated clockwise with a step size of 12$^{\text{o}}$ in azimuth for all bands to cover the full rotation for each elevation angle. Three different elevation angles were used with a step size of 15$^{\text{o}}$ starting from -15$^{\text{o}}$ to 15$^{\text{o}}$ for all bands, and the data were recorded for each azimuth-elevation combination angle.
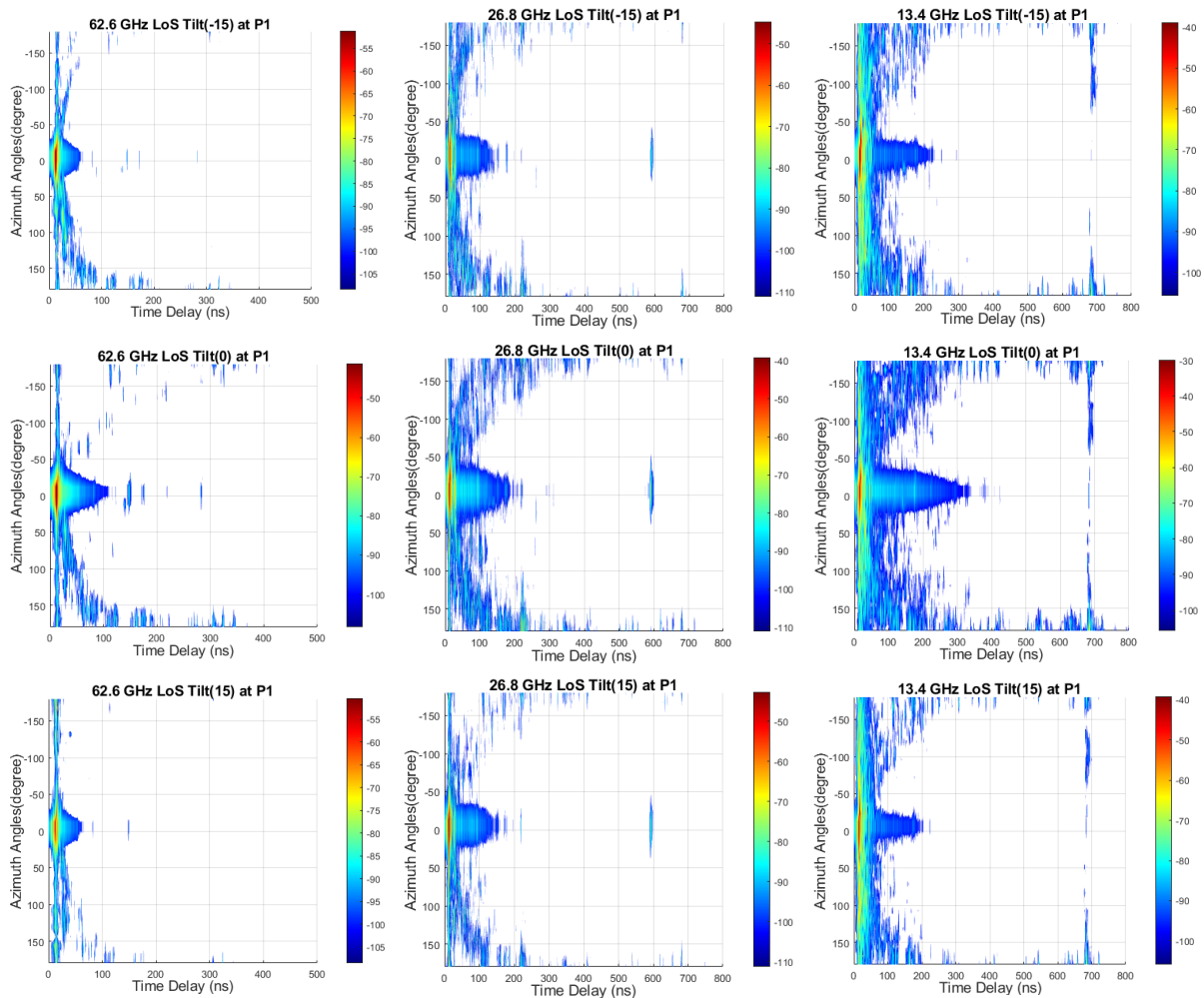
Figure 5-41 PDPs as a function of azimuth angles at three different elevation angles at position P1

Figure 5-41 presents the power delay profiles as a function of azimuth rotation angles at three different elevation angles, with the receiver positioned at P1 for all measured bands. The figure

shows a strong signal around the zero degrees angle within 25 nanoseconds, which corresponds to the line-of-sight angles where the antennas of the receiver and transmitter were oriented towards each other. Other signals with a lower power level of the reflected signals can also be seen between the -50° and +50° angles at different time delays of up to about 700 nanoseconds for the first two bands, and around 400 nanoseconds for the 62.6 GHz band. In addition, there were signals around the 180° angle at different time delays, which represent the reflected signals when the receiver was pointing away from the transmitter, as shown in figure 5-40. The existence of reflected signals mainly between the 50° and 310° azimuth angles can also be noticed (much more clearly for the 13.4 GHz band) at a time delay of about 700 nanoseconds, corresponding to a reflector at 105 metres distance from the receiver at position P1, which might represent the reflected signals from the metallic curved wall of the building next to Tx2, as shown in figure 5-40.

Figure 5-42 shows polar plots of the received power as a function of the azimuth angles from 0° to 360° and at three different elevation angles. The figure shows that the strongest signal for all bands and positions was around the zero degrees angle in azimuth and close to the zero degrees elevation angle, where the received power at the positive and negative elevation angles were close to each other in most of the positions and bands. The signal strength decreased for all bands as the distance between the transmitter and receiver increased. There was also another lobe around the 180° angle in azimuth with a low power level compared to the first one at the zero degrees angle.

62.6 GHz at P1

26.8 GHz at P1

13.4 GHz at P1

62.6 GHz at P2

26.8 GHz at P2

13.4 GHz at P2

62.6 GHz at P3

26.8 GHz at P3

13.4 GHz at P3
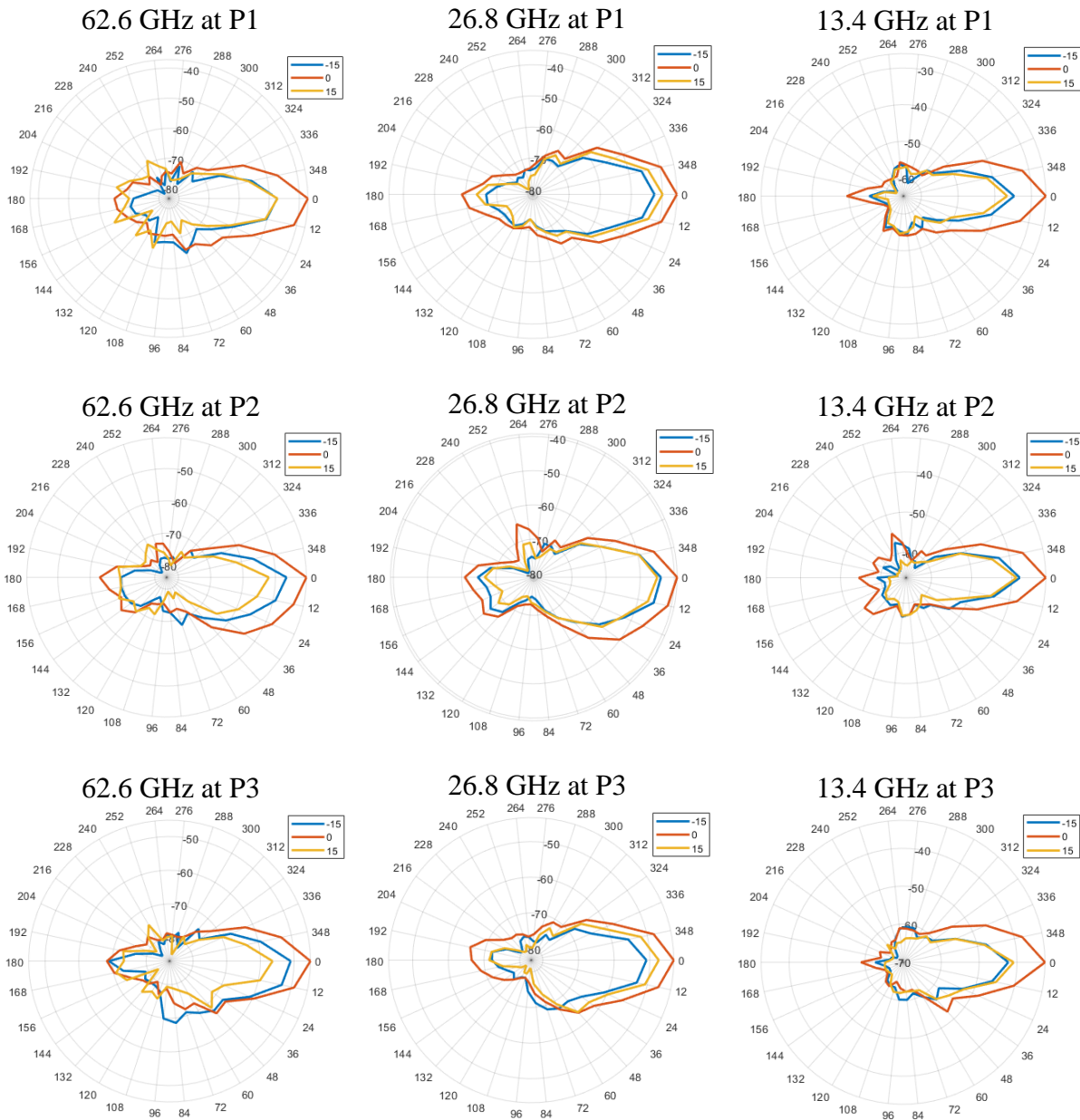
Figure 5-42 Polar plots of the received power as a function azimuth angles at the strongest three elevation angles for all bands

Figure 5-43 shows the 3D AoA images in azimuth and elevation within 10 dB from the maximum at three positions for all measured bands. The images show that at all the positions, the strongest AoA in azimuth was around the zero degrees angle for all three bands. For the elevation angle, there was a variation between the bands, especially at positions P2 and P3. For the 13.4 GHz band, the strongest elevation AoA at all positions was close to the zero degrees angle, where the received power at the positive and negative elevation angles were close to each other. For the 26.8 GHz band, the strongest AoA in elevation at positions P1 and P2 was close to zero degrees, and the received power at the other elevation angles were close to each other;

183

whereas at position P3, the strongest power was between the zero and positive elevation angles and closer to the zero elevation angle. For the 62.6 GHz band at P1, the best AoA in elevation was at the zero elevation angle, where the received power was almost the same at the other elevation angles, whereas at positions P2 and P3, the best elevation angle was between the zero and negative elevation angles and closer to zero elevation angle.
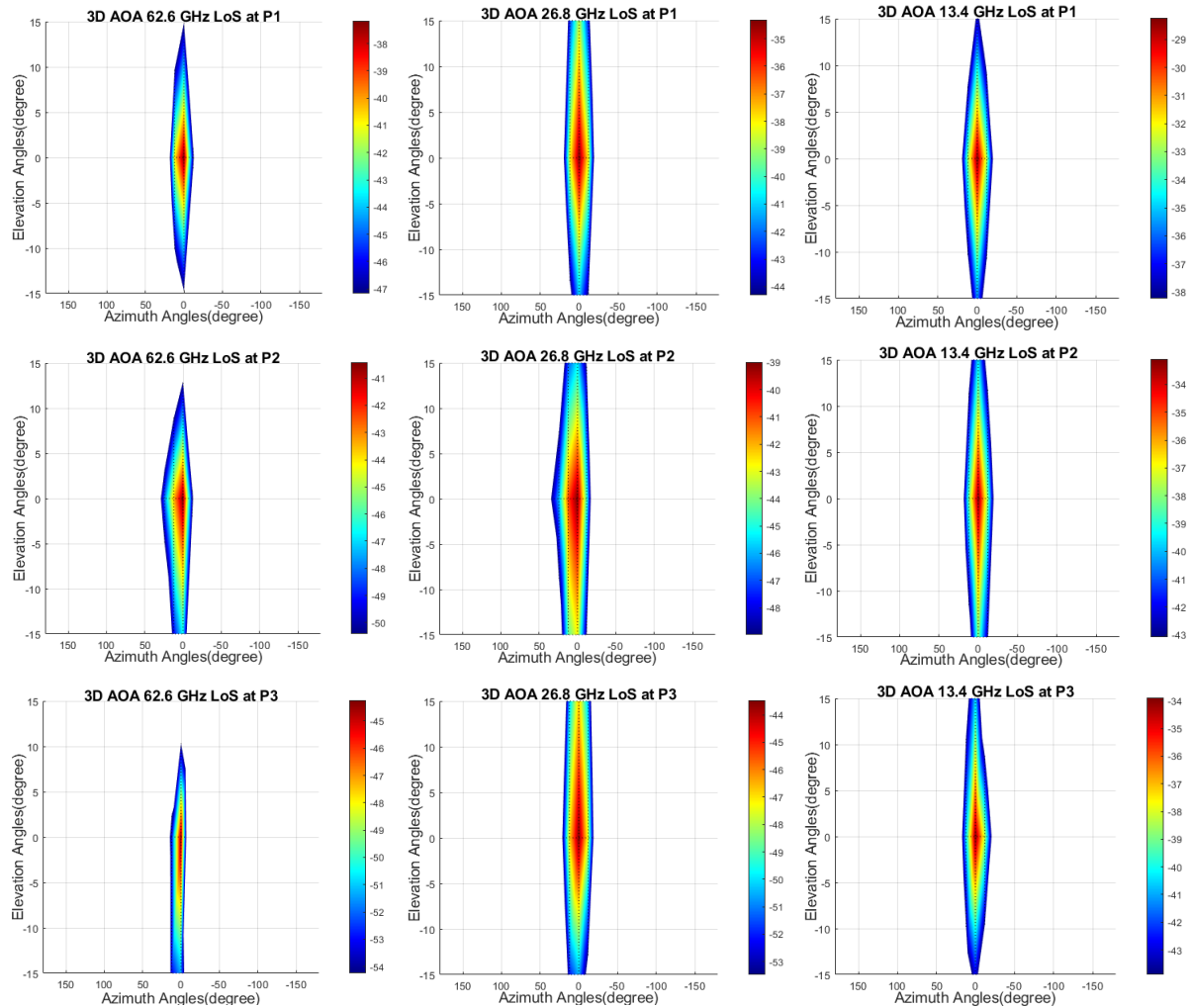
Figure 5-43 3-D AoA images for the LoS scenario at three measurement positions for all bands

Table 5-16 presents the estimated values of the AoA in azimuth and elevation for the strongest lobe and their RMS angular spread for all bands at each measurement position. The table indicates that the highest value of the RMS elevation angular spread was at position P2, where the elevation angle was negative for all bands at this position, which shows that the reflected signals from the ground at this position were stronger than those originating from the other directions. For the 62.6 GHz band, the best elevation angle was either zero or negative at all of the measured positions. The elevation angles for all bands and at all positions were within 3°

around the zero-elevation angle, which is much less than the antennas 3 dB half power beam-width. The highest values of the RMS azimuth angular spread occurred for the 26.8 GHz band at all measured positions.

Table 5-16 Estimated AoA in azimuth and elevation and the RMS angular spread values

Centre frequency	Position No.	3D Azi. AoA	RMS azimuth angular spread	3D Ele. AoA	RMS elevation angular spread	No. of lobes
13.4 GHz	P1	359.80º	7.64º	- 0.72º	7.25º	1
	P2	359.61º	7.44º	- 0.85º	8.88º	1
	P3	359.02º	7.23º	0.99º	7.56º	1
26.8 GHz	P1	359.99º	8.09º	1.46º	8.98º	1
	P2	4.18º	9.92º	-1.75º	9.28º	1
	P3	0.31º	8.13º	2.46º	9.19º	1
62.6 GHz	P1	2.40º	6.69º	0.00º	0.00º	1
	P2	4.69º	9.08º	- 2.92º	5.94º	1
	P3	1.97º	3.87º	- 2.46º	5.55º	1

5.4.1.2 Angle of departure (AoD)

For the AoD measurements, the received power was investigated for each angle to find the strongest received signal, and the angle of this signal was then selected as a fixed direction at which the receiver was positioned to measure the AoD. While the receiver was pointing to that angle, the transmitter was then rotated clockwise from zero degrees to 360º with a step size of 12º in azimuth for all bands to cover the full rotation, and the data were recorded at the receiver side for each Tx angle at -9º elevation angle.
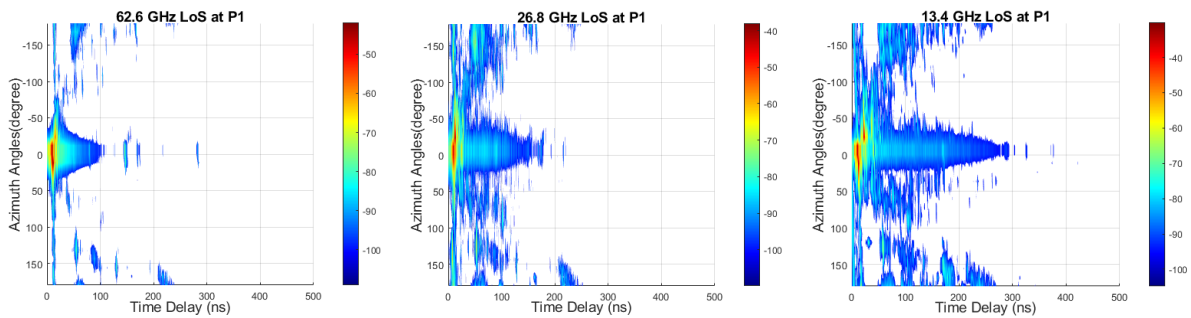
Figure 5-44 PDPs as a function of azimuth angles at a -9º elevation angle and position P1 for all bands

Figure 5-44 presents the PDPs as a function of the Tx azimuth rotation angles at a -9º elevation angle at the transmitter, with the receiver pointing to zero degrees (the angle of the strongest received power) at position P1 for all measured bands. The figure shows strong signals around zero degrees within 25 nanoseconds, which correspond to the line-of-sight angles when the antennas of the receiver and transmitter were oriented towards each other. Other signals with a lower power level of the reflected waves at different time delays of up to about 300 nanoseconds were also observed between -50º and +50º. In addition, there were also signals that appeared around 180º at different time delays, which represent the reflected signals when the transmitter was pointing away from the receiver and towards condensed trees area, which acted as a wall of vegetation.

Figure 5-45 presents polar plots of the received power as a function the Tx1 azimuth angles from 0º to 360º, with a step size of 12º for each band at position P1 with a 10 dB threshold from the maximum power. The figure shows that the strongest signal for all bands was around zero degrees in azimuth, which represents the line-of-sight when the Tx and Rx antennas were oriented towards each other, while the second strongest lobe was around 180º, representing the case when the Tx1 antenna was pointing to the vegetation area.
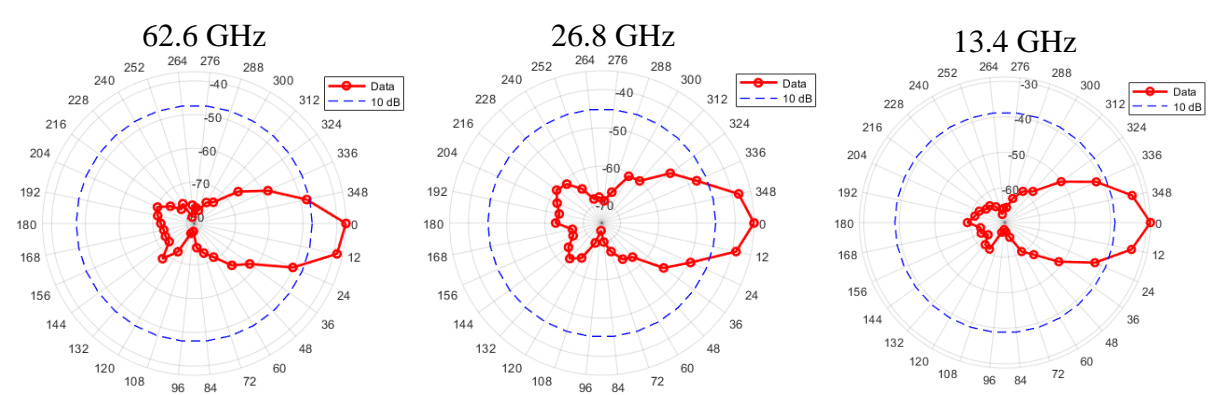
Figure 5-45 Polar plots of the received power as a function of Tx azimuth angles at -9º elevation angle at P1

Table 5-17 presents the estimated values of the AoD in azimuth for the strongest lobe and their RMS angular spread within 10 dB from the maximum for all bands at each measurement position. The table shows that the value of the AoD for the first two bands was closer to zero degrees than for the 62.6 GHz band, which might be due to the antenna size, where the antenna of a smaller size is typically more difficult to adjust compared to a bigger one for long distances between the Tx and Rx. The RMS angular spread for the 26.8 GHz band was the highest at

most of the positions compared to the other bands and decreased as the separation distance between the Tx and Rx increased. The lowest values of the RMS angular spread at all positions were recorded for the 62.6 GHz band.

Table 5-17 Estimated AoD in azimuth and the RMS angular spread values

Centre frequency	Position No.	AoD	RMS angular spread	No. of lobes
13.4 GHz	P1	359.88°	7.75°	1
	P2	0.23°	7.46°	1
	P3	1.02°	7.63°	1
26.8 GHz	P1	359.56°	8.20°	1
	P2	0.43°	7.63°	1
	P3	359.73°	6.73°	1
62.6 GHz	P1	4.83°	5.88°	1
	P2	3.98°	7.13°	1
	P3	4.77°	5.87°	1

5.4.2 Non-line-of-sight (NLoS) measurements

This section provides a detailed description of the NLoS measurements in the street canyon environment and presents the results and discussion of the measurements conducted, such as the AoA, AoD and their angular spread, for the three frequency bands.

5.4.2.1 Angle of arrival (AoA)

For the AoA measurements, the transmitter was fixed at location Tx2 pointing towards the wall (to illuminate the area between the two red dashed lines in figure 5-40) with a 333° angle, where the angle was calculated to cover the measurement area for NLoS measurements at the positions from NP1 up to NP9, as shown in figure 5-40. The zero azimuth angles for the transmitter and receiver at each location are indicated by a small arrow in the layout in figure 5-40. The receiver antenna was then rotated clockwise with a step size of 12° in azimuth for all bands to cover the full rotation for each elevation angle. Three different elevation angles were used with a step size of 15° starting from -15° to 15° for all bands, and the data were recorded for each azimuth-elevation combination angle.
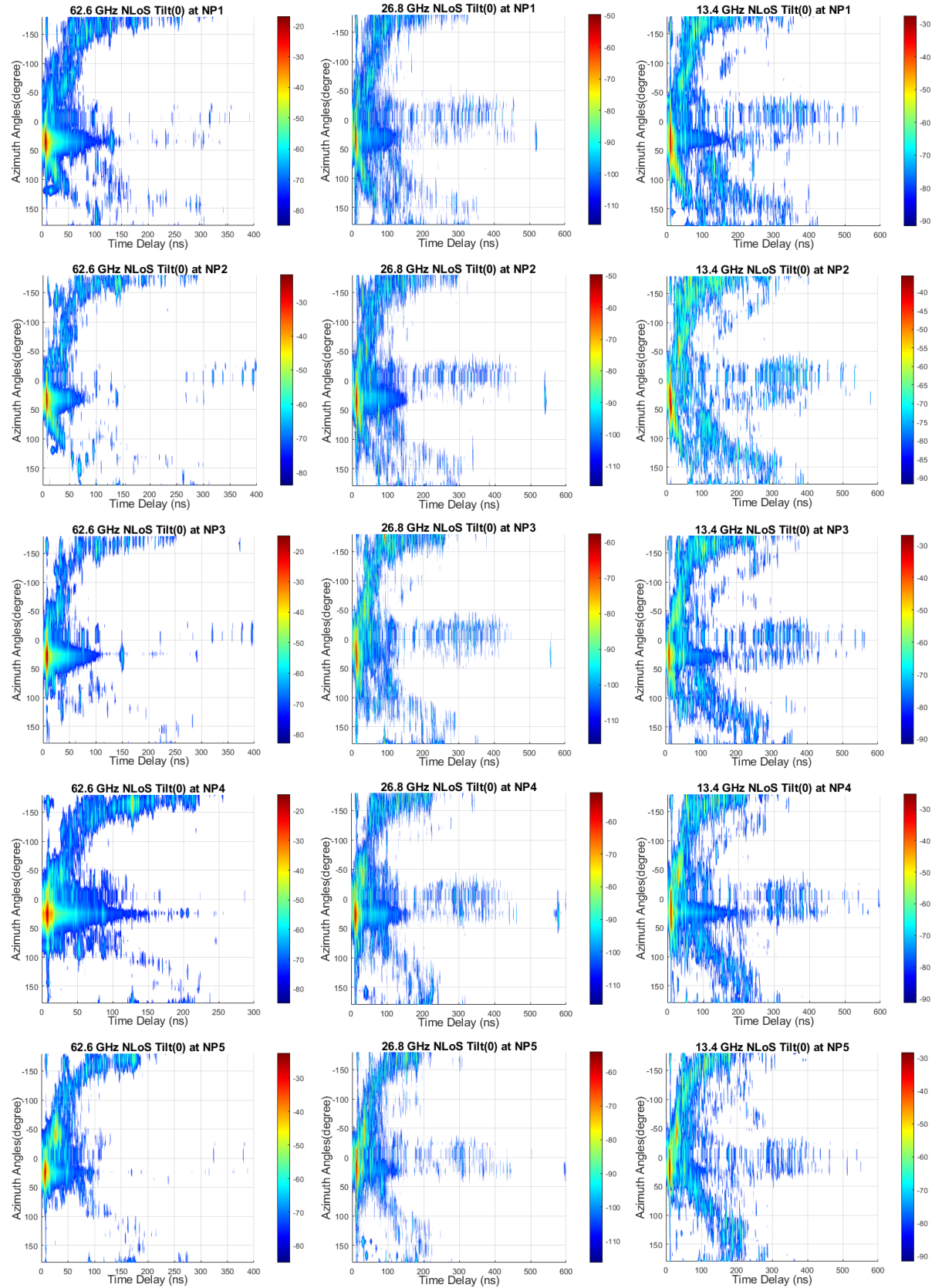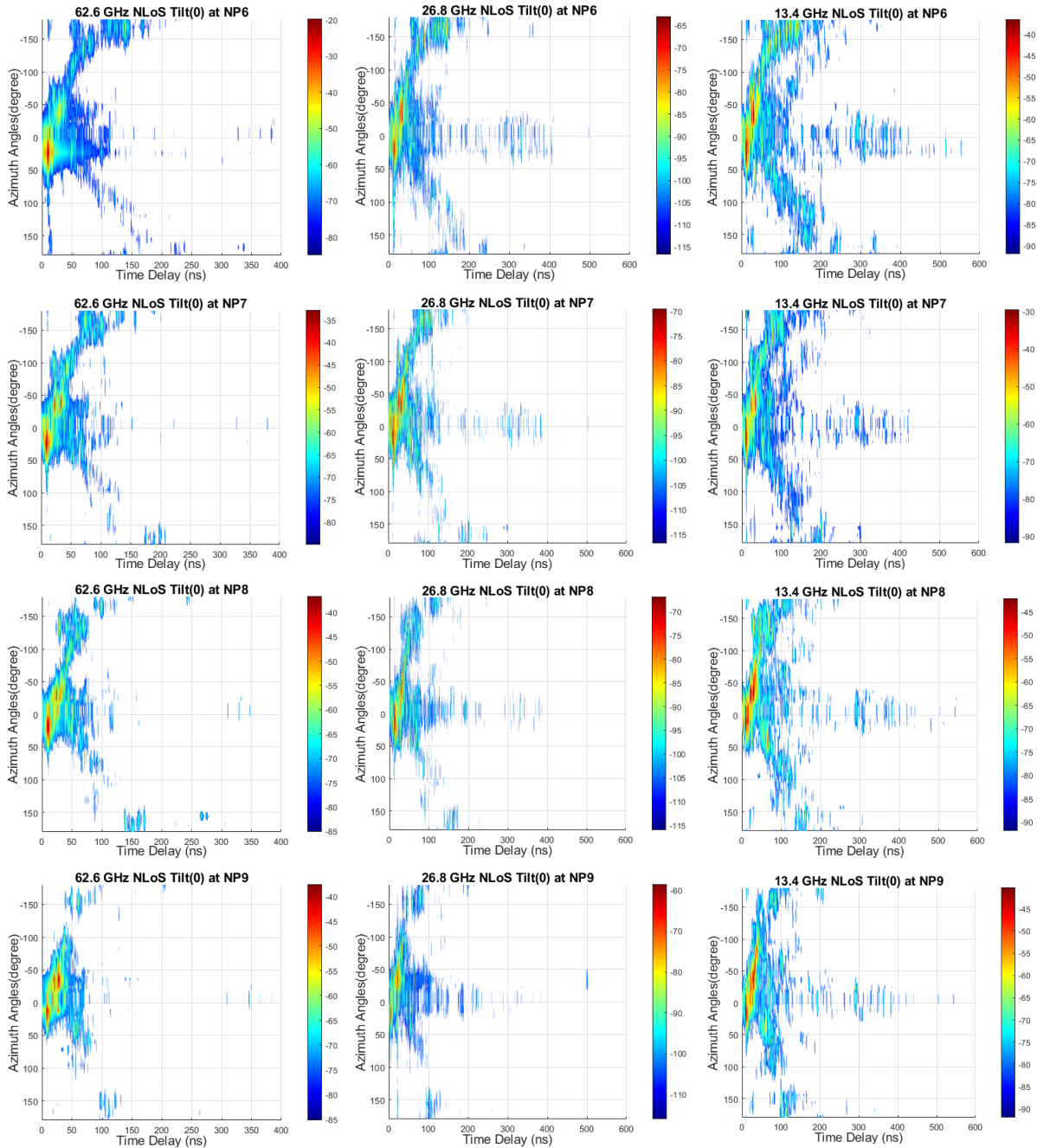
Figure 5-46 PDPs as a function of azimuth angles at zero elevation for all measured bands and positions

Figure 5-46 presents the power delay profiles as a function of azimuth rotation angles at the zero degrees elevation angle for each receiver position and for all measured bands. The figure shows strong multipath signals between the 10° and 60° angles at the same time delay for all bands and at all positions, and such signals moved closer to zero degrees as the receiver moved away from the transmitter. These signals represent the first order reflected multipath signals from the wall of the Mathematical Science Department building, as shown in figure 5-40. Other

multipath signals with a lower power level were detected around -50º starting from the position NP5, which indicate the presence of second order reflected signals from the walls of the Department of Engineering building. These signals moved towards the zero degrees angle to combine with the signals at the positive side in the last two positions. There were also signals present between the 180º and 210º angles (mainly at the first four positions), which reached up to 400 nanoseconds in delay for all bands.

62.6 GHz at NP1

26.8 GHz at NP1

13.4 GHz at NP1

62.6 GHz at NP2

26.8 GHz at NP2

13.4 GHz at NP2

62.6 GHz at NP3

26.8 GHz at NP3
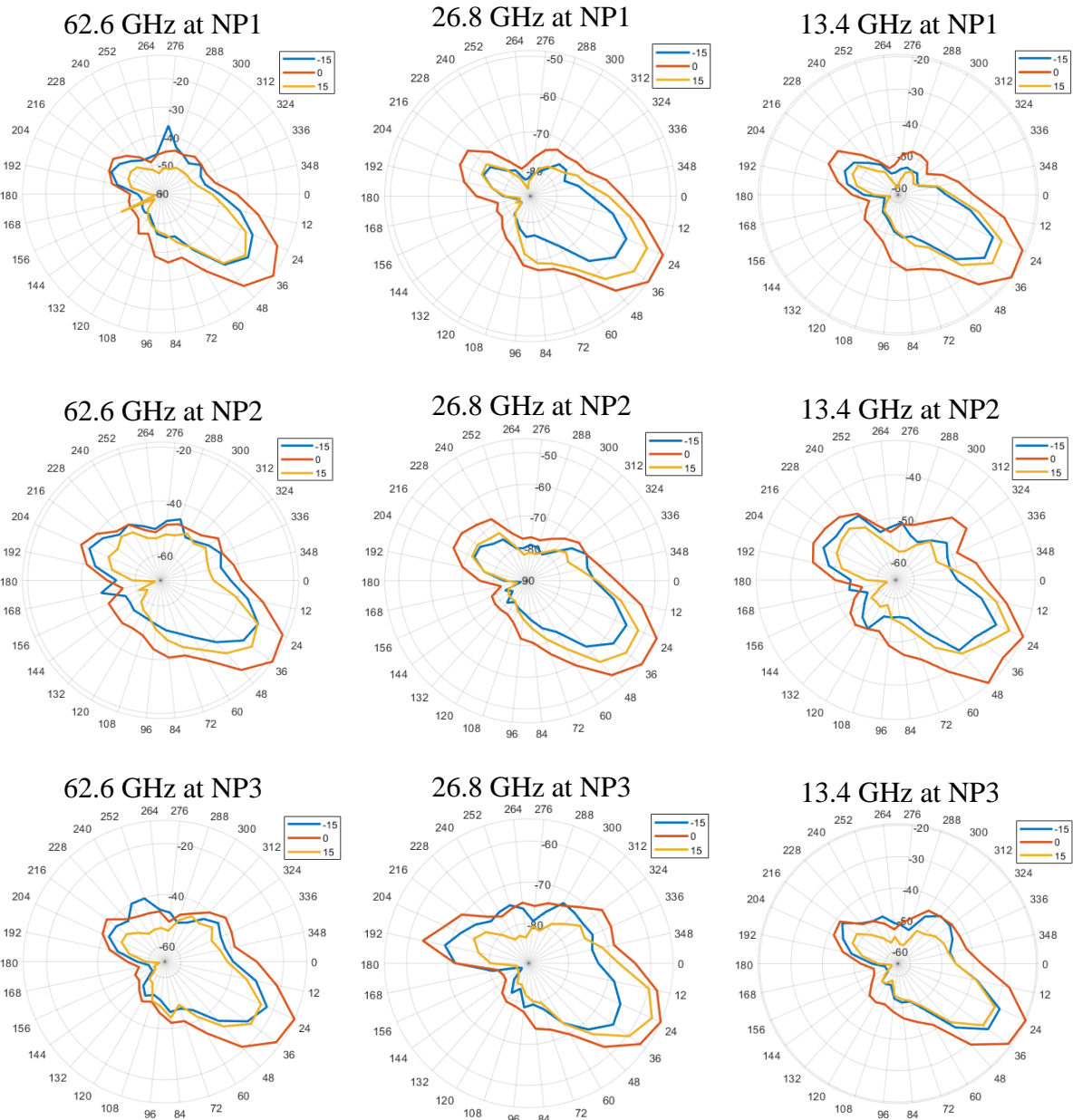
13.4 GHz at NP3
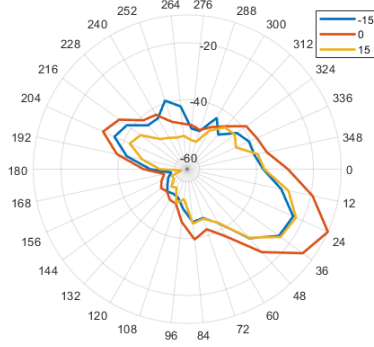
62.6 GHz at NP4

26.8 GHz at NP4
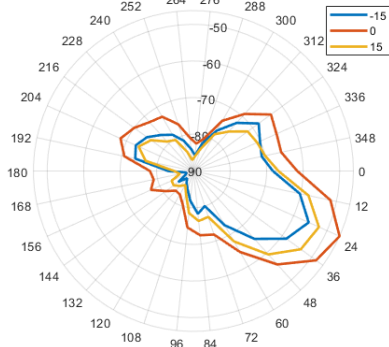
13.4 GHz at NP4
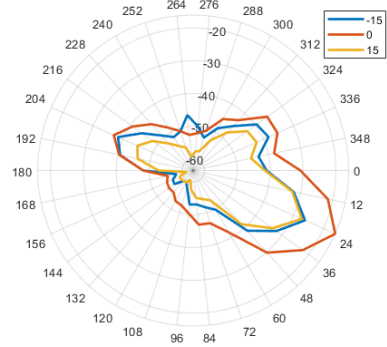
62.6 GHz at NP5
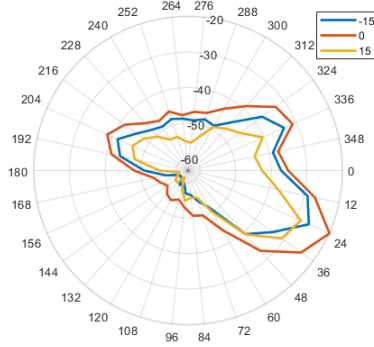
26.8 GHz at NP5
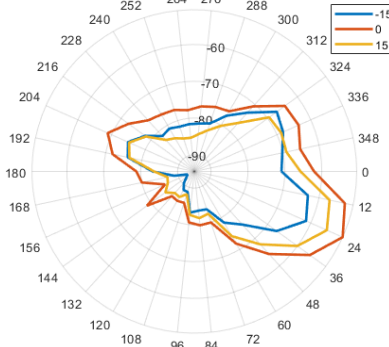
13.4 GHz at NP5
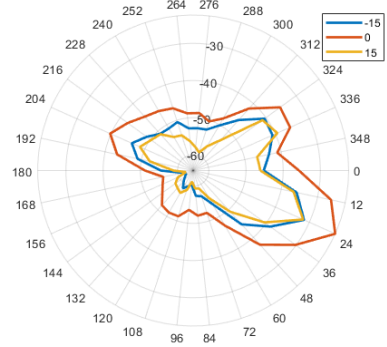
62.6 GHz at NP6
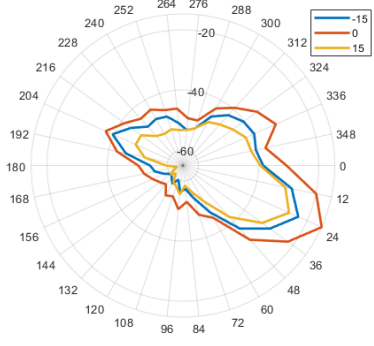
26.8 GHz at NP6
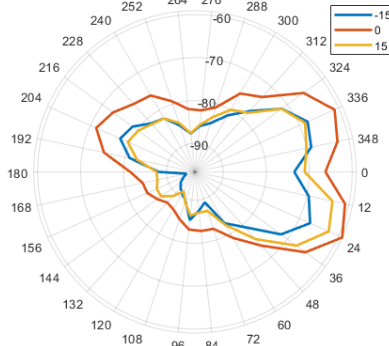
13.4 GHz at NP6
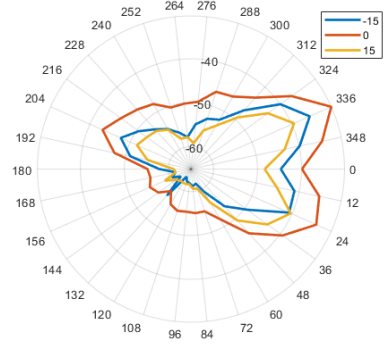
62.6 GHz at NP7
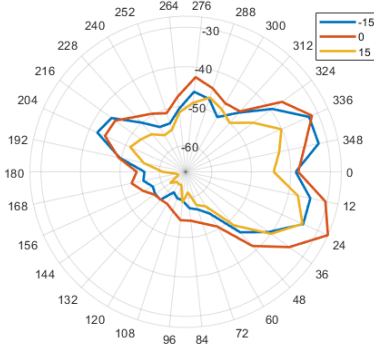
26.8 GHz at NP7
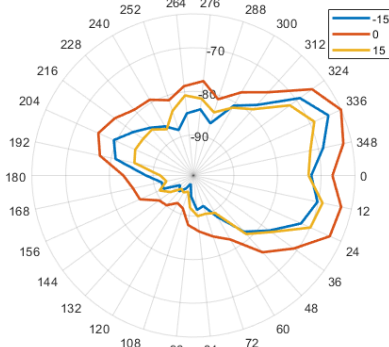
13.4 GHz at NP7
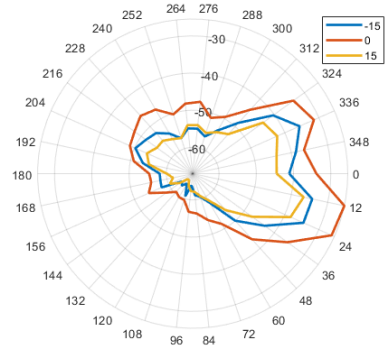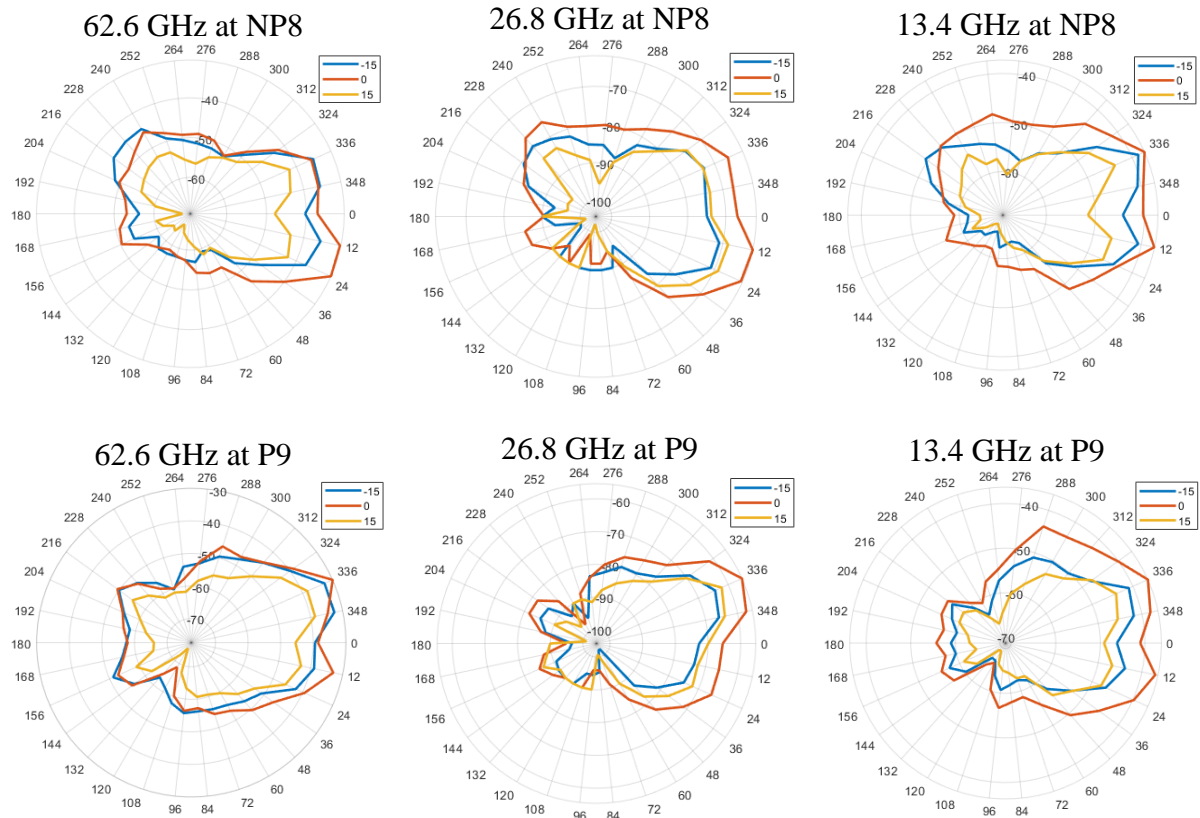
Figure 5-47 Polar plots of the received power as a function azimuth angles at the strongest three elevation angles for all bands

Figure 5-47 shows polar plots of the received power as a function of the azimuth angle from 0° to 360° at three different elevation angles for the NLoS scenario. The figure shows that the strongest signals for all bands at positions NP1, NP2 and NP3 were around the 36° angle in azimuth, while there was another lobe with a lower power level around the 216° angle. At positions NP4 and NP5, the strongest signals moved close to the 24° angle for all bands, while another lobe around 336° started to emerge. Then, starting from position NP6, the strongest lobe switched between the two sides around the zero degrees angle and moved closer to zero degrees from both sides. The two sides then combined to make a wide beam around the zero degrees angle, while another lobe emerged around the 180° angle, as shown in Figure 5-47. It is also noticeable that the strongest received power for most of the lobes was at the zero degrees elevation angle for all bands and at all positions.
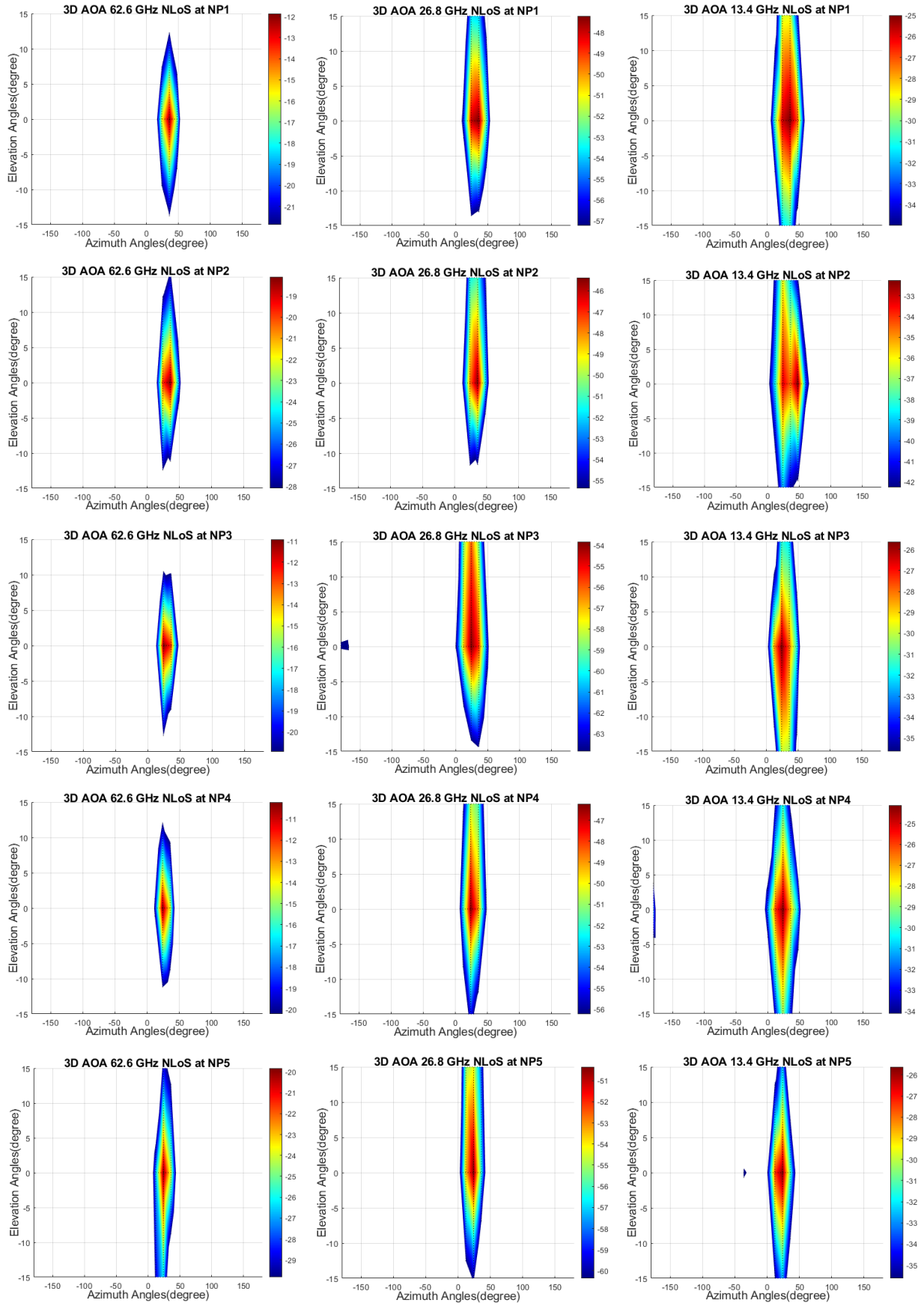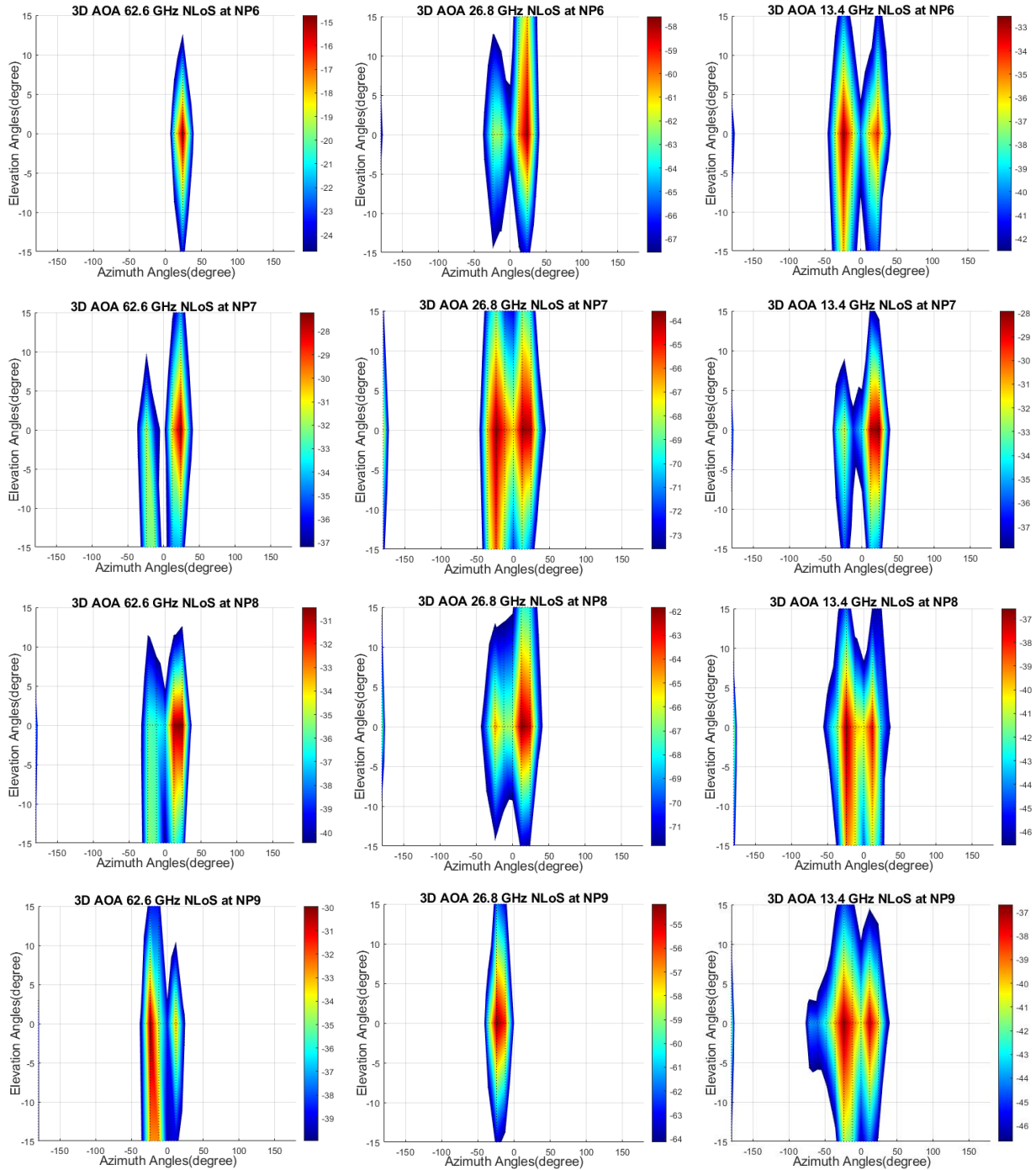
Figure 5-48 3-D AoA images for the NLoS scenario at three measurement positions and for all bands

Figure 5-48 shows the 3D images of the AoA in azimuth and elevation within 10 dB from the maximum at nine positions and for all bands. The images indicate that the strongest AoA in azimuth was between the 0° and 50° angles at the positions from NP1 to NP5 for all bands. Furthermore, another lobe could be seen between 0° and -50° degrees starting from position NP6 for the first two bands and from NP7 for the 62.6 GHz band. The two lobes moved towards

the zero degrees angle from both sides as the distance between the Tx and Rx increased, thus resulting in forming a wide lobe at positions NP8 and NP9, as shown in Figure 5-48. In terms of elevation, the strongest AoA at all positions and bands was closer to zero degrees with some variation between the bands and positions, where, for instance, the power at the positive elevation angle was larger than negative elevation angle in most of the positions for the 26.8 GHz band, whereas they were almost the same in most of the positions for the other two bands.

Table 5-18 Estimated AoA in azimuth and elevation and the RMS angular spread values

Centre frequency	Position No.	3D Azi. AoA	RMS azimuth angular spread	3D Ele. AoA	RMS elevation angular spread	No. of lobes
13.4 GHz	NP1	32.51º	11.11º	1.29º	9.37º	1
	NP2	34.76º	13.29º	2.63º	10.35º	1
	NP3	27.20º	10.89º	- 1.08º	9.31º	1
	NP4	23.53º	12.38º	- 0.67º	9.22º	2
	NP5	21.68º	7.99º	0.09º	8.09º	2
	NP6	349.03º	23.11º	-5.47º	12.24º	2
	NP7	16.17º	11.33º	- 1.26º	7.83º	2
	NP8	351.41º	21.21º	- 6.72º	7.46º	2
	NP9	346.98º	26.78º	- 1.62º	9.45º	2
26.8 GHz	NP1	31.26º	9.33º	2.76º	5.81º	1
	NP2	33.69º	7.73º	3.24º	6.17º	1
	NP3	25.09º	11.38º	5.70º	7.28º	2
	NP4	27.65º	9.12º	2.30º	8.38º	1
	NP5	22.33º	7.67º	2.98º	8.22º	1
	NP6	12.16º	20.79º	4.45º	10.05º	2
	NP7	356.15º	21.72º	- 2.83º	9.97º	2
	NP8	7.15º	20.09º	3.15º	10.32º	2
	NP9	338.65º	8.05º	0.69º	7.20º	1
62.6 GHz	NP1	35.29º	7.63º	0.00º	0.00º	1
	NP2	33.43º	7.72º	1.52º	4.53º	1
	NP3	28.87º	5.89º	0.00º	0.00º	1
	NP4	26.21º	6.69º	0.00º	0.00º	1
	NP5	24.97º	7.11º	- 1.11º	7.66º	1
	NP6	23.16º	6.80º	- 1.85º	4.93º	1
	NP7	22.03º	7.35º	- 0.09º	8.04º	2
	NP8	9.12º	16.38º	- 1.48º	4.47º	1
	NP9	347.52º	17.40º	- 5.91º	10.75º	1

Table 5-18 presents the estimated values of the AoA in azimuth and elevation for the lobe of the strongest received power and their RMS angular spread within 10 dB threshold from the maximum for all bands and at each measurement position in the NLoS scenario. The table shows that the elevation angle of the strongest lobe was either zero or negative at most of the positions for the 13.4 GHz and 62.6 GHz bands, while it was positive at most of the positions for the 26.8 GHz band. The elevation angle of the strongest lobe was within 5.7° from the zero degrees angle at all positions and for all bands, which is less than half of the 3-dB beam-width of the used antennas. The 13.4 GHz band showed a higher number of lobes at most of the positions than the other two bands, which means that the signals at this band could travel larger distances before losing strength compared to the other bands. In contrast, the 62.6 GHz band showed the lowest number of lobes at most of the positions.

Figure 5-49 highlights the similarity in azimuth AoA angles for all bands at the first five positions. At the last four positions, there were some variations in the AoA between the bands, where for the 62.6 GHz band, the AoA was in the positive side up to position NP8, while for the first two bands, a switching behaviour occurred around the zero degrees angle between the negative and positive angles and versa verse, before finally steadying at the negative angle side at position NP9 for all bands.
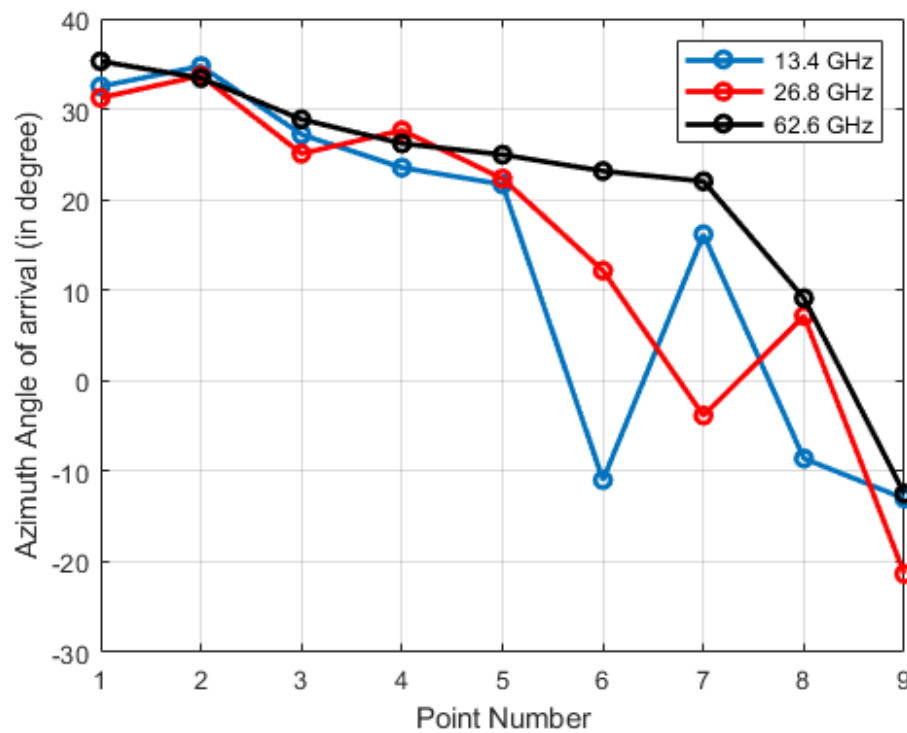
Figure 5-49 Azimuth AoA versus position number
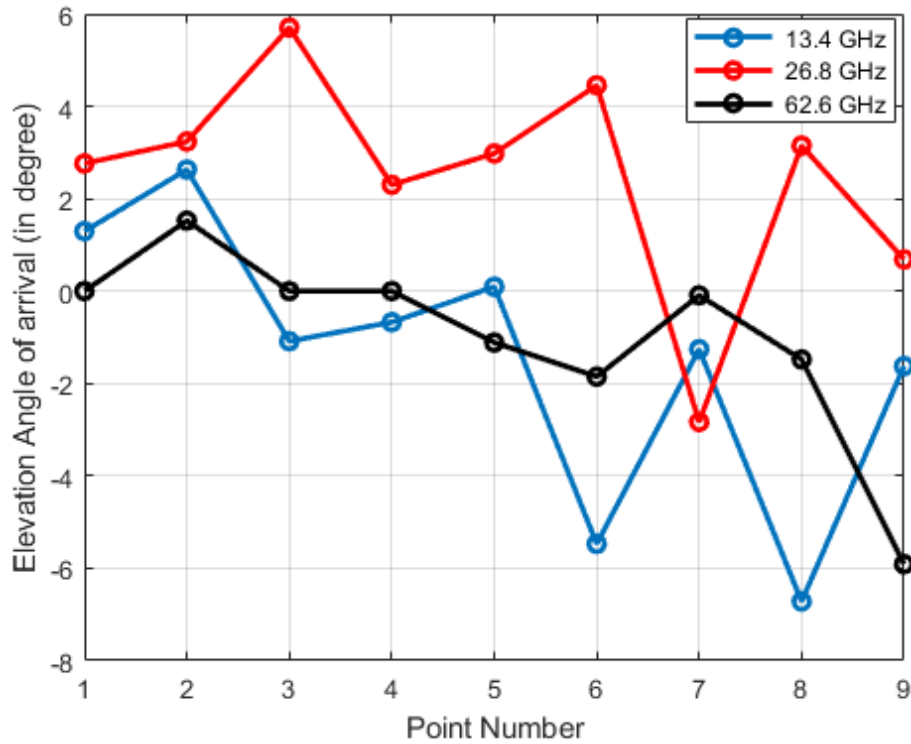
Figure 5-50 Elevation AoA versus position

Figure 5-50 shows the elevation AoA for all bands versus position. The figure shows that the elevation angles of arrival were close to each other for the 13.4 GHz and 62.6 GHz bands, where the elevation AoA was either zero or negative for most of the positions, while it was positive at most positions for the 26.8 GHz band, as shown in figure 5-50. This means that the received power for most of the measured positions was stronger at the positive elevation angle than the negative elevation angle for the 26.8 GHz band, while for the other two bands, the received power at the negative elevation angle was either stronger than that at the positive elevation angle or equal to it.

Figure 5-51 shows the CDF of the RMS AoA azimuth angular spread for the measured frequency bands. The figure shows that the CDF of the RMS AoA azimuth angular spread values decreased as the frequency band increased.
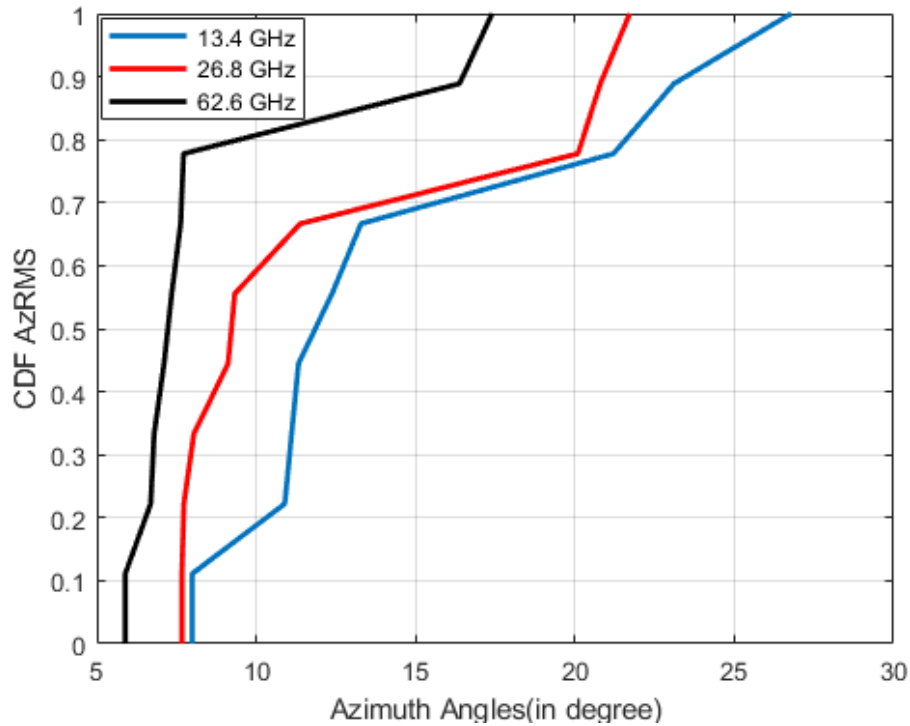
Figure 5-51 CDF of RMS AoA azimuth angular spread for all measured frequency bands

Table 5-19 Values of the azimuth AoA RMS angular spread

CDF	13.4 GHz	26.8 GHz	62.6 GHz
50%	11.85	9.22	7.23
90%	23.47	20.89	16.48
95%	25.13	21.31	16.94

Table 5-19 presents the recommended RMS angular spread values in the outdoor environment, where the 50% and 90% and 95% values of the cumulative distribution are presented for all measured frequency bands. The table shows a decrease in the CDF values of the RMS AoA azimuth angular spread as the frequency band increased for all recommended values.
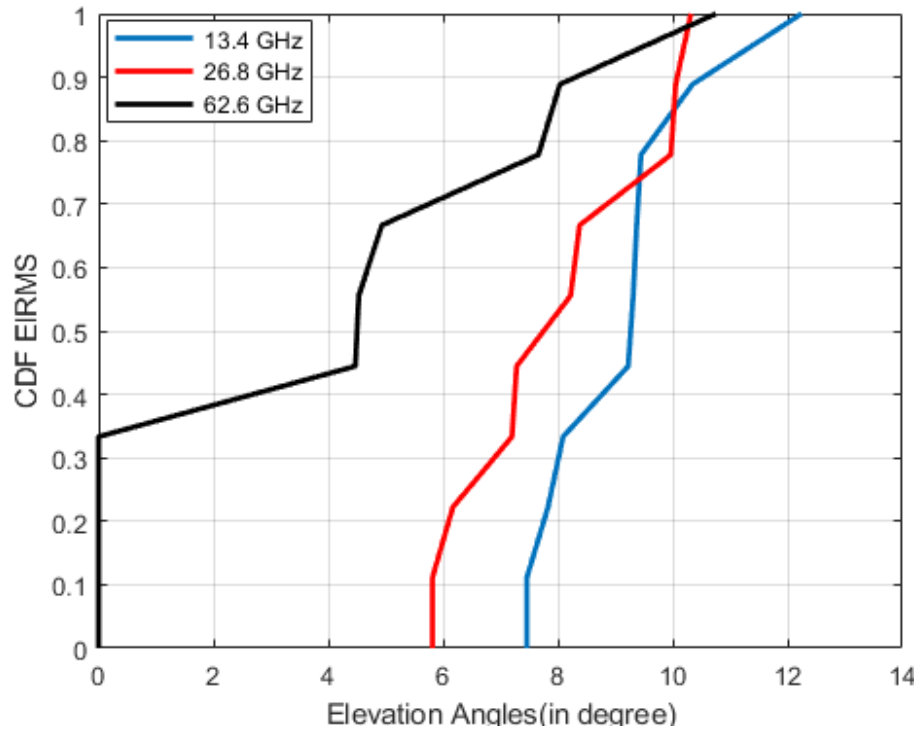
Figure 5-52 CDF of RMS AoA elevation angular spread for all measured frequency bands

Figure 5-52 shows the CDF of the RMS AoA elevation angular spread for all the measured frequency bands. The figure indicates that most of the CDF values of the RMS AoA elevation angular spread at the lower frequency bands were larger than those at the higher frequency bands. Table 5-20 presents the estimated RMS angular spread values in outdoor environments. The table shows a decrease in the CDF values of the RMS AoA elevation angular spread as the frequency increased for all recommended values.

Table 5-20 Values of the RMS AoA elevation angular spread

CDF	13.4 GHz	26.8 GHz	62.6 GHz
50%	9.27	7.75	4.50
90%	10.54	10.08	8.31
95%	11.39	10.19	9.53

5.4.2.2   Angle of departure (AoD)

To find the best receiving angle for the AoD measurements, the procedures used in section 5.1.1.2 were repeated at each position for all frequency bands.

Figure 5-53 presents the PDPs as a function of the Tx azimuth rotation angles from 0° to 360° in a clockwise direction (the zero direction angle of Tx2 is indicated by the small red arrow in figure 5-40). The transmitter was about 3.4 metres away from the brick wall with the antenna pointing to zero degrees azimuth angle, and about 3 metres from the metallic curved wall of the Calman Centre building with a 0° elevation angle at the transmitter, as shown in figure 5-40. The receiver was pointing to the azimuth angle of the strongest received power at each position for all the measured bands. The figure shows that for all bands and at all positions, the strongest signals came from the azimuth angles around -40° at the same time delays, which correspond to the signals when the antenna of the transmitter was oriented towards the area between the two red dashed lines in figure 5-40. There were also other reflected signals around zero degrees in some positions with different time delays for the measured bands, which represent the second order reflected signals, where the first order signals reflected from the brick wall, while the second order signals then originated from reflections off the metallic wall. Such signals showed shorter time delays at some positions than those corresponding to the signals around the -40° angle. The signals around zero degrees were detected at different time delays. Furthermore, at the angle of 180°, there were other signals for all bands and positions, which correspond to the reflected signals when the Tx antenna was pointing towards the metallic wall of the Calman Centre, as shown in figure 5-40.
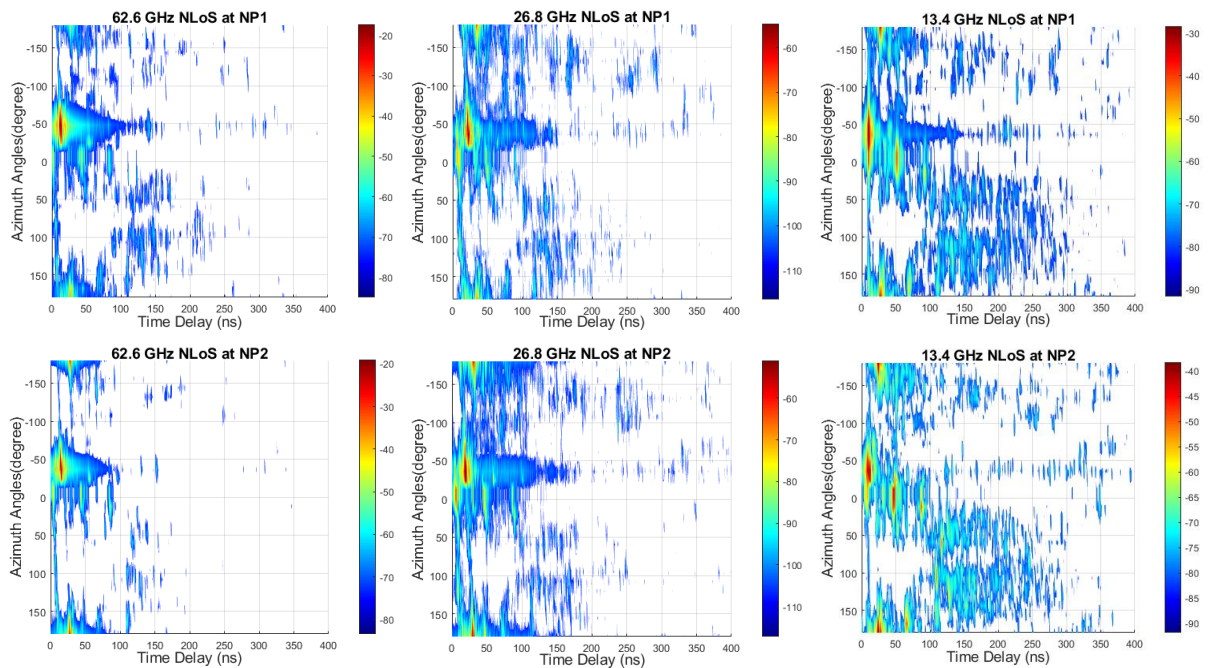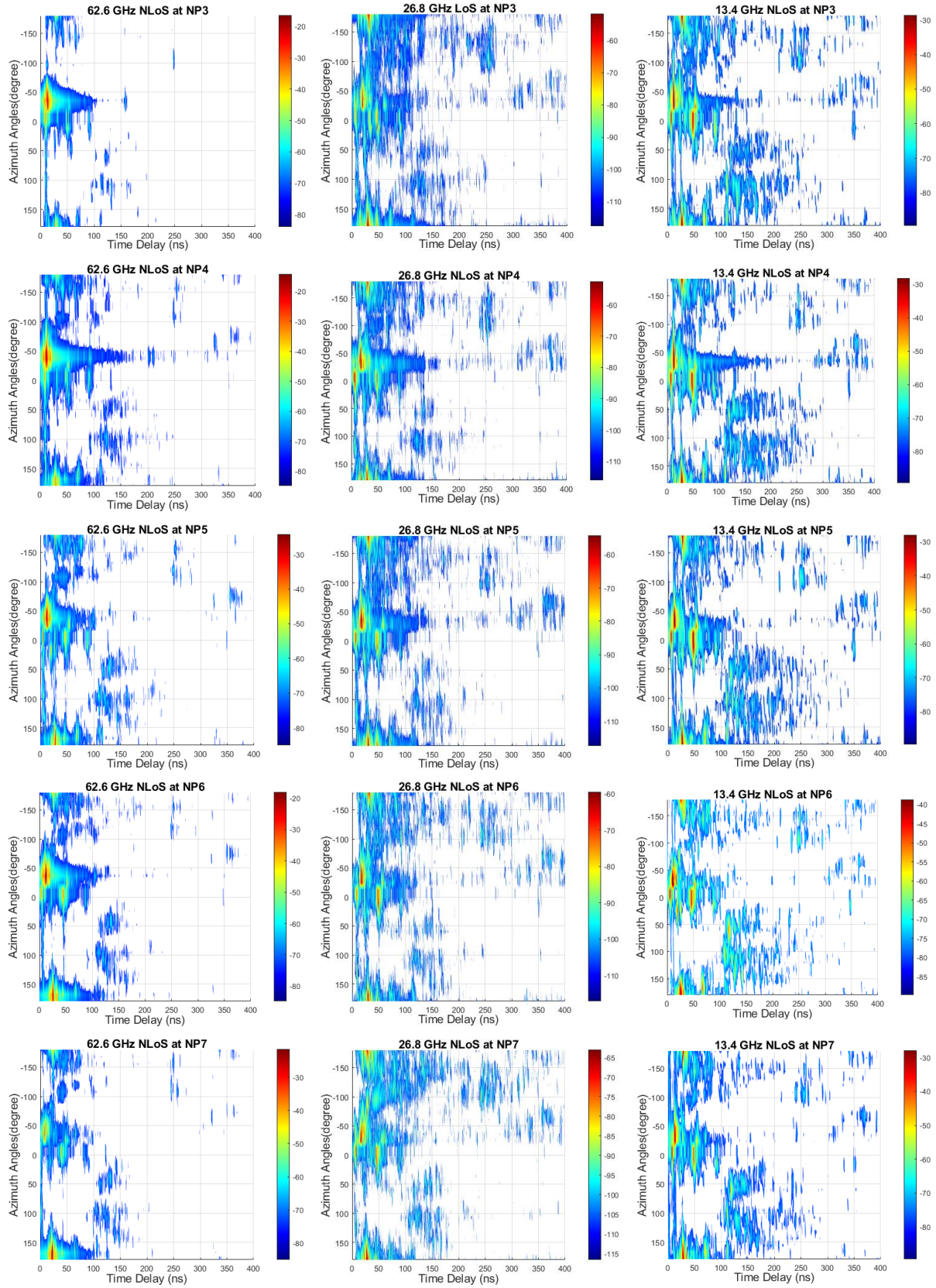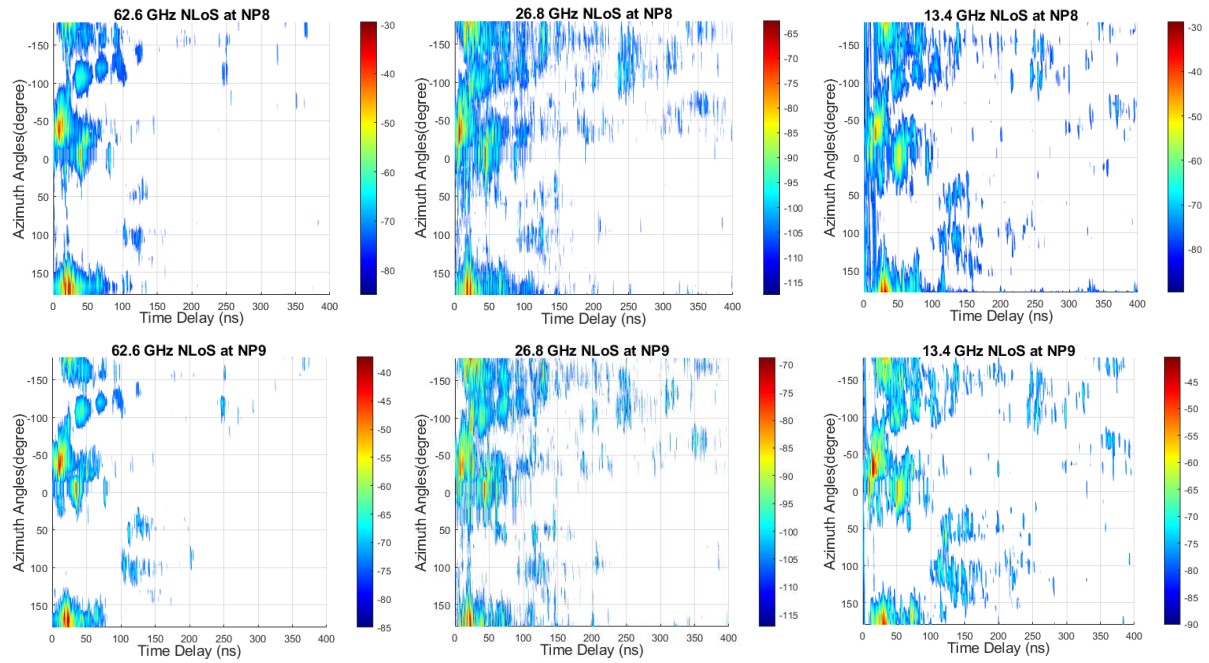
Figure 5-53 Tx PDPs as a function of azimuth angles at 0º elevation angle and at each position for all bands
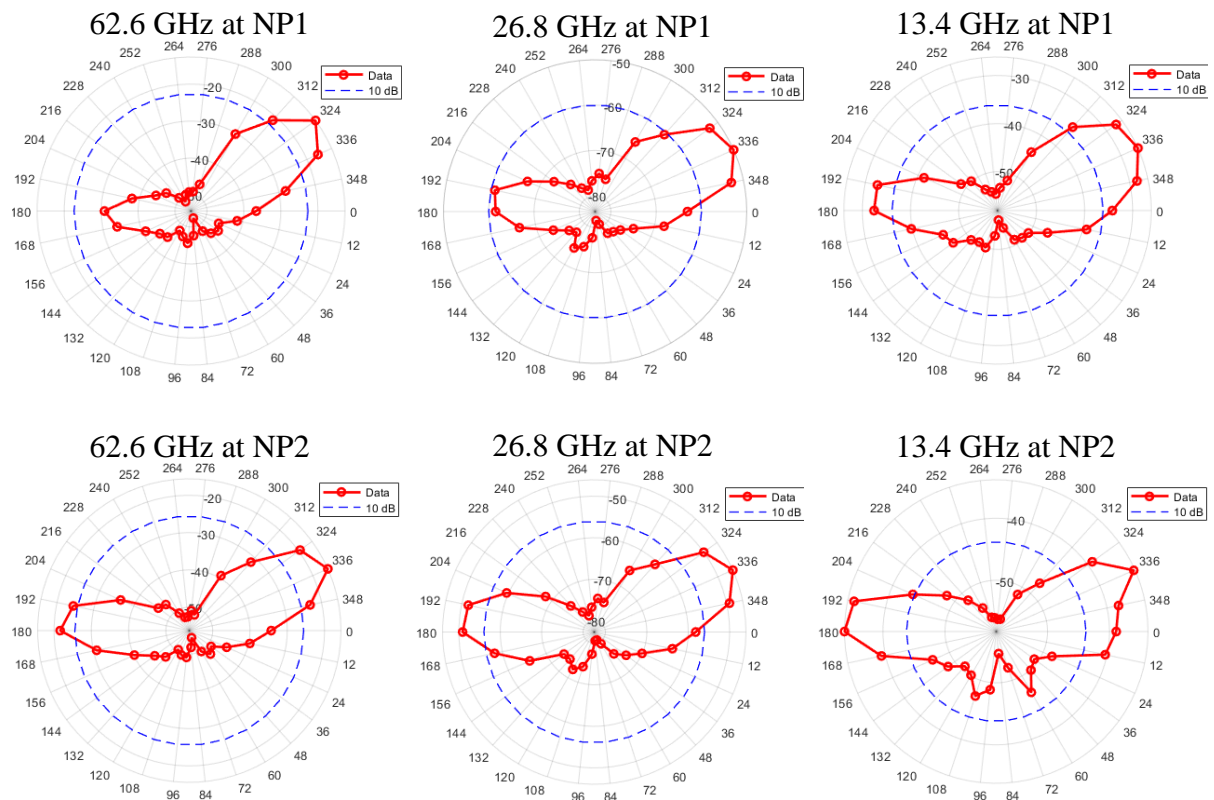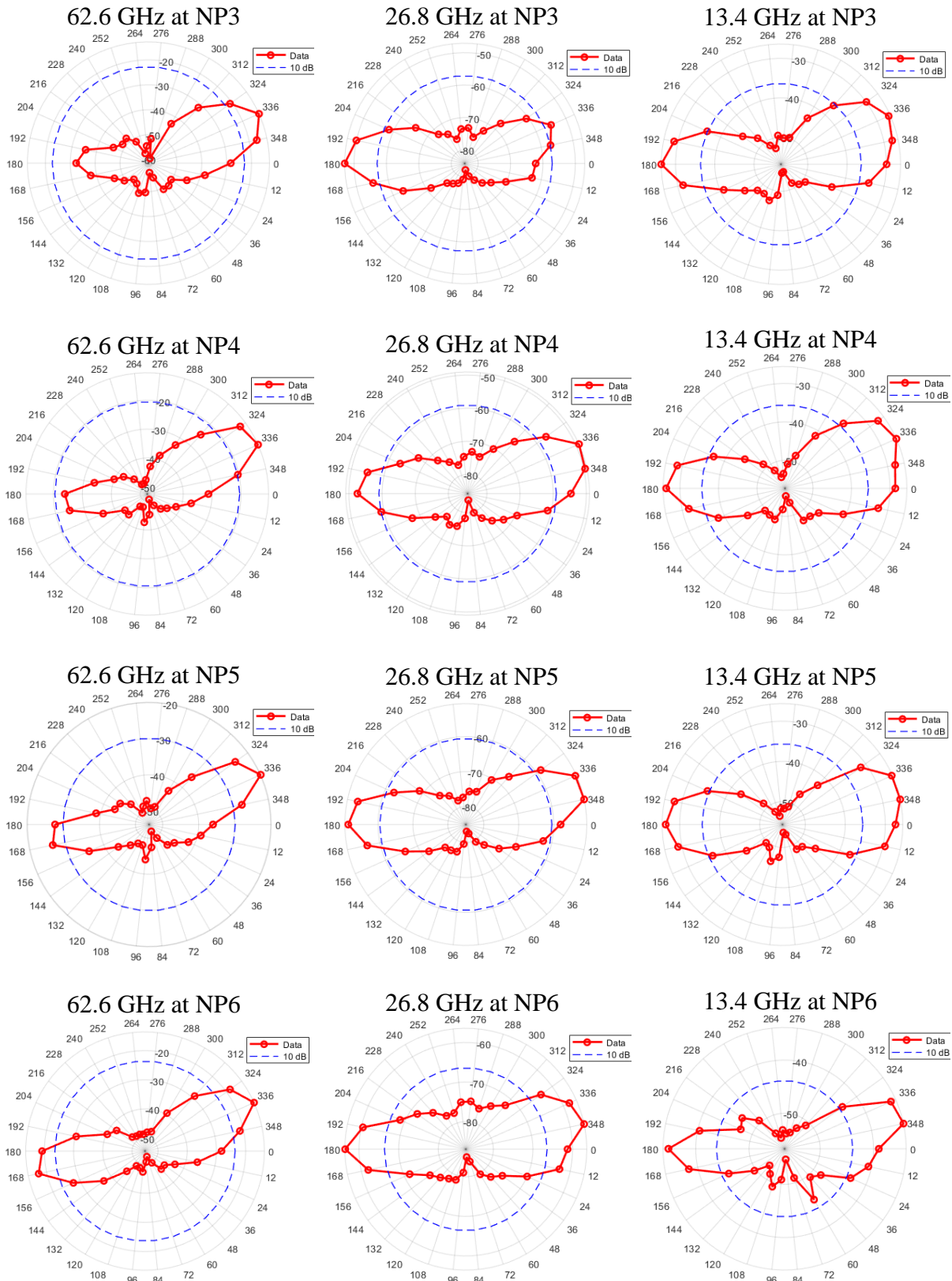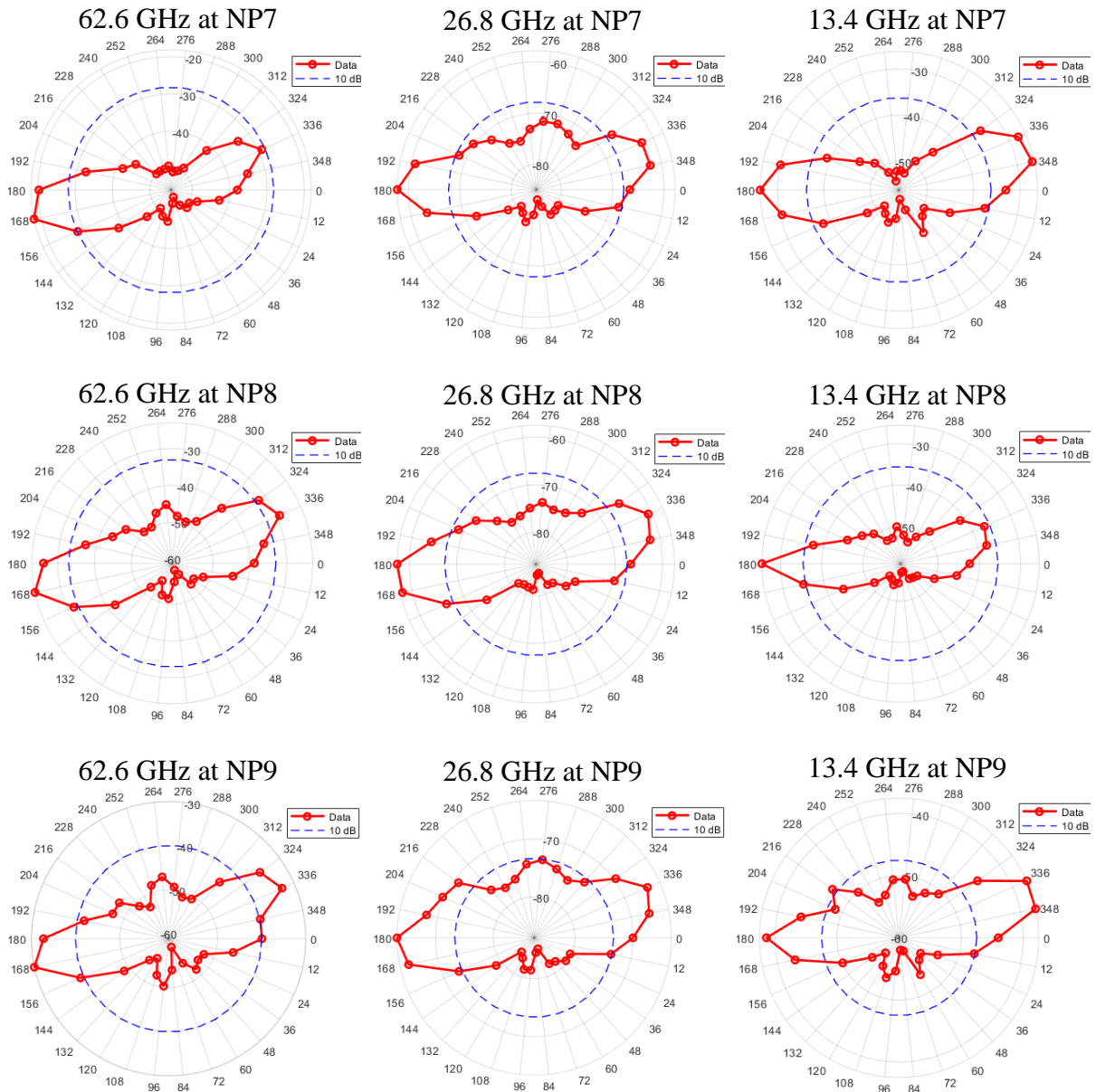
Figure 5-54 Polar plots of the received power as a function of Tx azimuth angles at a 0º elevation angle for all bands and at each position

Figure 5-54 shows polar plots of the received power as a function of Tx2 azimuth angles from 0º to 360º in the clockwise direction with a step size of 12º for all bands, with a 10 dB threshold from the maximum power when the receiver was fixed at the azimuth angle of the strongest received power at each position. The figure shows that, at all positions, there were two lobes, one around the 336º angle and the other around the 180º angle, where the strongest AoD for all bands was around 336º angle at positions NP1, NP4, NP5 and NP6; while for the other positions, the trend varied among the bands. For the 62.6 GHz band, the strongest AoD stayed around 336º up to position NP6, then switched to the other side for the last three positions. In

contrast, the other two bands switched between the two lobes more times and were at the same angle at most of the positions. Moreover, it is noticeable that for the 13.4 GHz band, the power levels at both lobes were close to each other at most of the measured positions.

Table 5-21 Estimated AoD in azimuth and their RMS angular spread values

Centre frequency	Position No.	AoD	RMS angular spread	No. of lobes
13.4 GHz	NP1	335.59°	11.72°	2
	NP2	183.97°	9.11°	2
	NP3	182.63°	9.27°	2
	NP4	340.98°	15.39°	2
	NP5	347.98°	13.69°	2
	NP6	348.28°	14.02°	2
	NP7	180.21°	7.99°	2
	NP8	178.81°	3.59°	1
	NP9	342.11°	9.31°	2
26.8 GHz	NP1	335.59°	8.74°	1
	NP2	336.45°	8.18°	2
	NP3	182.61°	7.14°	2
	NP4	342.46°	9.56°	2
	NP5	342.37°	8.84°	2
	NP6	346.77°	12.62°	2
	NP7	181.42°	7.87°	2
	NP8	174.89°	8.96°	2
	NP9	181.86°	14.87°	2
62.6 GHz	NP1	325.99°	6.78°	1
	NP2	334.28°	7.05°	2
	NP3	337.81°	6.88°	1
	NP4	332.49°	6.86°	1
	NP5	334.51°	6.95°	2
	NP6	334.77°	6.80°	2
	NP7	172.55°	5.82°	1
	NP8	170.62°	6.91°	2
	NP9	170.99°	6.90°	2

Table 5-21 presents the estimated values of the AoD in azimuth for the strongest lobe and their RMS angular spread within 10 dB from the maximum for all bands and at each measurement position. The table shows that the AoD at most positions was within the same direction, which is indicated by the two red dashed lines in figure 5-40. At the last three positions, the strongest transmission lobe was around the 180° angle for all bands, when Tx2 was pointing towards the metallic curved wall of the Calman Centre, as shown in figure 5-40. However, for the 13.4 GHz

band, the received power levels at position NP9 for the two lobes were close to each other, as shown in figure 5-54. The number of lobes was 2 at most of the positions for the first two bands, which shows the ability of the signals in these bands to travel long distances before losing their strength in this environment.

Figure 5-55 shows that the AoD at all the positions was mainly at one of two directions, the first representing when the Tx antenna was pointing between the two red dashed lines in figure 5-40, and the second representing when the Tx antenna was pointing to the metallic wall at the left hand side of Tx2. Furthermore, most of the positions showed a strong AoD when the transmitter antenna at Tx2 was pointing between the two red dashed lines over all bands. The figure also highlights the similarity in azimuth AoD plots for all bands between NP4 to NP8 positions, where all of the bands switched at position NP7 to the second direction. Some differences in the azimuth AoD trends among the three bands could also be seen at positions NP2, NP3 and NP9.
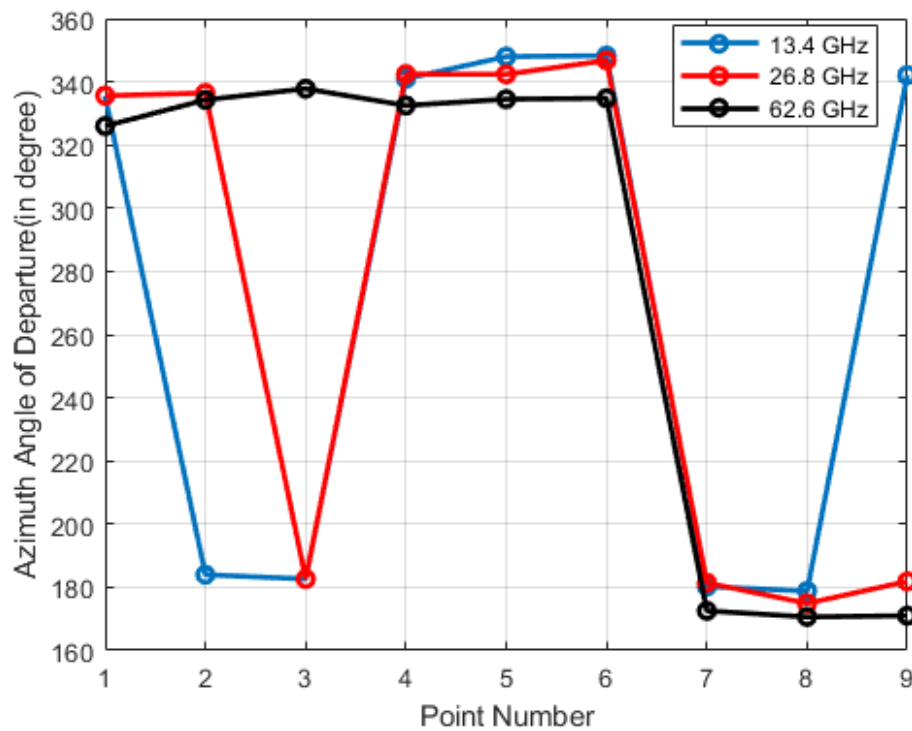
Figure 5-55 Azimuth AoD angles versus position
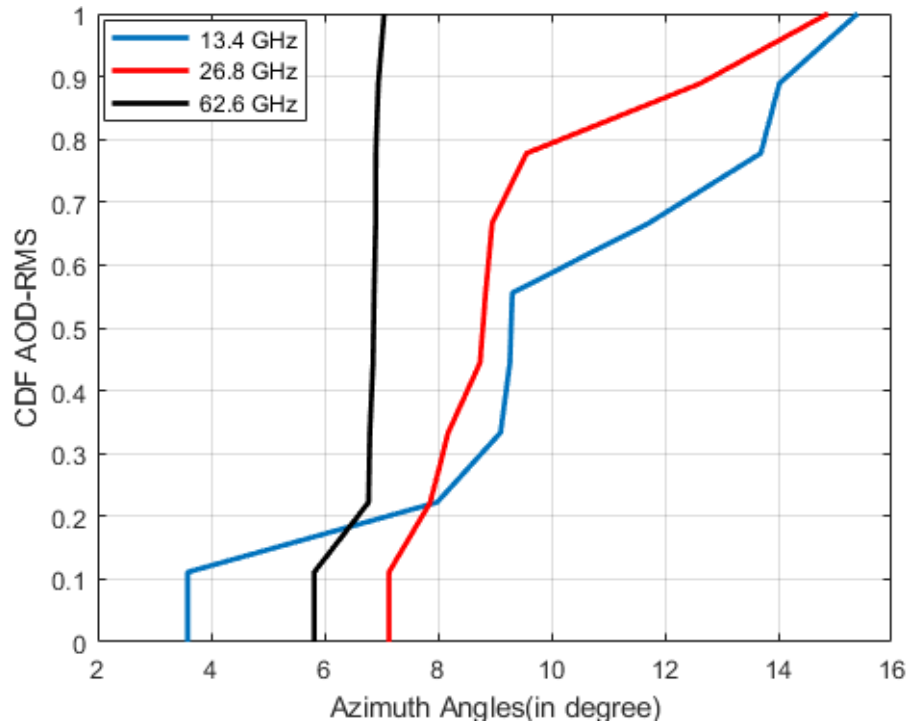
Figure 5-56 CDF of RMS AoD azimuth angular spread for all measured frequency bands

Figure 5-56 shows the CDF of the RMS AoD angular spread for all of the measured frequency bands. The figure demonstrates that the CDF of the RMS angular spread of the lower frequency bands was larger than that of the higher bands starting from about 20%. Table 5-22 presents the recommended CDF values of the RMS AoD angular spread in outdoor environments. The table shows a decrease in the CDF values of the RMS AoD angular spread as the frequency band increased at all of the recommended values.

Table 5-22 Values of the azimuth RMS AoD angular spread

CDF	13.4 GHz	26.8 GHz	62.6 GHz
50%	9.29	8.79	6.87
90%	14.16	12.85	6.96
95%	14.78	13.86	7.01

5.5 Summary and discussion

For the LoS measurements, the estimated AoA in azimuth and elevation and the AoD showed some pattern variations from one position to another for the different bands studied, where each frequency band responded differently to the environment's surroundings and the transmitter antenna's height. The 3D AoA in azimuth was within 8º around the zero degrees angle in the

indoor and outdoor scenarios for all bands, and the largest values of the CDF of the RMS AoA azimuth angular spread at 90% were at the 26.8 GHz band, while the smallest were at the 62.6 GHz band for most of the measured environments. In contrast, the 3D AoA in elevation was within 13° when the Tx antenna height was about 3 metres from the ground and within 6° for the other scenarios in the indoor environments. For the outdoor environment, the estimated elevation angle was within 3°, which might be due to the large distance between the Tx and Rx in this scenario. The largest values of the CDF of the RMS AoA elevation angular spread were at the 26.8 GHz band, while the smallest values were at the 62.6 GHz band, when the Tx antenna was at a 3 metres height from the ground; whereas some differences in the CDF patterns of the RMS AoA elevation angular spread values were noticeable for the other scenarios.

The estimated values of the AoD were within 3° around the zero degrees angle for all measured frequency bands in the indoor scenarios, while for the outdoor scenario, the estimated AoD values for the first two bands were within 1° around the zero degrees angle, and within 5° for the 62.6 GHz band. The largest values of the CDF of the RMS AoD angular spread at 90% were at the 26.8 GHz band for all scenarios studied, whereas the lowest values were at the 62.6 GHz band for most of the scenarios studied.

For the NLoS measurements, there were similarities in the patterns of the measured parameters of the estimated AoA in azimuth and elevation and the AoD at most positions. This is particularly evident true for the 3D patterns of the AoA in azimuth, where there was strong similarity between the bands at most of the positions. The largest values of the CDF of the RMS AoA azimuth angular spread at 90% were at the 13.4 GHz band when the Tx antenna was at a hight of 3 metres from the ground, while the largest values were at the 26.8 GHz band for the other scenarios, and the smallest values were at the 62.6 GHz band for all scenarios studied. For the 3D AoA in elevation, the estimated values were within 9° around the zero degrees elevation angle for all bands and in all scenarios. Furthermore, there was a strong similarity in AoA patterns between the 13.4 GHz and 62.6 GHz bands for most of the positions in all scenarios. On the other hand, there were some variations in the CDF of the RMS AoA elevation angular spread values between the bands from one scenario to another. For the AoD, the estimated values for the NLoS scenarios showed similar trends for all measured bands at most positions, where the values of the first two bands were close to each other at most positions. The largest and smallest values of the CDF of the RMS AoD angular spread at 90% were at the 13.4 GHz band and 62.6 GHz, respectively, for most of the scenarios studied.

From this summary, it can be seen that there was no dominant trend for all the measured parameters between the frequency bands for all measured environment. However, the 26.8 GHz and 62.6 GHz bands showed the highest and lowest values respectively, for most of the measured parameters for all the studied environments. While the 13.4 GHz band showed the highest values at some other parameters. This means that the results mainly, effected by the environments contents and how the shape and properties of these contents responding to the incident signals at different wavelengths which may require more focus on the propagation properties of the mmWave in these material. The directional measurements show that the mmWaves can be received with an acceptable power level even in the NLoS scenarios at different positions after several number of reflection orders which give a good information about the use of the high data rate data systems for 5G networks design.

CHAPTER 6

CONCLUSION AND FUTURE WORK

The question highlighted at the start of this work was to what extent there is a frequency dependency for different channel characteristics in the mmWave frequency bands above 6 GHz. A summary of the work performed in this thesis and recommendations for future work are presented in this chapter.

This thesis presented multi-band (above 6 GHz) ultra-wideband channel measurements up to 6 GHz bandwidth, carried out in three different indoor (i.e. large office, factory like and small office) and an outdoor (street canyon) environments in LoS and NLoS situations at the science site of Durham University in order to investigate mainly the frequency dependency of various channel characteristics such as path loss, delay spread and angular spread parameters. Two different measurement set up were used to measure these parameters, the first one performed in three indoor environments to measure the path loss and delay spread where a 3D steerable antenna at the Tx and an omnidirectional antenna at the Rx were used. While the second measurements were conducted in three indoor environments and one outdoor scenario using a 3D steerable antenna at both the Tx and Rx sides to measure the angular spread parameters at both ends of the link. For the first set two path loss models were used (i.e. close-in and floating intercept path loss) and maximum excess delay, average, RMS delay spread were studied. In the second set of measurements different angular parameters were studied such as the angle of arrival, angle of departure and RMS angular spread.

In this project, a wide-range literature review was provided for different indoor and outdoor propagation measurements performed in similar frequency bands in the mmWave bands, in order to better understand the obtained results in the perspective of prior research. The measurement details were described such as measurement environment layouts, sounding and simulation techniques used, measurements set-up and procedure including antenna type and heights at both the Tx and Rx sides.

Finally, primary results of multi-band wideband measurements at different indoor and outdoor channels were explained to offer understanding for next generation radio system channel models.

In general, for all the measured parameters there was no clear direct link between the variation in the calculated values and the frequency bands over all scenarios. However, the results mainly were affected by the contents of each scenario, where the material properties (i.e. electromagnetic reflection, transmission coefficients, dielectric constants and indices of refraction) are highly dependent on the frequency band used [55].

A- The first set of measurements were performed at five different frequency bands (i.e. 13.4 GHz, 26.8 GHz, 54.2 GHz, 62.6 GHz and 70 GHz), two omnidirectional path loss models were computed, the CI and FI models at all the three indoor environments in both LoS and NLoS situations and different time dispersion parameters were estimated such as the excess, average and RMS delay spread. There was high similarity between the equivalent parameters of the two path loss models (i.e. **n** compared to **β** and **σ** for both models) for each frequency band.

  1- For the LoS path loss, the large office scenario showed the highest values for all frequency bands, while the small office showed the lowest values. The highest and lowest values of standard deviation were at the small office and the large office scenarios respectively for both models, and the 26.8 GHz band showed the highest values at all scenarios.

    In terms of time dispersion parameters, there was a variation in the pattern from one scenario to another in the values of the CDF of RMS delay spread at 90%. However, the 13.4 GHz band and 62.6 GHz band showed the highest and lowest values respectively in most of the environments. It is noticeable that, there was high similarity in the values of CDF of the RMS delay spread between 54.2 GHz band and 70 GHz band at all of the measured scenarios.

  2- For the NLoS path loss, the highest and lowest values for both (n) and (β) at most of the bands were at the small office scenario and large office scenario respectively. There was a variation in the values of (n) and (β) between the bands at each scenario, where the highest values in most of the scenarios were at the 62.6 GHz band for both. While the lowest values for (n) were at the 54.2 GHz band and for (β) at the 26.8 GHz band at

211

most of the environments. For the standard deviation values the highest and lowest values at most of the bands were in the large office and small office scenarios respectively for both models, where the highest values were at 70 GHz in most of the scenarios.

In terms of time dispersion parameters, the CDF of the RMS delay spread at 90% values, showed a variation in the pattern from one scenario to another, where the highest and lowest values in most of the bands were at the factory like and large office environments respectively. The lowest values of the CDF at 90% were at the 62.6 GHz band at most of the measured scenarios. There was high similarity for NLoS situation also, in the CDF of the RMS delay spread values between the 54.2 GHz band and 70 GHz band at all the measured environments.

B- The second set of measurements were conducted at three different frequency bands (i.e. 13.4 GHz, 26.8 GHz, 62.6 GHz) using a 3D positioner to cover full rotation in azimuth plane at different elevation angles. From these set of measurements different angular parameters were estimated such as AoA, AoD and the RMS angular spread at both the Tx and Rx for LoS and NLoS situations at three indoor environments (i.e. large office, factory like and small office) and one outdoor scenario (street canyon).

1- For the LoS measurements, the estimated AoA in azimuth and elevation and the AoD showed variations in the pattern from one position to another for each frequency band studied, where each frequency band responded differently to the environment's surroundings and the transmitter antenna's height. The 3D AoA in azimuth was within 8° around the zero degrees angle in the indoor and outdoor scenarios for all bands, and the largest values of the CDF of the RMS AoA azimuth angular spread at 90% were at the 26.8 GHz band, while the smallest were at the 62.6 GHz band for most of the measured environments. In contrast, the 3D AoA in elevation was within 13° when the Tx antenna height was about 3 metres from the ground and within 6° for the other scenarios in the indoor environments. For the outdoor environment, the estimated elevation angle was within 3°, which might be due to the large distance between the Tx and Rx in this scenario. The smallest values of the CDF of the RMS of AoA in elevation were at the 62.6 GHz band for all scenarios, while the largest values were at the 26.8

GHz band, when the Tx antenna was at a 3 metres height from the ground; whereas the 13.4 GHz band showed the largest values for the other scenarios.

The estimated values of the AoD were within 3° around the zero degrees angle for all measured frequency bands in the indoor scenarios, while for the outdoor scenario, the estimated AoD values for the first two bands were within 1° around the zero degrees angle, and within 5° for the 62.6 GHz band. The largest values of the CDF of the RMS AoD angular spread at 90% were at the 26.8 GHz band for all scenarios studied, whereas the lowest values were at the 62.6 GHz band for most of the scenarios studied.

2- For the NLoS measurements, there were similarities in the patterns of the measured parameters of the estimated AoA in azimuth and elevation and the AoD at most of the positions. This is particularly true for the 3D patterns of the AoA in azimuth, where there was strong similarity between the bands at most of the positions. The largest values of the CDF of the RMS AoA azimuth angular spread at 90% were at the 13.4 GHz band when the Tx antenna was at a hight of 3 metres from the ground, while the largest values were at the 26.8 GHz band for the other scenarios, and the smallest values were at the 62.6 GHz band for all scenarios studied. For the 3D AoA in elevation, the estimated values were within 9° around the zero degrees elevation angle for all bands and in all scenarios. Furthermore, there was a strong similarity in AoA patterns between the 13.4 GHz and 62.6 GHz bands for most of the positions in all scenarios. On the other hand, there were some variations in the CDF of the RMS AoA elevation angular spread values between the bands from one scenario to another.

For the AoD, the estimated values for the NLoS scenarios showed similar trends for all measured bands at most positions, where the values of the first two bands were close to each other. The largest and smallest values of the CDF of the RMS AoD angular spread at 90% were at the 13.4 GHz band and 62.6 GHz, respectively, for most of the scenarios studied.

From this summary, it can be seen there was no dominant trend for all the measured parameters between the frequency bands for all measured environment. The results were mainly affected by the environments contents.

213

Future research possibilities and recommendations

1- Conducting measurements to study channel parameters in other common indoor and outdoor environments such as train stations, airports, shopping malls.

2- Investigating the shadowing of human body, ground and ceiling reflection and absorption effects in different indoor environments including various types of floors such as carpeted, wood, Marble, Ceramic Flooring.

3- Studying the common building materials properties and propagation at different mmWave frequency bands, where the values of the extracted parameters were mainly dependent on the environment's contents.

4- Regarding the directional measurements, improvement in the C programmes to reduce the time for collecting data could be done to perform measurements for larger number of points in each scenario and at more indoor and outdoor environments.

References

[1]   N. S. a. Networks, "2020: Beyond 4G: Radio Evaluation for the Gigabit Experience," 2011.

[2]   M. K. Samimi and T. S. Rappaport, "Characterization of the 28 GHz millimeter-wave dense urban channel for future 5G mobile cellular," *NYU Wireless TR,* vol. 1, 2014.

[3]   T. S. Rappaport, *Wireless communications : principles and practice*, 2nd ed. ed. Upper Saddle River, N.J. ; London: Upper Saddle River, N.J. ; London : Prentice Hall PTR, 2002.

[4]   B. Sklar, "Rayleigh fading channels in mobile digital communication systems .I. Characterization," *IEEE Communications Magazine,* vol. 35, no. 7, pp. 90-100, 1997, doi: 10.1109/35.601747.

[5]   S. Salous, *Radio propagation measurement and channel modelling.* Hoboken: John Wiley & Sons Inc., 2013, pp. xxi, 399 p.

[6]   J. J. Egli, "Radio Propagation above 40 MC over Irregular Terrain," *Proceedings of the IRE,* vol. 45, no. 10, pp. 1383-1391, 1957, doi: 10.1109/JRPROC.1957.278224.

[7]   D. C. E., "Radio networks and radio links surveys derived by computer from a terrain data base.," ed, 8 December 01, 1979.

[8]   E. T., *Foundations for Microstrip Circuit design.* Wiley, 1992.

[9]   A. G. Longley and P. L. Rice, "Prediction of tropospheric radio transmission loss over irregular terrain. A computer method-1968," INSTITUTE FOR TELECOMMUNICATION SCIENCES BOULDER CO, 1968.

[10]   Y. Okumura, "Field strength and its variability in VHF and UHF land-mobile radio service," *Rev. Electr. Commun. Lab.,* vol. 16, pp. 825-873, 1968 1968.

[11]   V. M. Hinostroza, "Indoor wideband Mobile Radio Channel Characterisation System," PhD, Electrical and Electronics engineering, Institution of Science and Technology Manchester, 2002.

[12]   P. Bello, "Measurement of random time-variant linear channels," *IEEE Transactions on Information Theory,* vol. 15, no. 4, pp. 469-475, 1969, doi: 10.1109/TIT.1969.1054332.

[13]   G. R. Maccartney, T. S. Rappaport, S. Sun, and S. Deng, "Indoor Office Wideband Millimeter-Wave Propagation Measurements and Channel Models at 28 and 73 GHz for Ultra-Dense 5G Wireless Networks," *IEEE Access,* vol. 3, pp. 2388-2424, 2015, doi: 10.1109/ACCESS.2015.2486778.

[14]   M. Samimi *et al.,* "28 GHz Angle of Arrival and Angle of Departure Analysis for Outdoor Cellular Communications Using Steerable Beam Antennas in New York City," in *2013 IEEE 77th Vehicular Technology Conference (VTC Spring),* 2-5 June 2013 2013, pp. 1-6, doi: 10.1109/VTCSpring.2013.6691812.

[15]   I. T. Union, "Multipath propagation and parameterization of its characteristics," in *Recommendation ITU-R P.1407-7,* ed, (08/2019).

[16]   T. S. Rappaport, E. Ben-Dor, J. N. Murdock, and Y. Qiao, "38 GHz and 60 GHz angle-dependent propagation for cellular & peer-to-peer wireless communications," in *2012 IEEE International Conference on Communications (ICC),* 10-15 June 2012 2012, pp. 4568-4573, doi: 10.1109/ICC.2012.6363891.

[17]   X. Hao, T. S. Rappaport, R. J. Boyle, and J. H. Schaffner, "Measurements and models for 38-GHz point-to-multipoint radiowave propagation," *IEEE Journal on Selected Areas in Communications,* vol. 18, no. 3, pp. 310-321, 2000, doi: 10.1109/49.840191.

[18]   Y. Chang, S. Baek, S. Hur, Y. Mok, and Y. Lee, "A novel dual-slope mm-Wave channel model based on 3D ray-tracing in urban environments," in *2014 IEEE 25th Annual International Symposium on Personal, Indoor, and Mobile Radio Communication (PIMRC),* 2-5 Sept. 2014 2014, pp. 222-226, doi: 10.1109/PIMRC.2014.7136164.

[19]   J. Liang, M. Kim, and J. Lee, "A geometrical approach for multipath characteristics study with 2 8 GHz measurements," in *2015 17th International Conference on Advanced Communication Technology (ICACT)*, 1-3 July 2015 2015, pp. 427-430, doi: 10.1109/ICACT.2015.7224831.

[20]   G. R. MacCartney, Z. Junhong, N. Shuai, and T. S. Rappaport, "Path loss models for 5G millimeter wave propagation channels in urban microcells," in *2013 IEEE Global Communications Conference (GLOBECOM)*, 9-13 Dec. 2013 2013, pp. 3948-3953, doi: 10.1109/GLOCOM.2013.6831690.

[21]   G. R. MacCartney, M. K. Samimi, and T. S. Rappaport, "Omnidirectional path loss models in New York City at 28 GHz and 73 GHz," in *2014 IEEE 25th Annual International Symposium on Personal, Indoor, and Mobile Radio Communication (PIMRC)*, 2-5 Sept. 2014 2014, pp. 227-231, doi: 10.1109/PIMRC.2014.7136165.

[22]   T. S. Rappaport, G. R. MacCartney, M. K. Samimi, and S. Sun, "Wideband Millimeter-Wave Propagation Measurements and Channel Models for Future Wireless Communication System Design," *IEEE Transactions on Communications,* vol. 63, no. 9, pp. 3029-3056, 2015, doi: 10.1109/TCOMM.2015.2434384.

[23]   X. Raimundo, S. El-Faitori, Y. Cao, and S. Salous, "Outdoor directional radio propagation measurements in the V-band," in *2018 IEEE 29th Annual International Symposium on Personal, Indoor and Mobile Radio Communications (PIMRC)*, 9-12 Sept. 2018 2018, pp. 790-794, doi: 10.1109/PIMRC.2018.8580771.

[24]   Y. Azar *et al.*, "28 GHz propagation measurements for outdoor cellular communications using steerable beam antennas in New York city," in *2013 IEEE International Conference on Communications (ICC)*, 9-13 June 2013 2013, pp. 5143-5147, doi: 10.1109/ICC.2013.6655399.

[25]   G. R. MacCartney and T. S. Rappaport, "73 GHz millimeter wave propagation measurements for outdoor urban mobile and backhaul communications in New York City," in *2014 IEEE International Conference on Communications (ICC)*, 10-14 June 2014 2014, pp. 4862-4867, doi: 10.1109/ICC.2014.6884090.

[26]   E. Ben-Dor, T. S. Rappaport, Y. Qiao, and S. J. Lauffenburger, "Millimeter-Wave 60 GHz Outdoor and Vehicle AOA Propagation Measurements Using a Broadband Channel Sounder," in *2011 IEEE Global Telecommunications Conference - GLOBECOM 2011*, 5-9 Dec. 2011 2011, pp. 1-6, doi: 10.1109/GLOCOM.2011.6133581.

[27]   T. S. Rappaport *et al.*, "Millimeter Wave Mobile Communications for 5G Cellular: It Will Work!," *IEEE Access,* vol. 1, pp. 335-349, 2013, doi: 10.1109/ACCESS.2013.2260813.

[28]   G. R. Maccartney, T. S. Rappaport, M. K. Samimi, and S. Sun, "Millimeter-Wave Omnidirectional Path Loss Data for Small Cell 5G Channel Modeling," *IEEE Access,* vol. 3, pp. 1573-1580, 2015, doi: 10.1109/ACCESS.2015.2465848.

[29]   A. I. Sulyman, A. T. Nassar, M. K. Samimi, G. R. Maccartney, T. S. Rappaport, and A. Alsanie, "Radio propagation path loss models for 5G cellular networks in the 28 GHZ and 38 GHZ millimeter-wave bands," *IEEE Communications Magazine,* vol. 52, no. 9, pp. 78-86, 2014, doi: 10.1109/MCOM.2014.6894456.

[30]   A. I. Sulyman, A. Alwarafy, G. R. MacCartney, T. S. Rappaport, and A. Alsanie, "Directional Radio Propagation Path Loss Models for Millimeter-Wave Wireless Networks in the 28-, 60-, and 73-GHz Bands," *IEEE Transactions on Wireless Communications,* vol. 15, no. 10, pp. 6939-6947, 2016, doi: 10.1109/TWC.2016.2594067.

[31]   M. K. Samimi, T. S. Rappaport, and G. R. MacCartney, "Probabilistic Omnidirectional Path Loss Models for Millimeter-Wave Outdoor Communications," *IEEE Wireless Communications Letters,* vol. 4, no. 4, pp. 357-360, 2015, doi: 10.1109/LWC.2015.2417559.

REFERENCES

[32]   M. K. Samimi and T. S. Rappaport, "Ultra-wideband statistical channel model for non line of sight millimeter-wave urban channels," in *2014 IEEE Global Communications Conference*, 8-12 Dec. 2014 2014, pp. 3483-3489, doi: 10.1109/GLOCOM.2014.7037347.

[33]   S. Sun *et al.*, "Propagation path loss models for 5G urban micro-and macro-cellular scenarios," 2016: IEEE, pp. 1-6.

[34]   T. S. Rappaport, F. Gutierrez, E. Ben-Dor, J. N. Murdock, Y. Qiao, and J. I. Tamir, "Broadband Millimeter-Wave Propagation Measurements and Models Using Adaptive-Beam Antennas for Outdoor Urban Cellular Communications," *IEEE Transactions on Antennas and Propagation,* vol. 61, no. 4, pp. 1850-1859, 2013, doi: 10.1109/TAP.2012.2235056.

[35]   J. N. Murdock, E. Ben-Dor, Y. Qiao, J. I. Tamir, and T. S. Rappaport, "A 38 GHz cellular outage study for an urban outdoor campus environment," in *2012 IEEE Wireless Communications and Networking Conference (WCNC)*, 1-4 April 2012 2012, pp. 3085-3090, doi: 10.1109/WCNC.2012.6214335.

[36]   T. S. Rappaport and S. Deng, "73 GHz wideband millimeter-wave foliage and ground reflection measurements and models," in *2015 IEEE International Conference on Communication Workshop (ICCW)*, 8-12 June 2015 2015, pp. 1238-1243, doi: 10.1109/ICCW.2015.7247347.

[37]   G. R. MacCartney, M. K. Samimi, and T. S. Rappaport, "Exploiting directionality for millimeter-wave wireless system improvement," in *2015 IEEE International Conference on Communications (ICC)*, 8-12 June 2015 2015, pp. 2416-2422, doi: 10.1109/ICC.2015.7248687.

[38]   S. Sun, T. A. Thomas, T. S. Rappaport, H. Nguyen, I. Z. Kovacs, and I. Rodriguez, "Path Loss, Shadow Fading, and Line-of-Sight Probability Models for 5G Urban Macro-Cellular Scenarios," in *2015 IEEE Globecom Workshops (GC Wkshps)*, 6-10 Dec. 2015 2015, pp. 1-7, doi: 10.1109/GLOCOMW.2015.7414036.

[39]   S. Salous, X. Raimundo, and A. Cheema, "Path loss model in typical outdoor environments in the 50–73 GHz band," 2017: IEEE, pp. 721-724.

[40]   D. Dupleich, R. Müller, S. Skoblikov, J. Luo, G. Del Galdo, and R. S. Thomä, "Multi-band Double-directional 5G Street Canyon Measurements in Germany," 2019: IEEE, pp. 123-127.

[41]   A. M. Al-Samman, T. A. Rahman, M. H. Azmi, and M. N. Hindia, "Large-scale path loss models and time dispersion in an outdoor line-of-sight environment for 5G wireless communications," *AEU-International Journal of Electronics and Communications,* vol. 70, no. 11, pp. 1515-1521, 2016.

[42]   B. Kim, H. Kim, C. Dongkyu, Y. Lee, H. Wonbin, and P. Jeongho, "28 GHz propagation analysis for passive repeaters in NLOS channel environment," in *2015 9th European Conference on Antennas and Propagation (EuCAP)*, 13-17 April 2015 2015, pp. 1-4.

[43]   M. Kyro *et al.*, "Measurement based path loss and delay spread modeling in hospital environments at 60 GHz," *IEEE Transactions on Wireless Communications,* vol. 10, no. 8, pp. 2423-2427, 2011.

[44]   D. Cassioli and N. Rendevski, "A statistical model for the shadowing induced by human bodies in the proximity of a mmWaves radio link," in *2014 IEEE International Conference on Communications Workshops (ICC)*, 10-14 June 2014 2014, pp. 14-19, doi: 10.1109/ICCW.2014.6881165.

[45]   S. Geng, J. Kivinen, X. Zhao, and P. Vainikainen, "Millimeter-Wave Propagation Channel Characterization for Short-Range Wireless Communications," *IEEE Transactions on Vehicular Technology,* vol. 58, no. 1, pp. 3-13, 2009, doi: 10.1109/TVT.2008.924990.

[46]   H. Sawada, K. Fujita, S. Kato, K. Sato, and H. Harada, "Impulse response model for the cubicle environments at 60GHz," in *2010 Asia-Pacific Microwave Conference*, 7-10 Dec. 2010 2010, pp. 2131-2134.

[47]   J. Wang, R. V. Prasad, and I. Niemegeers, "Analyzing 60 GHz radio links for indoor communications," *IEEE Transactions on Consumer Electronics,* vol. 55, no. 4, pp. 1832-1840, 2009, doi: 10.1109/TCE.2009.5373739.

[48]   C. Lounis, N. Hakem, and G. Y. Delisle, *Characterization of the 60 GHz channel in underground mining environment*. 2012, pp. 1-2.

[49]   A. G. Siamarou, "A Wideband Channel Sounding Technique at Millimetre-Waves and Experiment in an Indoor 63.4-64.4GHz Picocell," in *11th European Wireless Conference 2005 - Next Generation wireless and Mobile Communications and Services*, 10-13 April 2005 2006, pp. 1-5.

[50]   M. Fryziel, C. Loyez, L. Clavier, N. Rolland, and P. A. Rolland, "Path-loss model of the 60-GHz indoor radio channel," *Microwave and Optical Technology Letters,* vol. 34, pp. 158-162, 08/05 2002, doi: 10.1002/mop.10402.

[51]   S. Deng, M. K. Samimi, and T. S. Rappaport, "28 GHz and 73 GHz millimeter-wave indoor propagation measurements and path loss models," in *2015 IEEE International Conference on Communication Workshop (ICCW)*, 8-12 June 2015 2015, pp. 1244-1250, doi: 10.1109/ICCW.2015.7247348.

[52]   G. R. MacCartney, S. Deng, and T. S. Rappaport, "Indoor office plan environment and layout-based mmWave path loss models for 28 GHz and 73 GHz," 2016: IEEE, pp. 1-6.

[53]   J. Ryan, G. R. MacCartney, and T. S. Rappaport, "Indoor office wideband penetration loss measurements at 73 GHz," in *2017 IEEE International Conference on Communications Workshops (ICC Workshops)*, 21-25 May 2017 2017, pp. 228-233, doi: 10.1109/ICCW.2017.7962662.

[54]   X. Raimundo, S. Salous, and A. A. Cheema, "Indoor radio propagation measurements in the V-band," in *Radio Propagation and Technologies for 5G (2016)*, 3-3 Oct. 2016 2016, pp. 1-5, doi: 10.1049/ic.2016.0068.

[55]   X. Raimundo, S. Salous, and A. Cheema, "Indoor dual polarised radio channel characterisation in the 54 and 70 GHz bands," *IET Microwaves, Antennas & Propagation,* vol. 12, no. 8, pp. 1287-1292, 2018, doi: 10.1049/iet-map.2017.0711.

[56]   K. Haneda *et al.*, "Indoor 5G 3GPP-like channel models for office and shopping mall environments," in *2016 IEEE International Conference on Communications Workshops (ICC)*, 23-27 May 2016 2016, pp. 694-699, doi: 10.1109/ICCW.2016.7503868.

[57]   A. Fagiani, M. Vogel, and S. Cerqueira Jr, "Material Characterization and Propagation Analysis of mm-Waves Indoor Networks," *Journal of Microwaves, Optoelectronics and Electromagnetic Applications,* vol. 17, no. 4, pp. 628-637, 2018.

[58]   N. Zhang, X. Yin, S. X. Lu, M. Du, and X. Cai, "Measurement-based angular characterization for 72 GHz propagation channels in indoor environments," in *2014 IEEE Globecom Workshops (GC Wkshps)*, 8-12 Dec. 2014 2014, pp. 370-376, doi: 10.1109/GLOCOMW.2014.7063459.

[59]   Y. Xing and T. S. Rappaport, "Propagation measurement system and approach at 140 GHz-moving to 6G and above 100 GHz," 2018: IEEE, pp. 1-6.

[60]   M. B. Majed, T. A. Rahman, O. A. Aziz, M. N. Hindia, and E. Hanafi, "Channel Characterization and Path Loss Modeling in Indoor Environment at 4.5, 28, and 38 GHz for 5G Cellular Networks," *International Journal of Antennas and Propagation,* vol. 2018, 2018.

[61]   F. Qamar, M. H. S. Siddiqui, K. Dimyati, K. A. B. Noordin, and M. B. Majed, "Channel characterization of 28 and 38 GHz MM-wave frequency band spectrum for the future 5G network," in *2017 IEEE 15th Student Conference on Research and Development (SCOReD)*, 13-14 Dec. 2017 2017, pp. 291-296, doi: 10.1109/SCORED.2017.8305376.

[62]   E. M. Vitucci *et al.*, "A Study on Dual-Directional Mm-wave Indoor Channel Characteristics," in *2019 13th European Conference on Antennas and Propagation (EuCAP)*, 31 March-5 April 2019 2019, pp. 1-5.

[63]   A. Al-Samman *et al.*, "Comparative Study of Indoor Propagation Model Below and Above 6 GHz for 5G Wireless Networks," *Electronics,* vol. 8, no. 1, p. 44, 2019.

[64]   J. Huang, Y. Liu, J. Sun, W. Zhang, and C. Wang, "Effects of antenna height and directivity on 60 GHz indoor channels," in *2017 IEEE/CIC International Conference on Communications in China (ICCC)*, 22-24 Oct. 2017 2017, pp. 1-5, doi: 10.1109/ICCChina.2017.8330423.

[65]   A. M. Al-Samman, T. Abd Rahman, and M. H. Azmi, "Indoor corridor wideband radio propagation measurements and channel models for 5G millimeter wave wireless communications at 19 GHz, 28 GHz, and 38 GHz Bands," *Wireless Communications and Mobile Computing,* vol. 2018, 2018.

[66]   D. Dupleich *et al.*, "Multi-band Indoor Propagation Characterization by Measurements from 6 to 60 GHz," in *2019 13th European Conference on Antennas and Propagation (EuCAP)*, 31 March-5 April 2019 2019, pp. 1-5.

[67]   Q. Wang, S. Li, X. Zhao, M. Wang, and S. Sun, "Wideband Millimeter-Wave Channel Characterization Based on LOS Measurements in an Open Office at 26GHz," in *2016 IEEE 83rd Vehicular Technology Conference (VTC Spring)*, 15-18 May 2016 2016, pp. 1-5, doi: 10.1109/VTCSpring.2016.7504532.

[68]   P. F. M. Smulders, "Statistical Characterization of 60-GHz Indoor Radio Channels," *IEEE Transactions on Antennas and Propagation,* vol. 57, no. 10, pp. 2820-2829, 2009, doi: 10.1109/TAP.2009.2030524.

[69]   S. Geng, J. Kivinen, and P. Vainikainen, "Propagation characterization of wideband indoor radio channels at 60 GHz," in *2005 IEEE International Symposium on Microwave, Antenna, Propagation and EMC Technologies for Wireless Communications*, 8-12 Aug. 2005 2005, vol. 1, pp. 314-317 Vol. 1, doi: 10.1109/MAPE.2005.1617912.

[70]   H. Zhao *et al.*, "28 GHz millimeter wave cellular communication measurements for reflection and penetration loss in and around buildings in New York city," 2013: IEEE, pp. 5163-5167.

[71]   S. Sun, G. R. MacCartney, and T. S. Rappaport, "Millimeter-wave distance-dependent large-scale propagation measurements and path loss models for outdoor and indoor 5G systems," in *2016 10th European Conference on Antennas and Propagation (EuCAP)*, 10-15 April 2016 2016, pp. 1-5, doi: 10.1109/EuCAP.2016.7481506.

[72]   S. Salous and Y. Gao, "Wideband measurements in indoor and outdoor environments in the 30 GHz and 60 GHz bands," in *2016 10th European Conference on Antennas and Propagation (EuCAP)*, 10-15 April 2016 2016, pp. 1-3, doi: 10.1109/EuCAP.2016.7481454.

[73]   S. Nie, M. K. Samimi, T. Wu, S. Deng, G. R. MacCartney Jr, and T. S. Rappaport, "73 GHz millimeter-wave indoor and foliage propagation channel measurements and results," *NYU WIRELESS Technical Report, TR-2014–003,* 2014.

[74]   S. Sun *et al.*, "Investigation of Prediction Accuracy, Sensitivity, and Parameter Stability of Large-Scale Propagation Path Loss Models for 5G Wireless Communications," *IEEE Transactions on Vehicular Technology,* vol. 65, no. 5, pp. 2843-2860, 2016, doi: 10.1109/TVT.2016.2543139.

[75]   K. Haneda, J. Järveläinen, A. Karttunen, M. Kyrö, and J. Putkonen, "Indoor short-range radio propagation measurements at 60 and 70 GHz," in *The 8th European Conference on Antennas and Propagation (EuCAP 2014)*, 6-11 April 2014 2014, pp. 634-638, doi: 10.1109/EuCAP.2014.6901839.

[76]   S. Salous, S. M. Feeney, X. Raimundo, and A. A. Cheema, "Wideband MIMO Channel Sounder for Radio Measurements in the 60 GHz Band," *IEEE Transactions on Wireless Communications,* vol. 15, no. 4, pp. 2825-2832, 2016, doi: 10.1109/TWC.2015.2511006.

[77]   S. Salous, A. Cheema, and X. Raimundo, "Radio channel propagation measurements using a multiband agile chirp sounder," in *2014 XXXIth URSI General Assembly and Scientific Symposium (URSI GASS),* 16-23 Aug. 2014 2014, pp. 1-4, doi: 10.1109/URSIGASS.2014.6929650.

[78]   M. K. Samimi and T. S. Rappaport, "3-D Millimeter-Wave Statistical Channel Model for 5G Wireless System Design," *IEEE Transactions on Microwave Theory and Techniques,* vol. 64, no. 7, pp. 2207-2225, 2016, doi: 10.1109/TMTT.2016.2574851.

Appendix A – Software Programs

A.1 C program

Program name: Control 3D positioner and record data

```c
#include <Windows.h>
#include <stdio.h>
#include <string.h>
#include <time.h>
#include <dos.h>
void main(void)
{
    unsigned timeout = 5000;
    HANDLE hComm;                   // Handle to the Serial port
    char   ComPortName[] = "COM5"; // Name of the Serial port(May Change) to be opened,
    BOOL   Status;
    printf("\n\n +========================================+");
    printf("\n |  Serial Transmission (Win32 API)       |");
    printf("\n +========================================+\n");
    /*-------------------------------- Opening the Serial Port ------------------------------------*/
    hComm = CreateFile(ComPortName,                 // Name of the Port to be Opened
            GENERIC_READ | GENERIC_WRITE,     // Read/Write Access
            0,                      // No Sharing, ports cant be shared
            NULL,                   // No Security
            OPEN_EXISTING,              // Open existing port only
            0,                      // Non Overlapped I/O
            NULL);                  // Null for Comm Devices
    if (hComm == INVALID_HANDLE_VALUE)
            printf("\n   Error! - Port %s can't be opened", ComPortName);
    else
            printf("\n   Port %s Opened\n ", ComPortName);
    /*------------------------------ Setting the Parameters for the SerialPort ------------------------------*/
    DCB dcbSerialParams = { 0 };                // Initializing DCB structure
    dcbSerialParams.DCBlength = sizeof(dcbSerialParams);
    Status = GetCommState(hComm, &dcbSerialParams);    //retreives  the current settings
    if (Status == FALSE)
            printf("\n   Error! in GetCommState()");
    dcbSerialParams.BaudRate = CBR_2400;      // Setting BaudRate = 2400
    dcbSerialParams.ByteSize = 8;           // Setting ByteSize = 8
    dcbSerialParams.StopBits = ONESTOPBIT;   // Setting StopBits = 1
    dcbSerialParams.Parity = NOPARITY;      // Setting Parity = None
    Status = SetCommState(hComm, &dcbSerialParams); //Configuring the port according to settings in DCB
    if (Status == FALSE)
    {
            printf("\n   Error! in Setting DCB Structure");
    }
    else
    {
            printf("\n   Setting DCB Structure Successfull\n");
            printf("\n       Baudrate = %d", dcbSerialParams.BaudRate);
```

```
                printf("\n      ByteSize = %d", dcbSerialParams.ByteSize);
                printf("\n      StopBits = %d", dcbSerialParams.StopBits);
                printf("\n      Parity  = %d", dcbSerialParams.Parity);
}
/*-------------------------------- Setting Timeouts -------------------------------------------*/
COMMTIMEOUTS timeouts = { 0 };
timeouts.ReadIntervalTimeout = 50;
timeouts.ReadTotalTimeoutConstant = 50;
timeouts.ReadTotalTimeoutMultiplier = 10;
timeouts.WriteTotalTimeoutConstant = 50;
timeouts.WriteTotalTimeoutMultiplier = 10;
if (SetCommTimeouts(hComm, &timeouts) == FALSE)
                printf("\n   Error! in Setting Time Outs");
else
                printf("\n\n   Setting Serial Port Timeouts Successfull \n\n");
/*---------------------------- Writing a Character to Serial Port------------------------------*/
        // Elevation
int j, z, R, Q, K, k, m, n, V, CS1, x;
n = -40;// min tilt angle
V = 40; // max tilt angle
x = V - n;
 /* printf("\n\n   Input the Tilt Step Size (in degree) Note: the max step size is:%d\n\n",x );
  scanf_s("  %d  ", &z);*/
z = 40; // step size
DWORD  dNoOFBytestoWrite;          // No of bytes to write into the port
DWORD  dNoOfBytesWritten = 0;       // No of bytes written to the port
for (j = n; j <= V; j = j + z)
{
        if (j < 0) {m = 360 + j;}
        else { m = j; }
        k = m;
        K = k * 100;
        R = (K * 100) % 256;
        Q = (K / 256) % 256;
        CS1 = (78 + (R + Q)) % 256;
        byte message[] = { 0xFF, 0x01, 0x00, 0x4B, 0x00, 0x00, 0x4c }; // zero degree
        dNoOFBytestoWrite = sizeof(message);
        Status = WriteFile(hComm, message, dNoOFBytestoWrite, &dNoOfBytesWritten, NULL);
        byte Message[] = { 255, 1, 0, 77, Q, R, CS1 };
        Status = WriteFile(hComm, Message, dNoOFBytestoWrite, &dNoOfBytesWritten, NULL);
        Sleep(10000);
        int i, X, E, D, CS;
        int y =60;// pan step size
        for (i = 0; i < 360; i = i + y)
        {
                X = i * 100;
                E = (X * 100) % 256;
                D = (X / 256) % 256;
                CS = (76 + (E + D)) % 256;
                printf("\n Pan angle is: %d and Tilt angle is:%d ", i, j);
                byte Message[] = { 255, 1, 0, 75, D, E, CS };// 0 degree
                Status = WriteFile(hComm, Message, dNoOFBytestoWrite, &dNoOfBytesWritten, NULL);
                if (Status == TRUE)
                        printf("\n\n   %s - Written to %s", message, ComPortName);
                else
```

222

```
                              printf("\n\n   Error %d in Writing to Serial Port", GetLastError());
                    printf("\n ========================================\n");
                    Sleep(timeout);
          }
          byte Message4[] = { 0xFF, 0x01, 0x00, 0x4B, 0x46, 0x00, 0x92 };// 180 degree
          Status = WriteFile(hComm, Message4, dNoOFBytestoWrite, &dNoOfBytesWritten, NULL);
          Sleep(5000);
          byte Message5[] = { 0xFF, 0x01, 0x00, 0x4B, 0x00, 0x00, 0x4c };// 0 degree
          Status = WriteFile(hComm, Message5, dNoOFBytestoWrite, &dNoOfBytesWritten, NULL);
          Sleep(5000);
     }
     byte Message6[] = { 255, 1, 0, 77, 0, 0, 78 };
     Status = WriteFile(hComm, Message6, dNoOFBytestoWrite, &dNoOfBytesWritten, NULL);
     Sleep(3000);
     char c = getch();
                    CloseHandle(hComm);//Closing the Serial Port
               printf("\n ============= The END ================= \n");
               char c = getch();
}
```

A.2 MATLAB Codes

1- The Omni-directional codes

Program name: PDP separation with switch for each 20cm

```matlab
close all
clear all
fs = 40*10^6; %sampling frequency
Nsections = 2440; %Total number of sweeps measured
SectionLength = fs*819.2*(10^-6); %Length of one sweep in samples
DataLength = fix(SectionLength/3); %Number of samples for bandwidth, adjust the number
accordingly (currently 3 as 6 GHz bandwidth and only wanted 2 GHz)
BW=6;% the total bandwidth of the measured data
datastart = 1000;
dataend = datastart+DataLength-1; %calculates the end of the bandwidth according to DataLength

signalIndexStart = 2000; %Start of pdp index for empty signal detection, MAA (see line 85 for
more info)
SignalIndexEnd = 3000; %end of pdp index for empty signal detection, make sure this is large
enough to capture data when beat note shifts
a=4000;  %%Noise start point
b=5000;  %%Noise end point
thresholdCutoff = 11; %dB level above noise used to find channels.

filenameStore = strcat('E:\OmniDirectional measuerments\PRO');%file to store
mkdir(filenameStore);
p1=0;
po=0;
for s = 1:1:23
    S = num2str(s);
 p1=p1+1;
 [p1]

filename = strcat('E:\OmniDirectional measuerments\np_Pan_',S,'_Tilt_-9');%file to read

Address = strcat(filename,'.rd16'); % Folder path containing the data to be processed
fid=fopen(Address);
rawdata = fread(fid,'uint16'); %rawdata from file
fclose(fid);
```

223

```matlab
ch1data = rawdata(1:1:length(rawdata));

%Extract the Vpp from file and convert raw data into voltage data
 regexstr = '(?<prefix>.*?)(?<numbers>([-]*(\d+[\,]*)+[\.]{0,1}\d*[eEdD]{0,1}[-
+]*\d*[i]{0,1})|([-]*(\d+[\,]*)*[\.]{1,1}\d+[eEdD]{0,1}[-+]*\d*[i]{0,1}))(?<suffix>.*)';
 Data1 = importdata(strcat(Address,'.srdc'));
 result = regexp(Data1{15,1}, regexstr, 'names');
 Vpp = str2num(result.numbers);
 ch1data = (-Vpp/2) + ((ch1data/65532)*Vpp);

%Use this plot to determine whether ch1 is data or empty then
%switch the channels above so that data is ch1 and empty is ch2
%     plot(ch1data); shg
%  return;

%Cut data into an exact multiple of Sweep size
ch1data = ch1data(1:Nsections*SectionLength);

 %Separate Channel into the four individual sweeps
AdjustedData = reshape(ch1data,SectionLength,Nsections);
AdjustedDataOne = AdjustedData(datastart:dataend,1:4:Nsections);
AdjustedDataTwo = AdjustedData(adatastart:dataend,2:4:Nsections);
AdjustedDataThree = AdjustedData(datastart:dataend,3:4:Nsections);
AdjustedDataFour = AdjustedData(datastart:dataend,4:4:Nsections);

%Extract PDP for all of the sections from data for channel finding
pdpOne=pdpConversion(AdjustedDataOne,Nsections,4);
pdpTwo=pdpConversion(AdjustedDataTwo,Nsections,4);
pdpThree=pdpConversion(AdjustedDataThree,Nsections,4);
pdpFour = pdpConversion(AdjustedDataFour,Nsections,4);

%    The following plot should be used at the start of processing each
%    folder to select the index start and index end for the data.

%    figure
%        subplot(2,2,1); plot(pdpOne);shg
%        subplot(2,2,2); plot(pdpTwo);shg
%        subplot(2,2,3); plot(pdpThree);shg
%        subplot(2,2,4); plot(pdpFour);shg
%    return

    NoiseMean = mean(pdpOne(a:b));
    NoiseStd = std(pdpOne(a:b));

%Extract Noise parameters from an empty section of all pdp's


    %Variable is 1 if the sweep contains data and -1/0 if not.
    SweepOneData = sign(max(pdpOne(signalIndexStart:SignalIndexEnd))-thresholdCutoff-
      NoiseMean);%the threshold is 6 dB for the check this value can be varied accordingly
    SweepTwoData = sign(max(pdpTwo(signalIndexStart:SignalIndexEnd))-thresholdCutoff-
      NoiseMean);
    SweepThreeData = sign(max(pdpThree(signalIndexStart:SignalIndexEnd))-thresholdCutoff-
      NoiseMean);
    SweepFourData = sign(max(pdpFour(signalIndexStart:SignalIndexEnd))-thresholdCutoff-
      NoiseMean);
%     return;
    %Find the two Signal and two noise sections and concatenate them
    if(SweepOneData==1 && SweepTwoData == 1 && SweepThreeData == 1 &&SweepFourData == 1)
      bb = 1;
        while (bb)
        figure; subplot(2,2,1); plot((pdpOne),'m');title("channel 1")%Plot all of the channels
                                                        from the Data
      subplot(2,2,2); plot((pdpTwo),'k'); title("channel 2")
      subplot(2,2,3); plot(pdpThree); title("channel 3")
      subplot(2,2,4); plot(pdpFour); title("channel 4")

       hold off
       pause(2);
      prompt = strcat('##THRESHOLD TOO LOW## See the Figures and Pick The First Channel with
                    a signal',...
                    '\n Enter Figure number :');%Pick the first channel with a visible
                                            signal
```

```matlab
    chanStart = input(prompt);
   bb = not(isnumeric(chanStart));
   end
    close
  if(chanStart == 1)
     signalDataArray = horzcat(AdjustedDataOne,AdjustedDataTwo);
   NoiseDataArray = horzcat(AdjustedDataThree,AdjustedDataFour);

  elseif(chanStart==2)
   signalDataArray = horzcat(AdjustedDataThree,AdjustedDataTwo);
   NoiseDataArray = horzcat(AdjustedDataOne,AdjustedDataFour);

  elseif(chanStart==3)
   signalDataArray = horzcat(AdjustedDataThree,AdjustedDataFour);
   NoiseDataArray = horzcat(AdjustedDataTwo,AdjustedDataOne);

  else
   signalDataArray = horzcat(AdjustedDataOne,AdjustedDataFour);
   NoiseDataArray = horzcat(AdjustedDataThree,AdjustedDataTwo);

  end


elseif(SweepOneData==1)
   if(SweepTwoData==1)%[Data Data empty empty]
      signalDataArray = horzcat(AdjustedDataOne,AdjustedDataTwo);
      NoiseDataArray = horzcat(AdjustedDataThree,AdjustedDataFour);

   end
     if(SweepFourData==1)%[ Data empty empty Data]
       signalDataArray = horzcat(AdjustedDataOne,AdjustedDataFour);
       NoiseDataArray = horzcat(AdjustedDataThree,AdjustedDataTwo);

     end
elseif(SweepThreeData==1)
   if(SweepTwoData==1)%[ empty Data Data empty]
      signalDataArray = horzcat(AdjustedDataThree,AdjustedDataTwo);
      NoiseDataArray = horzcat(AdjustedDataOne,AdjustedDataFour);

   end

   if(SweepFourData==1)%[ empty empty Data Data]
      signalDataArray = horzcat(AdjustedDataThree,AdjustedDataFour);
      NoiseDataArray = horzcat(AdjustedDataTwo,AdjustedDataOne);

   end

else
      "Minimum Threshold" %Neither of the systems can detect a signal
      bb = 1;
      while (bb)
      figure; subplot(2,2,1); plot((pdpOne),'m');title("channel 1")%Plot all of the
                                                    channels from the Data
     subplot(2,2,2); plot((pdpTwo),'k'); title("channel 2")
     subplot(2,2,3); plot(pdpThree); title("channel 3")
     subplot(2,2,4); plot(pdpFour); title("channel 4")

      hold off
      pause(2);
     prompt = strcat('See the Figures and Pick The First Channel with a signal',...
                   '\n Enter Figure number :');%Pick the first channel with a visible
                                              signal
      chanStart = input(prompt);
      bb = not(isnumeric(chanStart));
      end
       close
     if(chanStart == 1)
        signalDataArray = horzcat(AdjustedDataOne,AdjustedDataTwo);
      NoiseDataArray = horzcat(AdjustedDataThree,AdjustedDataFour);

     elseif(chanStart==2)
       signalDataArray = horzcat(AdjustedDataThree,AdjustedDataTwo);
       NoiseDataArray = horzcat(AdjustedDataOne,AdjustedDataFour);
```

```matlab
        elseif(chanStart==3)
         signalDataArray = horzcat(AdjustedDataThree,AdjustedDataFour);
         NoiseDataArray = horzcat(AdjustedDataTwo,AdjustedDataOne);

        else
         signalDataArray = horzcat(AdjustedDataOne,AdjustedDataFour);
         NoiseDataArray = horzcat(AdjustedDataThree,AdjustedDataTwo);

        end
end
%/////////////////////////////////////////
SaiedSignalArray=signalDataArray;
SaiedNoiseArray=NoiseDataArray;
[q,w]=size(SaiedSignalArray);
L=fix(w/5);
L1=5*L;
SaiedSignalArray6=SaiedSignalArray(:,1:L1);
SaiedNoiseArray6=SaiedNoiseArray(:,1:L1);


            AdjustedOneSaied = SaiedSignalArray6(:,1:L);
            AdjustedTwoSaied = SaiedSignalArray6(:,L+1:2*L);
            AdjustedThreeSaied = SaiedSignalArray6(:,2*L+1:3*L);
            AdjustedFourSaied = SaiedSignalArray6(:,3*L+1:4*L);
            AdjustedFiveSaied = SaiedSignalArray6(:,4*L+1:5*L);


pdpSignalOneSaied = pdpConversion(AdjustedOneSaied,L1,5);
pdpSignalTwoSaied = pdpConversion(AdjustedTwoSaied,L1,5);
pdpSignalThreeSaied = pdpConversion(AdjustedThreeSaied,L1,5);
pdpSignalFourSaied = pdpConversion(AdjustedFourSaied,L1,5);
pdpSignalFiveSaied = pdpConversion(AdjustedFiveSaied,L1,5);


            AdjustedOneSaiedNoise = SaiedNoiseArray6(:,1:L);
            AdjustedTwoSaiedNoise = SaiedNoiseArray6(:,L+1:2*L);
            AdjustedThreeSaiedNoise = SaiedNoiseArray6(:,2*L+1:3*L);
            AdjustedFourSaiedNoise = SaiedNoiseArray6(:,3*L+1:4*L);
            AdjustedFiveSaiedNoise = SaiedNoiseArray6(:,4*L+1:5*L);

pdpNoiseSaiedOne = pdpConversion(AdjustedOneSaiedNoise,L1,5);
pdpNoiseSaiedTwo = pdpConversion(AdjustedTwoSaiedNoise,L1,5);
pdpNoiseSaiedThree = pdpConversion(AdjustedThreeSaiedNoise,L1,5);
pdpNoiseSaiedFour = pdpConversion(AdjustedFourSaiedNoise,L1,5);
pdpNoiseSaiedFive = pdpConversion(AdjustedFiveSaiedNoise,L1,5);



pdpSaiedOneClean = pdpSignalOneSaied - pdpNoiseSaiedOne;
pdpSaiedTwoClean = pdpSignalTwoSaied - pdpNoiseSaiedTwo;
pdpSaiedThreeClean = pdpSignalThreeSaied - pdpNoiseSaiedThree;
pdpSaiedFourClean = pdpSignalFourSaied - pdpNoiseSaiedFour;
pdpSaiedFiveClean = pdpSignalFiveSaied - pdpNoiseSaiedFive;


                [maxvalOne,maxindOne] = max(pdpSaiedOneClean);
            pdpClean1 = pdpSaiedOneClean +NoiseMean;
                [maxvalTwo,maxindTwo] = max(pdpSaiedTwoClean);
            pdpClean2 = pdpSaiedTwoClean +NoiseMean;
                [maxvalThree,maxindThree] = max(pdpSaiedThreeClean);
            pdpClean3 = pdpSaiedThreeClean +NoiseMean;
                [maxvalFour,maxindFour] = max(pdpSaiedFourClean);
            pdpClean4 = pdpSaiedFourClean +NoiseMean;
                [maxvalFive,maxindFive] = max(pdpSaiedFiveClean);
            pdpClean5 = pdpSaiedFiveClean +NoiseMean;


             pdpSignalSaied1 = pdpConversion(SaiedSignalArray,Nsections,2);%Extract


             pdpNoiseSaied1= pdpConversion(SaiedNoiseArray,Nsections,2);
             pdpSaiedClean = pdpSignalSaied1 - pdpNoiseSaied1;
```

```matlab
                    [maxval1,maxind1] =  max(pdpSaiedClean);
                        [maxvalN,maxindN] =  max(pdpNoiseSaied1(a:b));
                    pdpSaiedClean1 =  pdpSaiedClean +NoiseMean;


                    pdpNoiseSaied(p1,:)=pdpNoiseSaied1;
                    pdpSignalSaied(p1,:)=pdpSignalSaied1;

                    pdpSaiedClean1m(p1,:)= pdpSaiedClean1;

                       freqaxisSaied =linspace(0,fs/2,size(pdpSaiedClean1,2));

                      TimeAxisSaied = freqaxisSaied*(819.2e-6)/BW;

                      DistanceAxisSaied = (TimeAxisSaied*3e-1);

        pdpCleansignal=[pdpClean1; pdpClean2; pdpClean3; pdpClean4; pdpClean5];

                      freqaxisSaied20 =linspace(0,fs/2,size(pdpClean1,2));

                      TimeAxisSaied20 = freqaxisSaied20*(819.2e-6)/BW;

                      DistanceAxisSaied20 = (TimeAxisSaied20*3e-1);

pdpNoiseSaied=[pdpNoiseSaiedOne;pdpNoiseSaiedTwo;pdpNoiseSaiedThree;pdpNoiseSaiedFour;pdpNoise
SaiedFive];

    for j=1:5
          po=po+1;
          pdpSaiedClean20cm(po,:)= pdpCleansignal(j,:);

          pdpNoiseSaied20cm(po,:)= pdpNoiseSaied(j,:);
%          plot(TimeAxisSaied,pdpSaiedClean1m(po,:),'k')
%           return;

save(strcat(filenameStore,'\','PDP'),'pdpSaiedClean20cm','pdpNoiseSaied20cm','TimeAxisSaied20'
,'freqaxisSaied20','DistanceAxisSaied20','pdpNoiseSaied','pdpSignalSaied','pdpSaiedClean1m','T
imeAxisSaied','freqaxisSaied','DistanceAxisSaied');

    end


end


        function pdpOut = pdpConversion(Data,NumSections,NumSweeps)
        [M N] = size(Data);%Extract Noise PDP
        winNoise = repmat(hamming(M),1,NumSections/NumSweeps);
        SweepNoiseFreq= fftshift(ifft(Data.*winNoise));
        lmNoise=length(SweepNoiseFreq);
        LM=fix(lmNoise/2);
        SweepNoiseFreq(1:LM,:)=[];
        start=1; stop=length(SweepNoiseFreq(:,1));
        IRnoise=SweepNoiseFreq(start:stop,:);
        pdpOut=(20*log10(mean(abs(IRnoise)')));
         end
```

Program name: Received Power

```matlab
close all
clc
clear all

filename1i =strcat('M:\OmniDirectional measuerments\10GHz\Pro');

Address = strcat(filename1i);

load(strcat(Address,'\PDP.mat'));
[u v]=size(pdpSaiedClean20cm);
numFile = u;
n_side = 1; % Which side the noise is computed... '1' at the start; '0' at the end
%  plot(pdpSaiedClean20cm(1,:)); % to find a and b boundries
```

```matlab
% return
for P = 1:numFile

[K ind]=max(pdpSaiedClean1m(P,:));
a=fix(ind-250); %starting point for the actual signal without harmonics
b=fix(ind+500); %ending point for the actual signal without harmonics


Data_11_avgn = pdpSaiedClean1m(P,a:b);   %

 num_peaks= numel(findpeaks(Data_11_avgn));

     n_side =1; % Take the Noise from the last portion of the profile


    N_11_avgn = 10*log10(mean(10.^(pdpSaiedClean1m(end-200:end)./10))); % Noise Power...
                                                    Taking the last 200 samples
    N_11_avgn_s = std(pdpSaiedClean1m(end-200:end));

    noise_level_11_avgn = N_11_avgn;

    noise_std_11_avgn = N_11_avgn_s;

 Dy_range_avgn11 = max(Data_11_avgn)-N_11_avgn;    % Dynamic Range

              % Truncate the Noise Part & Calculate the Power
        % Calculate Power Received with 4* Noise Power Std Threshold

index = find(Data_11_avgn > N_11_avgn+4*N_11_avgn_s); % consider 4* Noise Power Std above
noise to be signal
Data_11_avgn = Data_11_avgn(index);

if Dy_range_avgn11 >30
     index1 = find(Data_11_avgn > max(Data_11_avgn)-30);
      P_rec_11_avgn = (sum(10.^(Data_11_avgn(index1)./10)));

else
     P_rec_11_avgn = (sum(10.^(Data_11_avgn./10)));
%
end
if isempty(Data_11_avgn)
   P_rec_11_avgn = 10.^(-150./10);   % If no signal present Power equal noise Assumed -150db
end

index = find(Data_11_avgn > N_11_avgn+3); % consider 3dB above noise to be signal
Data_11_avgn = Data_11_avgn(index);

if Dy_range_avgn11 >30
     index1 = find(Data_11_avgn > max(Data_11_avgn)-30);
      P_rec_11_avgn_3dB = (sum(10.^(Data_11_avgn(index1)./10)));

else
     P_rec_11_avgn_3dB = (sum(10.^(Data_11_avgn./10)));

end
if isempty(Data_11_avgn)
   P_rec_11_avgn = 10.^(-150./10);   % If no signal present Power equal noise Assumed -150db
end

save(strcat(Address,'\','PowerReceived'),'P_rec_11_avgn','P_rec_11_avgn_3dB');
save(strcat(Address,'\','NoiseStatis'),'Dy_range_avgn11','noise_level_11_avgn','noise_std_11_a
vgn');

P_rec11_avgn(P) = P_rec_11_avgn;

P_rec11avgn_3dB(P) = P_rec_11_avgn_3dB;

clear  P_rec_11_avgn  P_rec_11avgn_3dB
clear('Dy_range11','Dy_range_avgn11','noise_level_11','noise_std_11','noise_level_11_avgn','no
ise_std_11_avgn');
clear('P_rec_11','P_rec_11_avgn','P_rec_11_3dB','P_rec_11_avgn_3dB');

save(strcat(filename1i,'\','PowerReceived'),'P_rec11avgn_3dB');
```

228

```
end
figure

plot(10*log10(P_rec11avgn_3dB),'*r');
hold off;
legend('LOS 1m')
xlabel('File Number')
ylabel('[dB]')
title('Rec Power 1m Aver [3dB thresh]')
saveas(gcf,horzcat(filename1i,'\I_Received Power_3dB Thresh 20cm'),'fig');

figure

plot(10*log10(P_rec11_avgn),'*m');
hold off;
legend('LOS 1m')
xlabel('File Number 1m')
ylabel('[dB]')
title('Received Power 1m_Aver [4*Noise std Thres]')
saveas(gcf,horzcat(filename1i,'\I_Received Power_4Noise Thresh 20cm'),'fig');
```

Program name: Estimate Path Loss

```
clear all;
close all;

% %%%  LOS_electronic_lab Distance
% %
% %          Dist =3.55:0.2:23.55-.2;
%
% %%%  NLOS_electronic_lab Distance

        Dist1 =3.8:.2:14.8-.2;

        Dist=sqrt((4.534).^2+Dist1.^2);
%
% %%%  LOS_Ther_lab Distance
%
% %           Dist =6:.2:30-.2;
%
% %%  NLOS_Ther_lab Distance
% %          Dist1 =5.68:.2:29.68-.2;
% %
% %           Dist=sqrt((5.4).^2+Dist1.^2);
%
% %%%  LOS_Foyer Distance
%
% %           Dist =5:0.2:26-.2;
%
% %%%  NLOS_Foyer Distance
%          Dist1 =9:.2:28-.2;
%
%           Dist=sqrt((10.5).^2+Dist1.^2);

filename1i =strcat('E:\OmniDirectional measuerments\ElectronicLabNLOS\30\ProNew');
load(strcat(filename1i,'\PowerReceived 20cm.mat'));

 OverAll_Loss = 41.93; %%for 10 GHz
%Tx_height =2.355 meter;for the foyer ; Tx_height =2.5 meter for the electronic lab; Tx_height
=3 meter for thermo_lab
Tx_height=2.5;
Rx_height = 1.6;
dist = sqrt((Tx_height - Rx_height).^2+Dist.^2);

P_rec = 10*log10(P_rec11avgn_3dB20(1:end));

index = find(P_rec ==-150);
P_rec(index)=[];
dist(index)=[];
B = OverAll_Loss - (P_rec);
%  freq=13.4; %%for 10GHz
```

229

```
freq=26.8; %%for 30GHz
% freq=54.2; %%for 50GHz
% freq=62.6; %%for 60GHz
% freq=70; %%for 70GHz

[alpha, beta,Xstd] = PathLoss_FloatIntercept_Function(B,dist);
save(strcat(filename1i,'\','PathLoss_FloatIntercept1'),'alpha','beta','Xstd','B','freq');
saveas(gcf, strcat(filename1i,'\','PathLoss_FloatIntercept1'), 'fig');
 [n,Xstd_] = PathLoss_CloseIn_Function(B,dist,freq);

save(strcat(filename1i,'\','PathLoss_CloseIn1'),'n','Xstd_','dist','OverAll_Loss','B','freq');
saveas(gcf, strcat(filename1i,'\','PathLoss_CloseIn1'), 'fig');

return
```

Program name: Close-In Path Loss Function

```
function [n,Xstd] = PathLoss_CloseIn_Function(B,dist,freq)  % B - path loss data (dB); freq-
                                                    operating frequency (in GHz)
D = 10*log10(dist);% Vector of distances (m) for the corresponding PL points 10*log10(dist/1m)
FSPL =20*log10(4*3.141*freq*1e9/3e8); % Free space path loss at frequency freq for reference
                                distance 1 m
   A = B-FSPL;

   Sum_Dsq = sum(D.^2);
   Sum_DA = sum(D.*A);

   n = Sum_DA/Sum_Dsq;
   Xstd = std(A - n*D,1);

   dis=[1:1:max(dist)+10];
figure
semilogx(dist,B,'*r');
hold on;

PathLoss1= FSPL+10*n*log10(dis);
semilogx(dis,PathLoss1);
hold off;
xlabel('Distance (m)')
ylabel('[dB]')
grid on;
legend('Data','Fit')
title(strcat('n: ',num2str(n),' std: ',num2str(Xstd)));
```

Program name: Float-Intercept Path Loss Function

```
    function [alpha, beta,Xstd] = PathLoss_FloatIntercept_Function(B,dist)  % NN- length of PL
points
   N = length(dist);
   D = 10*log10(dist) % Vector of distances (m) for the corresponding PL points
                     10*log10(dist/1m)

   Sum_Dsq = sum(D.^2);
   Sum_D = sum(D);
   Sum_B = sum(B);
   Sum_DB = sum(D.*B);

   PL_Matr = [N Sum_D; Sum_D  Sum_Dsq];
   Out_Matr = [Sum_B Sum_DB];

   Ans_Matr = Out_Matr/PL_Matr;

   alpha = Ans_Matr(1); beta = Ans_Matr(2);

  Xstd = std(B - alpha-beta*D,1);

   dis=[1:1:max(dist)+10];

figure
semilogx(dist,B,'*r');
hold on;

PathLoss1= 10*beta*log10(dis)+alpha;
```

230

```
semilogx(dis,PathLoss1,'k');
hold off;
xlabel('Distance (m)')
ylabel('[dB]')
grid on;
legend('Data','Fit')
title(strcat('alpha: ',num2str(alpha),' beta: ',num2str(beta),' std: ',num2str(Xstd)));
```

Program name: RMS Delay Spread

```
close all
clc
clear all

filename1i =strcat('E:\OmniDirectional measuerments\Pro');
Address = strcat(filename1i,'\PDP.mat');
  load(Address);
  [u v]=size(pdpSaiedClean20cm);
           numFile =n;
%    plot(pdpSaiedClean20cm(1,:))
%    return

    for P = 1:numFile
        clc;

        load(strcat(filename1i,'\NoiseStatis20.mat'));

      close all

        TimeAxisSaied20=TimeAxisSaied;
        Data_11_avgn = pdpSaiedClean20cm(P,1500:1960);

        Dy_range_avgn11 = max(Data_11_avgn)-noise_level_11_avgn20;


    for ixxy=1:1  % COMPUNTING THE CHANNEL RMSS for Dynamic range greater than  20 dB

%A Dynamic range greater than  4*Noise varianca to be consider for Delay statistic calculation
           time_x = TimeAxisSaied20(abs((length(TimeAxisSaied20)-
             length(Data_11_avgn)))+1:end);


        if Dy_range_avgn11 >= 20+4*noise_std_11_avgn20   % If the SNR above 20 dB
          index1 = find(Data_11_avgn > max(Data_11_avgn)-30);
          [ch_rmss_11avgn_20dB ch_mean_11avgn_20dB ch_width_11avgn_20dB] =
            rmsspr(Data_11_avgn(index1),time_x(index1),-20);
         else
          ch_rmss_11avgn_20dB =-999; ch_mean_11avgn_20dB =-999; ch_width_11avgn_20dB =-999;
        end


    end


Position=P;

ch_rmss_11avgn_20dB_(Position)=ch_rmss_11avgn_20dB;
     ch_mean_11avgn_20dB_(Position)=ch_mean_11avgn_20dB;
     ch_width_11avgn_20dB_(Position)=ch_width_11avgn_20dB;


        filename = strcat(filename1i);


save(strcat(filename,'\','DelaySpread_AllPos'),'ch_rmss_11avgn_20dB','ch_mean_11avgn_20dB','ch
     _width_11avgn_20dB','ch_rmss_11avgn_20dB_','ch_mean_11avgn_20dB_','ch_width_11avgn_20dB_
     ');

        clear thrdb1


        clear('Dy_range_avgn11','noise_level_11_avgn','noise_std_11_avgn');
        clear Data_11 ch1Tx1_n  ch1Tx2_n Data_11_avgn ch1Tx1_avgn  ch1Tx2_avgn
```

231

```
end


%% THIS FUNCTION CALCULATES: THE "RMS" , "AVERAGE" and "WIDTH" OF THE CHANNEL

 function [ch_rmss ch_center ch_width] = rmsspr(ch,td,thrsh)

              Ch_dB_nor = (ch)- max((ch));


          ch_lin    = 10.^(Ch_dB_nor./10); % Convert the "ch" is in dB scale into normal scale

          index     = find(Ch_dB_nor >= thrsh);
        ch_center = sum(td(index) .* ch_lin(index)) / sum(ch_lin(index)); % Average channel
          delay
          ch_spread = (((td(index) - ch_center).^2) .* ch_lin(index)) / sum(ch_lin(index));
          ch_rmss   = sqrt(sum(ch_spread));    % rms of the channel

          ch_width  = td(index(end)) - td(index(1));   % Width of the channel
          ch_center = ch_center - td(index(1));

 End
```

Program name: CDF of the RMS Delay Spread

```
close all;
clear all;
clc;

% cdf_=[0.5 0.90 0.95];  % retrive the rms at these CDF values for outdoor
cdf_=[0.10 0.50 0.90];  % retrive the rms at these CDF values for indoor
legen =['20db'];
        %% Load the Delay Profile Data
ch_rmss_11avgn_20dB_1 = [];


          filename= 'E:\Measuerments\pro';
          filename1i =strcat(filename);

      %    load the Received Power
    FilenameAAA=strcat(filename1i,'\DelaySpread_AllPos.mat');

    load(FilenameAAA) % Load the received power

    [x y]=max(ch_rmss_11avgn_20dB_);

   ch_rmss_11avgn_20dB_1 = [ch_rmss_11avgn_20dB_1 ch_rmss_11avgn_20dB_];

   clear  filename1i  ch_rmss_11avgn_20dB_    ch_rmss_11_20dB_ ;

 mkdir(filename);
 filename =strcat(filename,'\');

%% Make the channels into a single array.

 for i=1:1

    ch_rmss_11avgn_20dB_1 = ch_rmss_11avgn_20dB_1(:);

 end

 %% Remove the "-999" field values from the array

 for i=1:1

    ch_rmss_11avgn_20dB_1(ch_rmss_11avgn_20dB_1==-999)=[];

  end

 for  i=1:1   % Plot the Delay Spread
     aa =zeros(1,1);
     figure;
```

```
    if (~isempty(ch_rmss_11avgn_20dB_1))
        [f,x] = ecdf(ch_rmss_11avgn_20dB_1);
        plot(x,f,'k');
        DS_11avgn_20dB = interp1(f,x,cdf_);
        aa(1)=1;                  % hold on;
    end

        aa(aa==0)=[];
     legend(legen(aa,:));
   xlabel('Time [ns]'); ylabel('CDF'); title('DS 11 20cm'); grid on;
   saveas(gcf,strcat(filename,'DS_11_20cm'), 'fig');
   hold off
 end

save(strcat(filename,'\','DelaySpread'), 'DS_11avgn_20dB','ch_rmss_11avgn_20dB_1');
```

2- The Directional codes

Program name: Angular PDP Separation

```
close all
clear all

fs = 40*10^6;%sampling frequency
Nsections = 300;%Total number of sweeps measured
SectionLength = fs*819.2*(10^-6);%Length of one sweep in samples
DataLength = fix(SectionLength.*2/3);%Number of samples for bandwidth, adjust the number
accordingly (currently 2/3 as 3 GHz bandwidth and only wanted 2 GHz)
BW=3;% the total bandwidth of the measured data
datastart = 1000;
dataend = arraydatastart+DataLength-1;%calculates the end of the bandwidth according to
DataLength

signalIndexStart = 4000; %Start of pdp index for empty signal detection
SignalIndexEnd = 5000; %end of pdp index for empty signal detection

a=9000; %%Noise start point
b=9500; %%Noise end point
thresholdCutoff = 12; %dB level above noise used to find channels.

po=0;
for j=1:3
    J=num2str(j);

        for t = -15:15:15
                T = num2str(t);

            filenameStore = strcat('E:\Directional
measuerments\NP',J,'\protest\Tilt(',T,')');%file to store
            mkdir(filenameStore);
            p1=0;

                for s = 0:12:348
                        S = num2str(s);
                    p1=p1+1;

                filename = strcat('E:\Directional
measuerments\NP',J,'\np',J,'_Pan_',S,'_Tilt_',T,'');%file to read

            Address = strcat(filename,'.rd16'); % Folder path containing the data to be processed
                fid=fopen(Address);
                rawdata = fread(fid,'uint16'); %rawdata from file
                fclose(fid);

                ch1data = rawdata(1:1:length(rawdata));%channel 1 should be the data

                %Extract the Vpp from file and convert raw data into voltage data
```

233

```
   regexstr = '(?<prefix>.*?)(?<numbers>([-]*(\d+[\,]*)+[\.]{0,1}\d*[eEdD]{0,1}[-
+]*\d*[i]{0,1})|([-]*(\d+[\,]*)*[\.]{1,1}\d+[eEdD]{0,1}[-
+]*\d*[i]{0,1}))(?<suffix>.*)';
  Data1 = importdata(strcat(Address,'.srdc'));
  result = regexp(Data1{15,1}, regexstr, 'names');
  Vpp = str2num(result.numbers);
  ch1data = (-Vpp/2) + ((ch1data/65532)*Vpp);


 %Cut data into an exact multiple of Sweep size
 ch1data = ch1data(1:Nsections*SectionLength);

  %Separate Channel into the four individual sweeps
 AdjustedData = reshape(ch1data,SectionLength,Nsections);
 AdjustedDataOne = AdjustedData(datastart:dataend,1:4:Nsections);
 AdjustedDataTwo = AdjustedData(datastart:dataend,2:4:Nsections);
 AdjustedDataThree = AdjustedData(datastart:dataend,3:4:Nsections);
 AdjustedDataFour = AdjustedData(datastart:dataend,4:4:Nsections);

 %Extract PDP for all of the sections from data for channel finding
 pdpOne=pdpConversion(AdjustedDataOne,Nsections,4);
 pdpTwo=pdpConversion(AdjustedDataTwo,Nsections,4);
 pdpThree=pdpConversion(AdjustedDataThree,Nsections,4);
 pdpFour = pdpConversion(AdjustedDataFour,Nsections,4);

 %    The following plot should be used at the start of processing each
 %    folder to select the index start and index end for the data is
  signalIndexStart, SignalIndexEnd              figure
        subplot(2,2,1); plot(pdpOne);shg
        subplot(2,2,2); plot(pdpTwo);shg
        subplot(2,2,3); plot(pdpThree);shg
        subplot(2,2,4); plot(pdpFour);shg
     return

     NoiseMean = mean(pdpOne(a:b));
     NoiseStd = std(pdpOne(a:b));

 %Extract Noise parameters from an empty section of all pdp's

  %Variable is 1 if the sweep contains data and -1/0 if not.
     SweepOneData = sign(max(pdpOne(signalIndexStart:SignalIndexEnd))-
 thresholdCutoff-NoiseMean);%the threshold is 6 dB for the check this value can be
 varied accordingly
  SweepTwoData = sign(max(pdpTwo(signalIndexStart:SignalIndexEnd))-thresholdCutoff-
   NoiseMean);
   SweepThreeData = sign(max(pdpThree(signalIndexStart:SignalIndexEnd))-
    thresholdCutoff-NoiseMean);
    SweepFourData = sign(max(pdpFour(signalIndexStart:SignalIndexEnd))-
      thresholdCutoff-NoiseMean);
 %      return;
     %Find the two Signal and two noise sections and concatenate them
if(SweepOneData==1 && SweepTwoData == 1 && SweepThreeData == 1 &&SweepFourData == 1)
       bb = 1;
         while (bb)
         figure; subplot(2,2,1); plot((pdpOne),'m');title("channel 1")
        subplot(2,2,2); plot((pdpTwo),'k'); title("channel 2")
        subplot(2,2,3); plot(pdpThree); title("channel 3")
        subplot(2,2,4); plot(pdpFour); title("channel 4")

         hold off
         pause(2);
        prompt = strcat('##THRESHOLD TOO LOW## See the Figures and Pick The First
         Channel with a signal','\n Enter Figure number :');%Pick the first
         channel with a visible signal
         chanStart = input(prompt);
        bb = not(isnumeric(chanStart));
         end
          close
        if(chanStart == 1)
           signalDataArray = horzcat(AdjustedDataOne,AdjustedDataTwo);
         NoiseDataArray = horzcat(AdjustedDataThree,AdjustedDataFour);

        elseif(chanStart==2)
         signalDataArray = horzcat(AdjustedDataThree,AdjustedDataTwo);
```

234

```matlab
        NoiseDataArray = horzcat(AdjustedDataOne,AdjustedDataFour);

    elseif(chanStart==3)
     signalDataArray = horzcat(AdjustedDataThree,AdjustedDataFour);
     NoiseDataArray = horzcat(AdjustedDataTwo,AdjustedDataOne);

    else
     signalDataArray = horzcat(AdjustedDataOne,AdjustedDataFour);
     NoiseDataArray = horzcat(AdjustedDataThree,AdjustedDataTwo);

    end

 elseif(SweepOneData==1)
    if(SweepTwoData==1)%[Data Array empty empty]
        signalDataArray = horzcat(AdjustedDataOne,AdjustedDataTwo);
        NoiseDataArray = horzcat(AdjustedDataThree,AdjustedDataFour);

    end
      if(SweepFourData==1)%[ Data empty empty Data]
        signalDataArray = horzcat(AdjustedDataOne,AdjustedDataFour);
        NoiseDataArray = horzcat(AdjustedDataThree,AdjustedDataTwo);

      end
elseif(SweepThreeData==1)
    if(SweepTwoData==1)%[ empty Data Data empty]
        signalDataArray = horzcat(AdjustedDataThree,AdjustedDataTwo);
        NoiseDataArray = horzcat(AdjustedDataOne,AdjustedDataFour);

    end

    if(SweepFourData==1)%[ empty empty Data Data]
        signalDataArray = horzcat(AdjustedDataThree,AdjustedDataFour);
        NoiseDataArray = horzcat(AdjustedDataTwo,AdjustedDataOne);

    end

else
    "Minimum Threshold" %Neither of the systems can detect a signal
    bb = 1;
    while (bb)
    figure; subplot(2,2,1); plot((pdpOne),'m');title("channel 1")%Plot all
     of the channels
   subplot(2,2,2); plot((pdpTwo),'k'); title("channel 2")
   subplot(2,2,3); plot(pdpThree); title("channel 3")
   subplot(2,2,4); plot(pdpFour); title("channel 4")

    hold off
    pause(2);
   prompt = strcat('See the Figures and Pick The First Channel with a
    signal',\n Enter Figure number :');%Pick the first channel with a
    visible signal
     chanStart = input(prompt);
    bb = not(isnumeric(chanStart));
    end
     close
   if(chanStart == 1)
       signalDataArray = horzcat(AdjustedDataOne,AdjustedDataTwo);
    NoiseDataArray = horzcat(AdjustedDataThree,AdjustedDataFour);

    elseif(chanStart==2)
     signalDataArray = horzcat(AdjustedDataThree,AdjustedDataTwo);
     NoiseDataArray = horzcat(AdjustedDataOne,AdjustedDataFour);

    elseif(chanStart==3)
     signalDataArray = horzcat(AdjustedDataThree,AdjustedDataFour);
     NoiseDataArray = horzcat(AdjustedDataTwo,AdjustedDataOne);

    else
     signalDataArray = horzcat(AdjustedDataOne,AdjustedDataFour);
     NoiseDataArray = horzcat(AdjustedDataThree,AdjustedDataTwo);

    end
end
```

235

```
                  SaiedSignalArray=signalDataArray;
                  SaiedNoiseArray=NoiseDataArray;

                  %
                              pdpSignalSaied1 = pdpConversion(SaiedSignalArray,Nsections,2);

                              pdpNoiseSaied1= pdpConversion(SaiedNoiseArray,Nsections,2);
                              pdpSaiedClean = pdpSignalSaied1 - pdpNoiseSaied1;

                              [maxval1,maxind1] =  max(pdpSaiedClean);
                                [maxvalN,maxindN] =  max(pdpNoiseSaied1(a:b));
                          pdpSaiedClean1 =  pdpSaiedClean +NoiseMean;

                              pdpNoiseSaied(p1,:)=pdpNoiseSaied1;
                              pdpSignalSaied(p1,:)=pdpSignalSaied1;

                              pdpSaiedClean1m(p1,:)= pdpSaiedClean1;

                               freqaxisSaied =linspace(0,fs/2,size(pdpSaiedClean1,2));

                              TimeAxisSaied = freqaxisSaied*(819.2e-6)/BW;

                              DistanceAxisSaied = (TimeAxisSaied*3e-1);


save(strcat(filenameStore,'\','PDP'),'pdpNoiseSaied','pdpSignalSaied','pdpSaiedClean1m','TimeA
xisSaied','freqaxisSaied','DistanceAxisSaied');



          end
      end
end


         function pdpOut = pdpConversion(Data,NumSections,NumSweeps)
        [M N] = size(Data);%Extract Noise PDP
        winNoise = repmat(hamming(M),1,NumSections/NumSweeps);
        SweepNoiseFreq= fftshift(ifft(Data.*winNoise));
        lmNoise=length(SweepNoiseFreq);
        LM=fix(lmNoise/2);
        SweepNoiseFreq(1:LM,:)=[];
        start=1; stop=length(SweepNoiseFreq(:,1));
        IRnoise=SweepNoiseFreq(start:stop,:);
        pdpOut=(20*log10(mean(abs(IRnoise)')));
         end
```

Program name: Angular Received Power

```
close all
clc
clear all
for s=1% number of points
         S = num2str(s);
          filename1 = horzcat('E:\Directional measuerments\NP',S,'\protestnew');
          filename = horzcat(filename1,'\Tilt(0)');
          angl = ((0:29)/30)*360; % In degree
          angl_rad = angl.*pi./180;

      n_side = 1;
        Address = strcat(filename,'\PDP.mat');
          load(Address);
            TimeDelay1 = TimeAxisSaied;
          pdpSaiedClean2 = pdpSaiedClean1m;
%   plot(pdpSaiedClean2(1,:)),
% return
a1=1000;  % To cut the number of samples at the beginning
b1=8000;  % To cut the number of samples at the end
Thrs=10;  % threshold from the maximum received power in polar plot
```

236

```matlab
      Data_11 = pdpSaiedClean2(:,a1:b1);
    len = size(Data_11,2);

    [p1 v1]=max(max(Data_11));  % To cut the number of samples at the beginning

     cut_s = min([v1]);

    [p1 v1]=min(min(Data_11));   % To cut the number of samples at the end

     [pa min_a] = min([p1]);
    min_b = [v1];


  figure('Position',get(0,'ScreenSize')) %View the Figure in Maximun of the screen size

    imagesc(Data_11)
    title(strcat('MinPow:',num2str(pa),' Pos: ',num2str(min_b(min_a))));

            aa = 1; % To control the user input parament loop below
            while (aa)
                prompt = strcat('Enter the side for the noise "0" picks on the start
                and "1" on the end:');
                thrdb = input(prompt);
                aa = not(isnumeric(thrdb));
            end

            if isempty(thrdb)||(thrdb==1)
               n_side=1;
            else
               n_side = thrdb;
            end
            thrsh = thrdb;
for ang_numb=1:30
            close all;

      if n_side ==1
         N_11 = 10*log10(mean(10.^(Data_11(ang_numb,end-200:end)./10))); % Noise
          Power... Taking the last 200 samples
         N_11_s = std(Data_11(ang_numb,end-200:end));

       else
          N_11 = 10*log10(mean(10.^(Data_11(ang_numb,10:210)./10))); % Noise Power...
         Taking the first 200 samples
          N_11_s = std(Data_11(ang_numb,10:210)); % Standard deviation

       end

         noise_pow11(ang_numb) = N_11;

         noise_var11(ang_numb) = N_11_s;

        Data_11n = Data_11(ang_numb,cut_s-100:len);

         time_trun = TimeDelay1(cut_s-100:len);


       snr11(ang_numb) = max(Data_11n)-N_11;

       index = find(Data_11n > N_11+4*N_11_s);
       Data_11n = Data_11n(index);

       if snr11(ang_numb) >30
            index1 = find(Data_11n > max(Data_11n)-30);
             pow_11_mw(ang_numb) = (sum(10.^(Data_11n(index1)./10)));
       else
            pow_11_mw(ang_numb) = (sum(10.^(Data_11n./10)));

       end
       if isempty(Data_11n)
          pow_11_mw(ang_numb) = 10.^(-120./10);
       end

end
```

```matlab
G=10*log10(max(pow_11_mw));

 clear angl angl_rad   TimeDelay1 TimeAxisSaied  pdpSaiedClean2 pdpSaiedClean1m Data_11 len
          pow_11_mw index Data_11n snr11 Data_11n time_trun;


for c =1-3 % number of Tilt angles
          T = num2str((c-2)*15);

        filename = horzcat(filename1,'\Tilt_(',T,')');

       angl = ((0:29)/30)*360; % In degree
      angl_rad = angl.*pi./180;

     n_side = 1; % Which side the noise is computed... '1' at the start; '0' at the end


         Address = strcat(filename,'\PDP.mat');
         load(Address);
        TimeDelay1 = TimeAxisSaied;
        pdpSaiedClean2 = pdpSaiedClean1m;

           Data_11 = pdpSaiedClean2(:,a1:b1);
         len = size(Data_11,2);

         [p1 v1]=max(max(Data_11));   % To cut the number of samples at the beginning

           cut_s = min([v1]);

         [p1 v1]=min(min(Data_11));   % To cut the number of samples at the end

         [pa min_a] = min([p1]);
         min_b = [v1];

       figure('Position',get(0,'ScreenSize')) %View the Figure in Maximun of the screen size

          imagesc(Data_11)
          title(strcat('MinPow:',num2str(pa),' Pos: ',num2str(min_b(min_a))));


                aa = 1; % To control the user input parament loop below
                 while (aa)
                prompt = strcat('Enter the side for the noise "0" picks on the start and
                "1" on the end:');
                      thrdb = input(prompt);
                      aa = not(isnumeric(thrdb));
                 end

                 if isempty(thrdb)||(thrdb==1)
                    n_side=1;
                 else
                    n_side = thrdb;
                 end
                 thrsh = thrdb;
      for ang_numb=1:30
                 close all;

            if n_side ==1
               N_11 = 10*log10(mean(10.^(Data_11(ang_numb,end-200:end)./10))); % Noise
                Power... Taking the last 200 samples
               N_11_s = std(Data_11(ang_numb,end-200:end));

             else
              N_11 = 10*log10(mean(10.^(Data_11(ang_numb,10:210)./10))); % Noise Power...
               Taking the first 200 samples
               N_11_s = std(Data_11(ang_numb,10:210)); % Standard deviation

            end

               noise_pow11(ang_numb) = N_11;

               noise_var11(ang_numb) = N_11_s;
```

```matlab
            Data_11n = Data_11(ang_numb,cut_s-100:len);


            time_trun = TimeDelay1(cut_s-100:len);


        snr11(ang_numb) = max(Data_11n)-N_11;


            % Truncate the Noise Part & Calculate the Power
    index = find(Data_11n > N_11+4*N_11_s); % consider 3dB above noise to be signal
        Data_11n = Data_11n(index);
        %          figure;       hold on;  % test the 30dB threshold profiles
        if snr11(ang_numb) >30
            index1 = find(Data_11n > max(Data_11n)-30);
             pow_11_mw(ang_numb) = (sum(10.^(Data_11n(index1)./10)));
        else
            pow_11_mw(ang_numb) = (sum(10.^(Data_11n./10)));
        %      a11= 2
        end
        if isempty(Data_11n)
        pow_11_mw(ang_numb) = 10.^(-90./10);  % If no signal present Power equal noise
        Assumed -90db
        end

    end
n=10*log10(max(pow_11_mw));
thr=-Thrs-n+G;

        [AngRad_rmss_20dB  AngRad_center_20dB  AngRad_width]=
        Angle_spread(pow_11_mw(1:30),angl_rad,thr);

        Ang_RMS_20dB=AngRad_rmss_20dB.*180/pi;

        AOA_20dB1=AngRad_center_20dB.*180/pi;

        Ang_width=AngRad_width;


        if AOA_20dB1>=360
            AOA_20dB=AOA_20dB1-360;
        else
            AOA_20dB=AOA_20dB1;
        end
 Address = strcat(filename); % Folder path containing the data to be processed
save(strcat(Address,'\','PowAnglProfile11'),'angl','pow_11_mw');
save(strcat(Address,'\','Angle_Statistic11'),'AOA_20dB','Ang_RMS_20dB','Ang_width');
save(strcat(Address,'\','SNR_Noise11'),'snr11','noise_pow11','noise_var11');

        power=10*log10(pow_11_mw(1:1:30));
        power(31)=power(1);
        angl_rad(31)=0;

        grid on
        hold on
        legendInfo{c} = T;

        a=min(power(:));
        b=max(power(:));
        angl_rad=angl_rad(1:1:31);
         figure
         pax = polaraxes;
         polarplot(angl_rad,power);
         thetaticks(0:12:360)
         pax.ThetaDir = 'clockwise';
         rlim([a-2 b])
         hold on
         polarplot([AOA_20dB; AOA_20dB]*pi/180, [-1; 1]*a);
         p=ones(1,length(angl_rad));
         q=(b+thr)*p;%-10dB
         polarplot(angl_rad,q)
         legend(legendInfo)
         legend(['Tilte=' num2str(T)],['AOA=' num2str(AOA_20dB)],['AngRMS='
         num2str(Ang_RMS_20dB)]);
```

239

```matlab
        saveas(gcf, strcat(filename1,'\','PowerAngleProfile11(',T,')'), 'fig');

   end

end


 function [Ang_rmss  Ang_center  Ang_width ] = Angle_spread(pow_ang,ang,thrsh)

        pow_ang_dB_nor = 10*log10((pow_ang))- max(10*log10((pow_ang)));

        pow_ang_lin    = 10.^(pow_ang_dB_nor./10);

      [A I]=max(pow_ang_lin);
            k=0;
     n1=7;
     n2=7;
   for a=I-n1:1:I+n2;
       if a<=0
           c=a+30;
       else
           c=a;
       end
       k=k+1;
          if c<=30
              d=c;
          else
              d=c-30;
          end
          z(k)=d;
    end
            m=I-(n1+1);
            index    = find(pow_ang_dB_nor(z) >= thrsh);
            q3=index+m;
            l=0;
          for y=1:length(q3)
             l=l+1;
             if q3(y)<=0
                q2=q3(y)+30;
             else
                q2=q3(y);
             end
               q(l)=q2;
          end
            g=0;

     for j=1:1:length(q)
        g=g+1;
        if q(j)<=30
              q1=q(j);
        else
              q1=q(j)-30;
        end
        Q(g)=q1;
     end
    for t=1:15;
       ang(t)=(t.*12+348).*pi/180;
    end
            Ang_center = sum((ang(Q)) .* pow_ang_lin(Q)) / sum(pow_ang_lin(Q));
            ang_spread = (((ang(Q) - Ang_center).^2) .* pow_ang_lin(Q))/
             sum(pow_ang_lin(Q));
            Ang_rmss   = sqrt(sum(ang_spread));
            ang1(Q)=ang(Q).*180/pi;
            f2=Q(end);
            f1=Q(1);
             if f2<=f1
               f3=f2+30;
            else
               f3=f2;
            end
            f4=f3;
             Ang_width = (f4 - f1).*12;

End
```

Appendix B – Antennas and 3D positioner specifications

LB-15-20
50 -75 GHz standard gain horn antenna

A-INFO

LB-15-20
50.0 - 75.0GHz Standard Gain Horn Antenna

Technical Specification

Frequency Range(GHz)	A Type	50.0 - 75.0
	C Type	50.0 - 65.0
Waveguide		WR15
Gain(dB)		20 Typ.
Polarization		Linear
3dB Beamwidth(deg)		18 Typ.
Cross Pol. Isolation(dB)		40 Typ.
VSWR	A Type	1.2:1 Typ.
	C Type	2.0:1 Typ.
Output	A Type	FUGP620 (UG-385/U modified)
	C Type	1.85mm-Female
Material		Cu
Size(mm)	A Type	21.6 x 19.1 x 47.3
	C Type	21.6 x 26.7 x 75.3
Net Weight(Kg)	A Type	0.03 Around
	C Type	0.06 Around

Outline Drawing (Size: mm)

A Type(With FUGP620 Output)
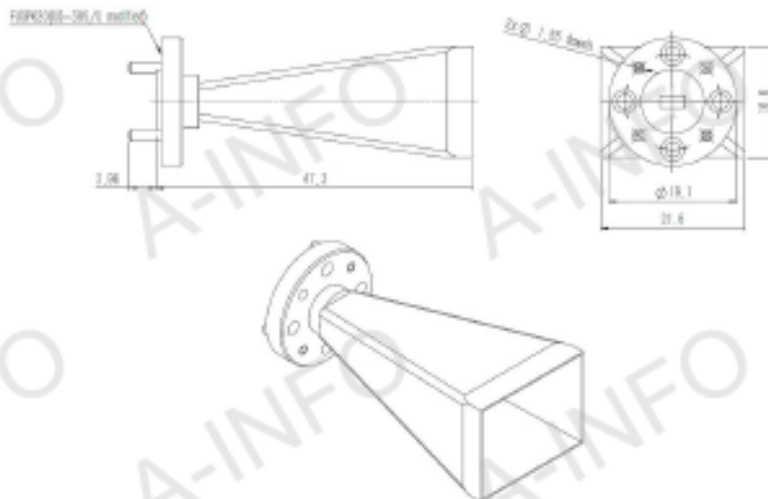
AINFO Inc.

Page 1 of 15

China(Beijing): Tel: (+86) 10-6266-7326, (+86) 10-6266-7327 Fax: (+86) 10-6266-7379
China(Chengdu): Tel: (+86) 28-8519-2786, (+86) 28-8519-3044 Fax: (+86) 28-8519-3068   Website: www.ainfoinc.com
USA :   Tel: (+1) 949-639-9688,   (+1) 949-639-9608 Fax: (+1) 949-639-9670   Email: sales@ainfoinc.com

Data subject to change without notice. For current data sheets, please contact Sales@ainfoinc.com

A-INFO

LB-15-20
50.0 - 75.0GHz Standard Gain Horn Antenna

C Type(With 1.85mm-Female Output)
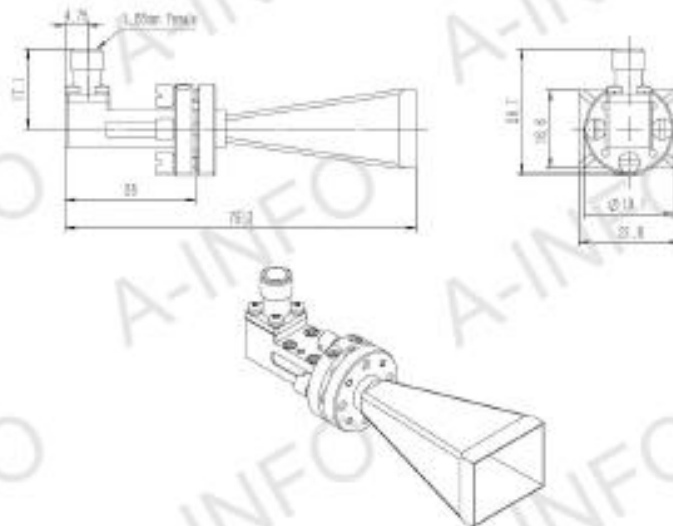
C Type(With 1.85mm-Female Output & Round Mounting Bracket)
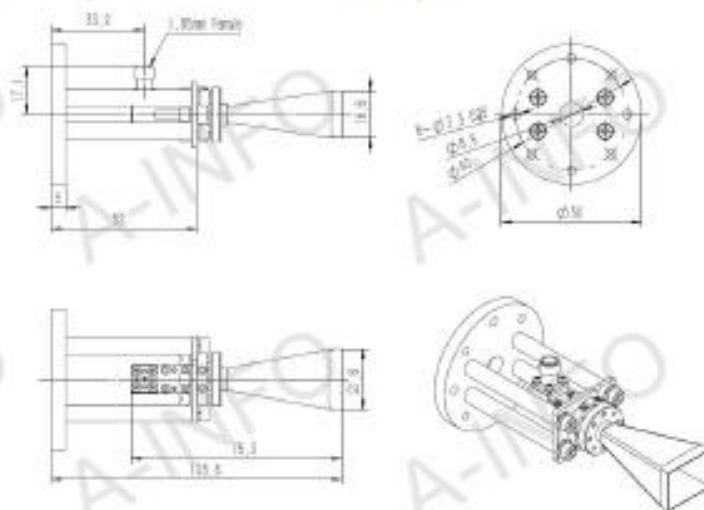
AINFO Inc.   Page 2 of 15

China(Beijing):   Tel: (+86) 10-6266-7326,   (+86) 10-6266-7327   Fax: (+86) 10-6266-7379
China(Chengdu):   Tel: (+86) 28-8519-2786,   (+86) 28-8519-3044   Fax: (+86) 28-8519-3068   Website: www.ainfoinc.com
USA: Tel: (+1) 949-639-9688,   (+1) 949-639-9608   Fax: (+1) 949-639-9670   Email: sales@ainfoinc.com

Data subject to change without notice. For current data sheets, please contact: Sales@ainfoinc.com

A-INFO

C Type(With 1.85mm-Female Output & L Type Mounting Bracket)

A Type(With Radome)

243

A-INFO

C Type(With 1.85mm-Female Output & Radome)

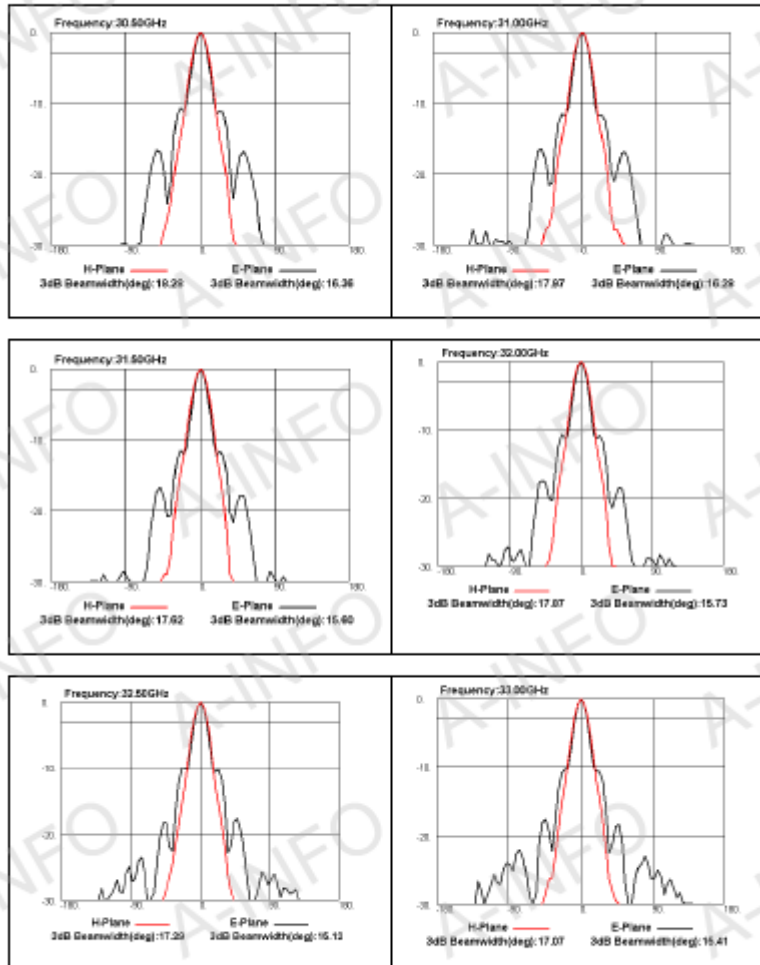C Type(With 1.85mm-Female Output & Round Mounting Bracket & Radome)
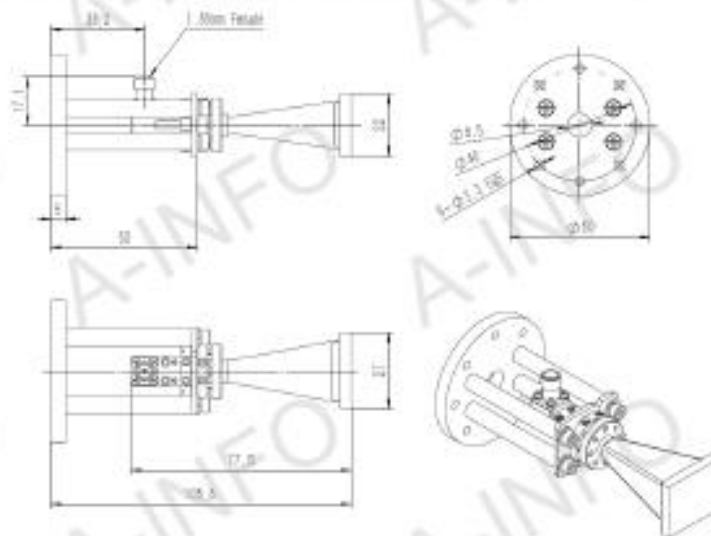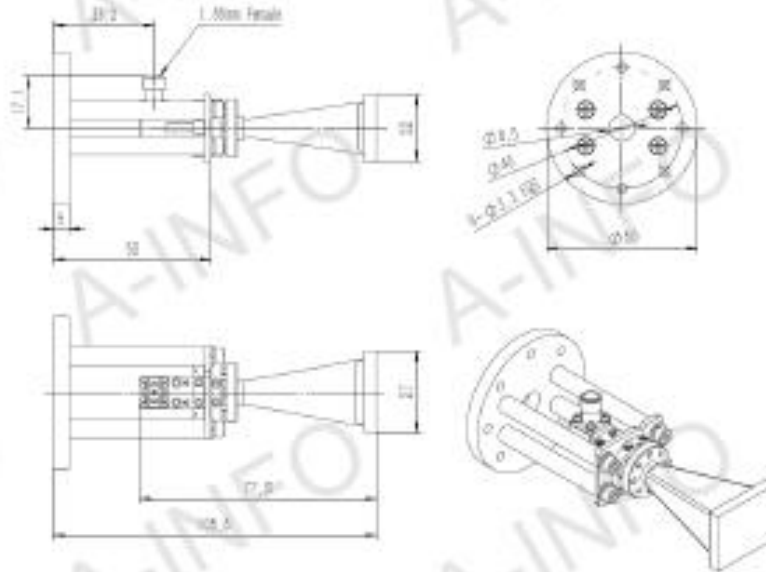
AINFO Inc.

Page 4 of 15

China(Beijing): Tel: (+86) 10-6266-7326, (+86) 10-6266-7327 Fax: (+86) 10-6266-7379
China(Chengdu): Tel: (+86) 28-8519-2786, (+86) 28-8519-3044 Fax: (+86) 28-8519-3068
USA: Tel: (+1) 949-639-9688, (+1) 949-639-9608 Fax: (+1) 949-639-9670
Website: www.ainfoinc.com
Email: sales@ainfoinc.com

Data subject to change without notice. For current data sheets, please contact: Sales@ainfoinc.com
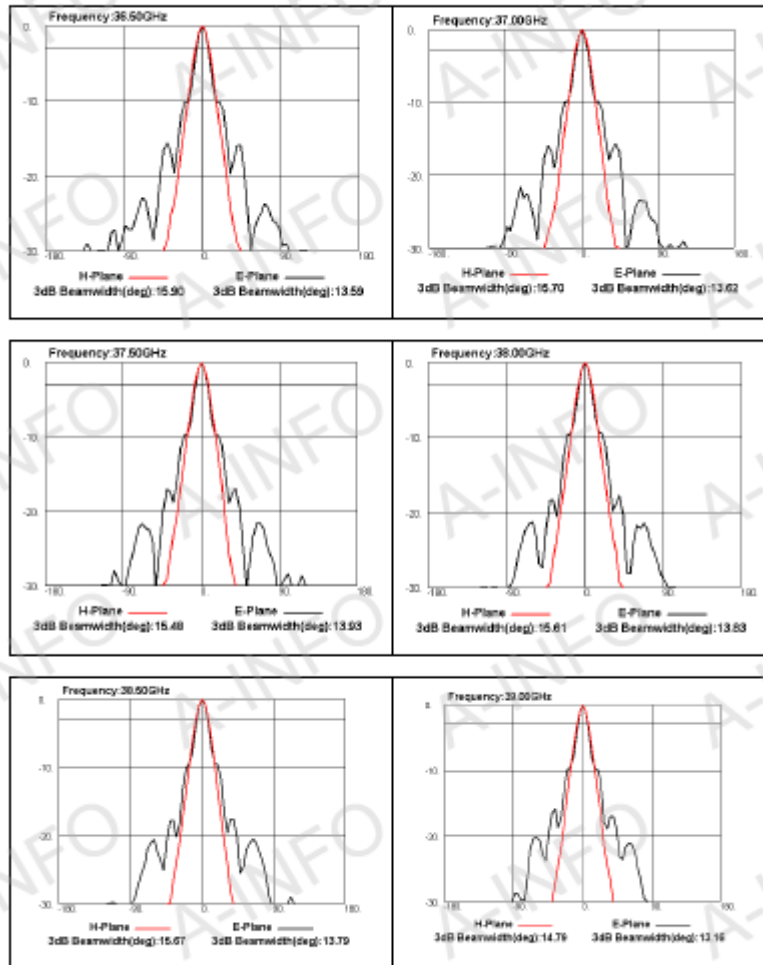
A-INFO

C Type(With 1.85mm-Female Output & L Type Mounting Bracket & Radome)

AINFO Inc.   Page 5 of 15

China(Beijing):   Tel: (+86) 10-6266-7326,   (+86) 10-6266-7327   Fax: (+86) 10-6266-7379   Website: www.ainfoinc.com
China(Chengdu):   Tel: (+86) 28-8519-2786,   (+86) 28-8519-3044   Fax: (+86) 28-8519-3068   Email: sales@ainfoinc.com
USA: Tel: (+1) 949-639-9688,   (+1) 949-639-9608   Fax: (+1) 949-639-9670

Data subject to change without notice. For current data sheets, please contact: Sales@ainfoinc.com

246

A-INFO

LB-16-20
60.0 - 75.0GHz Standard Gain Horn Antenna

Flange Drawing (Size: mm)
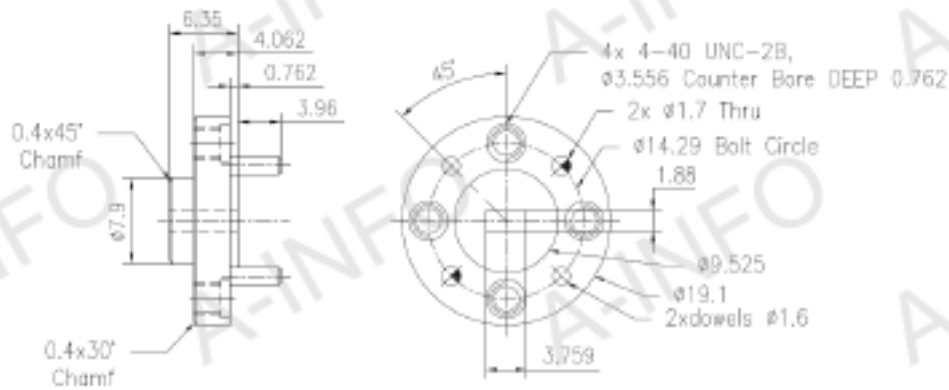
FUGP620
(equivalent to UG-385/U modified)

Test Results

1. Gain & Antenna Factor

A-INFO
LB-15-20
60.0 - 75.0GHz Standard Gain Horn Antenna
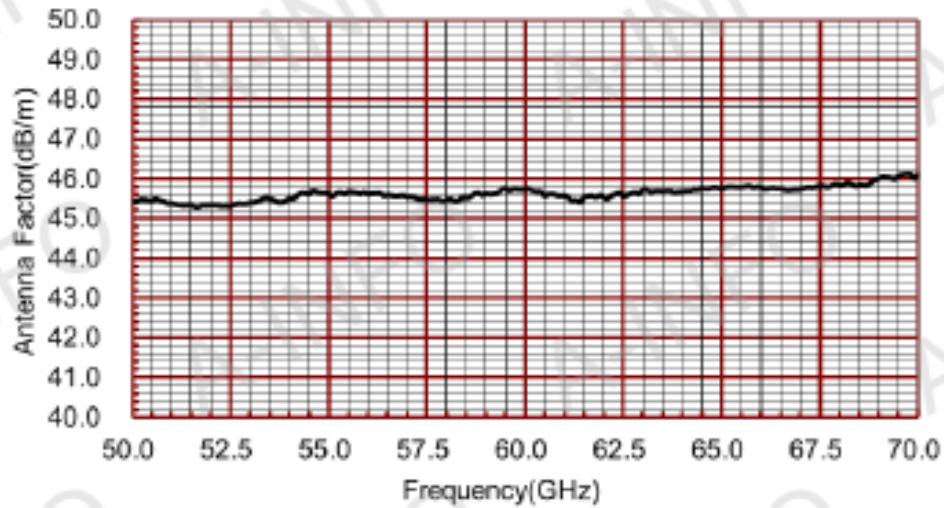
Frequency(GHz)	Gain(dB)	Antenna Factor(dB/m)
50.0	18.77	45.42
52.0	19.19	45.33
54.0	19.35	45.51
56.0	19.56	45.61
58.0	20.01	45.47
60.0	20.04	45.73
62.0	20.53	45.53
64.0	20.66	45.68
66.0	20.82	45.78
68.0	21.02	45.84
70.0	21.01	46.10

248

AINFO Inc.

249

50.0 - 75.0GHz Standard Gain Horn Antenna — LB-15-20
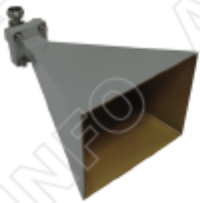
LB-28-20
26.5 - 40 GHz standard gain horn antenna

A-INFO
LB-28-20
26.5 - 40.0GHz Standard Gain Horn Antenna

Technical Specification

Frequency Range(GHz)		26.5 - 40.0
Waveguide		WR28
Gain(dB)		20 Typ.
Polarization		Linear
3dB Beamwidth(deg)		18 Typ.
Cross Pol. Isolation(dB)		40 Typ.
VSWR		1.25:1 Typ.
Output	A Type:	FBP320(UBR320)
	C Type:	2.92mm-Female or 2.4mm-Female
Material		Cu
Size(mm)	A Type:	31.9 x 40.4 x 70
	C Type:	32.1 x 40.4 x 94
Net Weight(Kg)	A Type:	0.05 Around
	C Type:	0.10 Around

Outline Drawing (Size: mm)

A Type(With FBP320 Output)
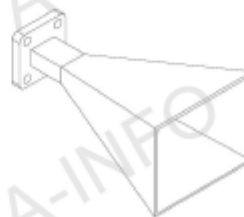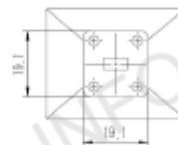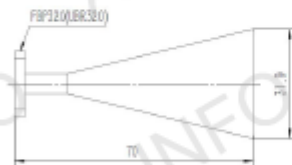
A-INFO

LB-28-20
26.5 - 40.0GHz Standard Gain Horn Antenna

C Type (With 2.92mm-Female Output)
For 2.4mm-Female output outline drawing, please contact A-INFO.

C Type (With 2.92mm-Female Output & Round Mounting Bracket)
For 2.4mm-Female output outline drawing, please contact A-INFO.

AINFO Inc.   Page 2 of 14

China(Beijing):   Tel: (+86) 10-6266-7326,   (+86) 10-6266-7327   Fax: (+86) 10-6266-7379
China(Chengdu):   Tel: (+86) 28-8519-2786,   (+86) 28-8519-3044   Fax: (+86) 28-8519-3060   Website: www.ainfoinc.com
USA: Tel: (+1) 949-639-9688,   (+1) 949-639-9608   Fax: (+1) 949-639-9670   Email: sales@ainfoinc.com

Data subject to change without notice. For current data sheets, please contact: Sales@ainfoinc.com

258

A-INFO

26.5 - 40.0GHz Standard Gain Horn Antenna

LB-28-20

C Type (With 2.92mm-Female Output & L Type Mounting Bracket)

For 2.4mm-Female output outline drawing, please contact A-INFO.

A Type (With Radome)

259

Appendix

260

C Type (With 2.92mm-Female Output & L Type Mounting Bracket & Radome)
For 2.4mm-Female output outline drawing, please contact A-INFO.

AINFO Inc.

Page 5 of 14

China(Beijing): Tel: (+86) 10-6266-7326, (+86) 10-6266-7327 Fax: (+86) 10-6266-7379
China(Chengdu): Tel: (+86) 28-8519-2786, (+86) 28-8519-3044 Fax: (+86) 28-8519-3068
USA: Tel: (+1) 949-639-9688, (+1) 949-639-9608 Fax: (+1) 949-639-9670

Website: www.ainfoinc.com
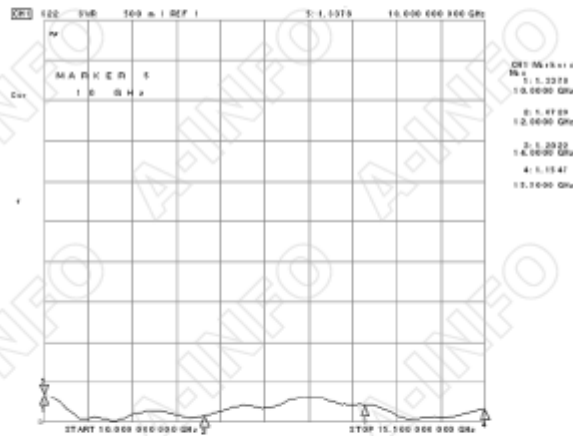Email: sales@ainfoinc.com

Data subject to change without notice. For current data sheets, please contact: Sales@ainfoinc.com

261

FBP320

A-INFO

Frequency (GHz)	Gain (dB)	Antenna Factor (dB/m)	Frequency (GHz)	Gain (dB)	Antenna Factor (dB/m)
26.5	18.54	40.13	33.5	20.47	40.24
27.0	18.75	40.09	34.0	20.59	40.25
27.5	19.01	39.99	34.5	20.60	40.37
28.0	19.18	39.97	35.0	20.60	40.49
28.5	19.31	40.00	35.5	20.81	40.40
29.0	19.43	40.03	36.0	20.92	40.42
29.5	19.61	40.00	36.5	20.94	40.52
30.0	19.88	39.87	37.0	20.95	40.62
30.5	19.89	40.01	37.5	21.12	40.57
31.0	19.89	40.15	38.0	21.18	40.63
31.5	20.10	40.08	38.5	21.21	40.71
32.0	20.31	40.00	39.0	21.23	40.80
32.5	20.33	40.12	39.5	21.36	40.78
33.0	20.35	40.23	40.0	21.50	40.75

2. VSWR

LB-75-20
10 - 15 GHz standard gain horn antenna

A - INFO

LB-76-20
10.0 – 15.0GHz Standard Gain Horn Antenna

Technical Specification

Frequency Range(GHz)	10.0 - 15.0
Gain(dB)	20 Typ.
3dB Beamwidth(deg)	18 Typ.
Waveguide	WR75
Material	Al
Output	A Type: FBP120 C Type: N/SMA/3.5mm/TNC/7mm
Size(mm) W x H x L	A Type: 103x83x155 C Type: 103x83x185
Net Weight(Kg)	A Type: 0.20 Around C Type: 0.25 Around

Outline Drawing (Size: mm)

A Type

W x H x L: 103x83x155
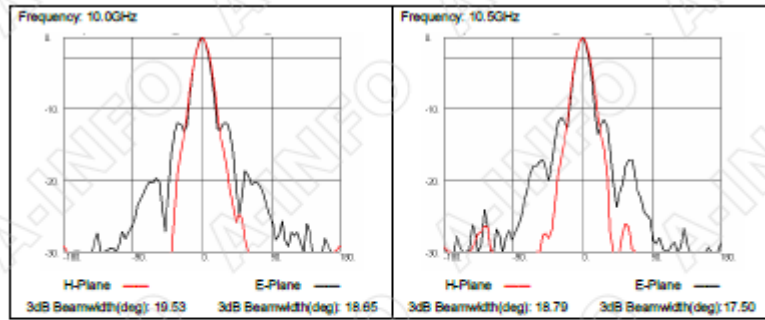
C Type

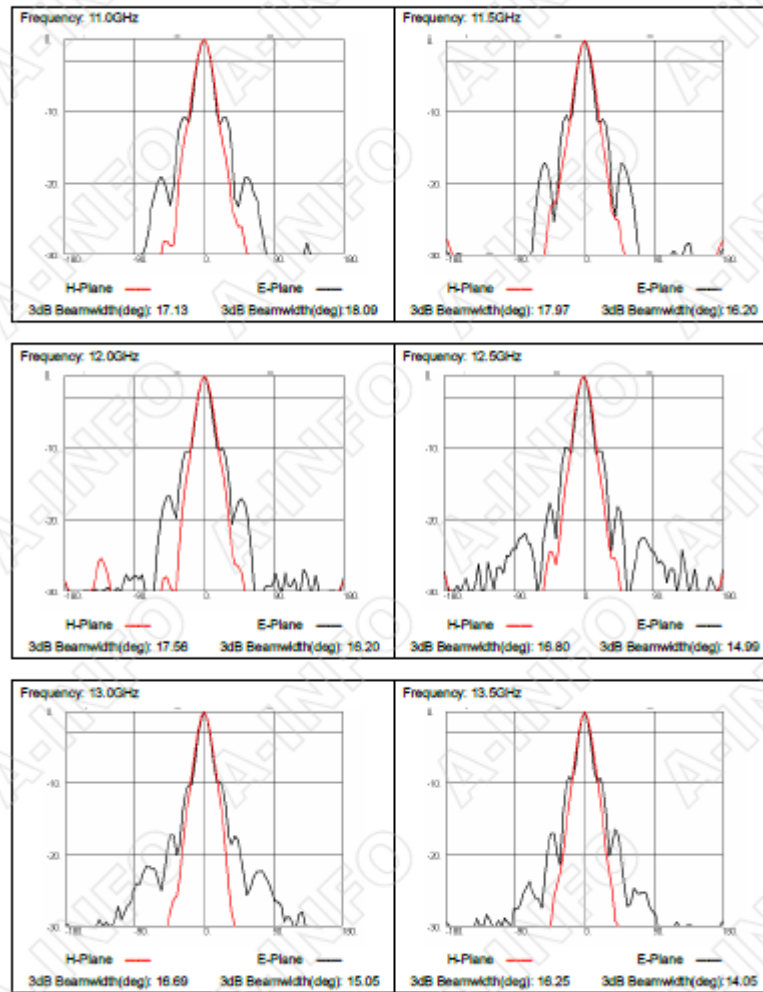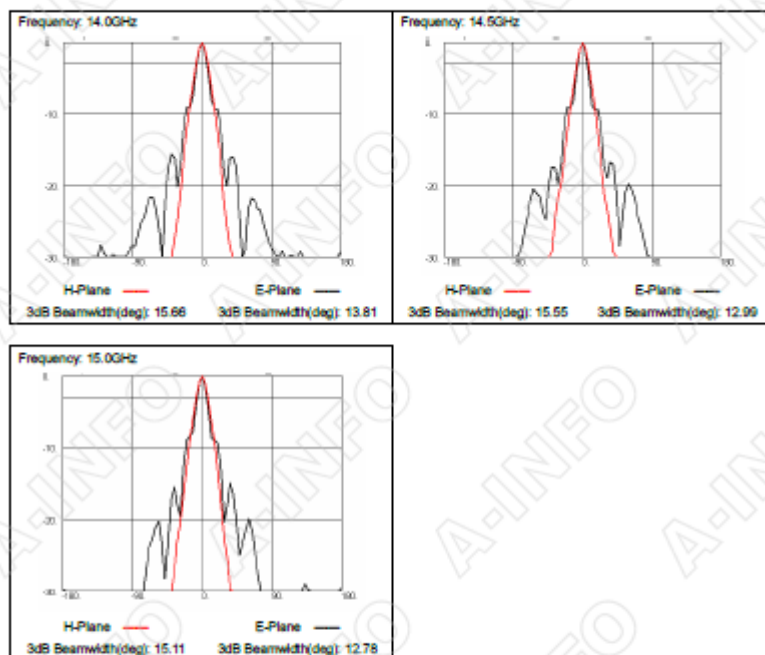W x H x L: 103x83x185

Chengdu AINFO Inc.
Tel: +86-28-8519-2786 or +86-28-8519-3047   Fax: +86-28-8519-3068   Website: www.ainfoinc.com
Data subject to change without notice. For current data sheets, please contact: Sales@ainfoinc.com
Page 1

271
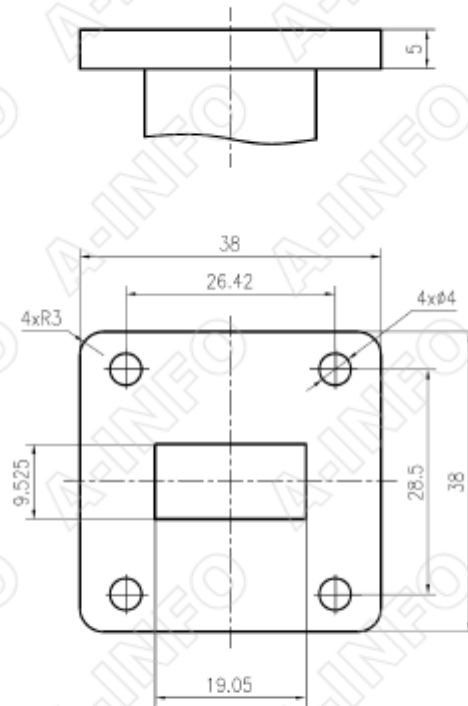
FBP120

A-INFO

LB-75-20
10.0 – 15.0GHz Standard Gain Horn Antenna

Frequency(GHz)	Gain(dB)	Antenna Factor(dB/m)
10.00	18.79	31.42
10.50	19.31	31.33
11.00	19.50	31.54
11.50	19.73	31.69
12.00	19.97	31.83
12.50	20.25	31.89
13.00	20.19	32.30
13.50	20.53	32.28
14.00	20.66	32.47
14.50	20.81	32.63
15.00	20.87	32.86

2. VSWR

Chengdu AINFO Inc.   Page 4
Tel: +86-28-8519-2786 or +86-28-8519-3047   Fax: +86-28-8519-3068   Website: www.ainfoinc.com
Data subject to change without notice. For current data sheets, please contact: Sales@ainfoinc.com

QOM-SL-0.8-40-K-SG-L
Ultra-Wideband Omni-directional Antenna
0.8 to 40 GHz

STEATITE
Q-PAR ANTENNAS

Ultra-Wideband Omni-directional Antenna

QOM-SL-0.8-40-K-SG-L

Ultra-Wideband Omni-directional Antenna

0.8 to 40 GHz

Catalogue number: QOM-SL-0.8-40-K-SG-L

Q-par reference: QMS-00017

Contents: Summary
Typical Antenna Gain
Typical Return Loss
Typical Beamwidth
Typical Radiation Patterns
Measured VSWR

Test Report

SD 15/01/2014 7083

STEATITE
Q-PAR ANTENNAS

Ultra-Wideband Omni-directional Antenna

QOM-SL-0.8-40-K-SG-L

Typical Specification

Frequency	0.8 to 40 GHz
Connector type	K type (2.9mm) jack
Power Handling	40 Watt c.w.
VSWR	< 3.2:1 max , typically < 2.5:1
Gain	-2.2 to 6.9 dBi for 1 to 40 GHz
Azimuth Ripple	Typically < +/- 1dB on horizon
3dB Beamwidth	20 to 140 degrees
10dB Beamwidth	45 to 170 degrees
Weight	860 g (with bracket)
Size- max.	100 mm dia. x 108 mm long inc. connector (minus bracket)
Mounting	Pole mounting bracket. To suit pole up to 28 mm diameter.
Construction	Composite aluminium / plastic, painted. PTFE radome

Note: cable may influence antenna performance at low frequencies

Typical Antenna Gain on Horizon / Return Loss

This is calculated by reference to standard gain horn antennas, and cross checked with reference to the antenna beamwidth, with an estimated error of +/- 0.8dB.

Omni Directional Antenna Series MD249
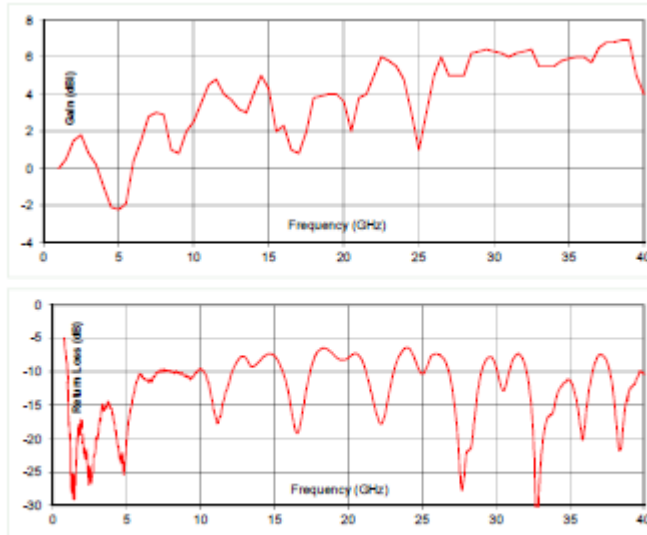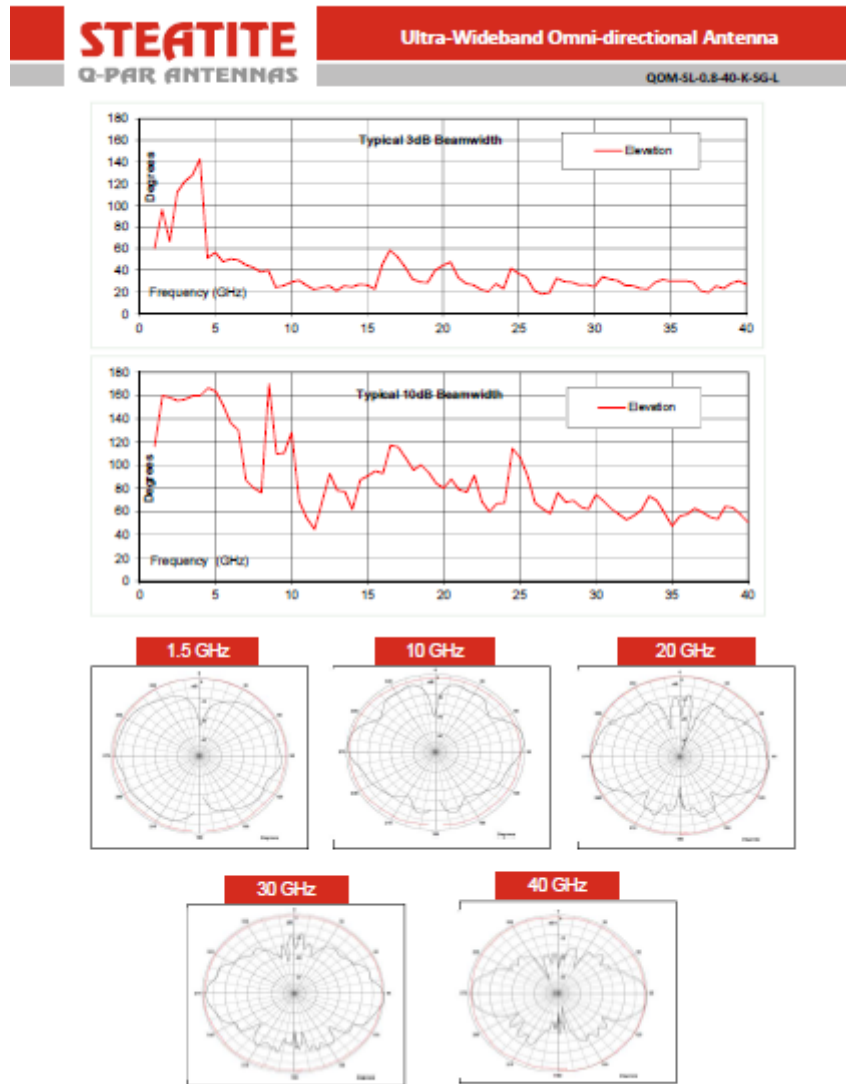
Omni Directional Antenna Series MD249

FLANN MICROWAVE LTD.
+44 (0) 1208 77777 - sales@flann.com

Model MD249-AB

FLANN MICROWAVE LTD.
+44 (0) 1208 77777 - sales@flann.com

FLANN MICROWAVE LTD. +44 (0) 1208 77777 - sales@flann.com

Features

- Low VSWR
- 360° Azimuth Coverage
- 60° Elevation Coverage
- Models within the range 1.5 GHz - 330 GHz available
- Waveguide Interface Models available

The Flann Omni Directional Antennas series
MD249, provide 360° coverage in azimuth
and 60° coverage in elevation; these antennas
are suitable for applications requiring a good
all round coverage.

Typical applications include:-

- Wireless LAN

FLANN MICROWAVE LTD.
+44 (0) 1208 77777 - sales@flann.com

FLANN MICROWAVE LTD. +44 (0) 1208 77777 - sales@flann.com

- Source Tracking
- Outside Broadcast
- Air to Ground Downlinks

Model MD249-AA

Typical Specfication:- (Model MD 249-AA)
Specified Frequency Range
Functional Frequency Range

FLANN MICROWAVE LTD.
+44 (0) 1208 77777 - sales@flann.com

FLANN MICROWAVE LTD. +44 (0) 1208 77777 - sales@flann.com

Nominal Gain
Gain Variation Elevation
Gain Variation Azimuth
Polarization
Nominal Half Angle 3 dB Beamwidth
Nominal Half Angle 10 dB Beamwidth
VSWR (Max)
Typical Power Handling
RF Coaxial Connectors

59 GHz to 65.5 GHz All Broadband widths up to 2:1
50 GHz to 70 GHz All Broadband widths up to 2:1
2 dB
±1.5 dB
±1 dB
Vertical
Typically Greater than 30˚

FLANN MICROWAVE LTD.
+44 (0) 1208 77777 - sales@flann.com

FLANN MICROWAVE LTD. +44 (0) 1208 77777 - sales@flann.com

Typically Greater than 60˚
1.65:1
5 Watts
1.85 mm Male or Female or Type N, SMA, K for lower frequency ranges

FLANN MICROWAVE LTD.
+44 (0) 1208 77777 - sales@flann.com

Key Features

- Variable speed, maximum 15kgs top load
- Internal cable wring from pan tilt to housing, only available with YAAN housing
- 360° continuous rotation, Pan: 0.01° ~60° /s, Tilt: 0.01° ~30° /s
- Up to 80 presets, 5 auto scans, 8 cruising tracks
- Support angle return function
- Anti-surge, lighting protection, pass EMC test

Technical Specifications

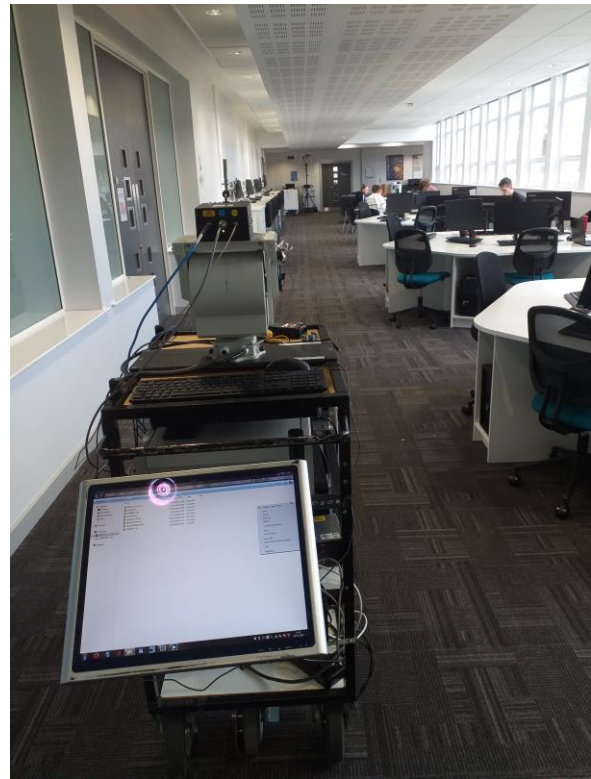| Model NO.	YS3051
PTZ	
Angle Return	Support with Pelco D, default enquiry return(Real time angle return is available)
Load Type	Top load
Max. Load Weight	15kgs
Angle Control	Support
Pan Rotation Range	0° ~ 360° continuous
Tilt Rotation Range	Top load: -75° ~ +40° (Optional -90° ~+ 40°)
Pan Speed	0.01° ~60° /s
Tilt Speed	0.01° ~30° /s
Lens Control	Support with default lens control interface
Preset	80
Auto Scan	5
Cruising Track	8
Guard Location	Call preset, cruise track or atuo scan if there is no command in a period of time
Protocol	Pelco P/D, YAAN
OSD	English/Chinese
Communication	RS485
Relay AUX Output	2 groups (Extendable to 4 groups without heating, or 3 groups with heating)
General	
Power Supply	AC 24V ± 25%
Power Consumption	≤85W (Heating system off), ≤95W(Heating system on)
Working Environment	Working temperature: -35°C ~ 60°C(with heating system),working humidity: ≤90% RH
Protection Level	IP66
Dimensions	249(L) x 230(W)x302(H) mm
Material	Aluminum alloy
Weight	13kgs
Accessories	
IR LEDs	F01
Housing	YA4718, YA4722, YA4218
Wall Mount Bracket	WS2770

Appendix C – Photographs of Environments

Factory Like Environment
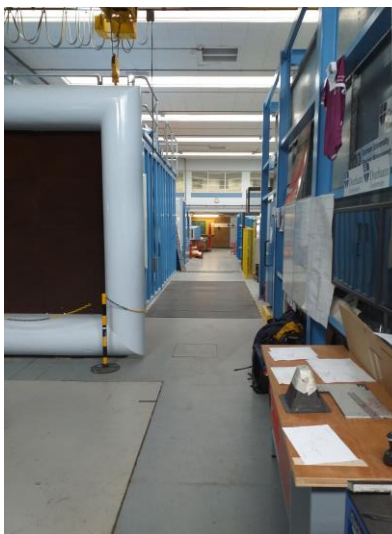
Large Office Environment
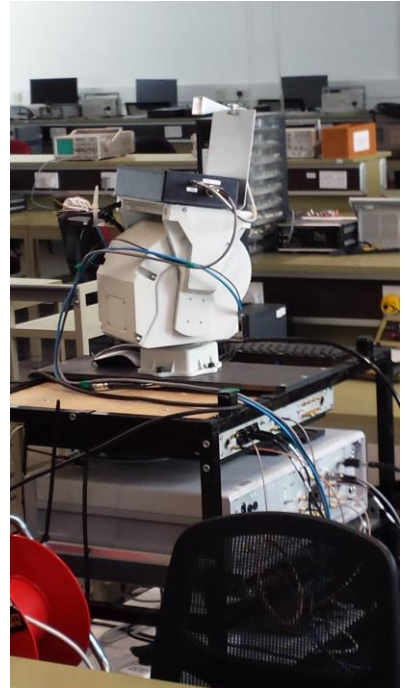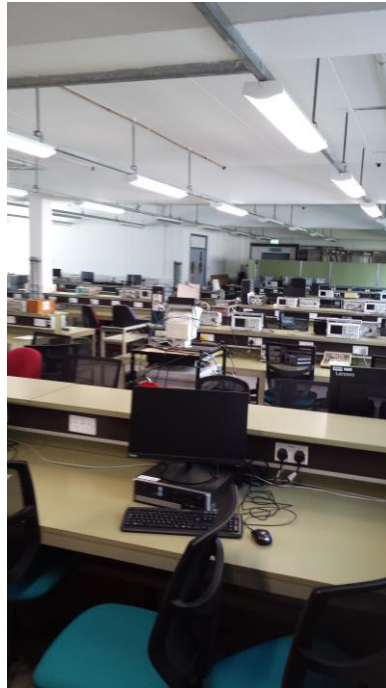
Small office Environment

Street Canyon Environment